博士論文

Nanostructure Control of Organic Semiconductor Films and Application for Photovoltaic Devices

（有機半導体薄膜中のナノ構造制御と太陽電池デバイスへの応用）

伊澤　誠一郎

Contents

Chapter 1.

General Introduction

1.1. Background and objective of this study

Organic photovoltaics (OPVs) have recently drawn much attention as a sustainable energy source due to their possible advantages such as low fabrication cost, light weight, flexibility, and large area device through a roll-to-roll production process. Photo-conversion processes in OPVs are different from inorganic photovoltaics due to intrinsic nature of organic semiconductors. After light irradiation, free charges are formed in inorganic photovoltaics. In contrast, excitons, i.e. charge pairs in one molecules which are stabilized by Coulomb attraction force, are formed in OPVs after light irradiation due to low dielectric constants of organic semiconductors. Typical diffusion length of the exciton is about 5 ~ 10 nm in the organic semiconductors. (Details in 1.2.2.) To dissociate the exciton efficiently, blend structures of electron donor and acceptor materials in active layers are often used in OPVs. The device structures are so-called mixed bulk heterojunctions (BHJs). (Details in 1.2.3.) The nanostructures in blend films in BHJs largely affect the device performances. The first reason is that the domain sizes of the donor and the acceptor are related to the exciton dissociation efficiency due to limited diffusion length of the excitons. Second, interpenetrating networks of the donor and the acceptor domains are necessary for efficient charge transport. Third, charge separation and recombination processes are influenced by the properties at donor/acceptor interface such as distance between the molecules, orientation, and energy levels. However, blend morphology of the donor and the acceptor in mixed BHJ is difficult to be controlled. Therefore ideal structures for realizing efficient photo-conversion processes in OPVs remain unclear, which limits the further enhancement of the power conversion efficiency of OPVs. (Details in 1.2.6. and 1.2.7.)

In this study, the relationship between the controlled nanostructure and photo-conversion processes in OPVs were investigated. Firstly, the nanostructures of donor/acceptor interface, especially energy structure, were controlled by combination of surface modification method and the use of bilayer devices as a model structure. The effect of difference in interfacial structure to charge separation and recombination processes were investigated (Chapter 2, 3). Secondly, domain structures of the donor and acceptor were controlled by using a dyad molecule, i.e. covalently attached donor and acceptor (Chapter 4, 5, 6, 7). The molecular designs of dyads affected the domain structures in the film, and the effects of difference in the nanostructure to the device performances were studied.

The thesis includes 8 chapters. I give the general introduction of OPVs and explain about the importance of nanostructure control for improving the device performances of OPVs in Chapter 1. In Chapter 2, a surface functionalization method of organic semiconductor films by fullerene-based surface modifiers is described. Fullerene derivatives with semifluoroalkyl chains bearing one of five different functional groups were synthesized. Fluoroalkyl chains have low surface energy, thus they were expected to form surface segregated monolayers (SSMs) spontaneously. In Chapter 3, energy levels of the first monolayer at the D/A interface was controlled by using the combination of SSM and bilayer device structure. The correlation between the energy landscape at D/A interface and photoelectric conversion process was investigated. In Chapter 4, low band gap dyad molecules with diketopyrrolopyrrole (DPP) units as the donor and a fullerene group as the acceptor were synthesized to match the molecule's absorption spectrum with the solar spectrum. The number of thiophene rings in the donor part was varied in order to tune the structure of the films. In Chapter 5, an effect of length of alkyl side chains in dyad molecules to the packing structure and device performance were examined. In chapter 6, a new dyad molecule with naphthalene diimide (NDI) as the acceptor was synthesized. The crystal structure of the dyad with NDI which has planar π-plane was investigated. Finally, the morphological stability on dyad molecules was studied in Chapter 7.

The goal of this study is to get the information about the nanostructure which can improve the device performances of OPVs further. I give the conclusion and future perspective of this study in Chapter 8.

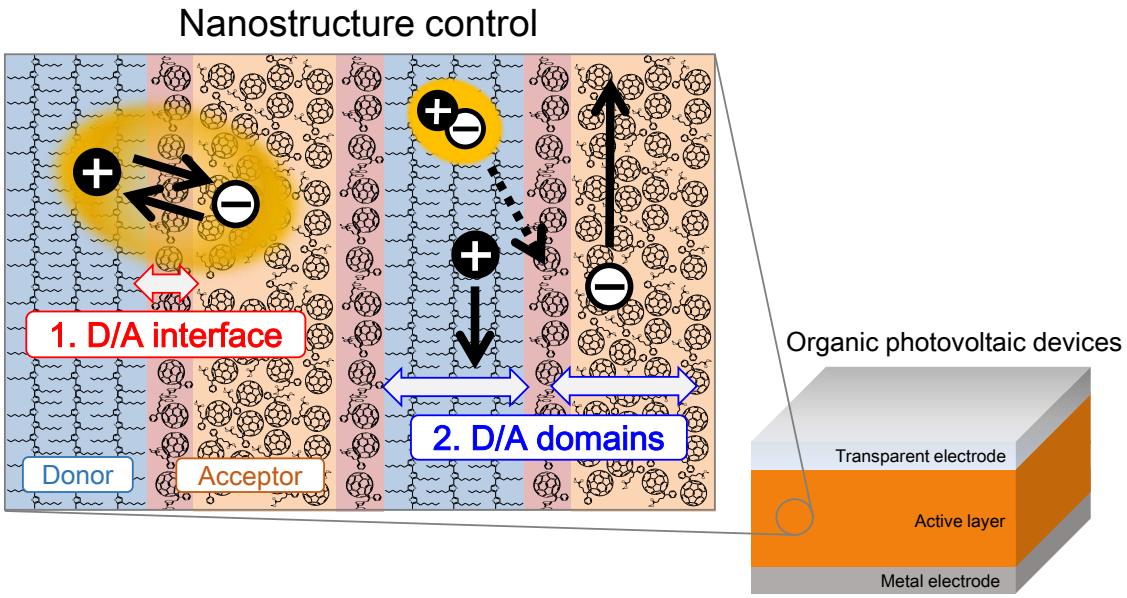

Figure 1.1. Schematic image of nanostructure control at the donor/acceptor interface and donor/acceptor domains in this study.

1.2. Introduction of organic photovoltaic devices

1.2.1. Background of organic photovoltaic devices

Up to now, main energy sources in human life are fossil fuels such as petroleum, coal or natural gas which cannot be regenerated. However, due to rapid consumption of fossil fuels in a modern life, residual amount of those become insufficient. Furthermore, consumption of fossil fuels causes environmental issues such as global warming or air pollution. Therefore, development of sustainable energy sources such as wind power, biomass power, geothermal power or solar energy conversion system is highly desired. Among these systems, photovoltaics are considered to be one of the most promising systems among them because solar energy is abundant and widely distributed in the world. Photovoltaics based on Silicon,[1] Copper Indium Gallium Selenide (CIGS),[2] dye materials,[3] organic semiconductors,[4] etc. are widely studied.

Crystalline Si solar cells are the most dominant types of photovoltaics at present.[5] Single crystal Si solar cells have achieved the world record of 25 %.[6] However, due to the high cost of fabrication processes in single crystal Si, photovoltaics still occupy less than 0.1 % of the total energy supply in the world.[5]

Organic photovoltaics (OPVs) have recently drawn much attention due to their possible advantages such as low fabrication cost, light weight, flexibility, and large are device through a roll-to-roll production process.[4] Up to now, the highest efficiency of about 10 % was reported in laboratory scale.[7] Further enhancement of the efficiency and solving the problems such as stability or reproducibility are required for the practical application of OPVs.

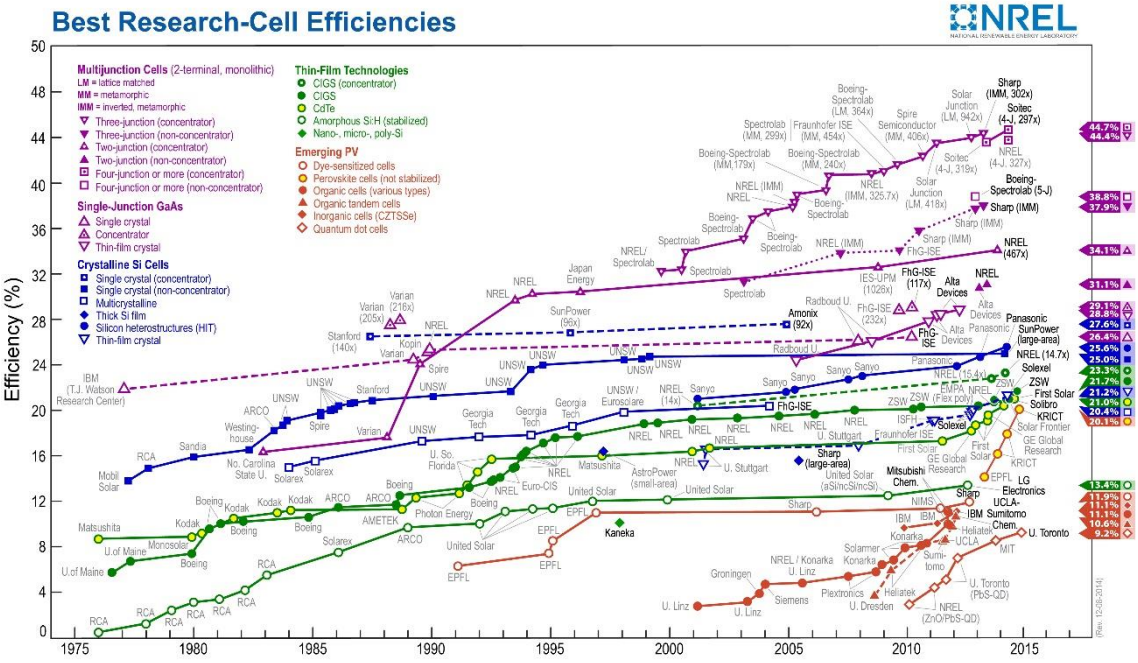

Figure 1.2. NREL research cell eficiency records in 2014.[6]

1.2.2. Working principle of organic photovoltaic devices

The photo-conversion process in OPVs is as follows, and schematic image of a working principle is depicted in Fig. 1.3. When the light is irradiated, organic semiconductors absorb solar light, and an exciton which is stabilized by strong Coulomb attraction is formed. Then, the exciton migrates to a donor and acceptor interface and is dissociated into a free electron and hole. These electron and hole are transported in acceptor and donor materials respectively and collected in electrodes.

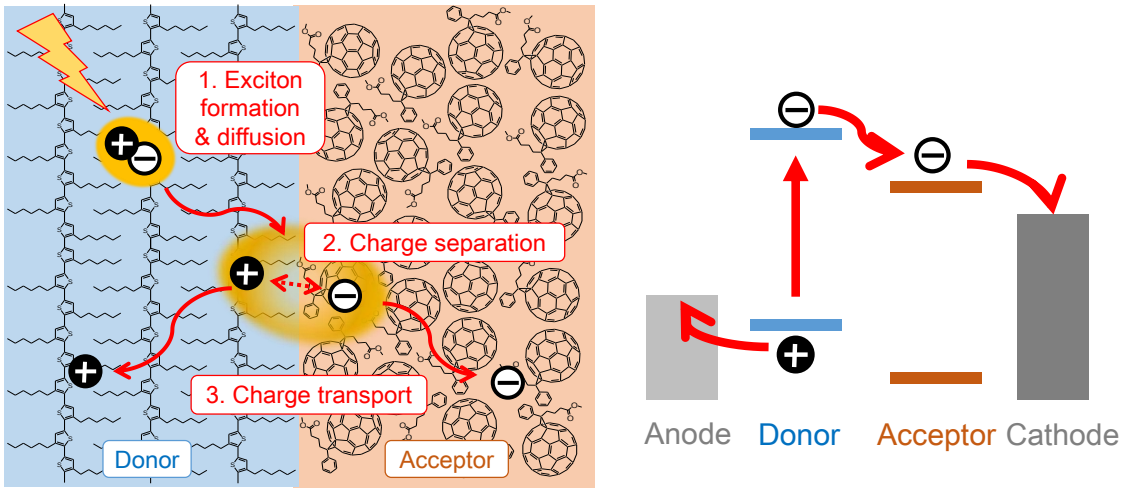

Figure 1.3. Schematic image of a working principle in OPVs.

Exciton formation and diffusion

The exciton is formed by light irradiation which excites the electron from the highest molecular orbital (HOMO) to the lowest unoccupied molecular orbital (LUMO) in organic semiconductors. This exciton in organic semiconductors is stabilized by Coulomb attraction force due to their low dielectric constants ($\varepsilon_r \approx 2$~4).[8] This is referred as Frenkel type exciton. The typical exciton binding energy in organic semiconductors is 0.1~1 eV[9] (See Table 1.1). The exciton is required to be dissociate to free charges within its lifetime. Heterojunction of the donor and the acceptor (D/A) is used in organic photovoltaics to dissociate this exciton. The exciton moves around in organic semiconductor by Förster energy transfer process. Typical exciton diffusion length is about 5 ~ 10 nm in organic semiconductors.[10] Thus, the size of the donor and the acceptor domains should be controlled to ≈ 10 nm scale, otherwise the exciton relaxes to the ground state without being separated to the free charges before it reaches D/A interface.

Table 1.1. Exciton binding energies of organic semiconductors. Reprinted with permission from ref. 9. Copyright 2003, Springer-Verlag.

Molecule	Binding energy E_B (eV)
Alq_3	1.4
α-NPD	1.0
Anthracene	1.0
PTCDA	0.8
CuPc	0.6
α-6T	0.4
MEH-PPV	$0-0.6$
PPV	$0.05-1.1$
Alkoxy-PPV	0.36
PFO	0.3
PPPV	0.4
DO-PPP	≤ 0.2
PT	0.6
PA	0.5
PDA	0.5

Charge separation

After the exciton forms at ether donor or acceptor materials, the exciton in the donor is quenched by the electron transfer from the donor to the acceptor, or the exciton in the acceptor is quenched by the hole transfer from the acceptor to the donor. The charge transfer does not necessarily generate free charges because Coulomb attraction force between the charge pairs is large and effective in long range due to the low dielectric constants of organic semiconductors. It was reported the estimated Coulomb capture length was about 4 nm.[8] Thus, charge transfer state (CTS), which is defined as electron hole pairs stabilized by Coulomb attraction force at the

donor/acceptor (D/A) interface, is potentially formed before the complete charge separation. This CTS could decay to ground state with a lifetime (geminate recombination), resulting in the loss of the photocurrent. The charge separation process needs dissociation of the CTS into free charges.

Although Coulomb attraction is large in the organic semiconductor film, some OPVs realized high internal quantum efficiency of nearly 100 %.[11] How charge pairs escape from Coulomb attraction at near D/A interface still remains a big mystery.[12] Recently, the mechanism for the free charge formation is one of the hottest topics in the research field of organic photovoltaics.[13] It was proposed that hot (delocalized) CTS could be important for the efficient charge separation.[14] There are several studies on ultrafast spectroscopy showing that the excess energy assist the free charge formation.[15] In contrast, Vandeval et al. reported that the excitation of relaxed CTS could be efficiently separated into free charges without the need for excess energy.[16] Some groups proposed the formation of gradient in free energy landscape at the near D/A interface because of widening the energy gap due to the disorder of the materials.[17] It was speculated that these unintentional "cascade" energy landscape at the interface could push the energy of CTS close to charge separated state, resulting in the highly efficient charge separation.[18] Many possible mechanisms for free charge formation have been proposed until now, but it is still ongoing debate.[13]

Charge transport and charge collection at the electrodes

After charge dissociation, free electrons and holes are transported in the donor and the acceptor domains respectively. Two kinds of currents flow by different mechanisms, referred as a drift current by a built in potential in the devices and a diffusion current by the gradient of the concentration of charges.[19] When the free charge pairs encounter at the D/A interface, CTS formed and could decay to ground state (non-geminate (or bimolecular) recombination). The kinetics of these processes strongly relate to the device parameter, such as fill factor and open circuit voltage which are mentioned later.[20] To suppress non-geminate recombination process, materials with high mobility are desirable and the mobility of the donor and the acceptor should be balanced.

Finally, the free charges are collected at the electrodes. The contact between electrodes and organic layer should be Ohmic by the choice of appropriate electrodes and buffer layers to reduce contact resistance.

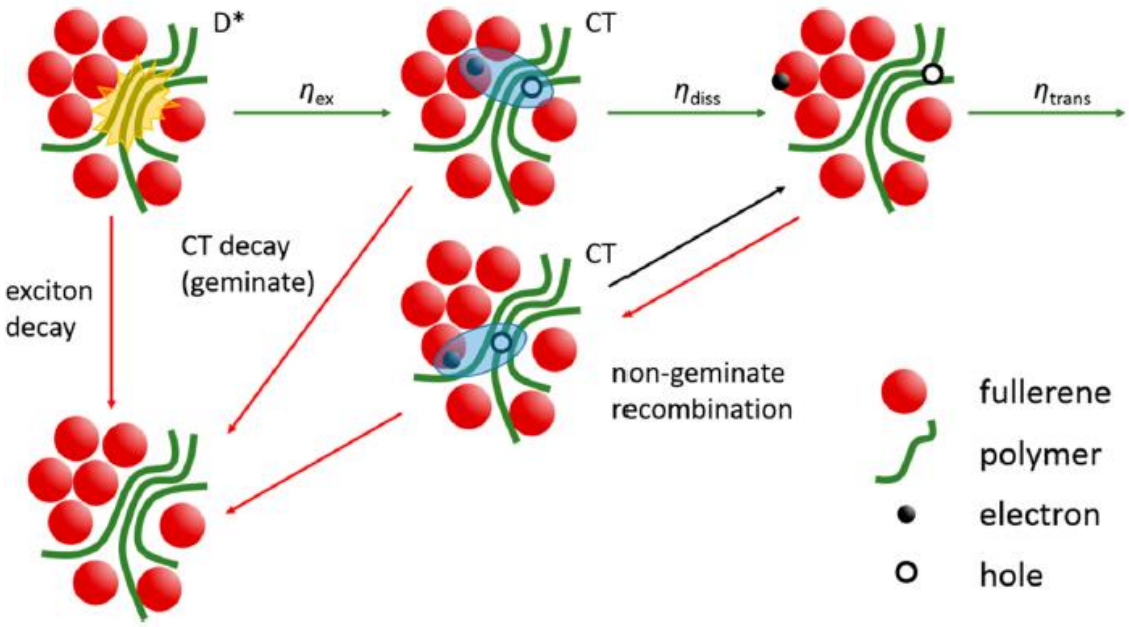

Figure 1.4. Schematic representation of charge separation and recombination processes. Reprinted with permission from ref. 21. Copyright 2013, American Chemical Society.

1.2.3. Historical change of device structure and fabrication method of organic photovoltaic devices

History of device structure

Bilayer devices

The research for organic photovoltaic devices firstly started from the single layer device which had electrode/organic semiconductor/electrode configuration, but the exciton could not be separated efficiently due to its large binding energy, the efficiency of the single layer devices was quite low.[21] In 1986, Tang reported a two layer organic photovoltaic cell, which consisted of copper phthalocyanine (CuPc) and perylene tetracarboxylic (PV) derivative layers fabricated by a vacuum deposition, achieving over 1 % (Fig. 1.5).[22] It was found dissociation of exciton was efficiently occurred at D/A heterojunction interface because the difference of electron affinity between two organic semiconducting materials provided the energy for charge separation. Later, Sariciftci et al. firstly reported conjugated polymer (poly-phenylenevinylene)/ fullerene (C_{60}) heterojunction devices.[23]

Exciton diffusion length of organic semiconductor is limited to several nanometer as mentioned above, thus the exciton forms at far away from the donor/acceptor interface cannot contribute to the photocurrent. Therefore quantum efficiency of bilayer device is generally low.

Recently, bilayer device is used for model structures to investigate relationship between D/A interfacial structures and the device performance because bilayer device has flat interface.[24] For

example, Tada et al. reported insertion of molecular dipole moment at the D/A interface induced change of open circuit voltage.[25] The details are explained in 1.2.6.

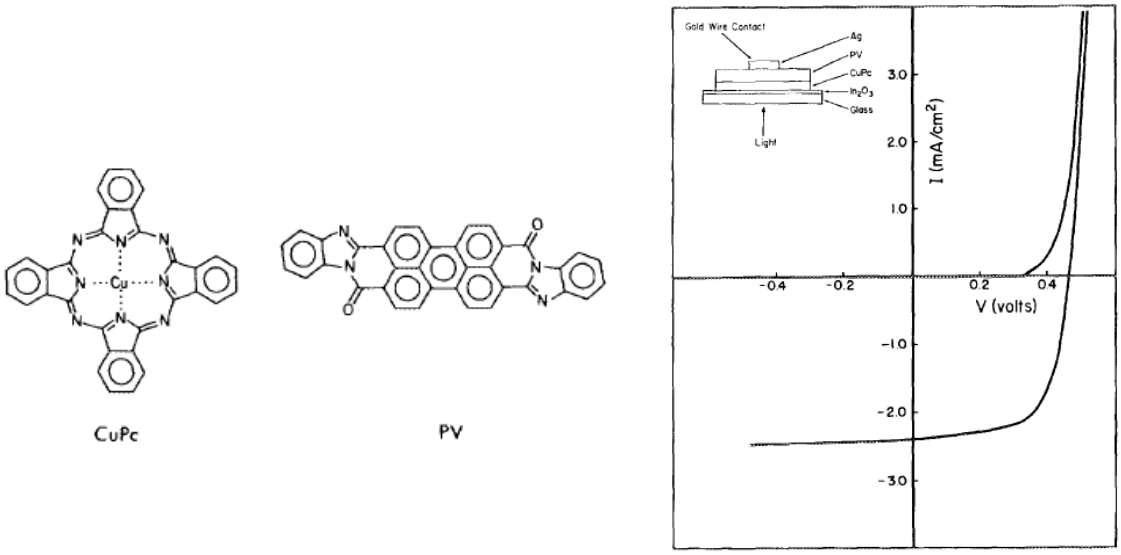

Figure 1.5. Chemical structures of CuPc and PV, and *J-V* curve of the bilayer device reported by Tang. Reprinted with permission from ref. 25. Copyright 1986, AIP Publishing LLC.

Bulk heterojunction (BHJ) devices

The effective light harvesting region is limited to thin layer near the D/A interface in the bilayer device due to short diffusion length of the exciton in organic semiconducting materials. This problem was solved by blending donor and acceptor in the film, so-called bulk heterojunction (BHJ). This BHJ concept increases interfacial area of the donor and the acceptor and constructs interpenetrating network of them at the same time. Therefore, BHJ realizes efficient dissociation of the exciton and charge transport.

Hiramoto et al. firstly reported that three layered organic solar cell with a mixed BHJ structure. These three layers consisted of *n*-type perylene tetracrboxylic derivative layer, *p*-type metal free phthalocyanine and middle layer of mixture of these two dye made by co-sublimation.[26] They observed increase of short circuit current due to the increase of interfacial area of the donor and the acceptor.

In 1995, Yu et al. reported the solution processed polymer bulk heterjunction photovoltaic device, which consisted of poly(2-methoxy-5-(2'-ethyl-hexyloxy)-1,4-phenylene vinylene) (MEH-PPV) and fullerene derivatives, made by spincoating (See Fig. 1.6).[27]

The BHJ has improved efficiency of organic solar cells due to increase of interfacial area of donor and acceptor. The polymer BHJ solar cells reached power conversion efficiency over 10 % so far.[7] But, the device performance of the BHJ device is largely affected by mixing morphology of the donor and the acceptor.[28] Because domain sizes of each component must be smaller than

the exciton diffusion length to separate all exciton formed by light absorption. At the same time, percolated charge transport pathways must be connected to collect the separated charges. However, control of mixing morphology of the materials in the films are generally difficult, therefore this causes problems in stability and reproducibility, and limits further enhancement of device performance. The details are described in 1.2.7.

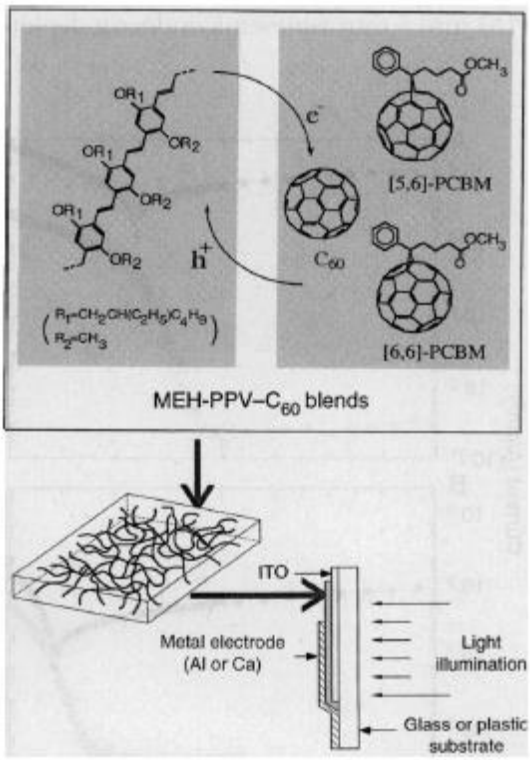

Figure 1.6. Schematic image of photovoltaic cell fabricated by bulk heterojunction. Reprinted with permission from ref. 31. Copyright 1995, American Association for the Advancement of Science.

Fabrication method

General device configurations

The organic photovoltaic device generally consists of a transparent electrode, an active layer, buffer layers (electron or hole transporting layer) and a metal electrode. Indium tin oxide (ITO) is generally used for the transparent electrode. The most generally used structure is ITO/hole transporting layer/active layer/Al. Poly(3,4-ethylenedioxylenethiophene):poly(styrenesulphonic acid) (PEDOT:PSS), MoO_3 and V_2O_5 are generally used for the hole transporting layer. Inverted structure whose device configuration is ITO/electron transporting layer/active layer/hole transporting layer/high work function metal is sometimes used. ZnO or TiO_2 are used for electron transporting layer, PEDOT:PSS, MoO_3 and V_2O_5 are used for the hole transporting layer, and Ag or Au are used for the metal electrode in the inverted device. Metal electrodes are generally

prepared by vacuum evaporation, metal oxide layers are prepared by a sol-gel method or vacuum evaporation, and PEDOT:PSS layer was prepared from spincoating of an aqueous solution.

Bilayer device

The active layer of the bilayer device has been conventionally prepared by vacuum evaporation of small molecules successively. Therefore, the active materials for the bilayer device prepared by vacuum evaporation are limited to volatile small molecules because semiconducting polymers cannot be evaporated.

Recently, some methods for the lamination of polymer layers were developed for the fabrication of the bilayer OPVs. Huang et al. reported so-called poly(dimethylsiloxane) (PDMS) stamp method for the bilayer device fabrication.[29] They spincoated polymer layer onto surface treated PDMS, then transferred polymer layer onto target substrate. Wei et al reported lamination method of polymer layer, called contact film transfer (CFT), for the fabrication of organic field effect transistor (See Fig. 1.8).[30] They spin-coated polymer layer on the top of PEDOT:PSS coated glass substrate, and then placed this substrate, upside down, on to another film, and dropped water on the edge of the film. Water selectively dissolve sacrificial layer (PEDOT:PSS) and polymer layer was transferred on the film. Tada et al. applied this method to bilayer organic photovoltaic device fabrication.[25] CFT method provides well defined interface because no heat and pressure are applied during lamination, so this method is appropriate for controlling interfacial structure of the donor and the acceptor.

Bulk heterojunction (BHJ) device

The device configuration of the BHJ device is same as the bilayer device other than the structure of the active layer. The active layer is generally prepared by spin-coating of mixed solution of donor and acceptor materials. The morphology of the D/A domains in the mixed films strongly depends upon the fabrication conditions, such as the mixing ratio, organic solvent, additives, spin-coating speed and thermal annealing conditions. Hence, optimizations of fabrication conditions are necessary. The details will be discussed in 1.2.7.

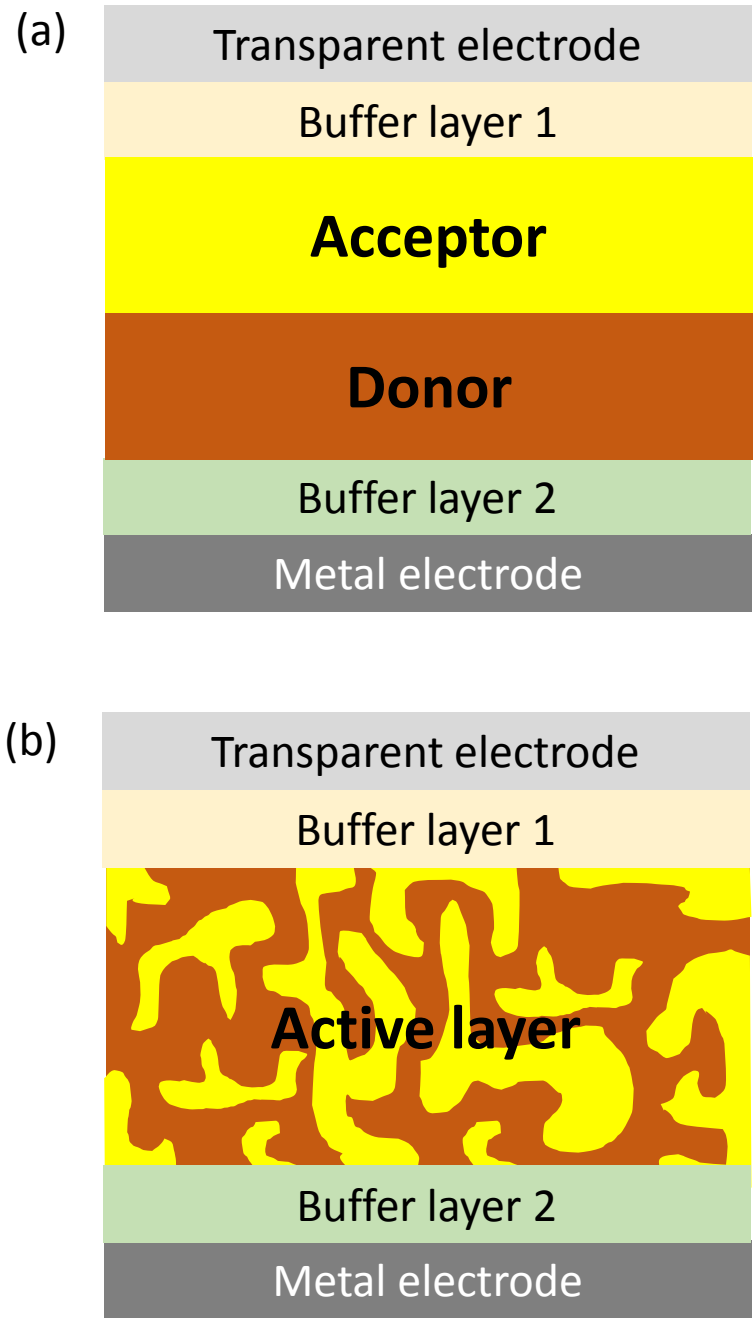

Figure 1.7. Schematic images of the device structures (a) bilayer and (b) BHJ.

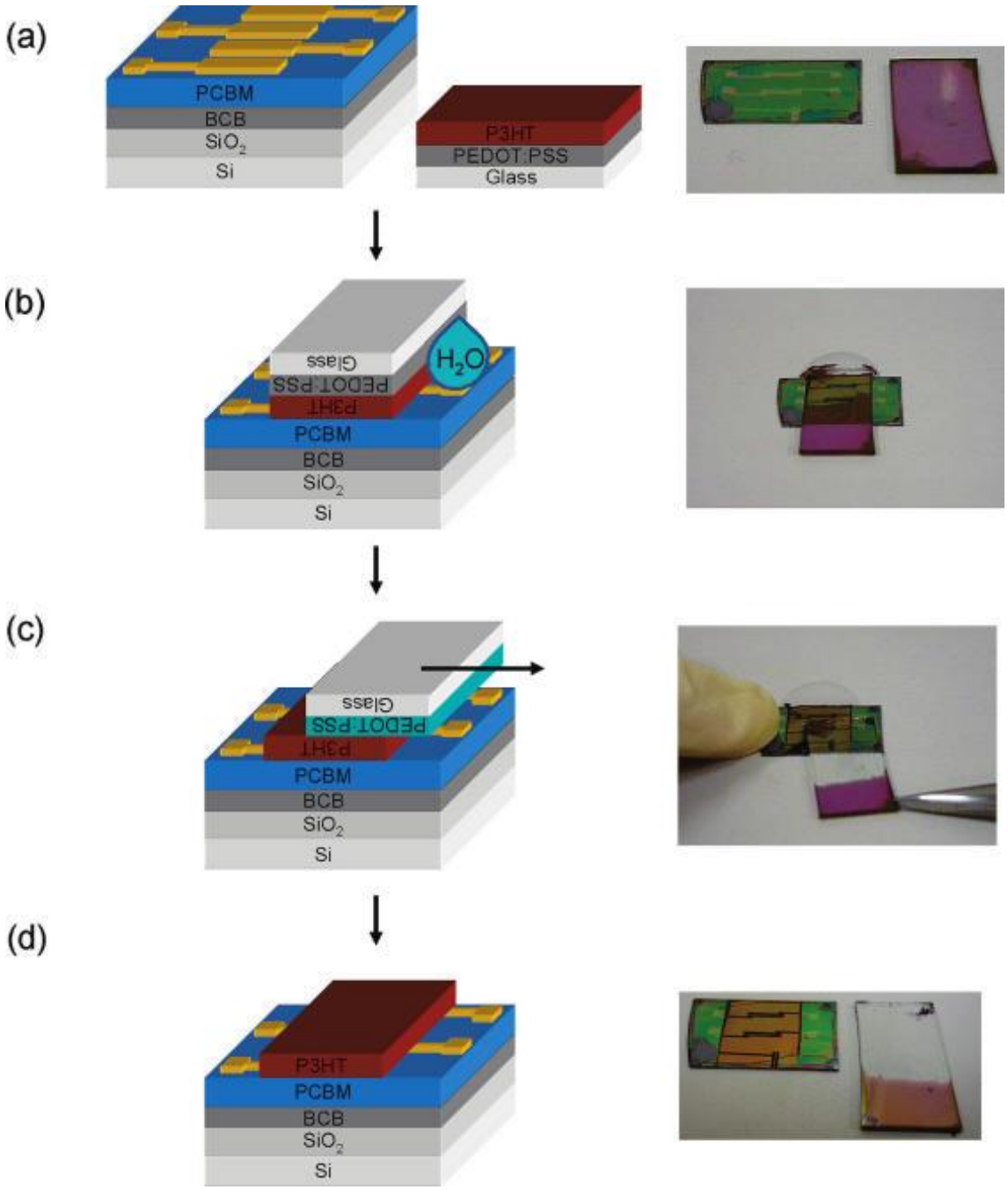

Figure 1.8. Schematic image of contact film transfer (CFT) method. Reprinted with permission from ref. 34. Copyright 2009, American Chemical Society.

1.2.4. Evaluation method of organic photovoltaic devices and physical meaning of device parameters

Evaluation method

The photovoltaic devices are evaluated by Power conversion efficiency (PCE) and External quantum efficiency (EQE)

Power conversion efficiency (PCE)

Power conversion efficiency (PCE) is calculated by *J-V* characteristic under irradiation of simulated solar light. The spectrum of light source is mainly adjusted to that of the sun light on the surface of earth at the incident angle of 48.2°, called Air Mass (A.M.) 1.5, and their intensity is generally adjusted to 100 mW cm^{-2}. Typical *J-V* characteristic is shown in Fig. 1.9. When the light is irradiated, *J-V* curve shifted to downward. The current at zero voltage is called short circuit current density (J_{SC}) and the voltage at zero current is called open circuit voltage (V_{OC}) under light irradiation. The maximum output power density (P_{max}) is the product of J_{max} and V_{max}.

$$P_{\max} = J_{\max} \times V_{\max} \quad \text{eq. 1}$$

The fill factor (FF) is defined by the ratio between the incident light power density (P_{in}) and the product of J_{SC} and V_{OC}.

$$\mathrm{FF} = \frac{J_{\mathrm{SC}} \times V_{\mathrm{OC}}}{J_{\max} \times V_{\max}} \quad \text{eq. 2}$$

The PCE of the photovoltaic cells is determined by the following formula,

$$\mathrm{PCE} = \frac{J_{\max} \times V_{\max}}{P_{\mathrm{in}}} \times 100 = \frac{J_{\mathrm{SC}} \times V_{\mathrm{OC}} \times \mathrm{FF}}{P_{in}} \times 100 \quad \text{eq. 3}$$

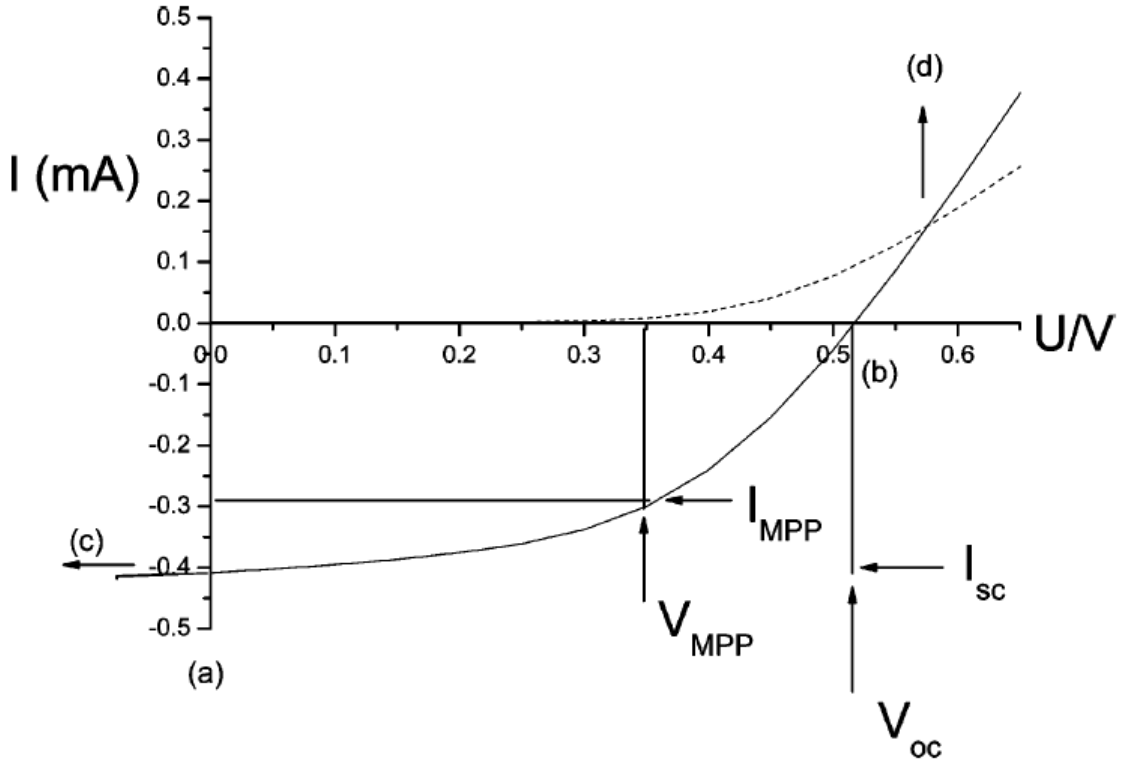

Figure 1.9. *J-V* characteristics in the dark (broken line) and under the light irradiation (solid line). Reprinted with permission from ref. 4. Copyright 2007, American Chemical Society.

External quantum efficiency (EQE)

External quantum efficiency (EQE) of the photovoltaic device is evaluated under monochromatic light illumination and is defined as the following formula,

$$\mathrm{EQE} = \frac{n_{\mathrm{electron}}}{n_{\mathrm{photon}}} = \frac{J_{\mathrm{SC}}}{P_{\mathrm{in}}}\frac{hc}{\lambda e} \quad \text{eq. 4}$$

Where n_{electron} is the number of electrons extracted from the device, n_{photon} is the number of photon irradiated to the device, h is Plank constant, c is the speed of light, λ is the wavelength of the monochromatic light, and e is elementary charge.

Internal quantum efficiency (IQE) of the device is calculated from EQE and the number of photon absorbed in the active layer.

Physical meaning of V_{OC}, J_{SC} and FF

Open circuit voltage (V_{OC})

In organic photovoltaic devices, V_{OC} has empirical linear dependence on the difference of the highest occupied molecular orbital (HOMO) of donor (p-type semiconductor) and the lowest unoccupied molecular orbital (LUMO) of acceptor (n-type semiconductor). Scharber et al.

reported linear correlation between onset of oxidation potential (HOMO level) of the donor polymer with the combination of same acceptor of PCBM (Fig. 1.10).[31] They reported V_{OC} followed empirical equation using -4.3 eV for LUMO of PCBM.

$$eV_{OC} = E_{Donor}^{HOMO} - E_{Acceptor}^{LUMO} - 0.3\ V \quad \text{eq. 5}$$

Recently, it was reported that V_{OC} was determined by the energy of charge transfer state (CTS), which is Coulombically bound charge pairs at the donor/acceptor interface. V_{OC} is expressed by the energy of CTS and the balance of charge generation and recombination by following equation,[32]

$$eV_{OC} = E_{CT} + nkT\ln\left(\frac{J_{ph}(V_{OC})}{J_{00}}\right) \quad \text{eq. 6}$$

Where E_{CT} is the energy of CTS, n is the ideality factor, k is the Boltzmann constant, T is the temperature, $J_{ph}(V_{OC})$ is photogeneration rate of the charge density under open circuit conditions, and J_{00} is the pre-exponential factor of the reverse saturation current density. The energy of CTS is expressed by following equation assuming the point charges,[32a]

$$E_{CT} = E_{DA} - \frac{e^2}{4\pi\varepsilon_0\varepsilon_r d} \quad \text{eq. 7}$$

Where E_{DA} is the energy level difference of HOMO of the donor and LUMO of the acceptor, ε_0 is the vacuum dielectric constant, ε_r is the relative dielectric constant, and d is the D/A distance. Street et al. reported linear correlation between energy of CTS and measured V_{OC} of the organic photovoltaic devices (Fig. 1.11).[33] Judging from these relationships, the destabilization of CTS and the suppression of charge recombination are the key factor to increase V_{OC}.

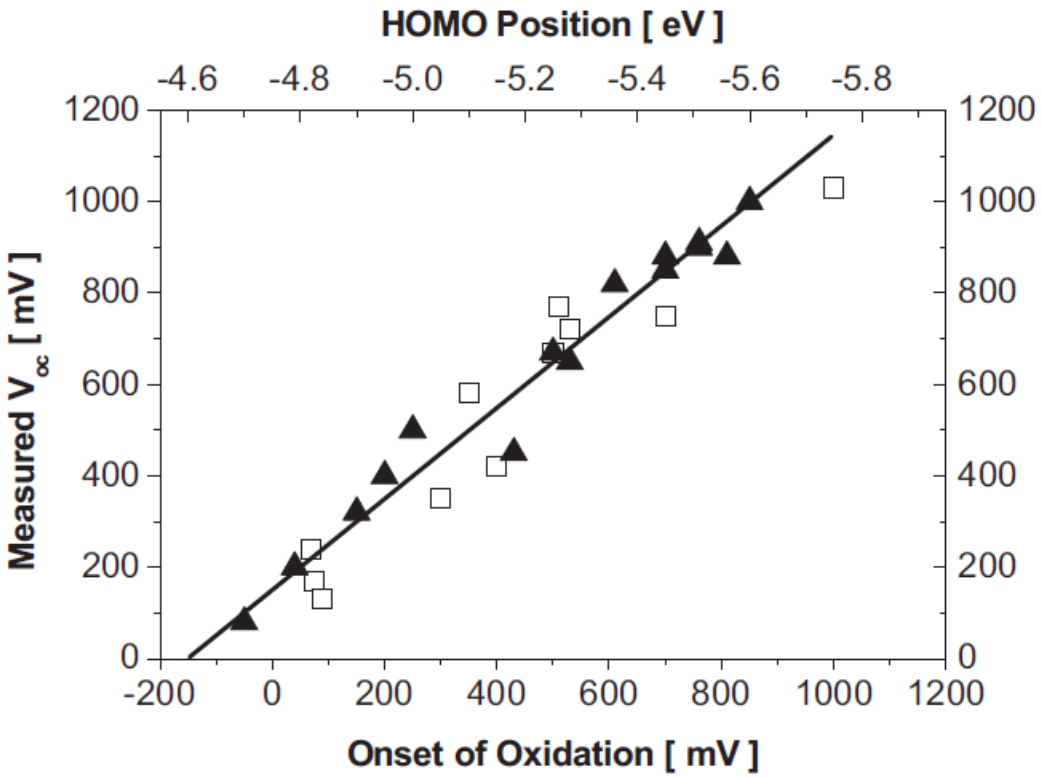

Figure 1.10. V_{OC} of different bulk-heterojunction solar cells plotted versus the oxidation potential/HOMO position of the donor polymer. The straight line represents a linear fit with a slope of 1. Reprinted with permission from ref. 35. Copyright 2006, WILEY-VCH Verlag GmbH & Co. KGaA, Weinheim.

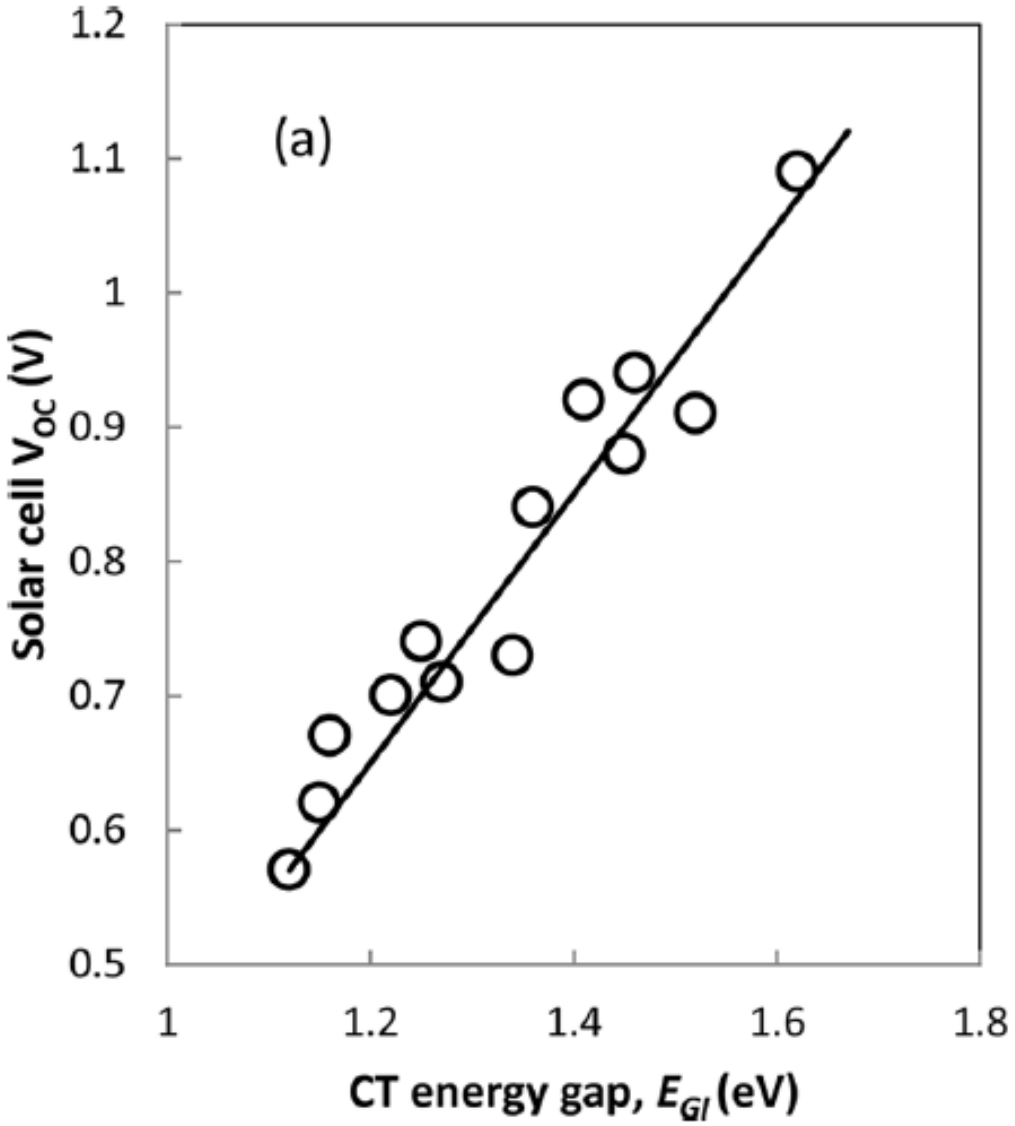

Figure 1.11. Plot of measured V_{OC} *v.s.* the energy of CTS. Reprinted with permission from ref. 38. Copyright 2014, American Chemical Society.

Short circuit current density (J_{SC})

In the ideal case of 100 % efficiency for the charge separation and no loss in the charge transport, J_{SC} is determined only by the photon absorption in the active layer. However, even at short circuit condition, which is under large internal electric field, there are loss mechanisms during charge separation and transport processes. Therefore J_{SC} also gives us the information about the charge recombinations. Generally, non-geminate recombination which occur after the charge separation is less dominant in the efficient systems reported to date, but geminate recombination before forming free charge pairs is major loss pathway at short circuit condition.[34]

Fill factor (FF)

Fill factor is determined by the bias dependence of the current flow. In general, charge carriers reaching to the electrodes decrease with the built in potential lowering to the open circuit voltage due to the charge carrier recombination. Thus, FF gives information about the bias dependence of the charge recombination. As explained in the previous section, both geminate and non-geminate recombination shows electric field dependence. Especially, non-geminate recombination during charge transporting after free charge generation is dominant at nearly V_{OC} condition.[34]

In addition, the series and parallel resistances of the device affect FF. For example, series resistance of ITO substrate sometimes limits the FF of the large area devices. The device should also avoid any electrical shorts in the active layers to increase parallel resistance.

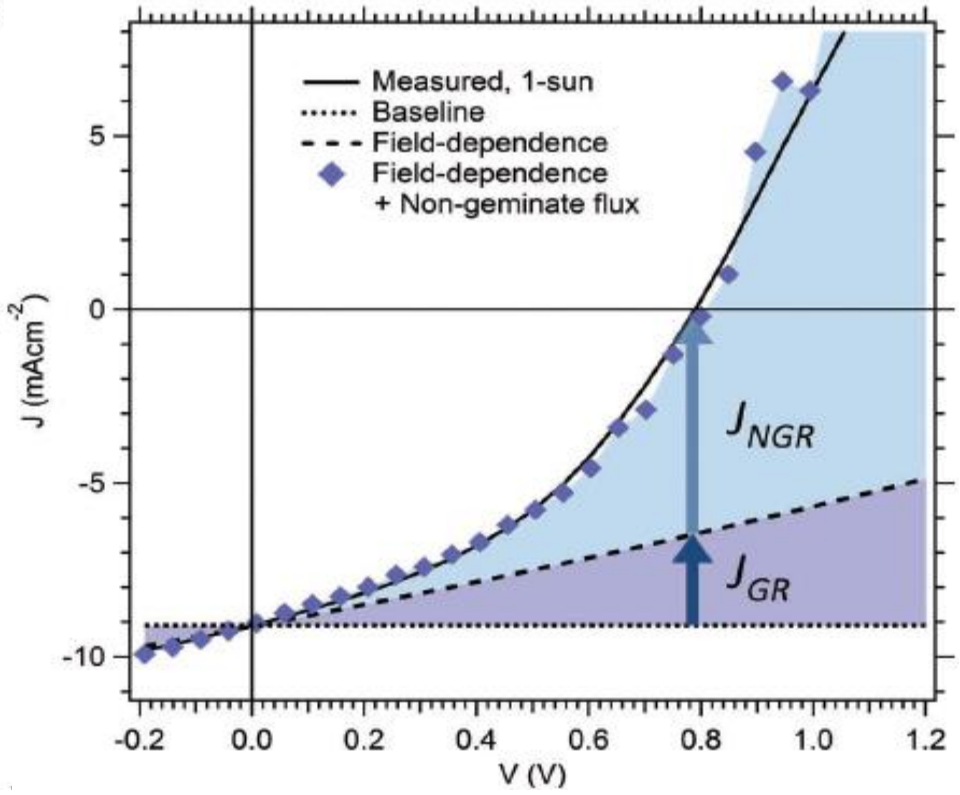

Figure 1.12. Schematic representation of field dependence of the recombination processes. J_{NGR} is the non-geminate recombination current density, and J_{GR} is geminate recombination current density. Reprinted with permission from ref. 39. Copyright 2012, WILEY-VCH Verlag GmbH & Co. KGaA, Weinheim.

1.2.5. Improvement of the efficiency by development of new materials

The power conversion efficiency of OPVs has been improved, and some groups recently achieved over 10 %.[7, 35] The main contribution for the improvement of the efficiency was developing new materials.[40]

Conjugated polymers are most commonly used materials for the electron donor. Among them, poly(3-hexylthiophene) (P3HT) is the most studied material. McCullough et al. reported synthetic method highly regioregular P3HT (rr-P3HT) by Reike or GRIM method,[36] and rr-P3HT achieved the efficiency of 4 ~ 5 %.[37] However, P3HT have a relatively large bandgap (1.9 eV), therefore this causes insufficient photon absorption. Material scientists have solved this problem by the developing new donor polymer which has appropriate energy levels match to the solar spectrum. At early stage, Mühlbacher et al. reported the alternating copolymer of cyclopentadithiophene and benzothiadiazole (PCPDTBT).[36c] The backbone of this polymer consisted of electron rich and electron deficient units, therefore PCPDTBT showed small bandgap of 1.5 eV due to strong intramolecular donor acceptor interactions. PCPDTBT showed the power conversion efficiency of 5.5 % when a few amount of alkanedithiols was added into the solution used for spincoating films.[38] Many electron withdrawing units such as benzothiadiazole (BT), diketopyrrolopyrrole (DPP) or isoindigo etc. and many electron donating units such as cyclopentadithiophene (CP), carbazole or benzodithiophene (BDT) etc. have been developed.[39] Many groups synthesized so many polymers with the combination of these monomer units. Another strategy for reducing bandgap is introducing a quinoid resonance structure into a polymer backbone. Yu et al. synthesized copolymers of thienothiophene (TT) and BDT.[40] The polymers had the bandgap of 1.6 eV. One of these polymers, called PTB7, showed the efficiency of 6.7 %.[41] Cao et al. reported PCE of 9.2 % by using PTB7 after optimizing the device configuration.[42] PTB7 is now becoming a new benchmark polymer with high efficiency, and the polymer which had similar structure with PTB7 achieved the power conversion efficiency over 10 %.[35]

Besides the conjugate polymers, conjugated molecules (or oligomers) are also used as donor materials. The use of a molecular based system can avoid many problems with polymers such as molecular weight distribution, batch-to-batch variation, end group contamination, and difficulty in purification. Therefore, molecular based systems have advantages on reproducible fabrication of the devices. To control the energy levels of conjugated molecules, intramolecular donor acceptor interactions are also used for the design strategy as same as the conjugated polymer cases. Nguyen et al. reported DPP based oligomers showing the efficiency of 4.4 %.[43] Bazan et al. reported efficient solution processed donor molecule called DTS($PTTh_2$)$_2$, which is the combination of thiadiazolo-pyridine and dithienosilole, showed the efficiency of 6.7 %.[44] A record of the efficiency in molecular based systems now is 9.95 % reported by Chen et al.[45] The molecular based system rapidly progressed and the efficiency is now comparable to the polymer

based systems.

The choice of the acceptor materials is rather limited than donor materials. In 1995, Wudl et al. synthesized soluble C_{60} derivative called PCBM,[46] and Heeger et al. incorporated PCBM into bulk heterojunction structure.[27] Many groups reported non-fullerene acceptors such as conjugated polymers[47] or molecules,[48] but PCBM and its corresponding C_{70} derivative ($PC_{70}BM$)[49] is still the choice for the most of the highly efficient OPVs.

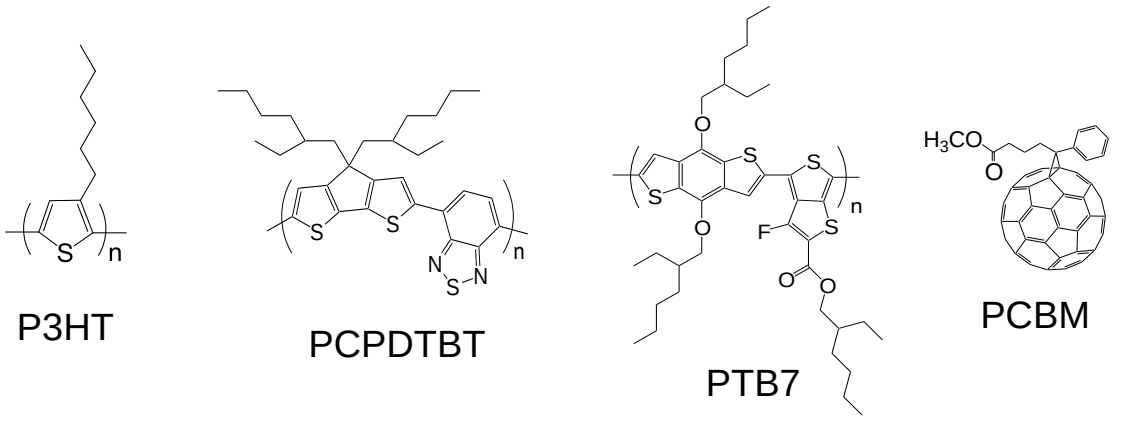

Figure 1.13. Chemical structures of P3HT, PCPDTBT, PTB7 and PCBM.

Limitation of the maximum efficiency predicted by empirical rule in organic photovoltaics

Brabec et al. estimated the attainable maximum efficiency of bulk heterojunction solar cells by using empirical rules.[31] Firstly, they plotted the relation between the HOMO position of the donor materials and V_{OC} when PCBM was used as acceptor (see Fig. 1.10). They found V_{OC} followed the relationship of eq. 5. As explained in 1.2.4, V_{OC} loss of -0.3 V from energy level difference between the HOMO of donor and the LUMO of PCBM exists and it originates from the stabilization by Coulomb potential (i.e. energy level difference between E_{DA} and E_{CT}) and a charge loss link to the bimolecular recombination.[50] To predict the maximum efficiency, FF was set to 0.65 which was a typical value in the optimized devices. Bulk heterojunction solar cells show smaller FF than other types of solar cells like c-Si because bimolecular recombination is likely to occur. They also set the EQE of 65 % at the photon energy larger than band gap. One of the origins of EQE loss was insufficient absorption of photons in the active layer with limited thickness because thicker devices caused severe bimolecular recombination. The plot of calculated power conversion efficiency versus the band gap of donor and LUMO level of donor is shown in Fig. 1.14. The estimated maximum efficiency was 10 %. As explained above, some groups already achieved power conversion efficiency over 10 %. In the current situation, the efficiency of OPVs has been getting very close to the limit of the maximum efficiency predicted by empirical rules. This means further improvement of the efficiency is very difficult only by developing the new materials which have appropriate energy levels. To go further, it is important to overcome

empirical relationships (i.e. loss in V_{OC}, FF and EQE) by different strategies. The loss processes such as charge recombination or relaxation of the exciton are strongly affected by nanostructures where these processes occur. Therefore nanostructure control in the active layer is one of the important strategies to improve the efficiency of OPVs further. The details are explained in 1.2.6 and 1.2.7.

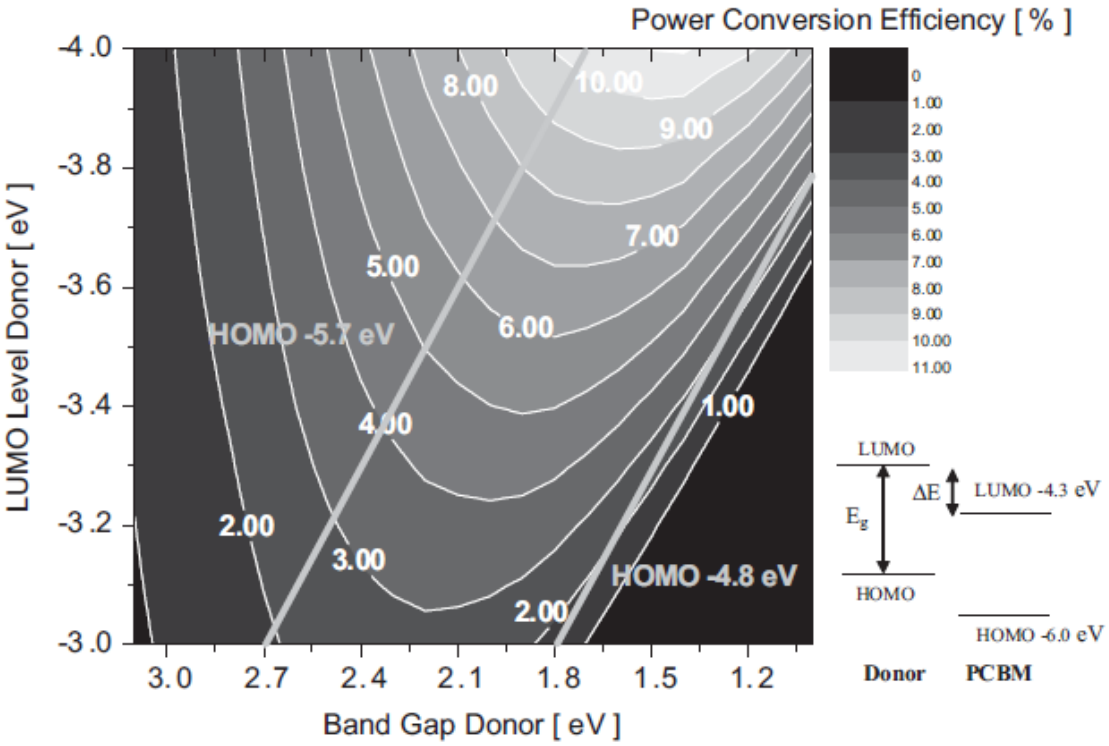

Figure 1.14. Plot of the estimated power conversion efficiency versus the bandgap and the LUMO level of the donor. Reprinted with permission from ref. 35. Copyright 2006, WILEY-VCH Verlag GmbH & Co. KGaA, Weinheim.

1.2.6. Importance of nanostructure control of donor/acceptor interface

1.2.6.1. Importance of nanostructure at donor/acceptor interface

Important processes such as charge separation and charge recombination occur at D/A interface. As explained in 1.2.2, The CT state (CTS) might form after the charge transfer, and CTS might decay to ground state by geminate recombination. Bimolecular recombination occurs via CTS, and energy of CTS directly relates to V_{OC} (See 1.2.4). Energy of CTS is affected by energy levels donor[32b] and acceptor, distance,[32a] orientation,[51] crystallinity,[52] or dipole moment.[25] Therefore these properties near D/A interface have critical effects to charge separation and recombination processes, consequently to device performances. Thus, exploring ideal D/A interfacial structure is important for further improvement of device efficiency.

Recently, some simulation works predicted change of the energy levels near at D/A interface

helped to suppress the recombinations.[53] Especially, Groves predicted by using kinetic Monte Carlo simulation that thin cascade layer (1 nm) substantially suppressed geminate recombination (See Fig. 1.15).[54]

However, modifications or investigations of the properties at the D/A interface in mixed BHJ devices, which are the most widely used device structure in OPVs, is generally difficult because the D/A interface is buried and exist randomly inside the film. Some have tried to modify D/A interface in bilayer devices instead of mixed BHJ devices to investigate the relationship between nanostructures and device performances as explained in the next section.

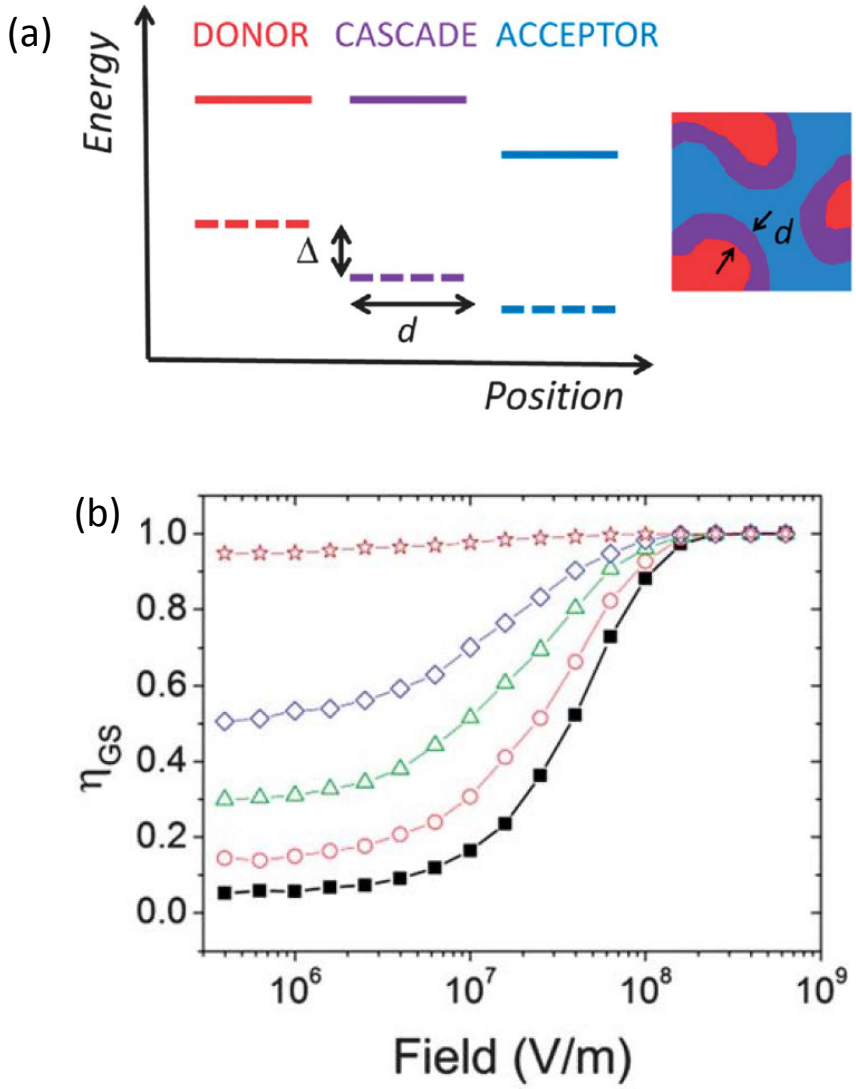

Figure 1.15. (a) Schematic energy diagrams of a donor-cascade- acceptor heterojunction (left) and image of blend morphology (right). (b) Plots of predicted charge separation efficiency (η_{GS}) versus electric field. Cascade thickness *d* is 1 nm, and energy difference Δ is 0 (black square), 50 meV (red circles), 100 meV (green triangles), 150 meV (blue diamonds) and 300 meV (purple stars). Reprinted with permission from ref. 64. Copyright 2013, Royal Society of Chemistry.

1.2.6.2. Modification of donor/acceptor interface

Several groups have tried to use bilayer devices as model structures to investigate relationship between nanostructures at D/A interface and the device performance. The reason of using the bilayer devices for D/A interfacial modification is a possibility to get layered structures. To get clear relationships between nanostructures and the device performance, surface modifications must be well-controlled. Some surface modification methods, which can form uniform and thin layers, will be explained in the next section, and finally some works about the modification of the D/A interface will be introduced.

Surface modification of organic semiconductor films

Vacuum evaporation is the easiest way to get layered structures. However, materials which can be used in evaporation are limited to volatile small molecules. Another disadvantage is a difficulty in obtaining uniform thin films because small molecules tend to aggregate due to their high crystallinity.

Spin-coating is generally used for coating of organic films. Successive spin-coating is needed to get layered structure, but organic solvents dissolve bottom layer or cause intermixing.[55] To avoid this, Friend et al. developed a fixation method of organic films by photo-crosslinking (See Fig. 1.16).[56] They spin-coated mixed solution with azide compounds, then photo-crosslinked after film formation. By using this method, they can spin-coat successively without dissolving bottom layer. Another choice for obtaining layered structure by spin-coating is using orthogonal solvents such as aqueous solvents or fluoro-solvents. These solvents do not dissolve the bottom layer.

Evaporation and spin-coating are rather easy methods but it is difficult to obtain very thin layers like monolayers by using them. Self-assembled monolayers (SAMs) are widely used for constructing densely packed monolayers (See Fig. 1.17).[57] SAMs rely on specific chemical interactions between the surface and the modifiers, such as thiol-metal or Si-O-Si bond formation. By placing functional groups at the other end of the modifiers, the SAM surfaces can be decorated with various chemical groups. However, SAMs are limited to metal or metal oxide surfaces in principle.

Wei et al. proposed that the self-segregation behavior of the molecules with low surface energy could be used to modify the surface of organic semiconductor thin films during the solution coating processes (See Fig. 1.18).[58] Surface segregated monolayers (SSMs) can be prepared easily by coating the substrate with a solution of the matrix semiconductors and surface modifiers. However, the surface functionalization of the organic semiconductor films by using SSMs was limited to low surface energy groups such as fluoroalkyl chains.

So far, there are no general methods for modifying the surface of the organic semiconductors.

Development of surface modification method itself is an important topic because it has potential to expand new application fields of organic semiconductors like biosensors.[59]

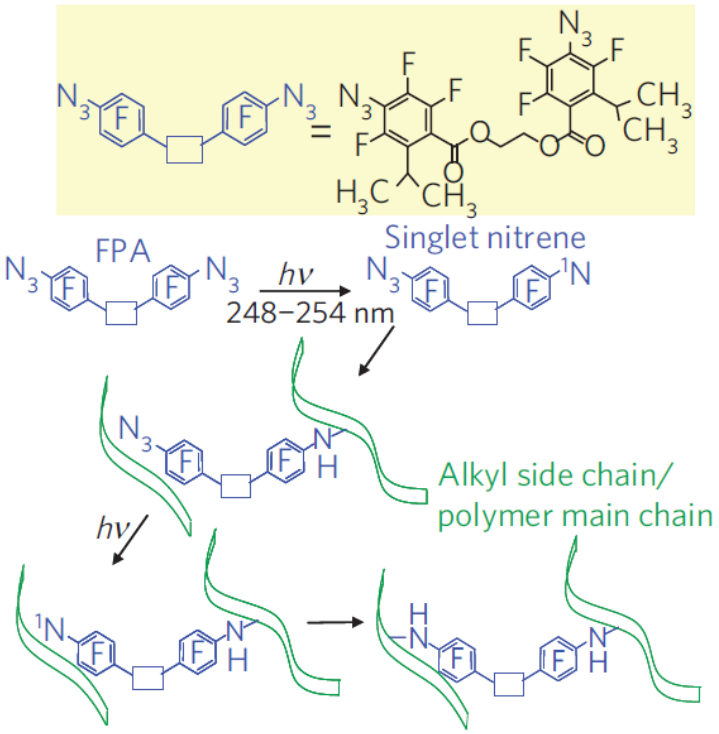

Figure 1.16. Schematic image of photocrosslinking process and chemical structure of azide compound (inset). Reprinted with permission from ref. 66. Copyright 2009, Rights Managed by Nature Publishing Group.

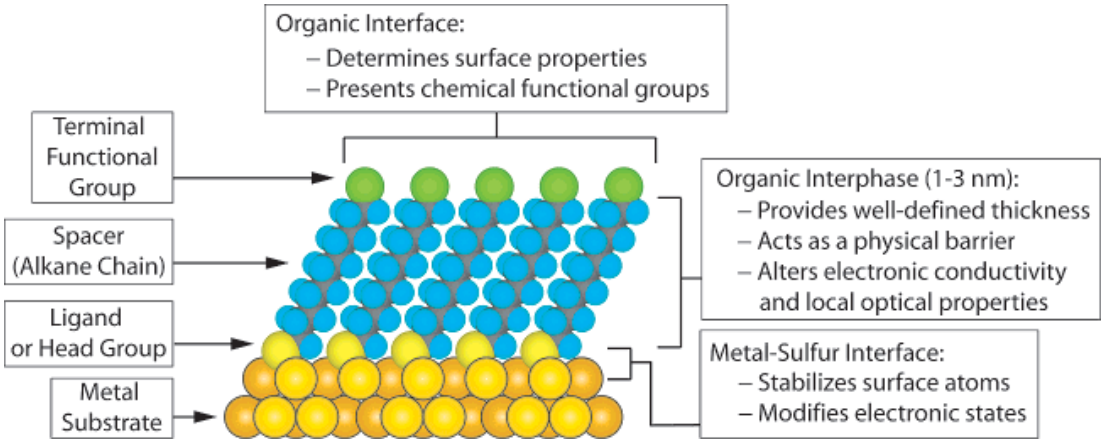

Figure 1.17. Schematic image of an ideal SAM of alkanethiolates on Au surface. Reprinted with permission from ref. 67. Copyright 2005, American Chemical Society.

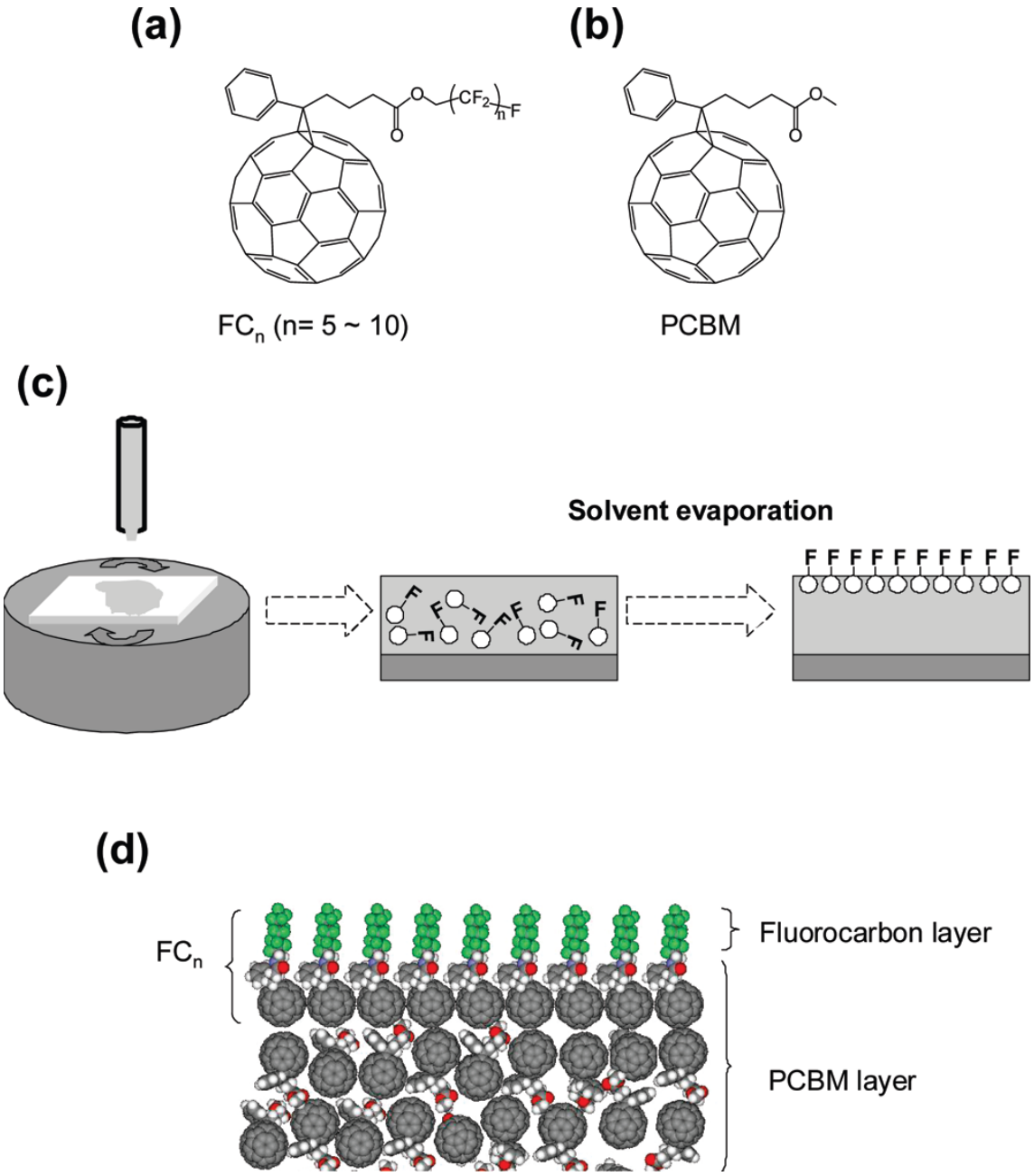

Figure 1.18. (a) Chemical structure of surface modifiers, (b) chemical structure of PCBM, (c) schematic image of SSM formation, (d) schematic image of surface segregation of fluoroalkyl chains. Reprinted with permission from ref. 68. Copyright 2009, American Chemical Society.

Modification of the donor/acceptor interface in bilayer devices

Some groups have tried to modify D/A interface in bilayer structure and investigated the relationships between nanostructures such as dipole moment, distance or energy levels and device performances.

Goh et al. investigated the effects of dipole moment at the D/A interface in the hybrid organic–inorganic bilayer devices.[60] They used TiO_2 as the acceptor and P3HT as the donor and the surface of TiO_2 was modified by using SAMs of *para*-substituted benzoic acid derivatives. The dipole moment of *para*-substituted benzoic acid derivatives induced shifts of V_{OC} (See Fig. 1.19).

Tada et al. reported on the insertion of the dipole moment into the D/A interface of P3HT/PCBM bilayer devices (See Fig. 1.20).[25] They used surface segregated monolayer (SSM) and surfaces of P3HT and PCBM layer were modified by fluoroalkyl chain. Then they used contact film transfer (CFT) method to make bilayer device, and the dipole moment of fluoroalkyl chain tuned the V_{OC} from 0.3 to 0.9 V. These results indicated dipole moment at the D/A interface is critical for determining V_{OC}.

Zhong et al. investigated the effects of distance between donor and acceptor in P3HT/PCBM bilayer device (See Fig. 1.21).[32a] They spincoated insulator called CYTOP, which is soluble in fluorosolvent, on PCBM layer, and P3HT layer was laminated on the surface modified PCBM layer by CFT method. Distance of donor and acceptor layer was tuned by the thickness of CYTOP layer (0 ~ 3 nm). Introduction of insulating layer destabilized the energy of CTS and suppressed recombination because of special separation of donor and acceptor layer, thus V_{OC} increased. Special separation also caused decrease of J_{SC} at the same time. This result suggested distance of donor and acceptor affect largely to V_{OC} and J_{SC}, but only controlling distance could not increase the efficiency because trade off relationship of V_{OC} and J_{SC} existed.

Murata et al. investigated the effect of energy levels at the D/A interface by inserting cupper-phthalocyanine (CuPc) layer into pentacene/C_{60} bilayer device by vacuum evaporation (See Fig. 1.22).[61] They observed increase of V_{OC} and decrease of J_{SC} by inserting 6 nm of CuPc. 6 nm of interlayer was rather thick and this might change charge separation and charge recombination center. Films were not fully covered by CuPc when the thickness of CuPc layer was less than 6 nm as they pointed out.

Friend et al reported insertion of thin interlayer into bilayer devices by successive spincoating and photo crosslinking method as mentioned above (Fig. 1.23).[62] They used P3HT as the donor material and poly{[N,N'-bis(2-octyldodecyl)-naphthalene-1,4,5,8-bis(dicarboximide)-2,6-diyl]-alt -5,5'-(2,2'-bithiophene)} (P(NDI2OD-T2)) as the acceptor material and poly[N-9'-hepta-decanyl-2,7-carbazole- alt -5,5-(4',7'-di-2-thienyl-2',1',3'-benzothiadiazole)] (PCDTBT) as the interlayer, which had a cascading energy level, with the thickness from 0.5 ~ 4 nm. They observed increase of V_{OC} and J_{SC}, but FF did not change. Simulation works suggested insertion of cascade

layer suppressed geminate recombination, consequently induced change of FF.[54] Preparing very thin layer by spin-coating is generally difficult, thus non-uniformity of interlayer could change charge separation and recombination center in their report. Therefore the origin of V_{OC} and J_{SC} change was unclear.

Energy levels near at D/A interface is very important as predicted by simulation works,[54] but the effects remain unclear because control of energy level near at D/A interface is very difficult. Therefore, there has been little information about nanostructures which can achieve efficient charge separation and suppression of recombination.

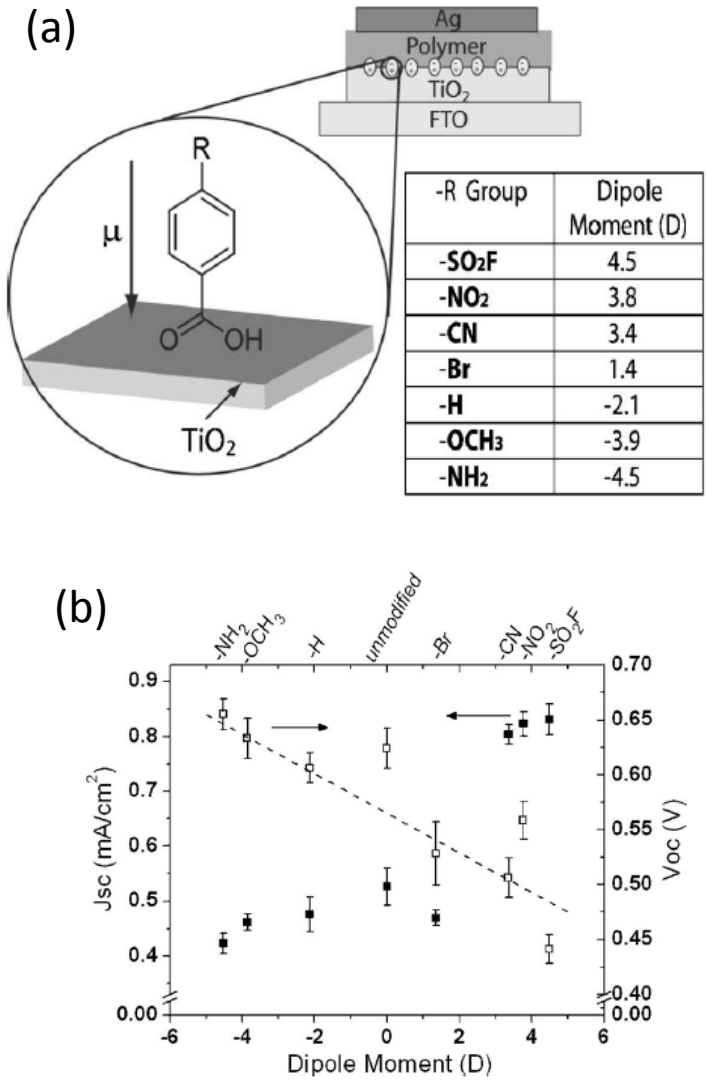

-R Group	Dipole Moment (D)
-SO_2F	4.5
-NO_2	3.8
-CN	3.4
-Br	1.4
-H	-2.1
-OCH_3	-3.9
-NH_2	-4.5

Figure 1.19. (a) Schematic image of the bilayer device and insertion of dipole moment into the D/A interface. (b) Plots of J_{SC} and V_{OC} versus dipole moment of *para*-substituted benzoic acid derivatives. Reprinted with permission from ref. 70. Copyright 2007, rights managed by AIP Publishing LLC.

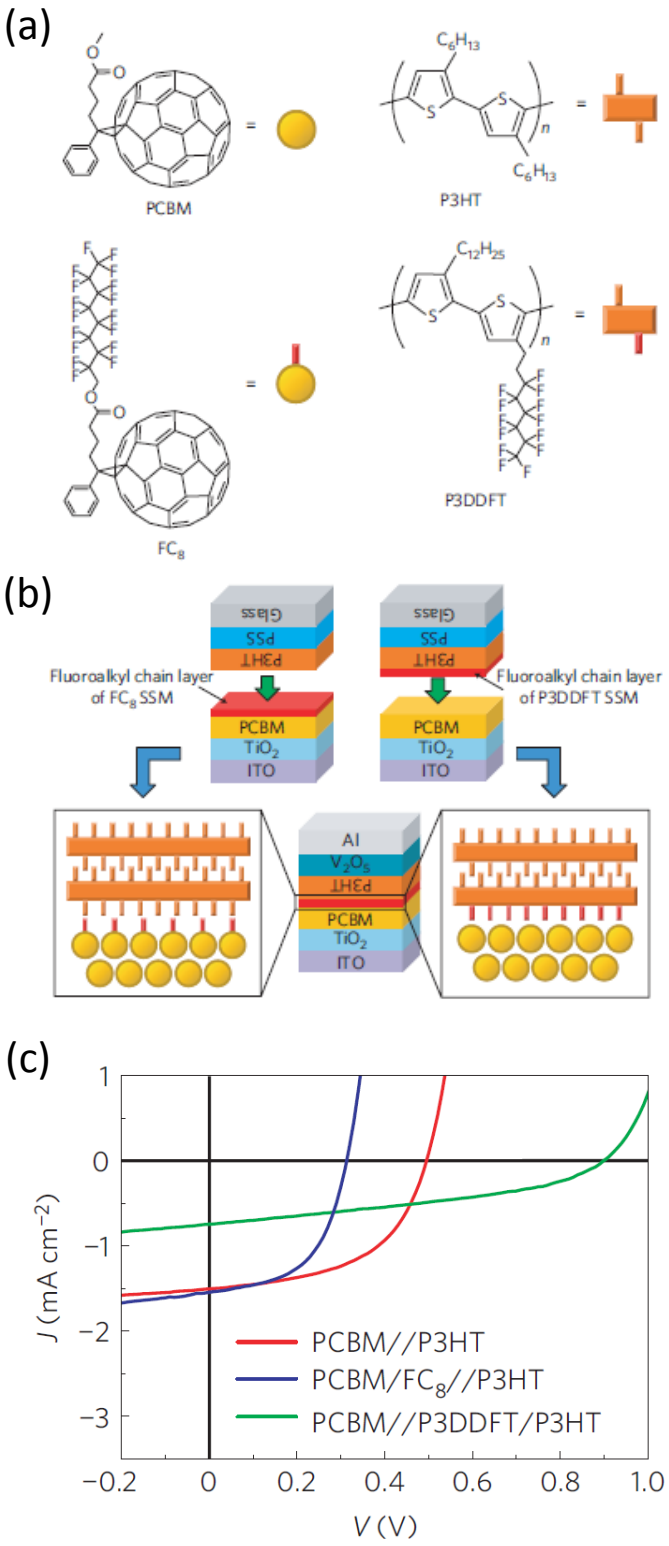

Figure 1.20. (a) Chemical structures of surface modifiers and bulk materials. (b) Schematic image of insertion of dipole moment by SSM. (c) *J*-*V* curves of three types of the devices. Reprinted with permission from ref. 28. Copyright 2011, Rights Managed by Nature Publishing Group.

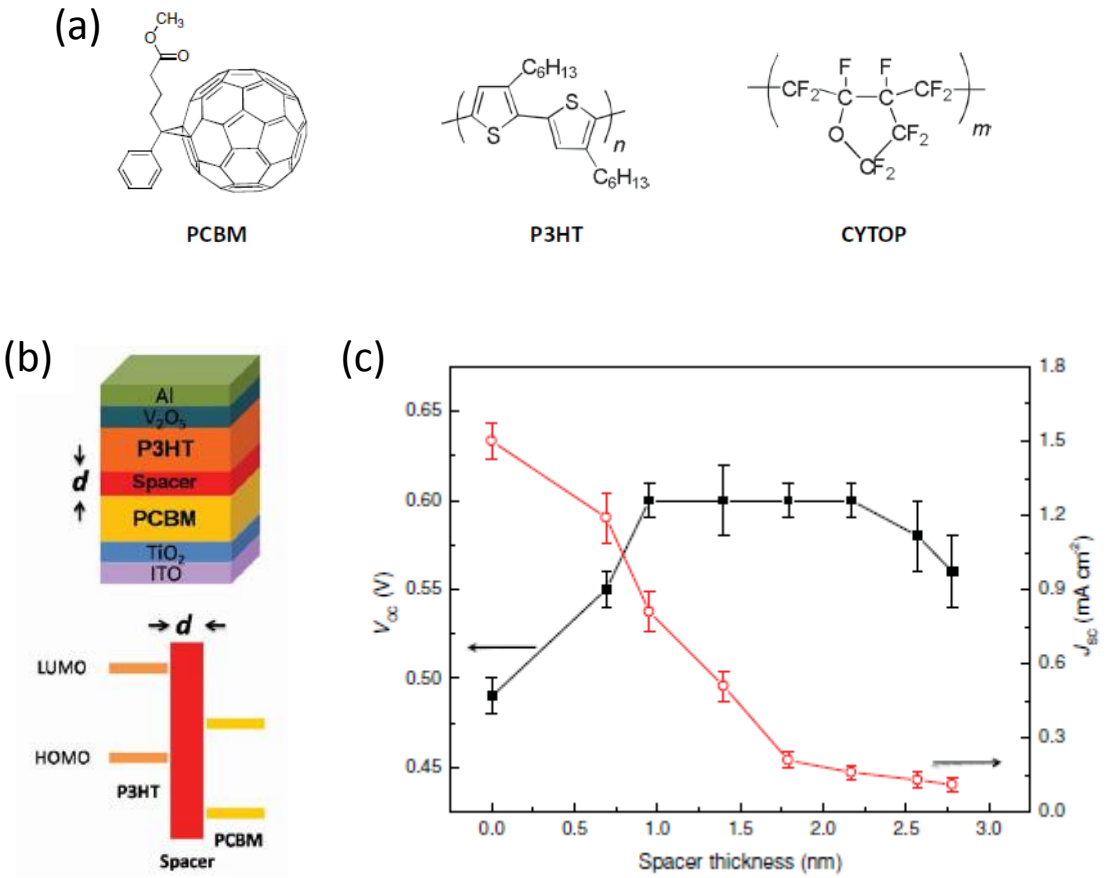

Figure 1.21. (a) Chemical structures of P3HT, PCBM and CYTOP. (b) Schematic image of the insertion of spacer into the D/A interface in the bilayer device. (c) Thickness dependence of spacer on V_{OC} and J_{SC}. Reprinted with permission from ref. 36. Copyright 2014, WILEY-VCH Verlag GmbH & Co. KGaA, Weinheim.

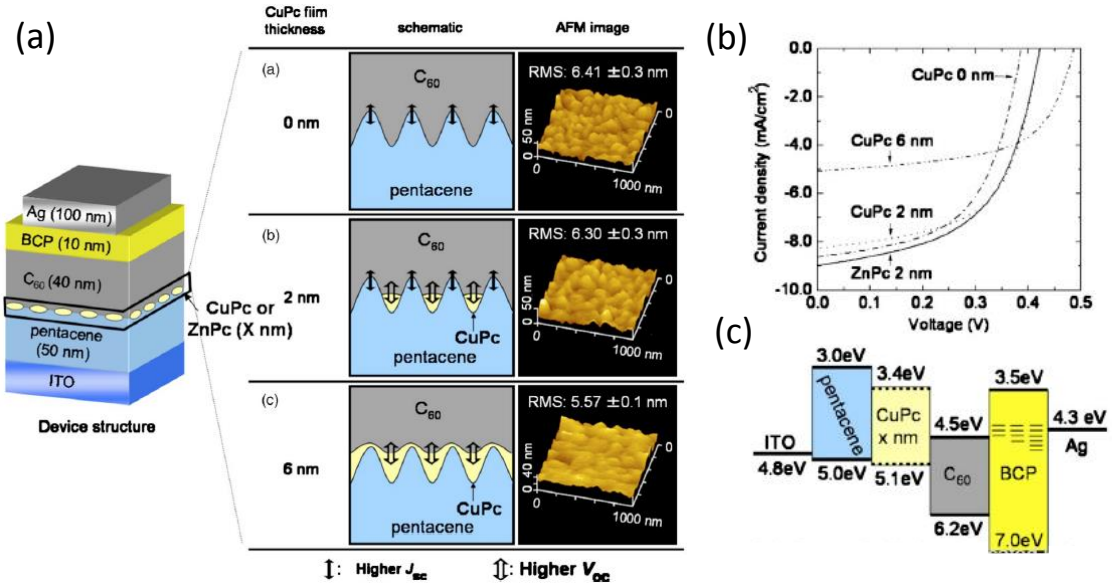

Figure 1.22. (a) Schematic image of interfacial modification by vacuum evaporation and AFM images after evaporation. (b) *J*-*V* curves with and without interlayers. (c) schematic representation of energy diagrams. Reprinted with permission from ref. 71. Copyright 2007, managed by AIP Publishing LLC.

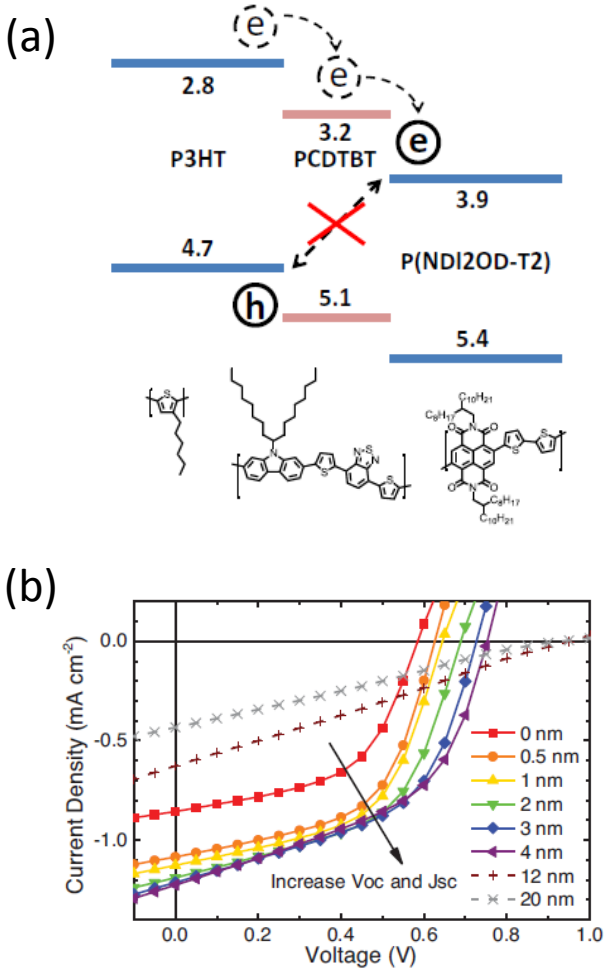

Figure 1.23. (a) Chemical structures of P3HT, PCDTBT and P(NDI2OD-T2) and energy diagram. (b) *J-V* curves of the devices with the interlayer. Reprinted with permission from ref. 72. Copyright 2013, WILEY-VCH Verlag GmbH & Co. KGaA, Weinheim.

1.2.7. Importance of nanostructure control of donor/acceptor domains

1.2.7.1. Importance of donor/acceptor domain structure

As explained in section 1.2.2, the photo-conversion processes in OPVs are expected to be largely affected by the morphology of the D/A domains. For example, large D/A interface is needed for efficient charge separation and interpenetrating network of D/A domains is needed for efficient charge transport. Shaheen et al. firstly reported the importance of molecular morphology in MDMO-PPV blend films on device performances in 2001 (See Fig. 1.24).[63] The devices of this system made by spin-coating of a chlorobenzene solution showed the PCE of 2.5 %, while the device made by a toluene solution showed 0.9 %. This difference in the efficiencies was attributed to the change in mixing morphology. Large aggregated domains were observed in AFM images when the films were made from a toluene solution, whereas smooth and well mixed films were obtained by making from a chlorobenzene solution.

In general, the morphology of the domains in the films is strongly dependent upon the fabrication conditions, such as the mixing ratio, organic solvent, additives, spin-coating speed and thermal annealing conditions (See Fig. 1.25).[64] Finding optimized conditions for the device fabrication is a tough job because many parameters mentioned above must be adjusted. Furthermore, even if the resulting film morphology is ideal immediately after fabrication, this could be easily changed by long-term operation or high temperature conditions, because this mixed structure is not the thermodynamically stable state. This causes stability issues. Precise nanostructure control of D/A domains by molecular design is important for realizing efficient and stable devices.

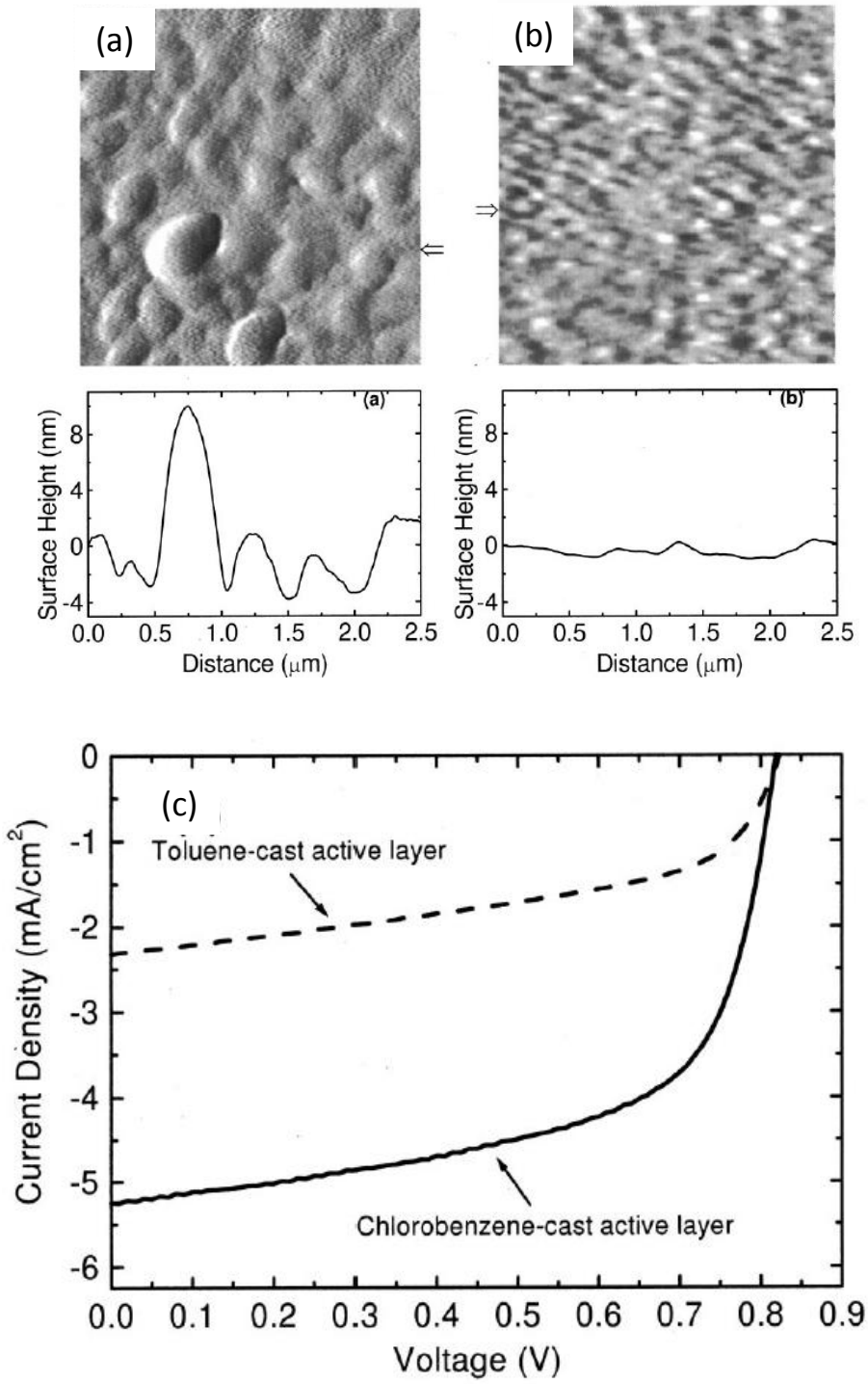

Figure 1.24. AFM images of the surface morphology of MDMOPPV:PCBM blend films spin-coated from (a) a toluene solution, (b) a chlorobenzene solution. The cross sections of the surface heights for the films are shown below. (c) *J-V* curves of the devices made by the toluene solution (broken line), and a chlorobenzene solution (solid line). Reprinted with permission from ref. 73. Copyright 2001, managed by AIP Publishing LLC.

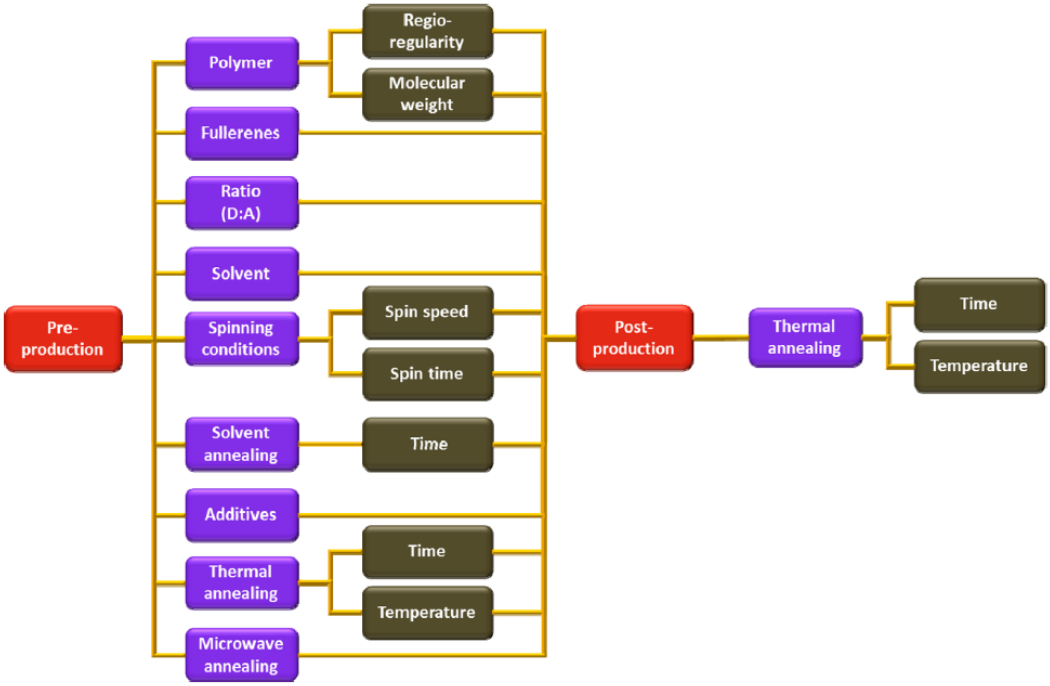

Figure 1.25. Various factors to affect the blend morphology in bulk heterojunction devices. Reprinted with permission from ref. 74. Copyright 2013, American Chemical Society.

Stability issues

Stability is one of the major issues in OPVs because OPV is likely to suffer from a lowering of the efficiency by operation for a long time.[75] Morphological stability is one of the biggest factors in the deterioration of the device performance. Bulk heterojunction active layer is meta-stable structure, thus large aggregation of domains evolve with time even at ambient temperature. The delicate nanostructure which is better for photoconversion processes should be stabilized. Note that there exist other important stability issues such as photo-stability or air stability of materials in active layers or buffer layers. All these problems must be solved for the commercialization of OPVs.

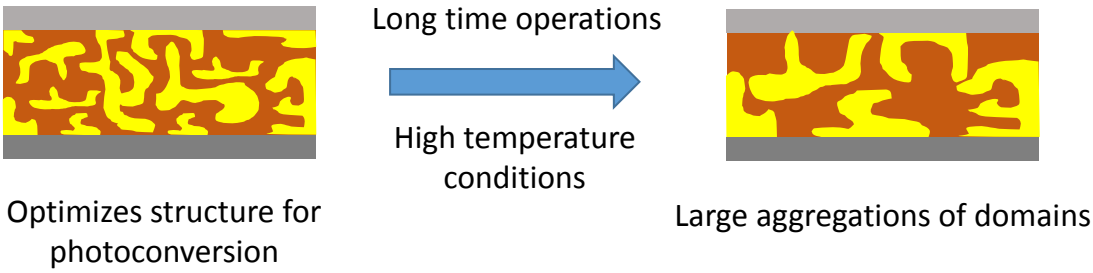

Figure 1.26. Schematic image of morphological change in bulk heterojunction devices by long time operations or high temperature conditions

1.2.7.2. Nanostructure control of donor/acceptor domains

Many groups have tried to control the nanostructure of D/A domains by designing molecules which could form suitable structure for efficient photoconversion or stabilize mixing morphology in the films. Representative works are explained in this section.

Cross linking

To stabilize the morphology of blend films, some have incorporated cross-linkable groups into donor or acceptor materials. Gaudiana et al. synthesized cross linkable fullerene derivative, C_{61}-butyric acid glycidol ester (PCBG) (See Fig. 27).[65] A polymerized network of fullerene derivatives was formed by cross linking reaction induced by heat. After thermal annealing at 140 °C for 1 h, PCBM formed large crystals in a P3HT/PCBM blend film, while such large aggregations were not observed in a P3HT/PCBG blend film as shown in TEM image in Fig. 1.28. This result suggested blend morphology was stabilized by cross linking of PCBG, but a strong degradation of the device efficiency was still observed in the P3HT/PCBG device after thermal annealing 140 °C for 10 min.

Miyanishi et al synthesized cross-linkable regioregular poly(3-(5-hexenyl)thiophene) (P3HNT).[66] Vinyl groups at the side chain of polymer cross linked by a thermal treatment. Optical microscope images represented that large aggregations of PCBM formed in a P3HT/PCBM film, whereas PCBM aggregations were suppressed in P3HNT/PCBM film (See Fig. 1.28). The device of P3HNT/PCBM showed similar efficiency with the device of P3HT/PCBM before thermal treatment, and higher efficiency after thermal annealing at 150 °C. This result indicated cross linkable conjugated polymer stabilized mixing morphology of films and the device performances.

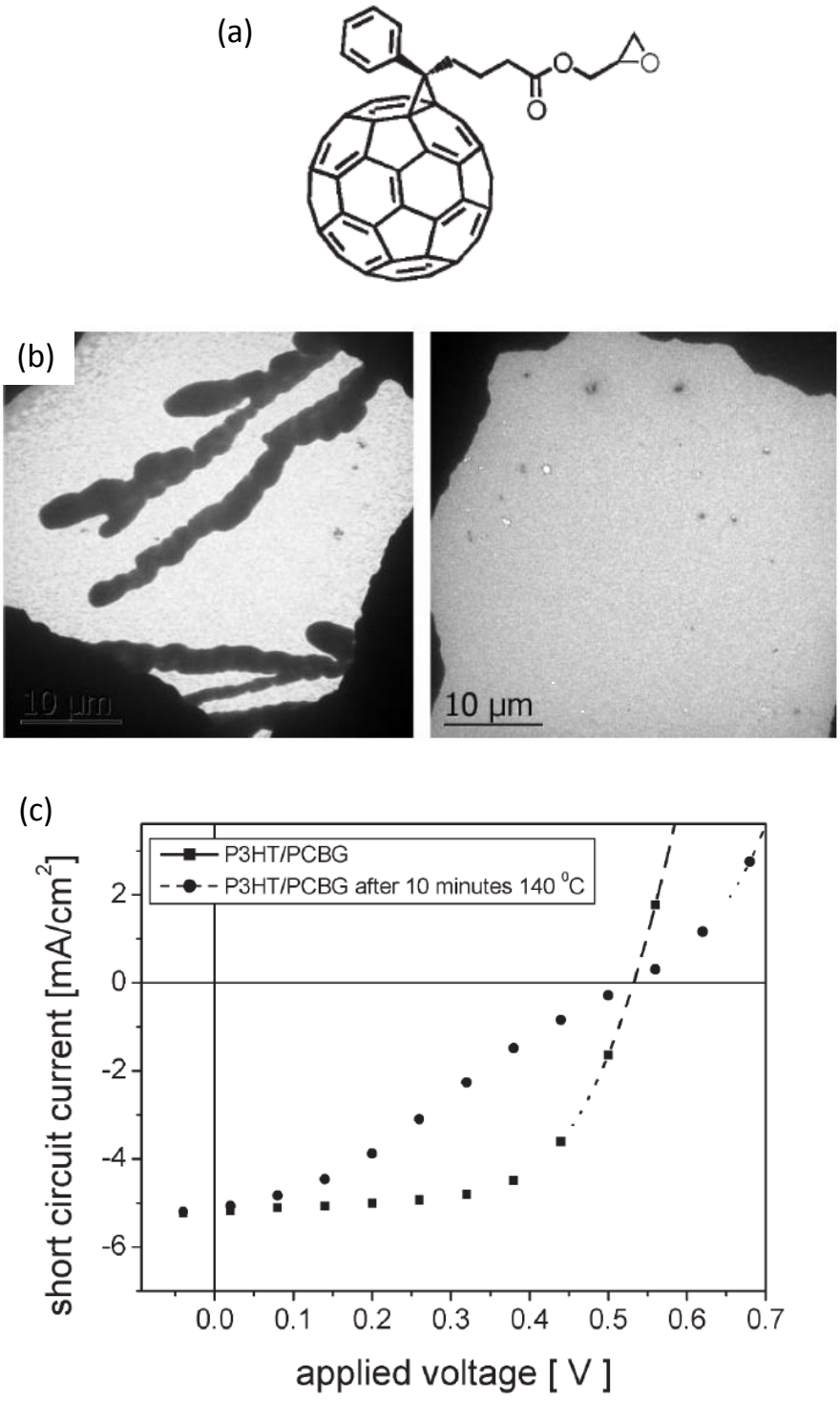

Figure 1.27. (a) Chemical structure of cross linkable fullerene derivative, C_{61}-butyric acid glycidol ester (PCBG), (b) TEM images of a P3HT/PCBG blend film (left) and a P3HT/PCBG blend film (right) after thermal annealing at 140 °C for 1 h. (c) *J-V* curves of a P3HT/PCBG device before (square) and after (circle) thermal annealing at 140 °C for 10 min. Reprinted with permission from ref. 76. Copyright 2005, Royal Society of Chemistry.

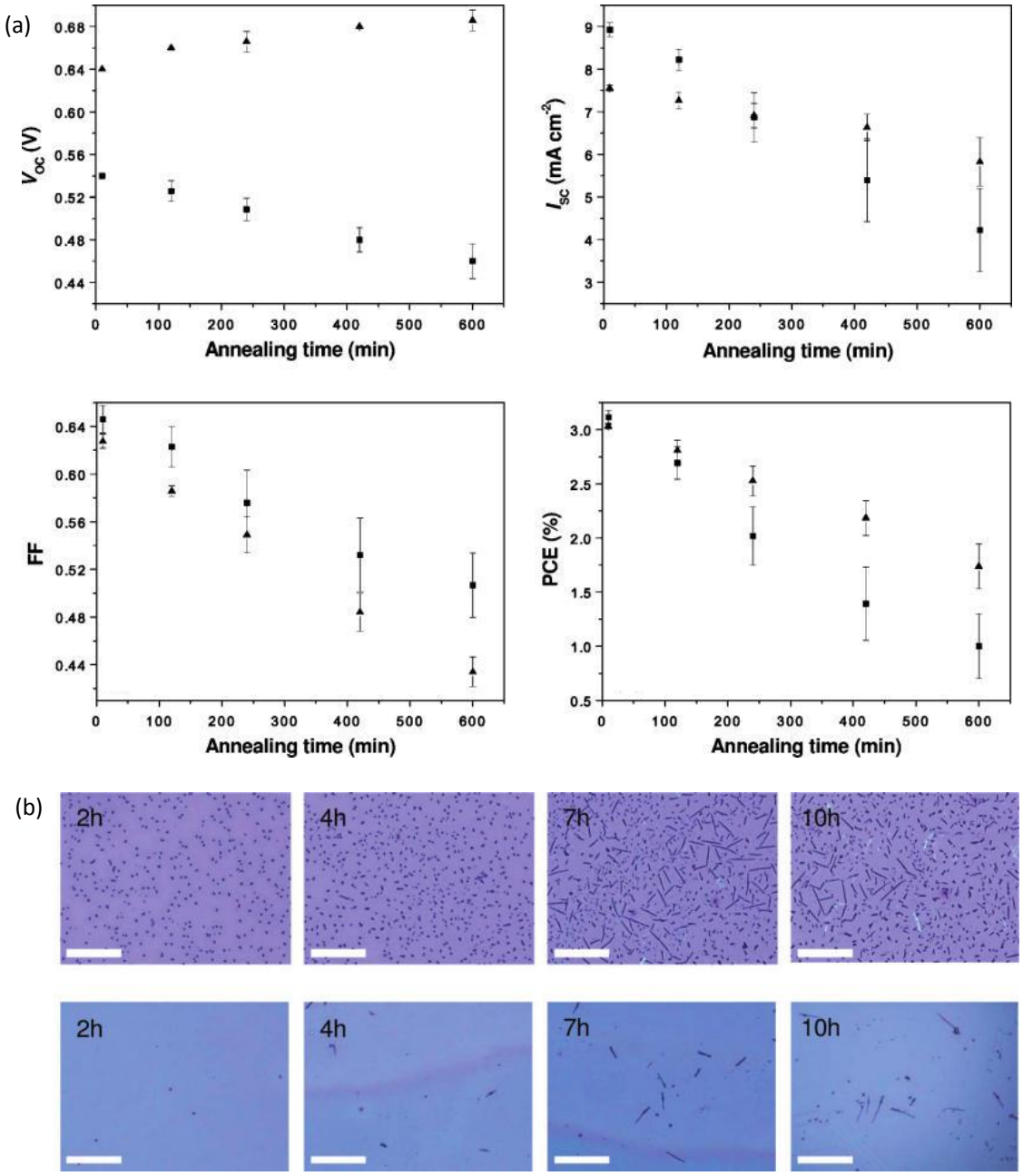

Figure 1.28. (a) Device performances of P3HT/PCBM (square) and P3HNT/PCBM (triangle) before and after thermal annealing at 150 °C. (b) Optical microscope images of P3HT/PCBM films (upper) and P3HNT/PCBM (below) films after thermal annealing at 150 °C. Reprinted with permission from ref. 77. Copyright 2009, American Chemical Society.

Block copolymer

Block copolymers have self-assembling behavior and tend to form well-ordered nanostructures with tens of nanometer scale. This nature is useful to control D/A domain structures in active layers of OPVs.[67]

Miyanishi et al. synthesized a fullerene attached all-conjugated semiconducting diblock copolymer based on polythiophene (See Fig. 1.30).[68] A film of the diblock copolymer showed micro phase separated structures as shown in AFM phase images. The devices with the diblock copolymer showed high FF of 0.63 and comparable PCE of 2.5 % with P3HT/PCBM bulk heterojunction devices. Furthermore, the diblock copolymer stabilized mixed morphology as shown in optical microscopic images, and a device of the block copolymer showed a stable efficiency even after 80 h thermal annealing at 130 °C.[69]

Verduzco et al. synthesized poly(3-hexylthiophene)−block−poly-((9,9-dioctylfluorene)-2,7-diyl-alt-[4,7-bis(thiophen-5-yl)- 2,1,3-benzothiadiazole]-2’,2’’-diyl) (P3HT-b-PFTBT) block copolymers (See Fig. 1.31).[70] Resonant soft X-ray scattering (RSOXS) results revealed that self-assembly into lamellar morphologies with roughly 10 nm. The device of the block copolymer showed PCE of 3.1 in the best device.

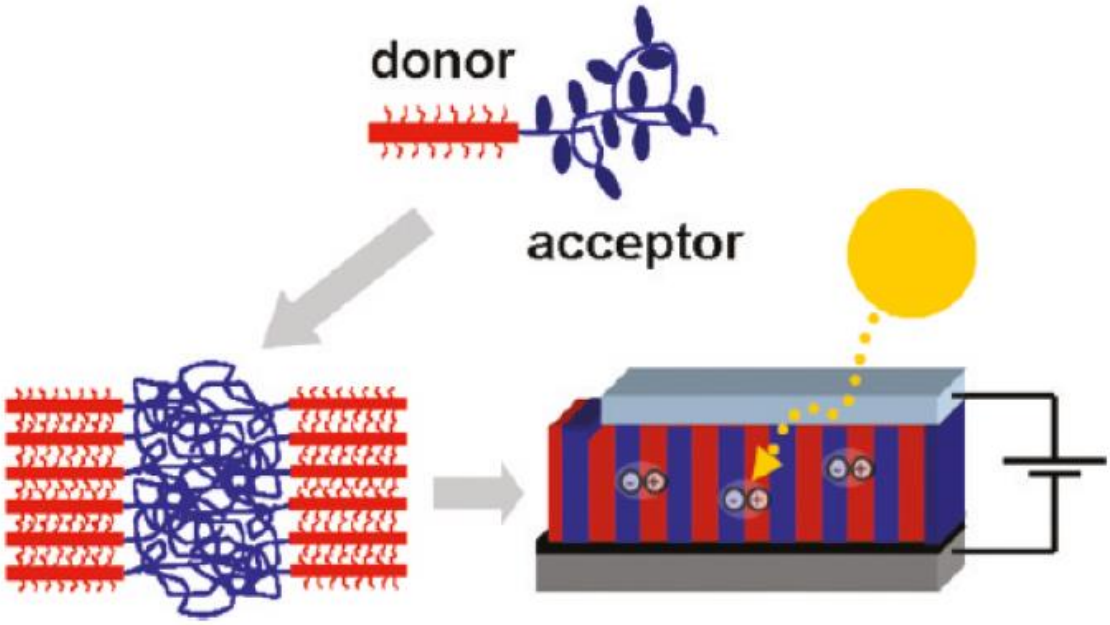

Figure 1.29. Schematic image of self assembly of block copolymer for creating controlled nanostructure. Reprinted with permission from ref. 78. Copyright 2009, American Chemical Society.

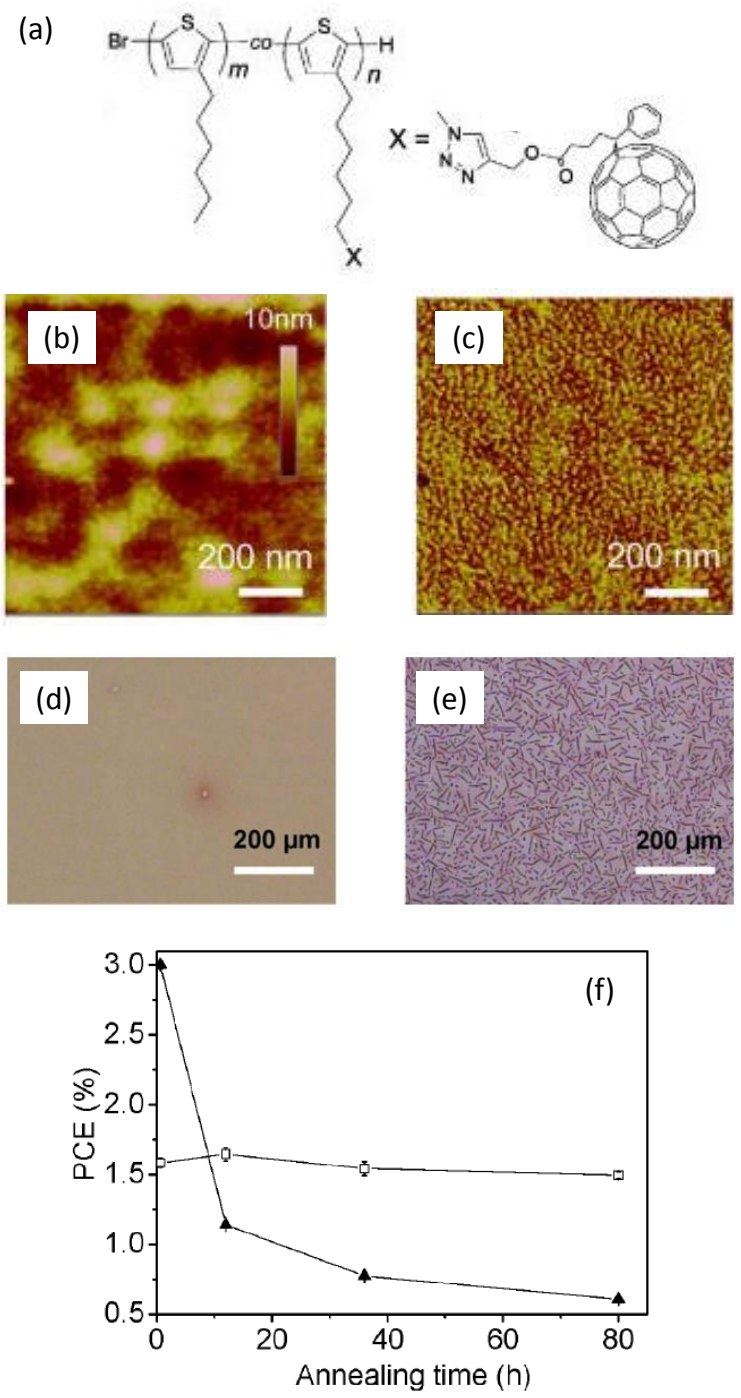

Figure 1.30. (a) Chemical structure of a fullerene attached all-conjugated semiconducting diblock copolymer. AFM (b) height and (c) phase images of an annealed film of the copolymer. Optical microscope images of films of (d) the copolymer and (e) P3HT/PCBM blend after thermal annealing at 130 °C for 80 h. Reprinted with permission from ref. 79. Copyright 2012, American Chemical Society. Reprinted with permission from ref. 80. Copyright 2010, Royal Society of Chemistry.

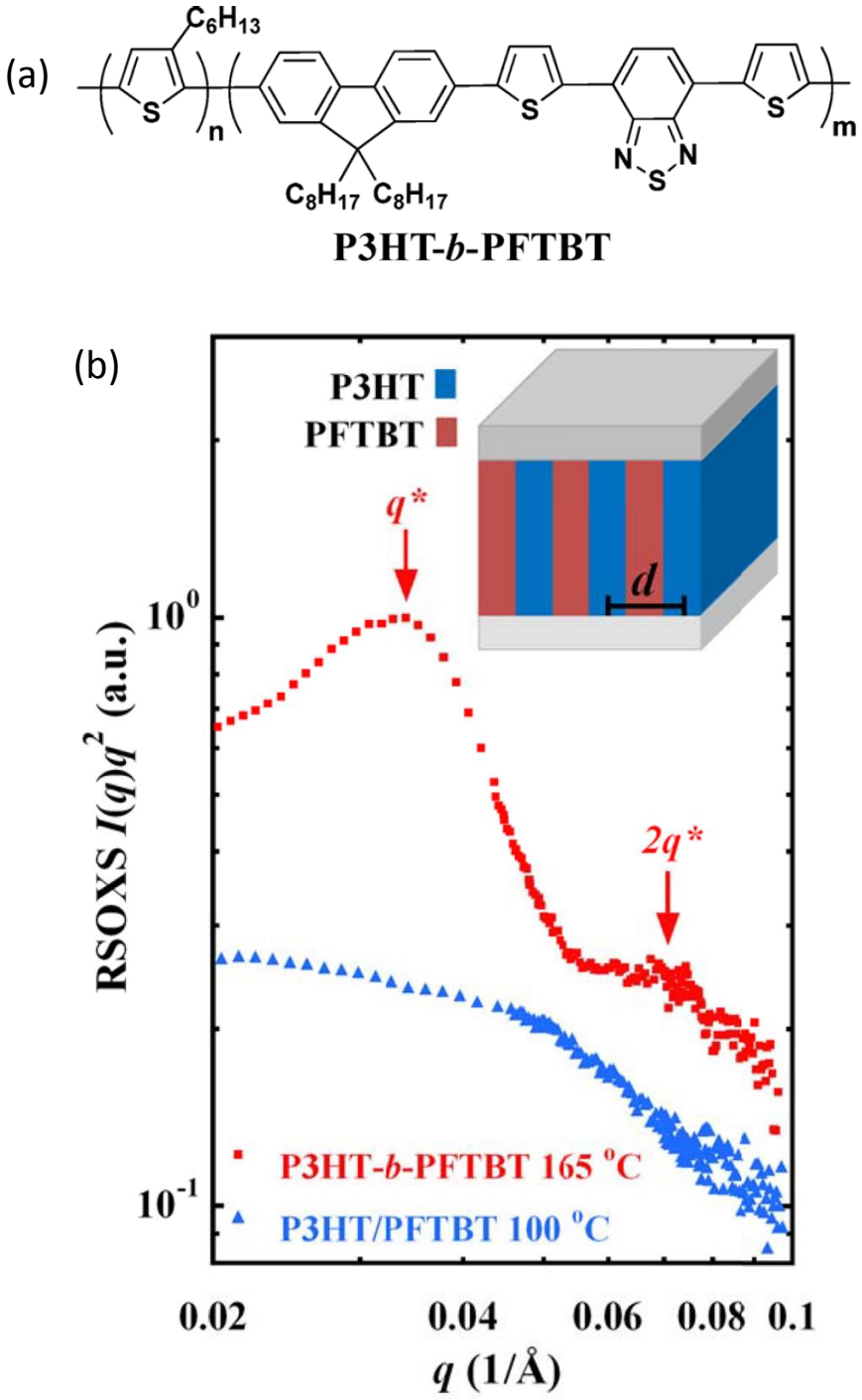

Figure 1.31. (ref26) (a) Chemical structure of the block copolymer. (b) RSOXS data and schematic image of lamellar morphologies in the device with the block copolymer (inset). Reprinted with permission from ref. 81. Copyright 2013, American Chemical Society.

Donor-acceptor dyad molecule

Dyad molecules (i.e. covalently attached donor and acceptor groups) have an advantage in terms of nanostructure control, and thus also hold promise for stabilizing the phase separation of domains.[71] Devices of the dyad molecules can be made by single component without using mixing. In contrast to fullerene-bearing block copolymers, small molecules do not have the problems of the polymers, such as molecular weight distribution, end-group contamination and difficulty in purification, leading to the advantages of less batch-to-batch variation, and better reproducibility.[72] Many groups have reported the synthesis of dyad molecules and their application in OSCs.[71] Their reports provided basic knowledge from spectroscopic analysis, however, the reported PCEs of OSCs based on dyads had been low at the early stage.[71]

Maggini et al. reported fullerene-azothiophene dyad (See Fig. 1.33) in 2002.[73] The dyad had absorption up to 700 nm. They optimized the thickness of the devices and the device showed the highest efficiency of 0.4 % in dyad based OPVs at that time. But, FF of the devices were quite low (0.28). This means charge transport was inefficient because connection of D/A domains were poor.

Nishizawa et al synthesized highly crystalline oligo(*p*-phenylenevinylene)-fullerene dyad.[74] Powder X-ray diffraction showed crystalline peaks of the dyads. This indicated D/A domain formation in the solid state. Devices of the dyad showed relatively high FF of 0.44 and PCE was improved to 1.28 %.

Geng et al synthesized three D-A co-oligomers, called F3T4-hP, F4T6-hP, and F5T8-hP in Fig. 1.35.[75] Transmission electron microscopy (TEM) images indicated formation of the lamellar nanostructure of D/A domains in the films of the co-oligomers. The device of F5T8-hP showed highest efficiency of 1.5 % in dyad based OPVs.

Dyad molecules are suitable for controlling nanostructure of D/A domains, but the photovoltaic performances have still been lower than mixed bulk heterojunction systems. Furthermore, no reports have covered the construction of morphologically stable OSCs using dyad molecules. Therefore, seeking suitable molecular designs for achieving efficient and stable systems based on dyads is an important topic.

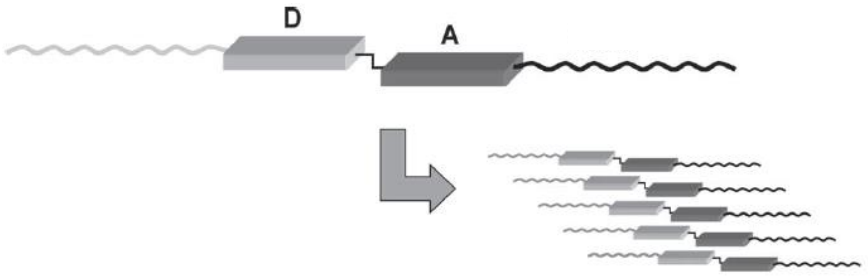

Figure 1.32. Schematic image of self-organization of dyad molecules. Reprinted with permission from ref. 82. Copyright 2011, WILEY-VCH Verlag GmbH & Co. KGaA, Weinheim.

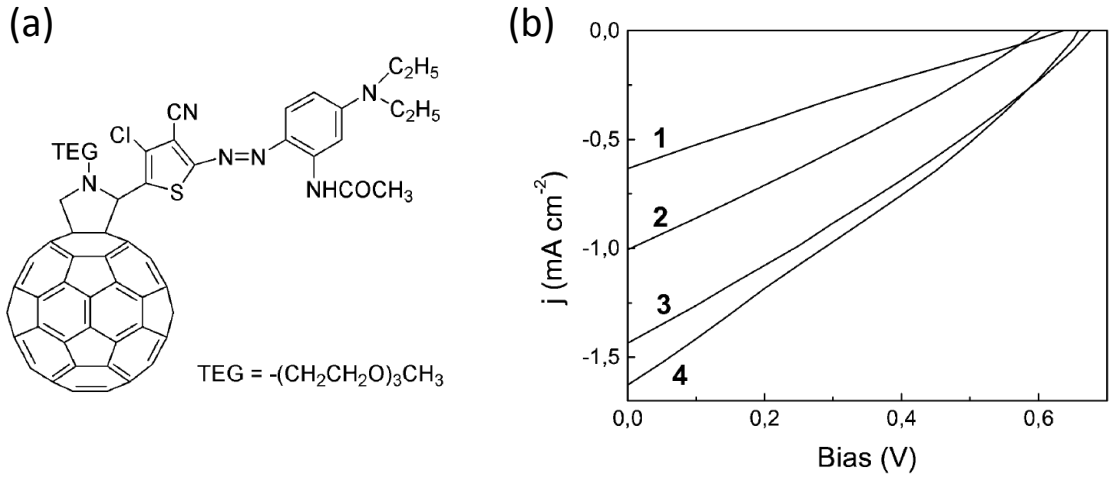

Figure 1.33. (a) Chemical structure of fullerene-azothiophene dyad. (b) *J-V* curves of the dyad devices with the film thickness of 105 nm (1), 85 nm (2), 60 nm (3) and 45 nm (4) under white light irradiation (80 mA cm^{-2}). Reprinted with permission from ref. 84. Copyright 2002, Royal Society of Chemistry.

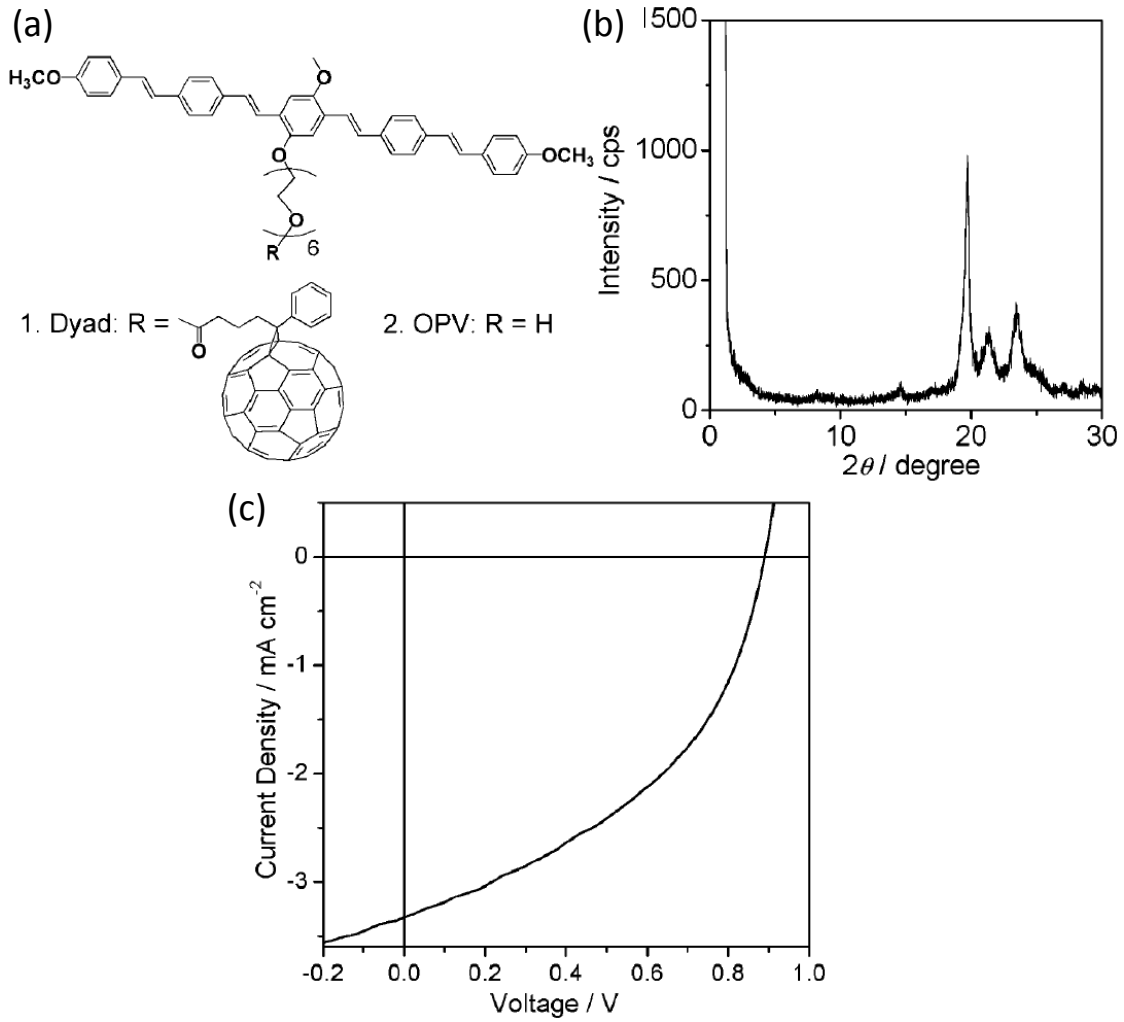

Figure 1.34. (a) Chemical structure of oligo(*p*-phenylenevinylene)-fullerene dyad. (b) Powder X-ray diffraction pattern of the dyad. (c) *J*-*V* curve of the dyad device. Reprinted with permission from ref. 85. Copyright 2009, Royal Society of Chemistry.

(a)

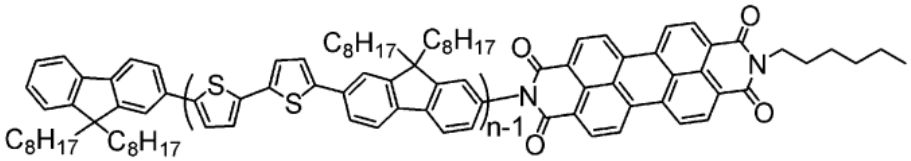

n = 3, **F3T4-hP** *G* 66.4 S_{X2} 212.3 S_{X1} 215.7 *I*
4, **F4T6-hP** *G* 83.4 S_{X3} 194.8 S_{X2} 204.7 S_{X1} 233.5 *I*
5, **F5T8-hP** *G* 90.4 S_X 189.5 *N* 248.5 *I*

[a] Symbols: *G*, glassy; *S*, smectic; *N*, nematic; *I*, isotropic.

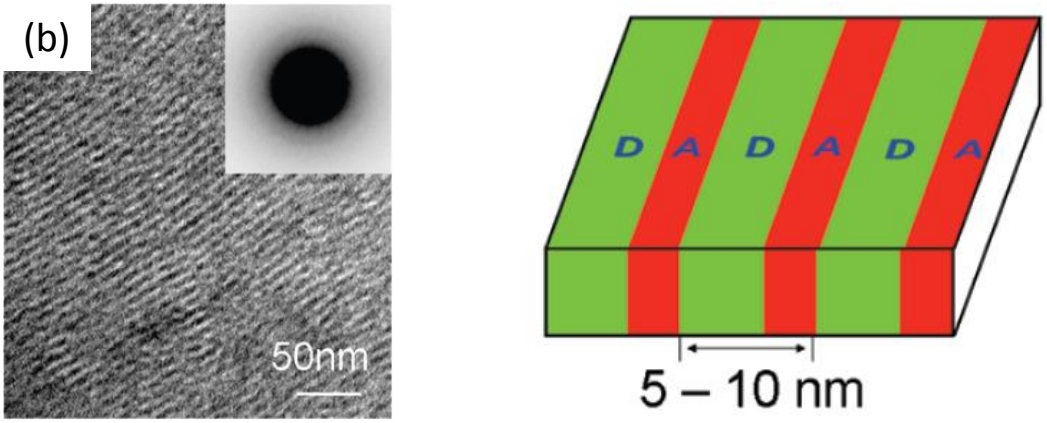

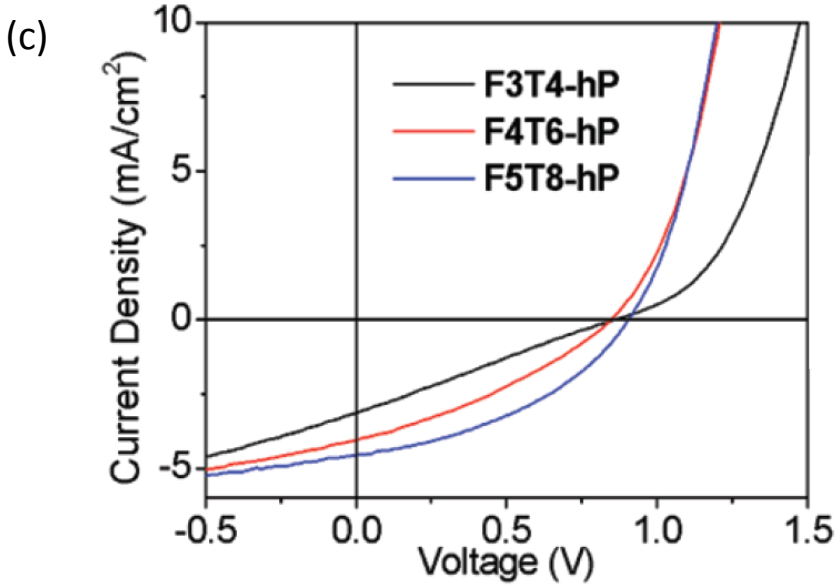

Figure 1.35. (a) Chemical structure of donor acceptor co-oligomers. (b) TEM image and selected area electron diffractions of a F5T8-hP film and schematic image of the lamellar nanostructure in film. (c) *J-V* curves of the co-oligomer. Reprinted with permission from ref. 86. Copyright 2009, American Chemical Society.

References

1. Green, M. A., The future of crystalline silicon solar cells. *Progress in Photovoltaics: Research and Applications* **2000,** *8* (1), 127-139.

2. Schock, H.-W.; Noufi, R., CIGS-based solar cells for the next millennium. *Progress in Photovoltaics: Research and Applications* **2000,** *8* (1), 151-160.

3. Grätzel, M., Perspectives for dye-sensitized nanocrystalline solar cells. *Progress in Photovoltaics: Research and Applications* **2000,** *8* (1), 171-185.

4. Gunes, S.; Neugebauer, H.; Sariciftci, N. S., Conjugated polymer-based organic solar cells. *Chemical Reviews* **2007,** *107* (4), 1324-1338.

5. Energy Technology Perspectives 2008. *International Energy Agency*.

6. NREL research cell eficiency records in 2014.

7. Yuhang Liu, J. Z., Zhengke Li, Cheng Mu, Wei Ma, Huawei Hu, Kui Jiang, Haoran Lin, Harald Ade, He Yan, Aggregation and morphology control enables multiple cases of high-efficiency polymer solar cells. *Nature Communications* **2014,** *4*, 5293-5301.

8. Clarke, T. M.; Durrant, J. R., Charge Photogeneration in Organic Solar Cells. *Chemical Reviews* **2010,** *110* (11), 6736-6767.

9. Knupfer, M., Exciton binding energies in organic semiconductors. *Applied Physics a-Materials Science & Processing* **2003,** *77* (5), 623-626.

10. (a) Luer, L.; Egelhaaf, H. J.; Oelkrug, D.; Cerullo, G.; Lanzani, G.; Huisman, B. H.; de Leeuw, D., Oxygen-induced quenching of photoexcited states in polythiophene films. *Organic Electronics* **2004,** *5* (1-3), 83-89; (b) Kroeze, J. E.; Savenije, T. J.; Vermeulen, M. J. W.; Warman, J. M., Contactless determination of the photoconductivity action spectrum, exciton diffusion length, and charge separation efficiency in polythiophene-sensitized TiO_2 bilayers. *Journal of Physical Chemistry B* **2003,** *107* (31), 7696-7705.

11. Park, S. H.; Roy, A.; Beaupre, S.; Cho, S.; Coates, N.; Moon, J. S.; Moses, D.; Leclerc, M.; Lee, K.; Heeger, A. J., Bulk heterojunction solar cells with internal quantum efficiency approaching 100%. *Nature Photonics* **2009,** *3* (5), 297-303.

12. Few, S.; Frost, J. M.; Nelson, J., Models of charge pair generation in organic solar cells. *Physical Chemistry Chemical Physics* **2015,** *17*, 2311-2325.

13. Gao, F.; Inganas, O., Charge generation in polymer-fullerene bulk-heterojunction solar cells. *Physical Chemistry Chemical Physics* **2014,** *16* (38), 20291-20304.

14. Nayak, P. K.; Narasimhan, K. L.; Cahen, D., Separating Charges at Organic Interfaces: Effects of Disorder, Hot States, and Electric Field. *Journal of Physical Chemistry Letters* **2013,** *4* (10), 1707-1717.

15. (a) Grancini, G.; Maiuri, M.; Fazzi, D.; Petrozza, A.; Egelhaaf, H. J.; Brida, D.; Cerullo,

G.; Lanzani, G., Hot exciton dissociation in polymer solar cells. *Nature Materials* **2013,** *12* (1), 29-33; (b) Jailaubekov, A. E.; Willard, A. P.; Tritsch, J. R.; Chan, W.-L.; Sai, N.; Gearba, R.; Kaake, L. G.; Williams, K. J.; Leung, K.; Rossky, P. J.; Zhu, X. Y., Hot charge-transfer excitons set the time limit for charge separation at donor/acceptor interfaces in organic photovoltaics. *Nature Materials* **2013,** *12* (1), 66-73.

16. Vandewal, K.; Albrecht, S.; Hoke, E. T.; Graham, K. R.; Widmer, J.; Douglas, J. D.; Schubert, M.; Mateker, W. R.; Bloking, J. T.; Burkhard, G. F.; Sellinger, A.; Frechet, J. M. J.; Amassian, A.; Riede, M. K.; McGehee, M. D.; Neher, D.; Salleo, A., Efficient charge generation by relaxed charge-transfer states at organic interfaces. *Nature Materials* **2014,** *13* (1), 63-68.

17. (a) Jamieson, F. C.; Domingo, E. B.; McCarthy-Ward, T.; Heeney, M.; Stingelin, N.; Durrant, J. R., Fullerene crystallisation as a key driver of charge separation in polymer/fullerene bulk heterojunction solar cells. *Chemical Science* **2012,** *3* (2), 485-492; (b) Sweetnam, S.; Graham, K. R.; Ndjawa, G. O. N.; Heumueller, T.; Bartelt, J. A.; Burke, T. M.; Li, W.; You, W.; Amassian, A.; McGehee, M. D., Characterization of the Polymer Energy Landscape in Polymer:Fullerene Bulk Heterojunctions with Pure and Mixed Phases. *Journal of the American Chemical Society* **2014,** *136* (40), 14078-14088.

18. Vandewal, K.; Himmelberger, S.; Salleo, A., Structural Factors That Affect the Performance of Organic Bulk Heterojunction Solar Cells. *Macromolecules* **2013,** *46* (16), 6379-6387.

19. Moliton, A.; Nunzi, J. M., How to model the behaviour of organic photovoltaic cells. *Polymer International* **2006,** *55* (6), 583-600.

20. Heeger, A. J., 25th Anniversary Article: Bulk Heterojunction Solar Cells: Understanding the Mechanism of Operation. *Advanced Materials* **2014,** *26* (1), 10-28.

21. Spanggaard, H.; Krebs, F. C., A brief history of the development of organic and polymeric photovoltaics. *Solar Energy Materials and Solar Cells* **2004,** *83* (2-3), 125-146.

22. Tang, C. W., 2-LAYER ORGANIC PHOTOVOLTAIC CELL. *Applied Physics Letters* **1986,** *48* (2), 183-185.

23. Sariciftci, N. S.; Braun, D.; Zhang, C.; Srdanov, V. I.; Heeger, A. J.; Stucky, G.; Wudl, F., SEMICONDUCTING POLYMER-BUCKMINSTERFULLERENE HETEROJUNCTIONS - DIODES, PHOTODIODES, AND PHOTOVOLTAIC CELLS. *Applied Physics Letters* **1993,** *62* (6), 585-587.

24. Tada, A.; Geng, Y.; Nakamura, M.; Wei, Q.; Hashimoto, K.; Tajima, K., Interfacial modification of organic photovoltaic devices by molecular self-organization. *Physical Chemistry Chemical Physics* **2012,** *14* (11), 3713-3724.

25. Tada, A.; Geng, Y.; Wei, Q.; Hashimoto, K.; Tajima, K., Tailoring organic heterojunction interfaces in bilayer polymer photovoltaic devices. *Nature Materials* **2011,** *10* (6), 450-455.

26. Hiramoto, M.; Fujiwara, H.; Yokoyama, M., 3-LAYERED ORGANIC SOLAR-CELL WITH A PHOTOACTIVE INTERLAYER OF CODEPOSITED PIGMENTS. *Applied Physics Letters* **1991,** *58* (10), 1062-1064.

27. Yu, G.; Gao, J.; Hummelen, J. C.; Wudl, F.; Heeger, A. J., POLYMER PHOTOVOLTAIC CELLS - ENHANCED EFFICIENCIES VIA A NETWORK OF INTERNAL DONOR-ACCEPTOR HETEROJUNCTIONS. *Science* **1995,** *270* (5243), 1789-1791.

28. Chirvase, D.; Parisi, J.; Hummelen, J. C.; Dyakonov, V., Influence of nanomorphology on the photovoltaic action of polymer-fullerene composites. *Nanotechnology* **2004,** *15* (9), 1317-1323.

29. Huang, J.-H.; Ho, Z.-Y.; Kuo, T.-H.; Kekuda, D.; Chu, C.-W.; Ho, K.-C., Fabrication of multilayer organic solar cells through a stamping technique. *Journal of Materials Chemistry* **2009,** *19* (24), 4077-4080.

30. Wei, Q.; Tajima, K.; Hashimoto, K., Bilayer Ambipolar Organic Thin-Film Transistors and Inverters Prepared by the Contact-Film-Transfer Method. *Acs Applied Materials & Interfaces* **2009,** *1* (9), 1865-1868.

31. Scharber, M. C.; Wuhlbacher, D.; Koppe, M.; Denk, P.; Waldauf, C.; Heeger, A. J.; Brabec, C. L., Design rules for donors in bulk-heterojunction solar cells - Towards 10 % energy-conversion efficiency. *Advanced Materials* **2006,** *18*, (6), 789-794.

32. (a) Zhong, Y.; Tada, A.; Izawa, S.; Hashimoto, K.; Tajima, K., Enhancement of V_{OC} without Loss of J_{SC} in Organic Solar Cells by Modification of Donor/Acceptor Interfaces. *Advanced Energy Materials* **2014,** *4*, 1301332-1301340. (5); (b) Yamamoto, S.; Orimo, A.; Ohkita, H.; Benten, H.; Ito, S., Molecular Understanding of the Open-Circuit Voltage of Polymer:Fullerene Solar Cells. *Advanced Energy Materials* **2012,** *2* (2), 229-237.

33. Street, R. A.; Hawks, S. A.; Khlyabich, P. P.; Li, G.; Schwartz, B. J.; Thompson, B. C.; Yang, Y., Electronic Structure and Transition Energies in Polymer-Fullerene Bulk Heterojunctions. *Journal of Physical Chemistry C* **2014,** *118* (38), 21873-21883.

34. Credgington, D.; Jamieson, F. C.; Walker, B.; Thuc-Quyen, N.; Durrant, J. R., Quantification of Geminate and Non-Geminate Recombination Losses within a Solution-Processed Small-Molecule Bulk Heterojunction Solar Cell. *Advanced Materials* **2012,** *24* (16), 2135-2141.

35. Chen, J.-D.; Cui, C.; Li, Y.-Q.; Zhou, L.; Ou, Q.-D.; Li, C.; Li, Y.; Tang, J.-X., Single-Junction Polymer Solar Cells Exceeding 10% Power Conversion Efficiency. *Advanced Materials* **2014**, Early View, DOI: 10.1002/adma.201404535.

36. (a) McCullough, R. D.; Lowe, R. D., Enhanced electrical conductivity in regioselectively synthesized poly(3-alkylthiophenes). *Journal of the Chemical Society, Chemical Communications* **1992,** (1), 70-72; (b) Loewe, R. S.; Khersonsky, S. M.; McCullough, R. D., A

Simple Method to Prepare Head-to-Tail Coupled, Regioregular Poly(3-alkylthiophenes) Using Grignard Metathesis. *Advanced Materials* **1999,** *11* (3), 250-253; (c) Chen, T. A.; Rieke, R. D., THE 1ST REGIOREGULAR HEAD-TO-TAIL POLY(3-HEXYLTHIOPHENE-2,5-DIYL) AND A REGIORANDOM ISOPOLYMER - NI VS PD CATALYSIS OF 2(5)-BROMO-5(2)-(BROMOZINCIO)-3-HEXYLTHIOPHENE POLYMERIZATION. *Journal of the American Chemical Society* **1992,** *114* (25), 10087-10088.

37. (a) Li, G.; Shrotriya, V.; Huang, J. S.; Yao, Y.; Moriarty, T.; Emery, K.; Yang, Y., High-efficiency solution processable polymer photovoltaic cells by self-organization of polymer blends. *Nature Materials* **2005,** *4* (11), 864-868; (b) Kim, Y.; Cook, S.; Tuladhar, S. M.; Choulis, S. A.; Nelson, J.; Durrant, J. R.; Bradley, D. D. C.; Giles, M.; McCulloch, I.; Ha, C. S.; Ree, M., A strong regioregularity effect in self-organizing conjugated polymer films and high-efficiency polythiophene: fullerene solar cells. *Nature Materials* **2006,** *5* (3), 197-203.

38. Peet, J.; Kim, J. Y.; Coates, N. E.; Ma, W. L.; Moses, D.; Heeger, A. J.; Bazan, G. C., Efficiency enhancement in low-bandgap polymer solar cells by processing with alkane dithiols. *Nature Materials* **2007,** *6* (7), 497-500.

39. Zhou, H.; Yang, L.; You, W., Rational Design of High Performance Conjugated Polymers for Organic Solar Cells. *Macromolecules* **2012,** *45* (2), 607-632.

40. He, Z.; Zhong, C.; Huang, X.; Wong, W.-Y.; Wu, H.; Chen, L.; Su, S.; Cao, Y., Simultaneous Enhancement of Open-Circuit Voltage, Short-Circuit Current Density, and Fill Factor in Polymer Solar Cells. *Advanced Materials* **2011,** *23* (40), 4636-4643.

41. Chen, H.-Y.; Hou, J.; Zhang, S.; Liang, Y.; Yang, G.; Yang, Y.; Yu, L.; Wu, Y.; Li, G., Polymer solar cells with enhanced open-circuit voltage and efficiency. *Nature Photonics* **2009,** *3* (11), 649-653.

42. He, Z.; Zhong, C.; Su, S.; Xu, M.; Wu, H.; Cao, Y., Enhanced power-conversion efficiency in polymer solar cells using an inverted device structure. *Nature Photonics* **2012,** *6* (9), 591-595.

43. Walker, B.; Tomayo, A. B.; Dang, X. D.; Zalar, P.; Seo, J. H.; Garcia, A.; Tantiwiwat, M.; Nguyen, T. Q., Nanoscale Phase Separation and High Photovoltaic Efficiency in Solution-Processed, Small-Molecule Bulk Heterojunction Solar Cells. *Advanced Functional Materials* **2009,** *19* (19), 3063-3069.

44. Sun, Y.; Welch, G. C.; Leong, W. L.; Takacs, C. J.; Bazan, G. C.; Heeger, A. J., Solution-processed small-molecule solar cells with 6.7% efficiency. *Nature Materials* **2012,** *11* (1), 44-48.

45. Kan, B.; Zhang, Q.; Li, M.; Wan, X.; Ni, W.; Long, G.; Wang, Y.; Yang, X.; Feng, H.; Chen, Y., Solution-Processed Organic Solar Cells Based on Dialkylthiol-Substituted Benzodithiophene Unit with Efficiency near 10%. *Journal of the American Chemical Society* **2014,** *136* (44), 15529-15532.

46. Hummelen, J. C.; Knight, B. W.; Lepeq, F.; Wudl, F.; Yao, J.; Wilkins, C. L., PREPARATION AND CHARACTERIZATION OF FULLEROID AND METHANOFULLERENE DERIVATIVES. *Journal of Organic Chemistry* **1995,** *60* (3), 532-538.
47. Zhou, E. J.; Cong, J. Z.; Wei, Q. S.; Tajima, K.; Yang, C. H.; Hashimoto, K., All-Polymer Solar Cells from Perylene Diimide Based Copolymers: Material Design and Phase Separation Control. *Angewandte Chemie-International Edition* **2011,** *50* (35), 2799.
48. Lin, Y.; Li, Y.; Zhan, X., Small molecule semiconductors for high-efficiency organic photovoltaics. *Chemical Society Reviews* **2012,** *41* (11), 4245-4272.
49. Wienk, M. M.; Kroon, J. M.; Verhees, W. J. H.; Knol, J.; Hummelen, J. C.; van Hal, P. A.; Janssen, R. A. J., Efficient methano 70 fullerene/MDMO-PPV bulk heterojunction photovoltaic cells. *Angewandte Chemie-International Edition* **2003,** *42* (29), 3371-3375.
50. Faist, M. A.; Kirchartz, T.; Gong, W.; Ashraf, R. S.; McCulloch, I.; de Mello, J. C.; Ekins-Daukes, N. J.; Bradley, D. D. C.; Nelson, J., Competition between the Charge Transfer State and the Singlet States of Donor or Acceptor Limiting the Efficiency in Polymer:Fullerene Solar Cells. *Journal of the American Chemical Society* **2011,** *134* (1), 685-692.
51. Chen, W.; Qi, D.-C.; Huang, H.; Gao, X.; Wee, A. T. S., Organic-Organic Heterojunction Interfaces: Effect of Molecular Orientation. *Advanced Functional Materials* **2011,** *21* (3), 410-424.
52. Shoaee, S.; Subramaniyan, S.; Xin, H.; Keiderling, C.; Tuladhar, P. S.; Jamieson, F.; Jenekhe, S. A.; Durrant, J. R., Charge Photogeneration for a Series of Thiazolo-Thiazole Donor Polymers Blended with the Fullerene Electron Acceptors PCBM and ICBA. *Advanced Functional Materials* **2013,** *23* (26), 3286-3298.
53. (a) Burke, T. M.; McGehee, M. D., How High Local Charge Carrier Mobility and an Energy Cascade in a Three-Phase Bulk Heterojunction Enable > 90% Quantum Efficiency. *Advanced Materials* **2014,** *26* (12), 1923-1928; (b) McMahon, D. P.; Cheung, D. L.; Troisi, A., Why Holes and Electrons Separate So Well in Polymer/Fullerene Photovoltaic Cells. *Journal of Physical Chemistry Letters* **2011,** *2* (21), 2737-2741.
54. Groves, C., Suppression of geminate charge recombination in organic photovoltaic devices with a cascaded energy heterojunction. *Energy Environ. Sci.* **2013,** *6* (5), 1546-1551.
55. Lee, K. H.; Schwenn, P. E.; Smith, A. R. G.; Cavaye, H.; Shaw, P. E.; James, M.; Krueger, K. B.; Gentle, I. R.; Meredith, P.; Burn, P. L., Morphology of All-Solution-Processed "Bilayer" Organic Solar Cells. *Advanced Materials* **2011,** *23* (6), 766-770.
56. Png, R.-Q.; Chia, P.-J.; Tang, J.-C.; Liu, B.; Sivaramakrishnan, S.; Zhou, M.; Khong, S.-H.; Chan, H. S. O.; Burroughes, J. H.; Chua, L.-L.; Friend, R. H.; Ho, P. K. H., High-performance polymer semiconducting heterostructure devices by nitrene-mediated photocrosslinking of alkyl side chains. *Nature Materials* **2010,** *9* (2), 152-158.

57. Love, J. C.; Estroff, L. A.; Kriebel, J. K.; Nuzzo, R. G.; Whitesides, G. M., Self-assembled monolayers of thiolates on metals as a form of nanotechnology. *Chemical Reviews* **2005,** *105* (4), 1103-1169.

58. Wei, Q.; Tajima, K.; Tong, Y.; Ye, S.; Hashimoto, K., Surface-Segregated Monolayers: A New Type of Ordered Monolayer for Surface Modification of Organic Semiconductors. *Journal of the American Chemical Society* **2009,** *131* (48), 17597-17604.

59. Magliulo, M.; Manoli, K.; Macchia, E.; Palazzo, G.; Torsi, L., Tailoring Functional Interlayers in Organic Field-Effect Transistor Biosensors. *Advanced Materials* **2014**, Early View, doi: 10.1002/adma.201403477..

60. Goh, C.; Scully, S. R.; McGehee, M. D., Effects of molecular interface modification in hybrid organic-inorganic photovoltaic cells. *Journal of Applied Physics* **2007,** *101* (11).

61. Kinoshita, Y.; Hasobe, T.; Murata, H., Control of open-circuit voltage in organic photovoltaic cells by inserting an ultrathin metal-phthalocyanine layer. *Applied Physics Letters* **2007,** *91* (8).

62. Tan, Z.-K.; Johnson, K.; Vaynzof, Y.; Bakulin, A. A.; Chua, L.-L.; Ho, P. K. H.; Friend, R. H., Suppressing Recombination in Polymer Photovoltaic Devices via Energy-Level Cascades. *Advanced Materials* **2013,** *25* (30), 4131-4138.

63. Shaheen, S. E.; Brabec, C. J.; Sariciftci, N. S.; Padinger, F.; Fromherz, T.; Hummelen, J. C., 2.5% efficient organic plastic solar cells. *Applied Physics Letters* **2001,** *78* (6), 841-843.

64. Minh Trung, D.; Hirsch, L.; Wantz, G.; Wuest, J. D., Controlling the Morphology and Performance of Bulk Heterojunctions in Solar Cells. Lessons Learned from the Benchmark Poly(3-hexylthiophene): 6,6 -Phenyl-C-61-butyric Acid Methyl Ester System. *Chemical Reviews* **2013,** *113* (5), 3734-3765.

65. Drees, M.; Hoppe, H.; Winder, C.; Neugebauer, H.; Sariciftci, N. S.; Schwinger, W.; Schaffler, F.; Topf, C.; Scharber, M. C.; Zhu, Z. G.; Gaudiana, R., Stabilization of the nanomorphology of polymer-fullerene "bulk heterojunction" blends using a novel polymerizable fullerene derivative. *Journal of Materials Chemistry* **2005,** *15* (48), 5158-5163.

66. Miyanishi, S.; Tajima, K.; Hashimoto, K., Morphological Stabilization of Polymer Photovoltaic Cells by Using Cross-Linkable Poly(3-(5-hexenyl)thiophene). *Macromolecules* **2009,** *42* (5), 1610-1618.

67. Segalman, R. A.; McCulloch, B.; Kirmayer, S.; Urban, J. J., Block Copolymers for Organic Optoelectronics. *Macromolecules* **2009,** *42* (23), 9205-9216.

68. Miyanishi, S.; Zhang, Y.; Hashimoto, K.; Tajima, K., Controlled Synthesis of Fullerene-Attached Poly(3-alkylthiophene)-Based Copolymers for Rational Morphological Design in Polymer Photovoltaic Devices. *Macromolecules* **2012,** *45* (16), 6424-6437.

69. Miyanishi, S.; Zhang, Y.; Tajima, K.; Hashimoto, K., Fullerene attached all-

semiconducting diblock copolymers for stable single-component polymer solar cells. *Chemical Communications* **2010,** *46* (36), 6723-6725.

70. Guo, C.; Lin, Y.-H.; Witman, M. D.; Smith, K. A.; Wang, C.; Hexemer, A.; Strzalka, J.; Gomez, E. D.; Verduzco, R., Conjugated Block Copolymer Photovoltaics with near 3% Efficiency through Microphase Separation. *Nano Letters* **2013,** *13* (6), 2957-2963.

71. Roncali, J., Single Material Solar Cells: the Next Frontier for Organic Photovoltaics? *Advanced Energy Materials* **2011,** *1* (2), 147-160.

72. Walker, B.; Kim, C.; Nguyen, T.-Q., Small Molecule Solution-Processed Bulk Heterojunction Solar Cells. *Chemistry of Materials* **2011,** *23* (3), 470-482.

73. Maggini, M.; Possamai, G.; Menna, E.; Scorrano, G.; Camaioni, N.; Ridolfi, G.; Casalbore-Miceli, G.; Franco, L.; Ruzzi, M.; Corvaja, C., Solar cells based on a fullerene-azothiophene dyad. *Chemical Communications* **2002,** (18), 2028-2029.

74. Nishizawa, T.; Lim, H. K.; Tajima, K.; Hashimoto, K., Efficient dyad-based organic solar cells with a highly crystalline donor group. *Chemical Communications* **2009,** (18), 2469-2471.

75. Bu, L.; Guo, X.; Yu, B.; Qu, Y.; Xie, Z.; Yan, D.; Geng, Y.; Wang, F., Monodisperse Co-oligomer Approach toward Nanostructured Films with Alternating Donor-Acceptor Lamellae. *Journal of the American Chemical Society* **2009,** *131* (37), 13242-13243.

Chapter 2.

Surface Functionalization of Organic Semiconductor Films by Segregated Monolayers

2.1. Introduction

Surface modifications of films are important for controlling the chemical and physical properties of the surfaces, including polarity, wettability, adsorptivity, and reactivity. Self-assembled monolayers (SAMs) are widely used for constructing densely packed monolayers and rely on specific chemical interactions between the surface and the modifiers, such as thiol-metal or Si-O-Si bond formation.[1] By placing functional groups at the other end of the modifiers, the SAM surfaces can be decorated with various chemical groups. For instance, aromatic groups at an Au substrate surface altered the conductivity between the Au substrate and top contact metal.[2] Alkyne groups on a Si substrate allowed the surface to be functionalized with various biomolecules, such as proteins, enzymes, or DNA, through azide-alkyne Huisgen click chemistry for biosensors based on Si-based circuits.[3] However, SAMs are limited to metal or metal oxide surfaces in principle.[1]

Organic electronics, such as organic field effect transistors (OFETs) and organic photovoltaic (OPV) devices, fabricated by solution processes have attracted much attention.[4] The surface and interfacial structures of organic semiconductor films are important because these properties have a profound effect on the device performance. The energy levels and overlap of molecular orbitals at the interface between the electron donor and acceptor in OPV devices determine the photocurrent generation efficiency.[5] In addition, general methods for modifying the surface of organic semiconductor films may pave the way for new applications, such as biosensors based on organic electronics analogous to SAMs on a Si surface.[6] There are some studies of the surface modification of organic semiconductors by the vapor phase deposition of SAM molecules.[7] However, the lack of specific interactions on the surface of the organic films makes post-modification difficult and there is no general method for modifying the surface of the organic semiconductors that is as flexible and widely applicable as SAMs.[7]

In a previous study, Wei et al. proposed that the self-segregation behavior of the molecules with low surface energy could be used to modify the surface of organic

semiconductor thin films during the solution coating processes.[8] Surface segregated monolayers (SSMs) can be prepared easily by coating the substrate with a solution of the matrix semiconductors and surface modifiers.[8a] The author designed fullerene derivatives with semifluoroalkyl chains (FC_n) and polythiophene derivative modifiers, and showed that they spontaneously formed monolayers on the surface of [6,6]-phenyl-C_{61}-butyric acid methyl ester (PCBM) and poly(3-alkylthiophene) films, respectively, with the fluoroalkyl chains aligned vertically on the surface. The surface dipole moment of the SSM altered the ionization potentials of the organic semiconductor films without changing the bulk structures.[8] SSMs were used to change the energy levels at the active layer/electrode interfaces in OPVs and to control the open circuit voltage when it was inserted at the donor/acceptor interface in bilayer OPVs.[9] However, the surface modification of the organic semiconductor films with functional groups by using SSMs has not been reported.

In this study, the author synthesized fullerene-based surface modifiers for SSMs with semifluoroalkyl chains bearing one of five different functional groups (Figure 2.1a). Previously, Wei et al. showed the fullerene derivatives with semifluoroalkyl chains (**F**) segregated at the surface of PCBM film after spin-coating.[8a] The surface modifiers had semifluoroalkyl chains with methoxy (**Me**), benzyloxy (**Bn**), propargyloxy (**A**), 2-thiophenemethoxy (**T**), or hydroxyl groups (**OH**) at one end and methanofullerene was attached at the other end through the ester bond. The surface energy difference between the semifluoroalkyl and the fullerene groups and the anchoring effects caused by strong interactions between the fullerene and the PCBM film aligned the molecules at the surface. Therefore, the author expected that these modifiers could segregate to the surface of the PCBM film during spin coating to form SSMs with the functional groups exposed to the surface (Figure 2.1b). The surface segregation behavior and the alignment of the molecules were investigated by X-ray photoelectron spectroscopy (XPS) and water contact angle measurements.

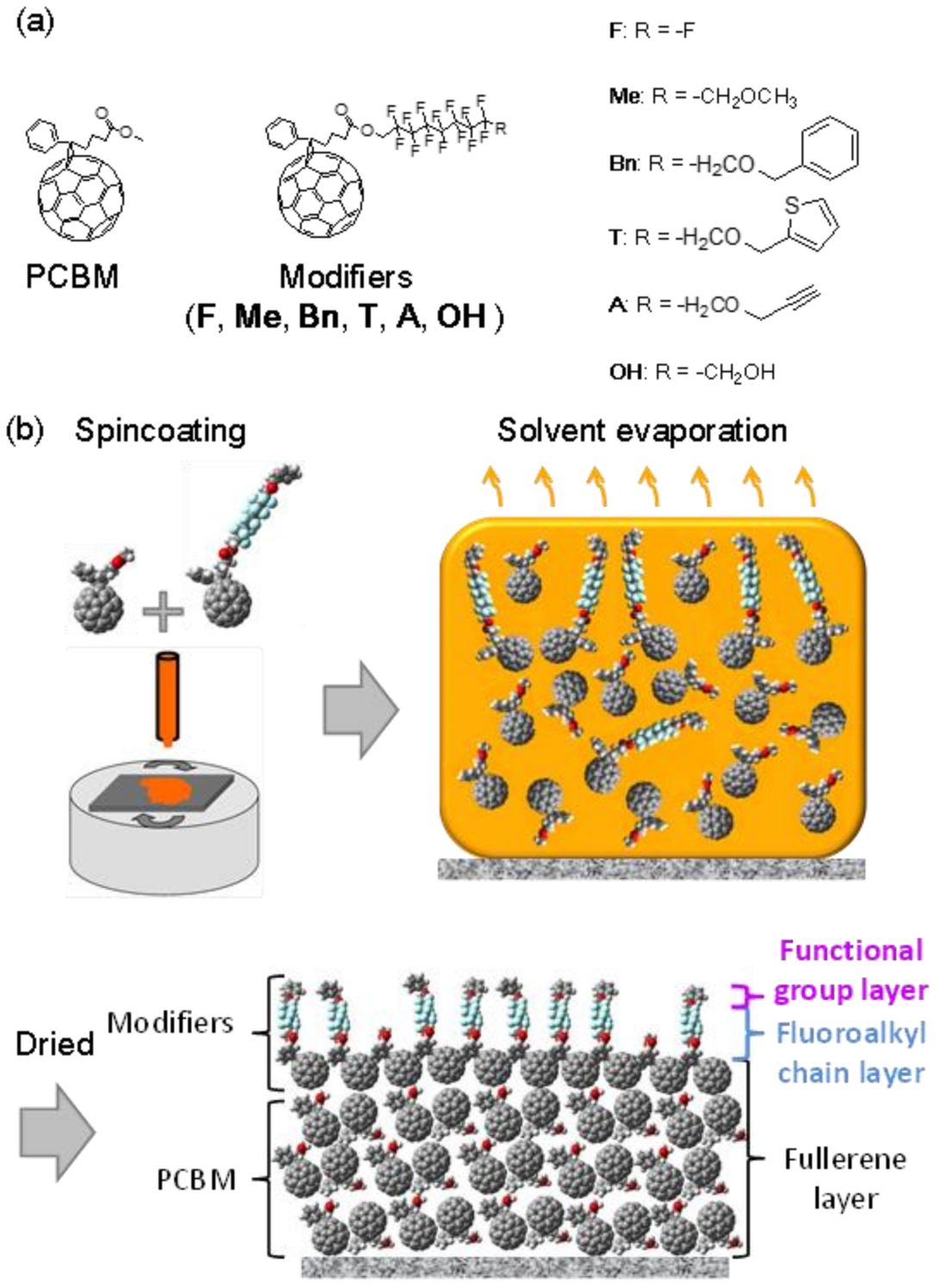

Figure 2.1. (a) Chemical structure of modifiers and (b) schematic representation of the surface modification by SSM during the spin coating process.

2.2. Experimental

Materials and instruments

All the chemicals were purchased from commercial suppliers and used without further purification. High-performance liquid chromatography was carried out on a system with a CBM-20A controller (Shimadzu), an LC-6AD pump (Shimadzu), an SPD-20A UV-vis detector and a Luna Silica column (particle size: 5 μm; column length: 250 mm; inner diameter: 21.2 mm) (Phenomenex). ^{1}H NMR spectra were measured in $CDCl_3$ containing 1% v/v TMS on an Oxford superconducting magnet system (500 MHz). MALDI-TOF-MS spectra were measured on Ultraflex RO (Bruker Daltonics) with dithranol as the matrix. Density functional theory (DFT) calculations were conducted using Gaussian 03 with the B3LYP functional and 6-31G (d) basis set. The molecular structures were optimized by minimizing the energy.

Film preparation

An indium tin oxide (ITO)-coated glass substrate (sheet resistance: 10 Ω sq^{-1}, Geomatech, Japan) was cleaned by ultrasonication in detergent, water, acetone, and 2-propanol. The substrate was dried, and then exposed to UV-O_3 for 30 min. The solution was prepared by dissolving PCBM (10 mg) and different amounts of **F**, **Me**, **Bn**, **A**, **T**, or **OH** in chlorobenzene (1 mL). The solution was spin coated at 600 rpm for 1 min. The film was annealed at 150 °C under N_2 for 5 min.

Surface analysis

X-ray photoelectron spectroscopy (XPS) and ultraviolet photoelectron spectroscopy (UPS) was performed on an AXIS-ULTRADLD spectrometer (Kratos Analytical) and a PHI 5000 Versa Probe II surface analysis instrument (ULVAC-PHI). Monochromated Al *K*α radiation was used in all the XPS measurements. The carbon 1s (non-fluorinated carbon: 282 eV, fluorinated carbon: 288 eV), fluorine 1s (686 eV), and S 2p (162 eV) peaks were used for the characterization. To obtain the XPS depth profile, each sample was etched using an argon ion etcher at an acceleration voltage of 500 V with an etching rate of approximately 0.1 nm/s. He I radiation was used in all the UPS measurements. The static contact angle of a dichlorobenzene solution of modifiers and PCBM on glass substrate and distilled water on the each film was measured on a DMe-201 (Kyowa) and a CA-X contact angle meter (Kyowa) at room temperature.

Synthesis

[6,6]-Phenyl-C_{61}-butyric acid was synthesized according to procedures in the literature.[10]

2-bromomethylthiophene

2-Thiophenemethanol (2.00 g, 17.5 mmol), anhydrous pyridine (100 μL), and anhydrous dichloromethane (75 mL) were added to a 100 mL two-neck round-bottom flask under N_2. The mixture was cooled to 0 °C and phosphorus tribromide (2.49 mL, 26.3 mmol) was added dropwise. The reaction mixture was stirred at 0 °C for 1 h, and then at room temperature for 1 h. Water was added to quench the reaction and the mixture was extracted with dichloromethane. The organic layer was dried with sodium sulfate and filtered. The solvent was removed in vacuo, yielding the product as a pale yellow liquid (2.82 g, 91%).

^{1}H NMR ($CDCl_3$, 500 MHz): δ (ppm): 7.31-7.32 (d, 1H), 7.11-7.12 (d, 1H), 6.94-6.95 (m, 1H), 4.75 (s, 2H).

General synthesis for the ω-functionalized semifluoroalkyl alcohols (1-4)

2,2,3,3,4,4,5,5,6,6,7,7,8,8,9,9-Hexadecafluoro-1,10-decanediol (1.00 g, 2.16 mmol), NaH (oil dispersion 50–72%, 118 mg), and dry THF were added to a 100 mL two-neck round-bottom flask under N_2. The reaction mixture was stirred at room temperature for 1 h. Iodomethane, benzyl bromide, propargyl bromide, or 2-thiophenemethanol (3.24 mmol) was added for the synthesis of corresponding product **1-4**, respectively. The reaction mixture was stirred overnight at 60 °C. Water was added to quench the reaction and the mixture was extracted with ethyl acetate. The organic layer was dried with magnesium sulfate and filtered. The product was purified by column chromatography using silica gel and chloroform as the eluent, yielding a white solid.

12-Methoxy-3,3,4,4,5,5,6,6,7,7,8,8,9,9,10,10-hexadecafluoro-1-dodecanol (1) (Yield: 31%)

^{1}H NMR ($CDCl_3$, 500 MHz): δ (ppm): 4.06-4.15 (m, 2H), 3.86-3.93 (t, 2H), 3.52 (s, 3H), 2.03-2.07 (t, 1H).

12-Benzyloxy-3,3,4,4,5,5,6,6,7,7,8,8,9,9,10,10-hexadecafluoro-1-dodecanol (2) (Yield: 32%)

^{1}H NMR ($CDCl_3$, 500 MHz): δ (ppm): 7.32-7.40 (m, 5H), 4.69 (s, 2H), 4.06-4.15 (m, 2H), 3.91-3.98 (t, 2H), 1.99-2.02 (t, 1H).

12-Propargyloxy-3,3,4,4,5,5,6,6,7,7,8,8,9,9,10,10-hexadecafluoro-1-dodecanol (3) (Yield: 30%)

^{1}H NMR ($CDCl_3$, 500 MHz): δ (ppm): 4.32-4.33 (d, 2H), 4.02-4.14 (m, 4H), 2.54-2.55 (t, 1H), 2.06-2.10 (t, 1H).

12-(Thiophene-2-methoxy)-3,3,4,4,5,5,6,6,7,7,8,8,9,9,10,10-hexadecafluoro-1-dodecanol (4) (Yield: 30%)

^{1}H NMR ($CDCl_3$, 500 MHz): δ (ppm): 7.35-7.36 (d, 1H), 7.05-7.06 (d, 1H), 7.00-7.01 (m, 1H), 4.84 (s, 2H), 4.07-4.11 (m, 2H), 3.90-3.96 (t, 2H), 2.10-2.13 (t, 1H).

General synthesis for Me, Bn, A, and T

[6,6]-Phenyl-C_{61}-butyric acid (100 mg, 0.112 mmol) was added to a 50 mL two-neck round-

bottom flask under N_2, and then distilled CS_2 (30 mL) and thionyl chloride (966 μL, 17.9 mmol) were added. The reaction mixture was refluxed overnight at 55 °C. The solvent was removed, and the crude product was dried at 80 °C for 3 h. Then, anhydrous toluene (10 mL) and NaH (oil dispersion 50–72%, 12.0 mg), which had been washed with hexane, were added. The flask was covered with aluminum foil, and **2**, **3**, **4**, or **5** (0.168 mmol) was added for **Me**, **Bn**, **A**, or **T**, respectively. The reaction mixture was stirred at room temperature for 48 h and then purified by column chromatography using silica gel and chloroform as the eluent and by HPLC using chloroform as the eluent. The product was reprecipitated in methanol and filtered, yielding a brown solid.

2,13-Dioxa-4,4,5,5,6,6,7,7,8,8,9,9,10,10,11,11-hexadecafluoro-14-carbonyl-18-phenyl-18-[6.6]-C_{61}-octadecane (Me) (Yield: 80%)

^{1}H NMR ($CDCl_3$, 500 MHz): δ (ppm): 7.91-7.94 (m, 2H), 7.53-7.57 (m, 2H), 7.46-7.47 (m, 1H), 4.56-4.63 (t, 2H), 3.86-3.93 (t, 2H), 3.52 (s, 3H), 2.90-2.94 (m, 2H), 2.62-2.65 (m, 2H), 2.20-2.26 (m, 2H). MALDI-TOF-MS calcd. 1354.74, found 1354.24.

1-Phenyl-2,13-dioxa-4,4,5,5,6,6,7,7,8,8,9,9,10,10,11,11-hexadecafluoro-14-carbonyl-18-phenyl-18-[6.6]-C_{61}-octadecane (Bn) (Yield: 70%)

^{1}H NMR ($CDCl_3$, 500 MHz): δ (ppm): 7.92-7.94 (m, 2H), 7.53-7.57 (m, 2H), 7.48-7.50 (m, 1H), 7.33-7.38 (m, 5H), 4.69 (s, 2H), 4.56-4.63 (t, 2H), 3.91-3.98 (t, 2H), 2.90-2.94 (m, 2H), 2.61-2.65 (m, 2H), 2.20-2.24 (m, 2H). MALDI-TOF-MS calcd. 1430.77, found 1430.27.

1-Yne-4,15-dioxa-6,6,7,7,8,8,9,9,10,10,11,11,12,12,13,13-hexadecafluoro-16- carbonyl-20-phenyl-20-[6.6]-C_{61}-icosane (A) (Yield: 56%)

^{1}H NMR ($CDCl_3$, 500 MHz): δ (ppm): 7.92-7.94 (m, 2H), 7.53-7.57 (m, 2H), 7.48-7.50 (m, 1H), 4.56-4.63 (t, 2H), 4.31-4.32 (d, 2H), 4.02-4.09 (t, 2H), 2.90-2.94 (m, 2H), 2.61-2.65 (m, 2H), 3.54-3.55 (t, 1H), 2.18-2.26 (m, 2H). MALDI-TOF-MS calcd. 1378.74, found 1378.23.

1-(Thiophene-2-yl)-2,13-dioxa-4,4,5,5,6,6,7,7,8,8,9,9,10,10,11,11-hexadecafluoro-14-carbonyl-18-phenyl-18-[6.6]-C_{61}-octadecane (T) (Yield: 58%)

^{1}H NMR ($CDCl_3$, 500 MHz): δ (ppm): 7.92-7.94 (m, 2H), 7.53-7.57 (m, 2H), 7.48-7.50 (m, 1H), 7.34-7.36 (m, 1H), 7.05-7.06 (m, 1H), 7.00-7.02 (m, 1H), 4.84 (s, 2H), 4.56-4.63 (t, 2H), 3.90-3.97 (t, 2H), 2.90-2.94 (m, 2H), 2.61-2.65 (m, 2H), 2.20-2.26 (m, 2H). MALDI-TOF-MS calcd. 1436.73, found 1436.21.

General synthesis for F and OH[11]

2,2,3,3,4,4,5,5,6,6,7,7,8,8,9,9,9-Heptadecafluoro-1-nonanol (4.94 g, 11.0 mmol) or 2,2,3,3,4,4,5,5,6,6,7,7,8,8,9,9-hexadecafluoro-1,10-decanediol (5.08 g, 11.0 mmol), [6,6]-phenyl-C_{61}-butyric acid methyl ester (1.00 g, 1.10 mmol), *p*-toluenesulfonic acid monohydrate, and anhydrous *o*-dichlorobenzene (100 mL) were added to a 100 mL two-neck round-bottom flask

under N_2. The reaction mixture was stirred at 180 °C for 3 days and then poured into methanol (2 L). The resulting solid was collected by vacuum filtration and the crude product was purified by column chromatography using silica gel and toluene as the eluent. The product was reprecipitated in methanol and filtered, yielding a brown solid.

1,1,1,2,2,3,3,4,4,5,5,6,6,7,7,8,8-Heptadecafluoro-10-oxa-11-carbonyl-15-phenyl-15-[6.6]-C_{61}-pentadecane (F) (Yield: 90%)

^{1}H NMR ($CDCl_3$, 500 MHz): δ (ppm): 7.92-7.94 (m, 2H), 7.53-7.57 (m, 2H), 7.46-7.49 (m, 1H), 4.57-4.64 (t, 2H), 2.90-2.94 (m, 2H), 2.62-2.65 (m, 2H), 2.17-2.26 (m, 2H). MALDI-TOF-MS calcd. 1328.21, found 1328.71.

1-ol-2,2,3,3,4,4,5,5,6,6,7,7,8,8,9,9-Hexadecafluoro-11-oxa-12-carbonyl-16-phenyl-16-[6.6]-C_{61}-hexadecane (OH) (Yield: 46%)

^{1}H NMR ($CDCl_3$, 500 MHz): δ (ppm): 7.91-7.93 (m, 2H), 7.53-7.57 (m, 2H), 7.46-7.50 (m, 1H), 4.56-4.63 (t, 2H), 4.06-4.15 (m, 2H), 2.90-2.96 (m, 2H), 2.61-2.65 (m, 2H), 2.18-2.26 (m, 2H), 1.99-2.02 (t, 1H). MALDI-TOF-MS calcd. 1340.73, found 1340.18.

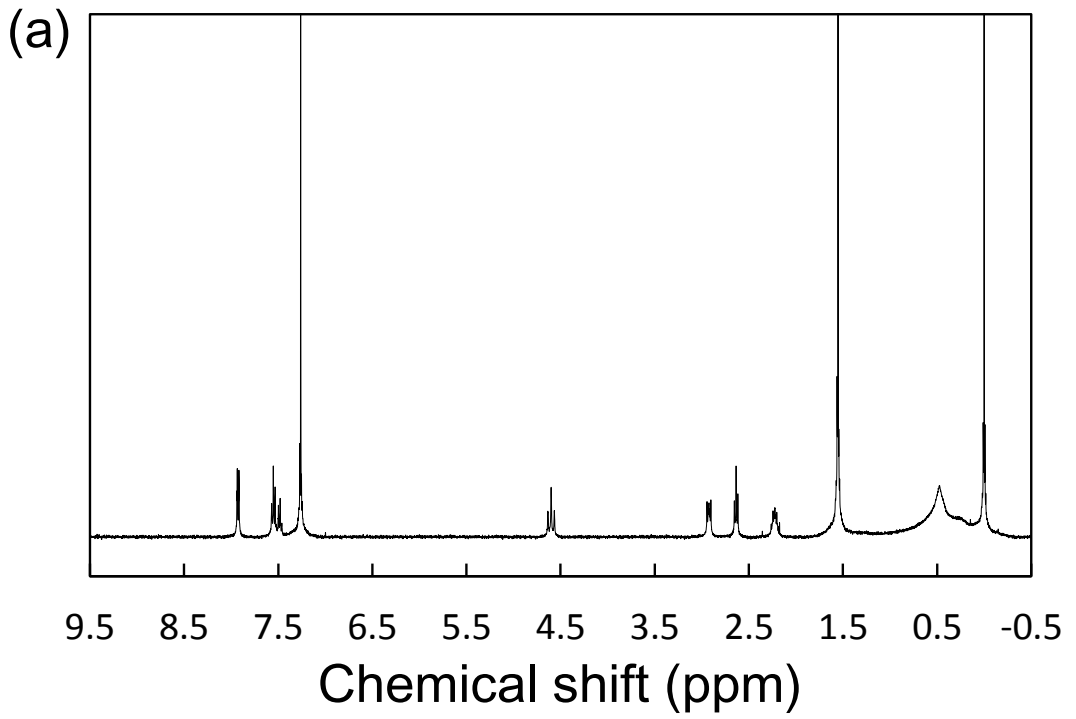
(a)
9.5
8.5
7.5
6.5
5.5
4.5
3.5
2.5
1.5
0.5
-0.5
Chemical shift (ppm)

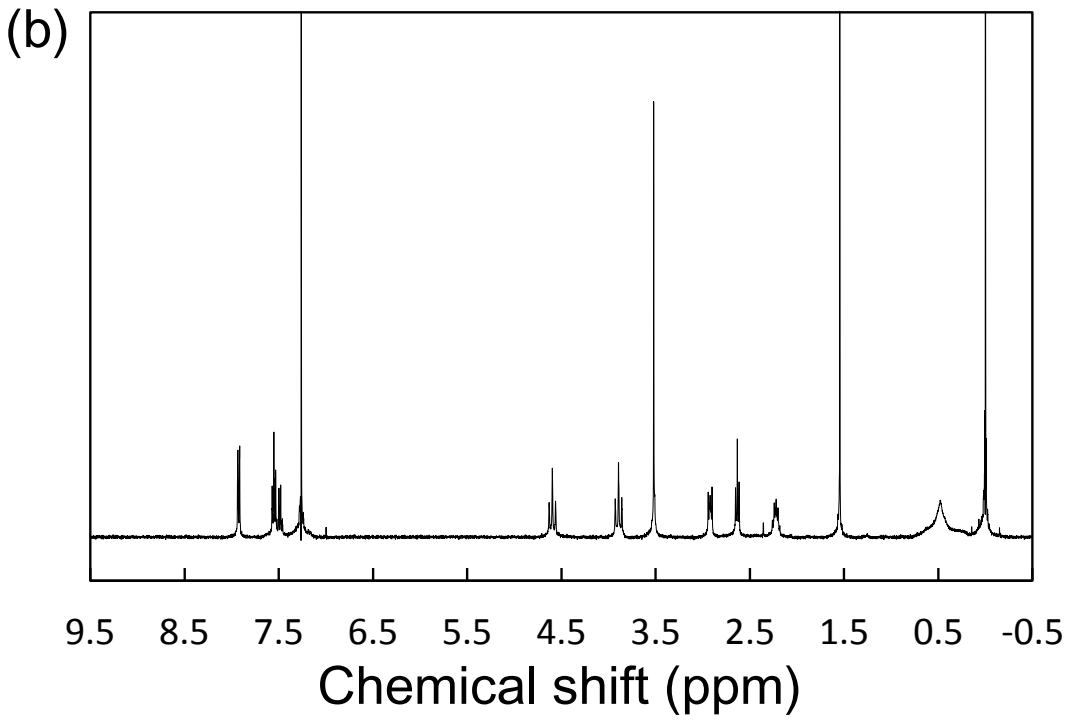
(b)
9.5
8.5
7.5
6.5
5.5
4.5
3.5
2.5
1.5
0.5
-0.5
Chemical shift (ppm)

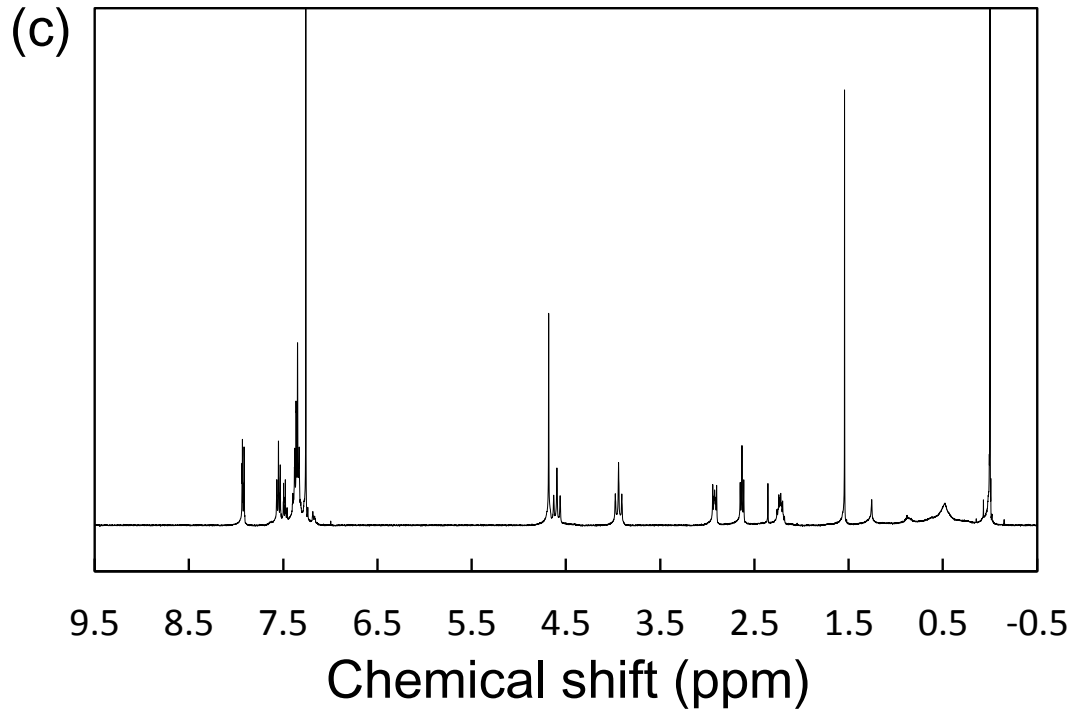
(c)
9.5
8.5
7.5
6.5
5.5
4.5
3.5
2.5
1.5
0.5
-0.5
Chemical shift (ppm)

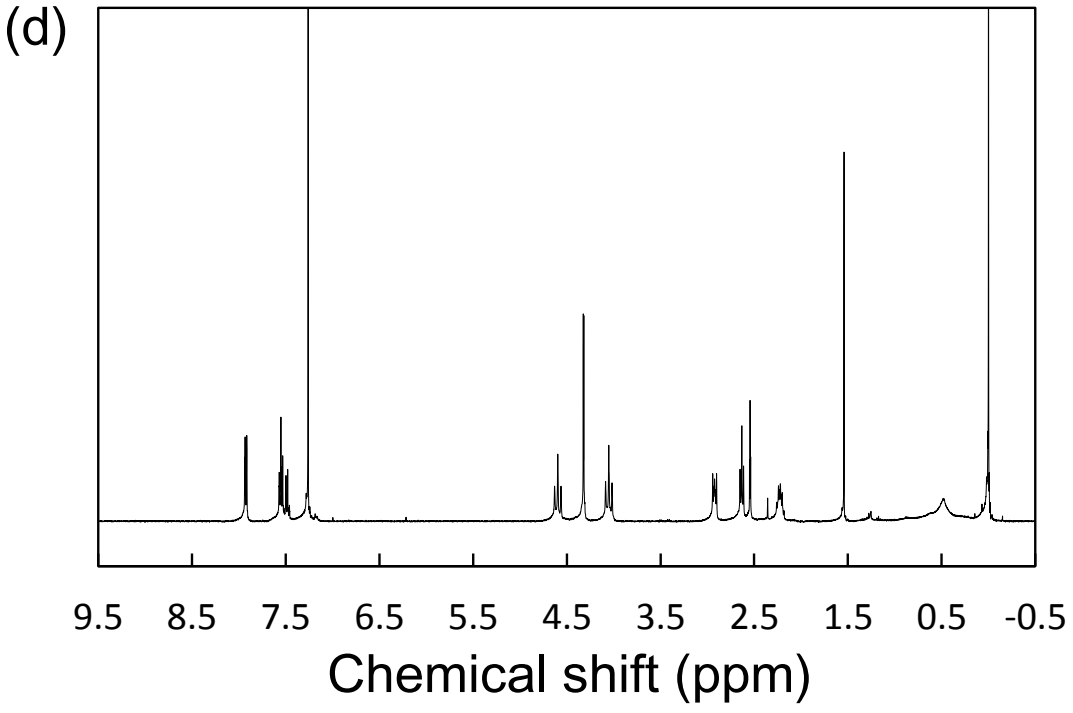
(d)
9.5
8.5
7.5
6.5
5.5
4.5
3.5
2.5
1.5
0.5
-0.5
Chemical shift (ppm)

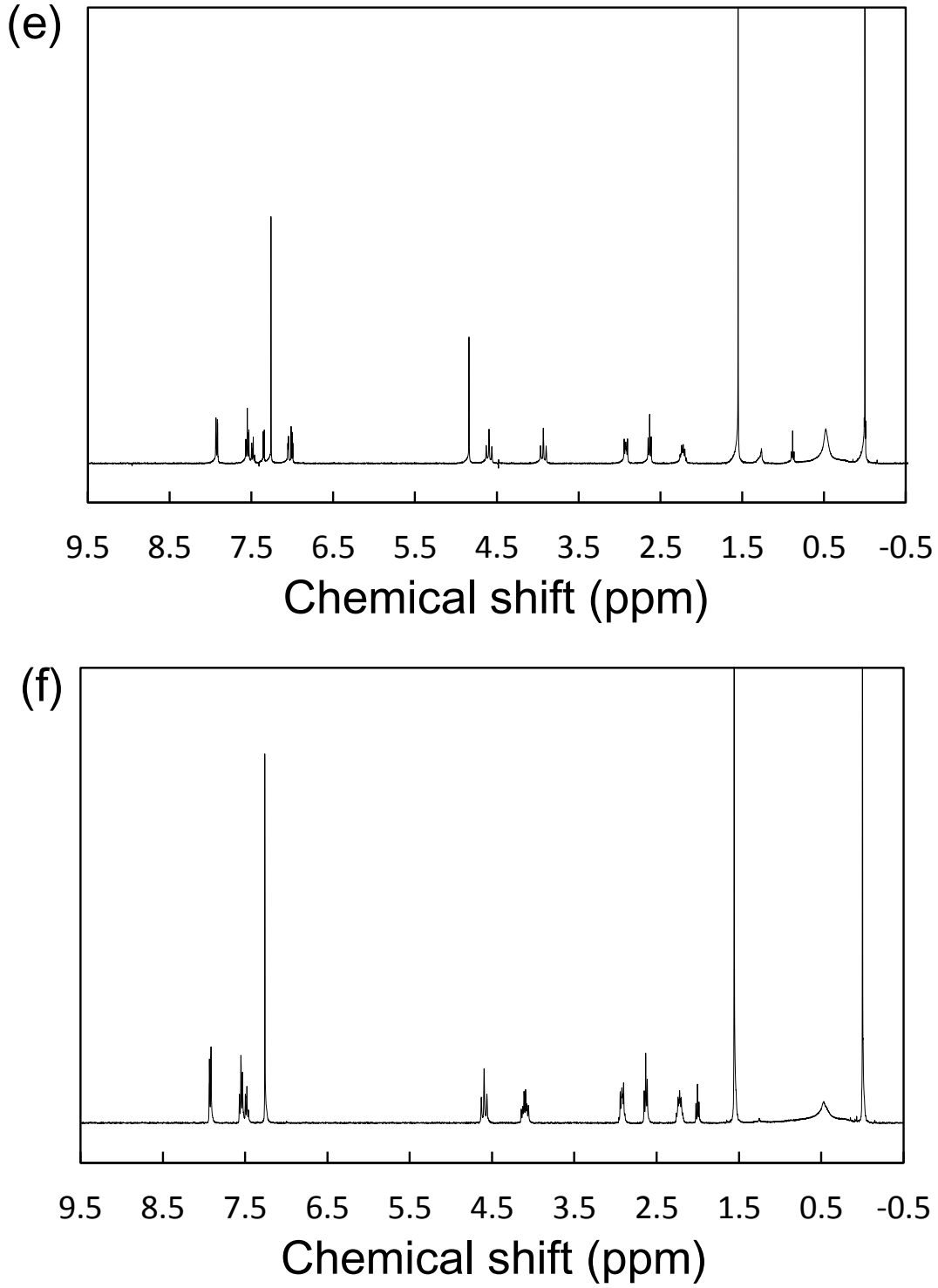

Figure 2.2. ^{1}H-NMR charts of (a) **F**, (b) **Me**, (c) **Bn**, (d) **A**, (e) **T** and (f) **OH**.

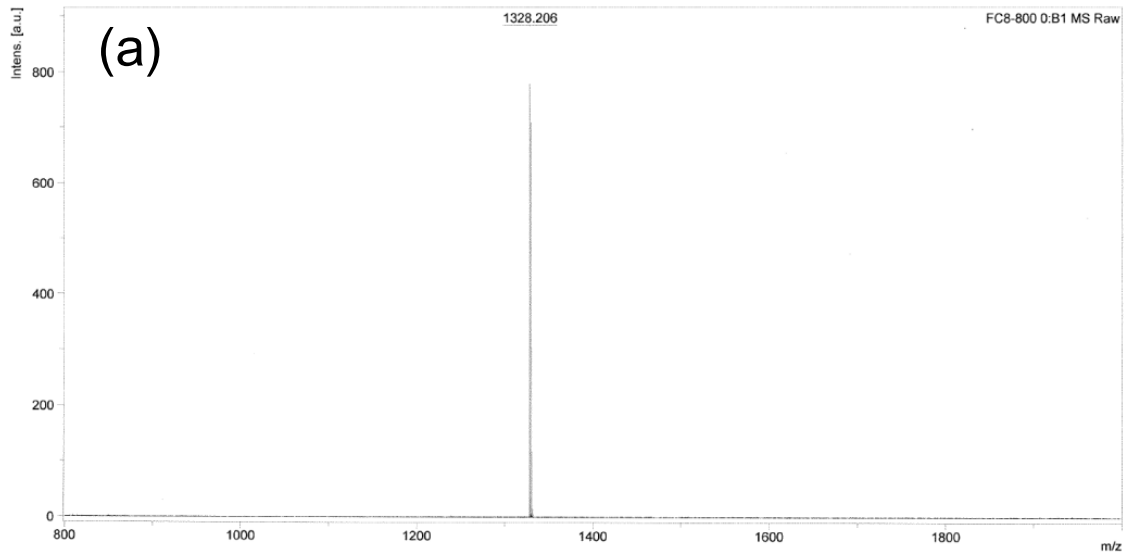
(a)
1328.206
FC8-800 0:B1 MS Raw
Intens. [a.u.]
800
600
400
200
0
800
1000
1200
1400
1600
1800
m/z

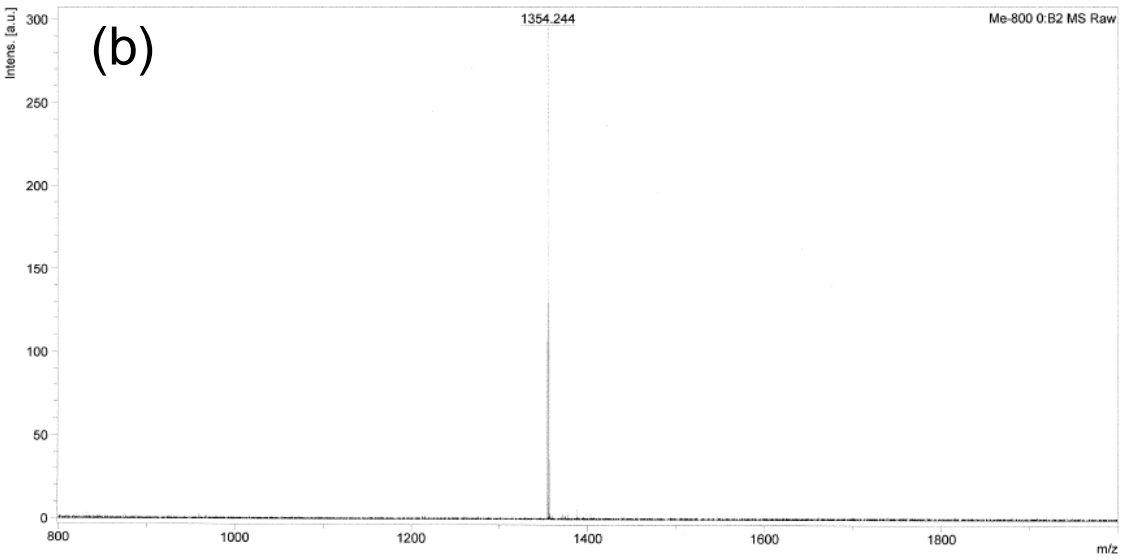
(b)
1354.244
Me-800 0:B2 MS Raw
Intens. [a.u.]
300
250
200
150
100
50
0
800
1000
1200
1400
1600
1800
m/z

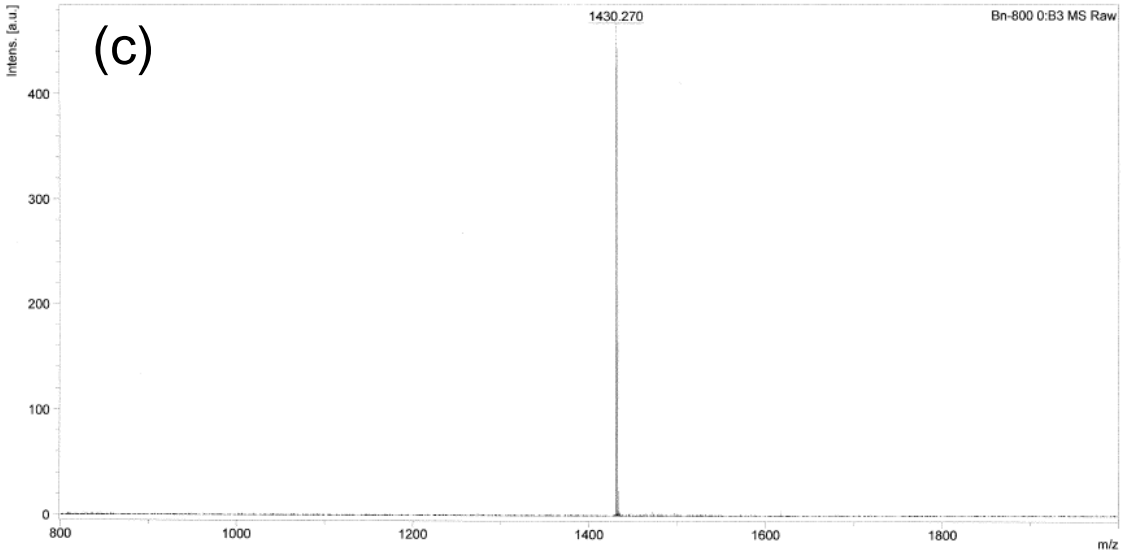
(c)
1430.270
Bn-800 0:B3 MS Raw
Intens. [a.u.]
400
300
200
100
0
800
1000
1200
1400
1600
1800
m/z

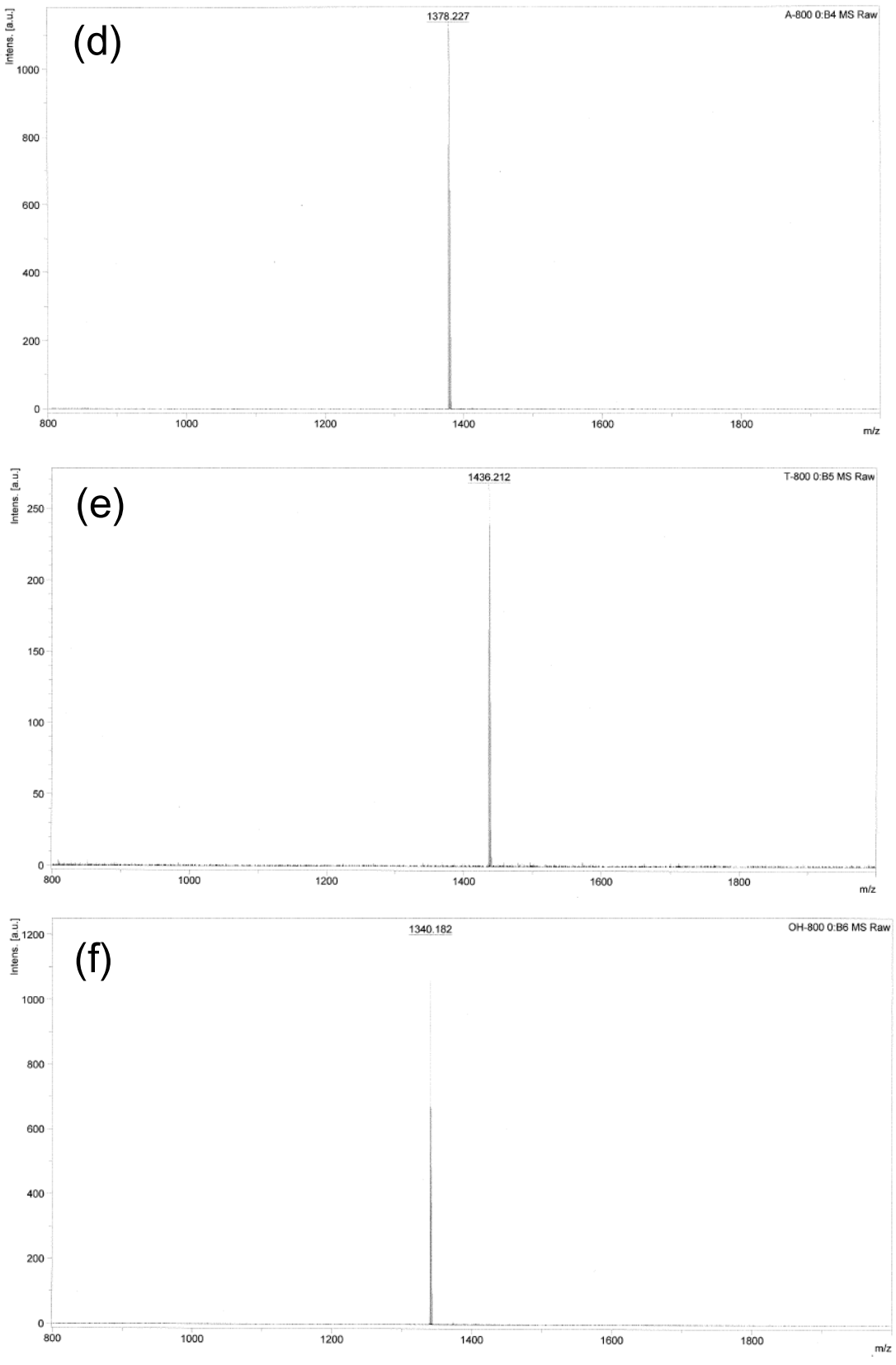

Figure 2.3. MALDI-TOF-MS charts of (a) **F**, (b) **Me**, (c) **Bn**, (d) **A**, (e) **T** and (f) **OH**.

2.3. Results and discussion

The synthetic routes for modifiers are shown in Scheme 1. **Me**, **Bn**, **A**, and **T** were synthesized in moderate yields by etherification of the semifluoroalkyl diol and subsequent esterification with the acid chloride of PCBM.[10] **F** and **OH** were synthesized by the acid-catalyzed ester exchange reaction with PCBM.[11]

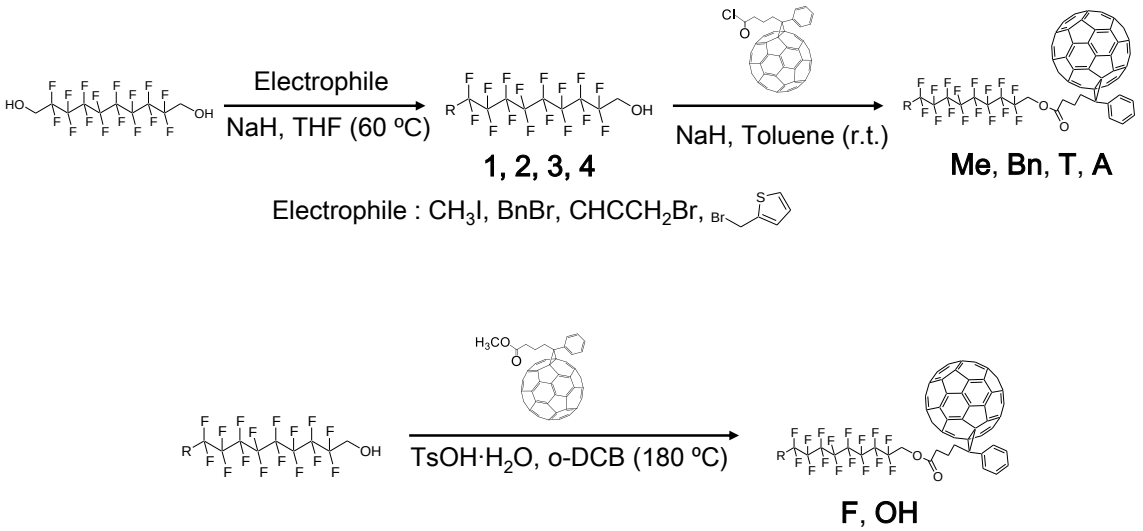

Scheme 2.1. Synthetic route to the surface modifiers.

The surface segregation behavior of the modifiers in the blended films with PCBM was investigated by XPS. Films were prepared by spin coating from solutions containing different concentrations of the modifiers (0.25–2 g/L) and a fixed concentration of PCBM (10 g/L). The F/C atomic ratios at the surface were calculated from the peak intensity of F1s and non-fluorinated C 1s in XPS and they are plotted in Figure 2.4 as a function of the modifier concentration in the solution. The F/C atomic ratios calculated for homogeneously mixed films are also plotted for comparison. The F/C ratios measured by XPS were higher than the calculated ratios for homogeneous mixed films for all the modifiers at all concentrations. This indicated that the surface segregation of the modifiers during spin coating as a result of the low surface energy of the semifluoroalkyl chain, even though the ends of the semifluoroalkyl chains were modified with the functional groups. The F/C ratios reached saturation at concentrations of around 0.8–1.0 g/L for **F** and **Me**. However, gradual saturation was observed for **Bn**, **A**, **T**, and **OH**. This could be explained by the functional groups at the ends increasing the surface energy and reducing the energetic driving force of the modifiers to segregate at the film surface.

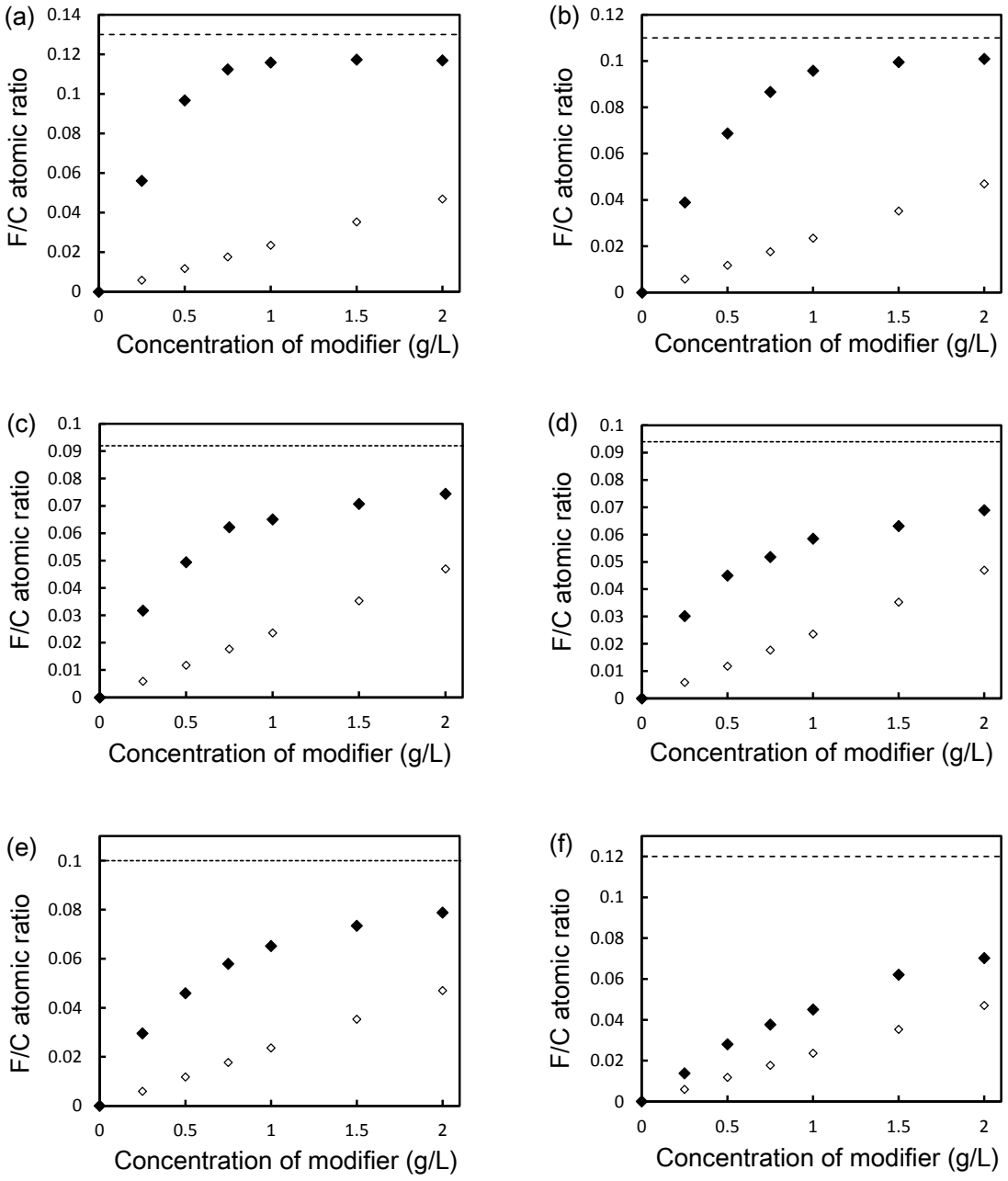

Figure 2.4. F/C atomic ratio on the surfaces of modifier/PCBM thin films measured by XPS (black squares) and calculated from the composition of the solution (white squares) plotted as a function of the modifier concentrations in the solution. The modifiers are (a) **F**, (b) **Me**, (c) **Bn**, (d) **T**, (e) **A**, and (f) **OH**.

To estimate the maximum XPS F/C ratios for surfaces fully covered with SSMs (Γ_{max}^{calc}), it was assumed that the surface of the PCBM film was covered with a densely packed uniform monolayer of the modifiers and simple bilayer or trilayer models were used.[12] The molecular

conformations were optimized by density functional theory calculations. The density of the fullerene groups in SSMs was assumed to be the same as that in the PCBM crystal. Γ_{max}^{calc} for the PCBM films with surface modifiers were 0.13, 0.11, 0.092, 0.094, 0.10, and 0.12 for **F**, **Me**, **Bn**, **T**, **A**, and **OH**, respectively, shown as dashed lines in Figure 2.4. The experimental F/C atomic ratios become very close to the calculated values above the saturation concentrations for **F** and **Me**, indicating the high coverage of the surface of PCBM with the modifiers. In contrast, **Bn**, **T**, **A**, and particularly **OH** showed large differences between the experimental and calculated values. This indicates that the surfaces of the films are not fully covered with the surface modifiers even at high concentrations above 1 g/L.

The F atom XPS depth profiles were measured for the films prepared from the solution containing 1 g/L of the modifiers and 10 g/L of PCBM. The film surfaces were etched by Ar ion beams at an etching rate of approximately 0.1 nm/s. The F/C atomic ratio was measured repeatedly after each 20 s etching for a total of 400 s. The F/C ratios of all the films decreased sharply after 20 s etching (see Figure 2.5). These results also demonstrated that most of the F atoms are within several nanometers of the surface due to the surface segregation of the modifiers.

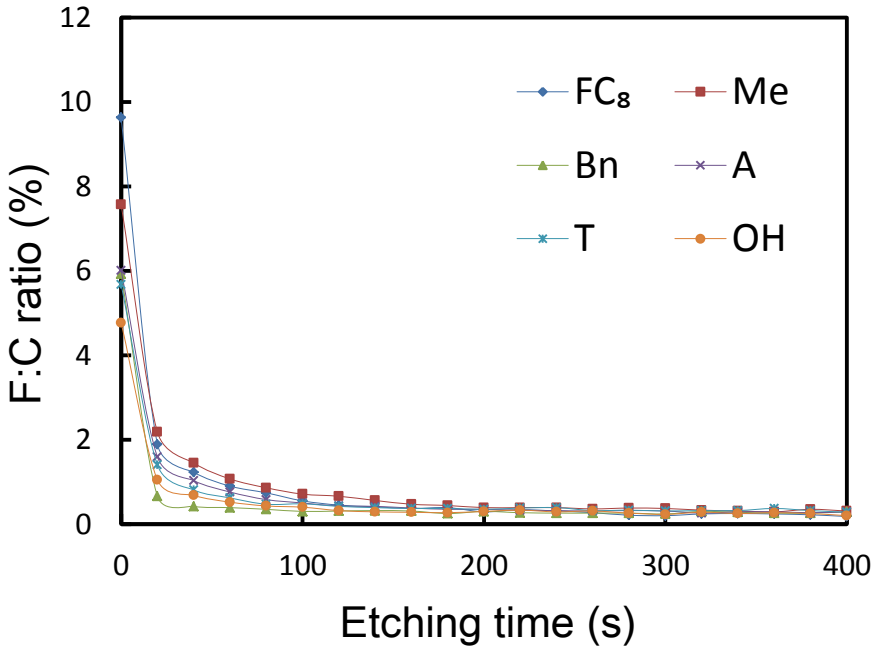

Figure 2.5. XPS depth profile: the F:C ratio of the films fabricated from 1 g/L solutions of the modifiers.

The dependence of the F/C ratios on the concentration is quantitatively understood in an analogous way to the Langmuir adsorption isotherm of surfactants at liquid/air interfaces. During spin coating, a thin liquid film is formed on the substrate and the surface adsorption of the

modifiers is partly equilibrated with the solution. The amount of adsorbed modifiers should depend on the surface energy of the modifier. After the solvent evaporation, the modifiers may remain on the surface of the solid films with a similar orientation. In reality, the system is not equilibrated and part of the solution spreads out during the coating, which makes it difficult to estimate the effective concentration of the surfactant in the liquid films. Quantitative values for the equilibrium constants could not be obtained with simple Langmuir isotherm analysis of the data.

To investigate the surface activation effect of the modifiers qualitatively, static contact angles of the solution of modifiers and PCBM were measured on a glass substrate. The solution concentration was 1 g/L for all the modifiers and 10 g/L for PCBM. *o*-Dichlorobenzene was used as the solvent for suppressing evaporation during the measurements (Figure 2.6a). All the contact angles for mixed solutions containing modifiers were lower than for the PCBM solution. This demonstrated that the molecules acted as a surfactant by segregating at the air/solution interface and decreased the surface energy of the solution. It also suggested that the segregation of modifiers at the surface of the solution happened during spin coating before the films were formed. The order of contact angles was **F** > **Bn** > **OH**, which could be related to the surface energy depending on the functional groups.

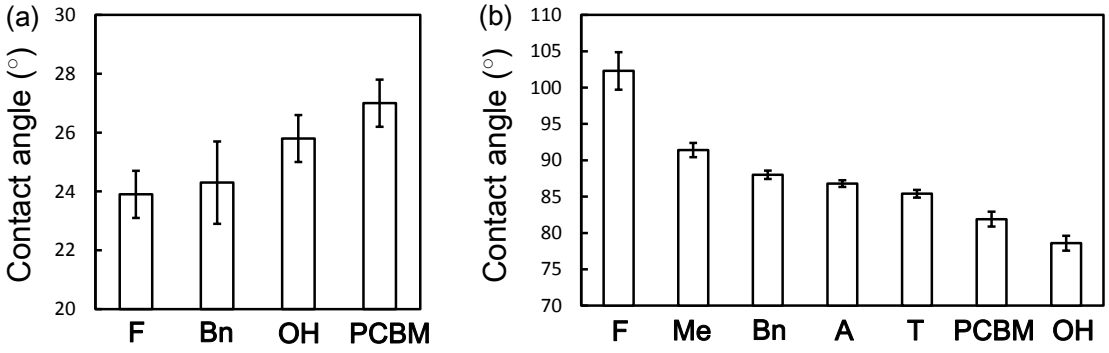

Figure 2.6. Static contact angles of (a) dichlorobenzene solution with 1 g/L of the modifiers and 10 g/L of PCBM on glass substrates (b) water on the films made from solution with 1 g/L of the modifiers and 10 g/L of PCBM.

To obtain information about the orientation of the modifiers and the exact location of the functional group at the film surfaces, the author used angle resolved XPS (ARXPS) of the **T**/PCBM film made from the solution with 1 g/L of **T** with S as the probe for thiophene.[12-13] The peak ratio of S 2p to C 1s was used for measurements. Assuming that the S atoms are a distance of d_S from the surface with coverage α and that the C atoms are distributed uniformly in all regions of the film, the S/C atomic ratio is described by

$$\mathrm{S/C}\ atomic\ ratio = \frac{I_S/I_S^{\circ}}{I_C/I_C^{\circ}} = \frac{\alpha X_S}{X_C}\left\{1 - \exp\left(-\frac{d_S}{\lambda_S \cos\theta}\right)\right\} \quad \text{eq. 1}$$

where λ_S is the attenuation length of an S 2p photoelectron and a literature value of 4.1 nm was used;[12, 14] X_S is the local atomic concentration of sulfur in the functional group layer; and X_C is the local atomic concentration of carbon in all regions, which approximates the local atomic concentration of carbon in the fullerene layer. Coverage α was assumed to be 0.65, calculated from the experimental F/C atomic ratio and Γ_{max}^{calc}. The intensities of the S 2p and C 1s peaks were measured with various take-off angles from 0° to 60°, and $I_S I_C^{\circ}/I_C I_S^{\circ}$ was plotted as the function of $1/\cos\theta$ (Figure 2.7). Plots of the measured peak intensity ratio were fitted with eq. 1 and the thickness, d_S, was obtained. The model of the structure where the thiophene group is at the top surface fits the experimental data well; R^2 had a value of 0.99. The value of d_S was calculated as 0.16 nm, which indicates that S atoms were present in the first atomic layer and that the thiophenyl groups were at the film surface. Similar ARXPS analysis was not feasible for the other modifiers because they did not contain functional groups with probe atoms.

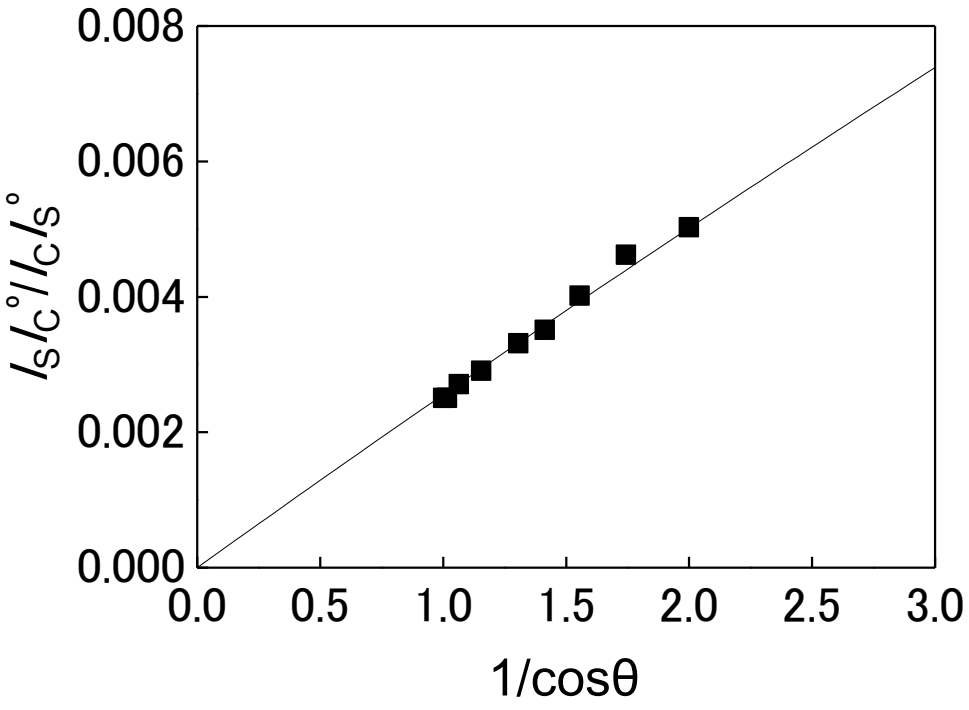

Figure 2.7. Plot of $1/\cos\theta$ vs $I_S I_C^{\circ}/I_C I_S^{\circ}$ the T surface layer by using C 1s and S 2p peaks from the ARXPS spectra.

Ultraviolet photoelectron spectroscopy (UPS) measurements were carried out to investigate the energy levels of the films. The films were prepared from a concentration of 1 g/L for the all modifiers and a PCBM concentration of 10 g/L on ITO substrate. Figure 2.8a, b and c show the UPS data at whole, cut off and HOMO regions, respectively, using the He I irradiation. By using the spectrum width determined from the distance between the cut off to the HOMO edge, the ionization potential (IP) of the films can be extracted. IPs and the positions of HOMO peaks are summarized in Table 2.1. Ionization potentials of the films with the modifiers were reduced by 0.25-0.38 eV compared to that of PCBM film, while HOMO peak positions relative to Fermi level were constant. It suggests that the vacuum levels shifted due to aligned surface dipole moment of the modifiers. The degree of the shifts with the modifiers bearing the functional groups was smaller than that of **F** as expected from the molecular structures and the lower coverages. However, quantitative discussions on the surface dipole moment based on the molecular structure are difficult at this stage since the surface coverage is lower than 100% and the surface structures and the molecular orientations are not clear yet.

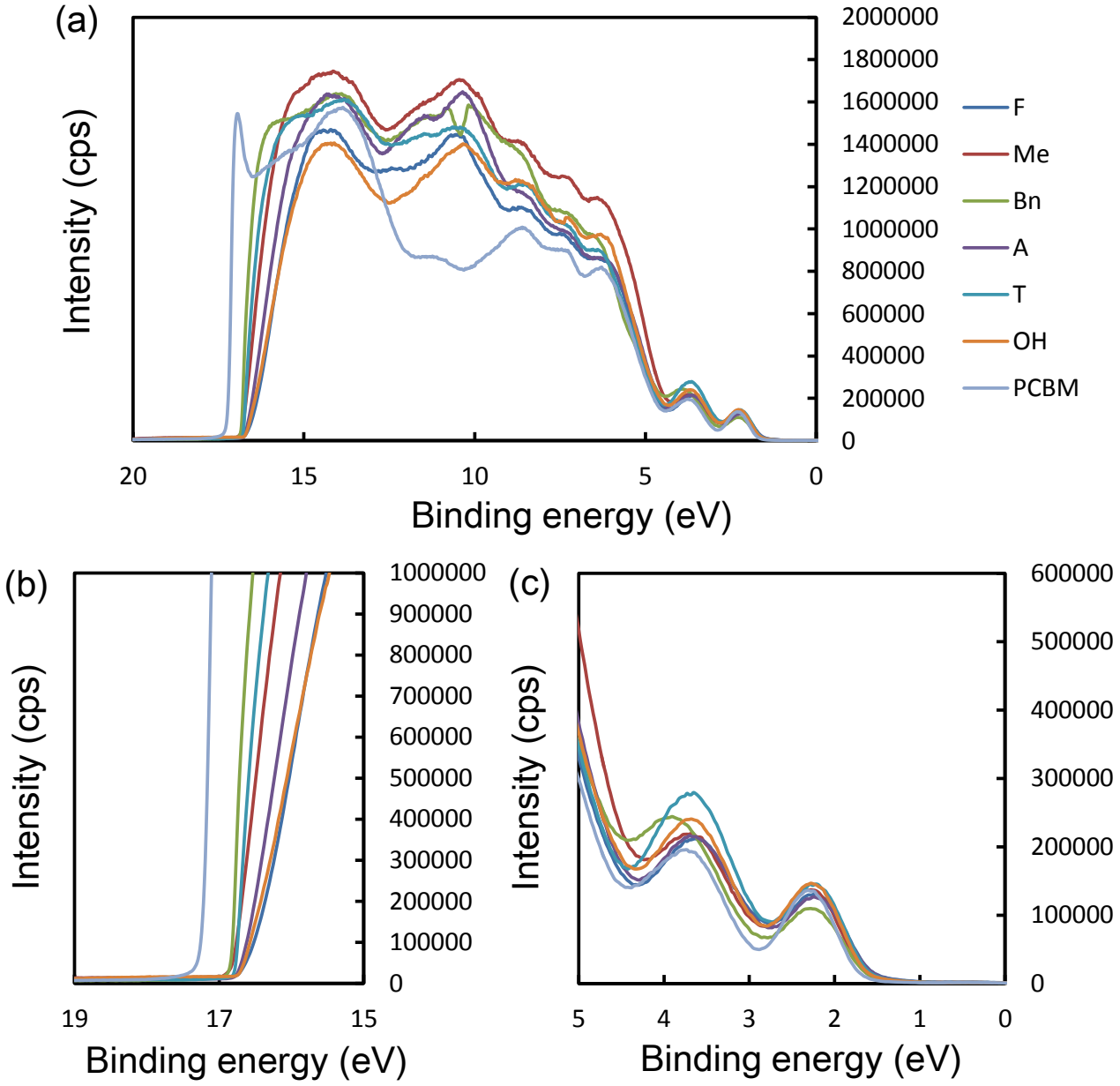

Figure 2.8. UPS spectra: the F:C ratio of the films fabricated from 1 g/L solutions of the modifiers. (a) whole spectra, (b) cut off regions, (c) HOMO regions.

Table 2.1. Ionization potentials and HOMO peak positions of the films

Films	Ionization potentials (eV)	HOMO peak positions (eV)
PCBM	5.66	2.30
F	6.04	2.23
Me	5.93	2.28
Bn	5.91	2.28
A	5.94	2.24
T	5.96	2.24
OH	5.98	2.26

Static water contact angles were measured for the films to observe wettability changes caused by the different functional groups exposed to the surfaces. The films were prepared from a concentration of 1 g/L for the all modifiers and a PCBM concentration of 10 g/L, and a pure PCBM film was prepared from a 10 g/L PCBM solution. The results are summarized in Figure 2.6b. The contact angles on the films of PCBM and **F**/PCBM were similar to previously reported values.[15] The contact angles of the films were in the order **F** > **Me** > **Bn** > **A** > **T** > **PCBM** > **OH**, which could be related to the surface energy of the functional groups. The **OH** film had a lower value than the PCBM film, indicating that the **OH** film had a more hydrophilic surface. This demonstrated that a hydrophilic hydroxyl group could be located at the surface to compensate for the hydrophobicity of the fluoroalkyl chain, although the surface coverage of **OH** was expected to be small.

2.4. Conclusions

The author demonstrated that the end-functionalized fluoroalkyl surfactants with a fullerene group were segregated to the surface of modifier/PCBM films during spin coating from the mixture. This surface modification method was achieved by simple spin coating from mixed solutions of the modifiers and PCBM matrix material, and the functional groups of the modifiers were automatically aligned at the surface of the films. The simplicity of the process and variety of the functionalization means that SSMs are now closer to being a practical method for the surface modification of organic materials, similar to SAMs for metal or metal oxides.[1]

Chapter 2 is reproduced by permission of the PCCP Owner Societies.
S. Izawa, K. Hashimoto, and K. Tajima, *Phys. Chem. Chem. Phys.*, **2014**, *16*, 16383-16387.

References

1. Love, J. C.; Estroff, L. A.; Kriebel, J. K.; Nuzzo, R. G.; Whitesides, G. M., Self-assembled monolayers of thiolates on metals as a form of nanotechnology. *Chemical Reviews* **2005,** *105* (4), 1103-1169.

2. (a) van Dijk, E. H.; Myles, D. J. T.; van der Veen, M. H.; Hummelen, J. C., Synthesis and properties of an anthraquinone-based redox switch for molecular electronics. *Organic Letters* **2006,** *8* (11), 2333-2336; (b) Fracasso, D.; Valkenier, H.; Hummelen, J. C.; Solomon, G. C.; Chiechi, R. C., Evidence for Quantum Interference in SAMs of Arylethynylene Thiolates in Tunneling Junctions with Eutectic Ga-In (EGaIn) Top-Contacts. *Journal of the American Chemical Society* **2011,** *133* (24), 9556-9563.

3. Qin, G.; Santos, C.; Zhang, W.; Li, Y.; Kumar, A.; Erasquin, U. J.; Liu, K.; Muradov, P.; Trautner, B. W.; Cai, C., Biofunctionalization on Alkylated Silicon Substrate Surfaces via "Click" Chemistry. *Journal of the American Chemical Society* **2010,** *132* (46), 16432-16441.

4. (a) Dou, L.; You, J.; Hong, Z.; Xu, Z.; Li, G.; Street, R. A.; Yang, Y., 25th Anniversary Article: A Decade of Organic/Polymeric Photovoltaic Research. *Advanced Materials* **2013,** *25* (46), 6642-6671; (b) Sirringhaus, H., 25th Anniversary Article: Organic Field-Effect Transistors: The Path Beyond Amorphous Silicon. *Advanced Materials* **2014,** *26* (9), 1319-1335.

5. (a) McMahon, D. P.; Cheung, D. L.; Troisi, A., Why Holes and Electrons Separate So Well in Polymer/Fullerene Photovoltaic Cells. *Journal of Physical Chemistry Letters* **2011,** *2* (21), 2737-2741; (b) Chen, W.; Qi, D.-C.; Huang, H.; Gao, X.; Wee, A. T. S., Organic-Organic Heterojunction Interfaces: Effect of Molecular Orientation. *Advanced Functional Materials* **2011,** *21* (3), 410-424.

6. (a) Angione, M. D.; Cotrone, S.; Magliulo, M.; Mallardi, A.; Altamura, D.; Giannini, C.; Cioffi, N.; Sabbatini, L.; Fratini, E.; Baglioni, P.; Scamarcio, G.; Palazzo, G.; Torsi, L., Interfacial electronic effects in functional biolayers integrated into organic field-effect transistors. *Proceedings of the National Academy of Sciences of the United States of America* **2012,** *109* (17), 6429-6434; (b) Hammock, M. L.; Knopfmacher, O.; Naab, B. D.; Tok, J. B. H.; Bao, Z., Investigation of Protein Detection Parameters Using Nanofunctionalized Organic Field-Effect Transistors. *ACS Nano* **2013,** *7* (5), 3970-3980.

7. Calhoun, M. F.; Sanchez, J.; Olaya, D.; Gershenson, M. E.; Podzorov, V., Electronic functionalization of the surface of organic semiconductors with self-assembled monolayers. *Nature Materials* **2008,** *7* (1), 84-89.

8. (a) Wei, Q.; Tajima, K.; Tong, Y.; Ye, S.; Hashimoto, K., Surface-Segregated Monolayers: A New Type of Ordered Monolayer for Surface Modification of Organic Semiconductors. *Journal of the American Chemical Society* **2009,** *131* (48), 17597-17604; (b)

Geng, Y.; Wei, Q.; Hashimoto, K.; Tajima, K., Dipole Layer Formation by Surface Segregation of Regioregular Poly(3-alkylthiophene) with Alternating Alkyl/Semifluoroalkyl Side Chains. *Chemistry of Materials* **2011,** *23* (18), 4257-4263.

9. (a) Wei, Q.; Nishizawa, T.; Tajima, K.; Hashimoto, K., Self-organized buffer layers in organic solar cells. *Advanced Materials* **2008,** *20* (11), 2211-2216; (b) Tada, A.; Geng, Y.; Wei, Q.; Hashimoto, K.; Tajima, K., Tailoring organic heterojunction interfaces in bilayer polymer photovoltaic devices. *Nature Materials* **2011,** *10* (6), 450-455; (c) Geng, Y.; Ma, J.; Wei, Q.; Hashimoto, K.; Tajima, K., Effects of a side chain sequence on surface segregation of regioregular poly(3-alkylthiophene) and interfacial modification of bilayer organic photovoltaic devices. *Journal of Materials Chemistry A* **2013,** *1* (38), 11867-11873.

10. Hummelen, J. C.; Knight, B. W.; Lepeq, F.; Wudl, F.; Yao, J.; Wilkins, C. L., PREPARATION AND CHARACTERIZATION OF FULLEROID AND METHANOFULLERENE DERIVATIVES. *Journal of Organic Chemistry* **1995,** *60* (3), 532-538.

11. Lai, Y. C.; Higashihara, T.; Hsu, J. C.; Ueda, M.; Chen, W. C., Enhancement of power conversion efficiency and long-term stability of P3HT/PCBM solar cells using C-60 derivatives with thiophene units as surfactants. *Solar Energy Materials and Solar Cells* **2012,** *97*, 164-170.

12. Ton-That, C.; Shard, A. G.; Bradley, R. H., Thickness of spin-cast polymer thin films determined by angle-resolved XPS and AFM tip-scratch methods. *Langmuir* **2000,** *16* (5), 2281-2284.

13. Yokoyama, H.; Tanaka, K.; Takahara, A.; Kajiyama, T.; Sugiyama, K.; Hirao, A., Surface structure of asymmetric fluorinated block copolymers. *Macromolecules* **2004,** *37* (3), 939-945.

14. (a) Ma, J.; Hashimoto, K.; Koganezawa, T.; Tajima, K., End-On Orientation of Semiconducting Polymers in Thin Films Induced by Surface Segregation of Fluoroalkyl Chains. *Journal of the American Chemical Society* **2013,** *135* (26), 9644-9647; (b) Cumpson, P. J., Estimation of inelastic mean free paths for polymers and other organic materials: use of quantitative structure-property relationships. *Surface and Interface Analysis* **2001,** *31* (1), 23-34.

15. Bijleveld, J. C.; Gevaerts, V. S.; Di Nuzzo, D.; Turbiez, M.; Mathijssen, S. G. J.; de Leeuw, D. M.; Wienk, M. M.; Janssen, R. A. J., Efficient Solar Cells Based on an Easily Accessible Diketopyrrolopyrrole Polymer. *Advanced Materials* **2010,** *22* (35), E242-E246.

Chapter 3.

Dominant Effects of First Monolayer Energetics at Donor/Acceptor Interfaces on Organic Photovoltaics

3.1. Introduction

After the past 20 years of research history, it still remained as a big mystery why the charges are separated and collected so efficiently in OPVs.[1] The charge separation takes place via charge transfer across the interface of donor (D) and acceptor (A) from photogenerated excitons to form the pairs of hole and electron. However, Coulomb attraction force between the charge pair is strong compared to the thermal energy and effective in long range due to the low dielectric constants of organic semiconductors, thus bound charge transfer state (CTS) is potentially formed at the D/A interface before the complete charge separation. CTS could decay to ground state with a lifetime (geminate recombination), resulting in the loss of the photocurrent. CTS is also formed when the free charge pairs encounter at the D/A interface and could decay to ground state (non-geminate (bimolecular) recombination), kinetics of these processes are strongly related to fill factor (FF) and open circuit voltage (V_{OC}).

Recently, it was proposed that hot (delocalized) CTS could be important for the efficient charge separation.[2] There are several studies on ultrafast spectroscopy showing that the excess energy assist the free charge formation.[3] In contrast, Vandeval *et al*. reported that the excitation of relaxed CTS could be efficiently separated into free charges without the need for excess energy.[4] Some groups proposed the formation of gradient in free energy landscape at the near D/A interface because of widening the energy gap due to the disorder of the materials.[5] It was speculated that these unintentional “cascade” energy landscape at the interface could push the energy of CTS close to charge separated state, resulting in the highly efficient charge separation.[6] Especially, Groves predicted by using kinetic Monte Carlo simulation that thin cascade layer (1 nm) substantially suppressed geminate recombination while those effects were limited with thicker cascade layers.[7] The mechanism for free charge formation is still ongoing debate,[8] but the structures very close to the D/A interface could be important for realizing efficient OPVs in terms of the efficient charge separation and suppressed recombinations. There have been several reports on the model systems to explore the effects of the energy cascade at the D/A interface. However, since they relied on either successive spin-coating or evaporation of the materials, interfacial

layers were rather thick and/or the structures were mixed at the molecular levels.[9] Thus the effects of the energy cascade very close to the interface (molecular monolayer) remain unclear.

In this work, the author study on the effect of the energy levels of the first monolayer at the D/A interface by using the combination of contact film transfer (CFT) method and self-organized surface segregated monolayer (SSM), both of which have been developed in our group and enable us to fabricate the bilayer OPVs with well-defined D/A interfaces. Tada et al. previously demonstrated that the insertion of molecular dipole moment into the D/A interface of bilayer OPVs change the V_{OC} of the devices.[10] However, since the dipole moments change the energetics of the whole layers (the shift of the vacuum levels at the D/A interfaces), the effect of the local energetics at the interface is still unclear. To elucidate this, a new surface modifier based on bis(1-[3-(methoxycarbonyl)propyl]-1-phenyl)-[6.6]C_{62} (bisPCBM) with fluoroalkyl (F-bisPCBM for short, Fig. 3.1a) was synthesized. It is known that fullerene bisadducts have generally lower electron acceptability (i.e. higher-lying LUMO) than monoadducts due to the breaking of π-conjugation.[11] By using two surface modifiers with different LUMO energy levels (F-PCBM and F-bisPCBM) and combined with two fullerene acceptors (PCBM and bisPCBM), four kind of energy landscapes at the D/A interface as shown in Fig. 3.1b can be constructed in bilayer devices by the CFT method. Firstly, the author show by various surface analyses that the surface modification with the SSMs can be used to precisely change the energetics at the surface. After constructing working bilayer OPVs by using CFT method, the author investigated the correlation between the energy landscape at D/A interface and photoelectric conversion process.

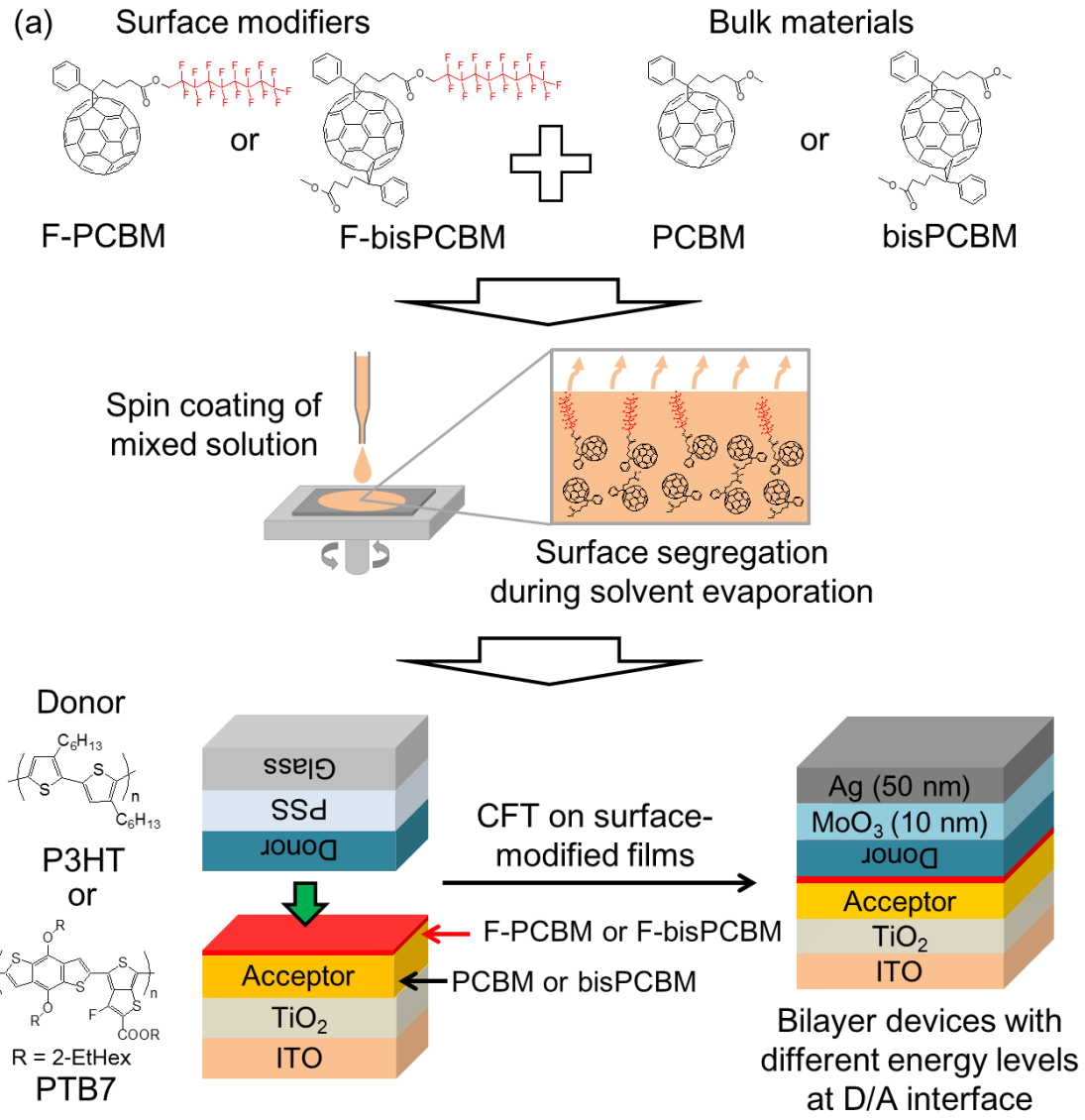
(a)
Surface modifiers
Bulk materials
or
or
F-PCBM
F-bisPCBM
PCBM
bisPCBM
Spin coating of mixed solution
Surface segregation during solvent evaporation
Donor
P3HT
or
R = 2-EtHex
PTB7
Glass
PSS
Donor
Acceptor
TiO2
ITO
CFT on surface-modified films
F-PCBM or F-bisPCBM
PCBM or bisPCBM
Ag (50 nm)
MoO3 (10 nm)
Donor
Acceptor
TiO2
ITO
Bilayer devices with different energy levels at D/A interface

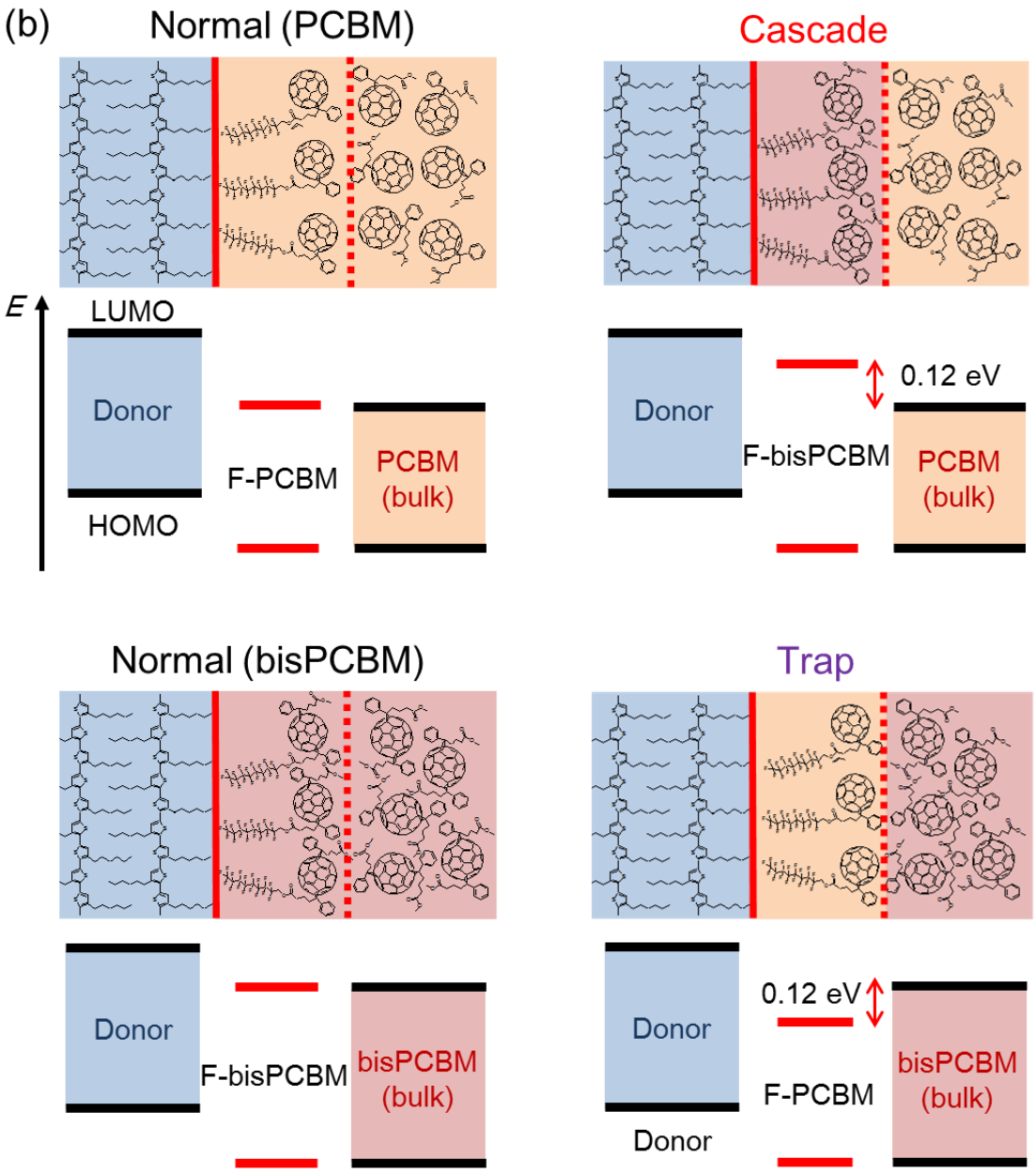

Figure 3.1. (a) Chemical structures of the surface modifiers and the bulk materials, and schematic images of surface modification by SSM and bilayer device fabrication by CFT. (b) Schematic images of different energy landscap at the D/A interface in four types of the bilayer OPVs.

3.2. Experimental

Materials and instruments

All chemicals were purchased from the chemical suppliers and used without further purification. ^{1}H NMR spectra were measured on a JNM-AL300 (JEOL). MALDI-TOF-MS were measured on an Ultraflex RO (Bruker Daltonics) in negative ion mode with dithranol as the matrix. UV-vis absorption spectra were measured on a V-670 spectrometer (JASCO). Cyclic voltammetry (CV) was performed on an HSV-100 automatic polarization system (Hokuto Denko) in N_2. 0.1 M Tetrabutylammomium hexafluorophosphate in anhydrous CH_2Cl_2 was used as the supporting electrolyte. A glassy carbon working electrode, a Pt wire counter electrode, and a Ag/AgCl reference electrode were used. X-ray photoelectron spectroscopy (XPS) and ultraviolet photoelectron spectroscopy (UPS) were performed on an AXIS-ULTRADLD spectrometer (Kratos Analytical) and a PHI 5000 Versa Probe II surface analysis instrument (ULVAC-PHI). Monochromated Al Kα radiation was used in all the XPS measurements. The carbon 1s (non-fluorinated carbon: 282 eV, fluorinated carbon: 288 eV), and fluorine 1s (687 eV) peaks were used for the characterization. To obtain the XPS depth profile, each sample was etched using an argon ion etcher at an acceleration voltage of 500 V with an etching rate of approximately 0.25 nm/s. He I radiation was used in all the UPS measurements. Atomic force microscopy (AFM) images were obtained on a 5400 Scanning Probe Microscope (Agilent Technologies) in tapping mode. Film thickness was measured by surface profilometry (Dektak 6M, ULVAC). The static water contact angle was measured on a DMe-201 (Kyowa) at room temperature.

Synthesis of F-bisPCBM

2,2,3,3,4,4,5,5,6,6,7,7,8,8,9,9,9-Heptadecafluoro-1-nonanol (409 mg, 0.909 mmol), bis(1-[3-(methoxycarbonyl)propyl]-1-phenyl)-[6.6]C_{62} (bisPCBM, mixture of isomers) (100 mg, 0.0908 mmol), *p*-toluenesulfonic acid monohydrate (18.8 mg, 0.0988 mmol), and anhydrous *o*-dichlorobenzene (10 mL) were added to a 100 mL two-neck round-bottom flask under N_2. The reaction mixture was stirred at 180 °C for 1 days and then poured into methanol (200 mL). The resulting solid was collected by vacuum filtration and the crude product was purified by column chromatography using silica gel and toluene as the eluent. The product was reprecipitated in methanol and filtered, yielding a brown solid (47 mg, 34%).

^{1}H NMR ($CDCl_3$, 300 MHz): δ (ppm): 7.26-8.14 (m, 10H), 4.53-4.60 (m, 2H), 3.57-3.75 (m, 3H), 1.95-3.20 (m, 12H). MALDI-TOF-MS calcd. 1518.9, found 1518.8.

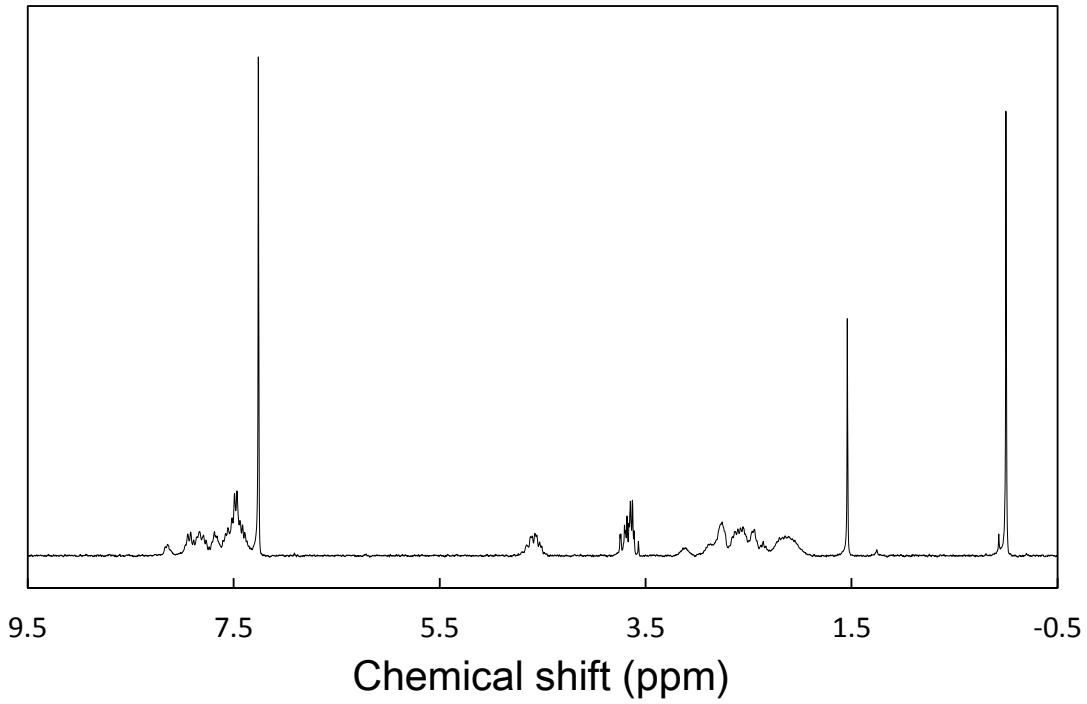

Figure 3.2. ^{1}H NMR charts of F-bisPCBM in $CDCl_3$.

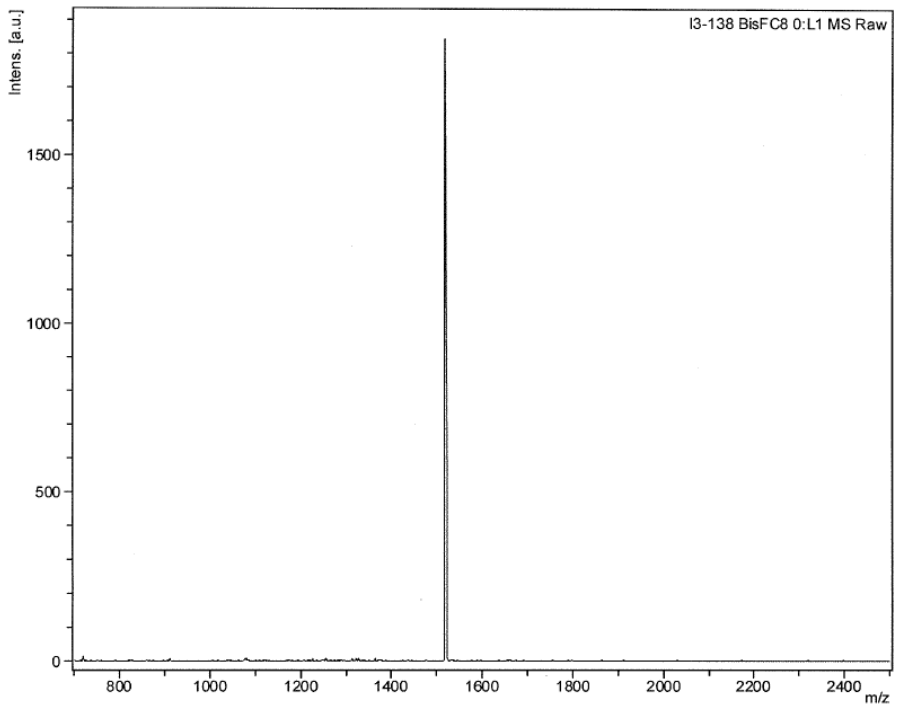

Figure 3.3. MALDI-TOF-MS chart of F-bisPCBM.

Film preparation for surface analysis

An indium tin oxide (ITO)-coated glass substrate (ITO thickness: 167 nm, sheet resistance: 8.98 Ω sq^{-1}, glass thickness: 0.7 mm, Geomatech) was cleaned by ultrasonication in detergent, water, acetone, and 2-propanol. The substrate was dried, and then exposed to UV-O_3 for 30 min. The solution was prepared by dissolving PCBM or bisPCBM (10 mg) and F-PCBM (0.75 mg) or F-bisPCBM (0.86 mg) in chlorobenzene (1 mL). The solution was spin coated at 600 rpm for 1 min. The film was annealed at 155 °C under N_2 for 10 min.

Photovoltaic device preparation and measurement

The inverted bilayer device was fabricated as follows.[10] An indium tin oxide (ITO)-coated glass substrate was cleaned by sequential ultra-sonication in detergent solution, water, acetone, 2-propanol, and water. TiO_2 precursor solution (NDH-510C, Nippon Soda) diluted by ethanol was spin-coated on the ITO substrates at a spinning rate of 3000 rpm for 30 s followed by drying at 140 ℃ for 40 min and calcination at 500 ℃ for 30 min to form an electron-transporting layer. The thickness of TiO_2 layer was 40 nm. Then, the substrates were again cleaned by ultra-sonication in acetone and 2-propanol. Chlorobenzene solution containing 10 g L^{-1} of PCBM (Solenne) or bisPCBM (Frontier carbon) and F-PCBM (0.75 mg), F-bisPCBM (0.86 mg), PCBM (0.51 mg), or bisPCBM (0.62 mg) was spin-coated onto the ITO/TiO_2 substrates at a spinning rate of 600 rpm for 60 s. The thickness of all acceptor layers was about 35 nm. The substrates were thermally annealed at 155 ℃ for 10 min inside a N_2-filled glove box. The substrates with the structure glass/poly(sodium 4-styrenesulfonate) (PSS, Mw: 4300, Aldrich)/P3HT(Merck) or PTB7 (1-Material) were prepared by successive spin-coatings. PSS was a sacrificial layer prepared by spin-coating of aqueous solution containing 30 g L^{-1} of PSS at a spinning rate of 4,000 rpm for 30 s on the glass substrates that were pre-cleaned and exposed to UV-O_3 in the same way as were the ITO substrates. Chlorobenzene solution containing 10 g L^{-1} of P3HT or PTB7 was spin-coated on the glass/PSS substrates at a spinning rate of 1,000 rpm for 60 s. The thicknesses of P3HT and PTB7 layer were 50 and 40 nm respectively. Then, the glass/PSS/P3HT or PTB7 substrate was gently placed upside down onto the ITO/TiO_2/PCBM substrate, and one drop of water was placed on the edge of the two substrates. Water selectively penetrated and dissolved the PSS layer, and as a result the P3HT layer was transferred onto the PCBM layer. A MoO_3 hole-transporting layer (10 nm) and Ag electrodes (100 nm) were deposited by thermal evaporation under high vacuum (~10^{-4} Pa) in a vacuum evaporation system (H-2807 vacuum evaporation system with E-100 load lock, ALS Technology).

The *J-V* characteristics of the devices were measured under simulated solar illumination (AM 1.5, 100 mW cm^{-2}) from a solar simulator based on 150 W Xe lamp (PEC-L11, Peccell Technologies). The light intensity was calibrated with a standard silicon solar cell (BS520,

Bunkoh-Keiki). The active area of the devices was defined by using a 0.12 cm^2 photo mask. The external quantum efficiency (EQE) of the devices was measured on a Hypermonolight SM-250F system (Bunkoh-Keiki). Electroluminescence (EL) was measured on a spectrofluorometer equipped with InGaAs detector (Nanolog, HORIBA) and constant DC voltage was applied to the devices by DC power supply (PAN 110-3A, KIKUSUI). The *J-V* characteristics of the devices under different temperature (r.t. ~ −40 °C) were measured under white light LED whose operation power was 3.4 W (10W LED XM-L, CREE) using Keithley 2400 source-meter. Transient photovoltage (TPV) and transient photocurrent measurements were carried out at room temperature. Light source of small perturbation of V_{OC} (ΔV_{OC}) was N_2-dye pulse laser (KEC-160, USHO) which excitation wave length, repetition rate, and pulse duration were ~510 nm, 2.5 Hz, and 0.4 ps, respectively. The intensity of the laser pulse was controlled by neutral density filter to keep ΔV_{OC} was less than 5 mV. Bias light source was white light LED (10W LED XM-L, CREE) with neutral density filter. Electrical signal was detected with a digital oscilloscope (DS-5632, IWATSU). For TPV measurement, 1 MΩ resistance was used for input impedance of the oscilloscope, which could hold the measured sample under open circuit condition. the author used two channels of oscilloscope to detect the signals of both side of the sample, and ΔV_{OC} was calculated from difference of these channels. For TPC measurement, 50 Ω resistance was put as parallel to the input impedance of the oscilloscope, and transient photocurrent was calculated using Ohm's low. Carrier density and lifetime were calculated following the report by Durrant's group.[12] To calculate the carrier density, the differential capacitance method was used: differential capacitance $C_{diff} = \Delta Q_{SC}/\Delta V_{OC}$ was calculated, and plotted as a function of V_{OC}. ΔQ_{SC} is perturbation of carrier density calculated by time-integrating of photocurrent in TPC measurement. Total carrier density $n(V)$ is determined by integrating the C_{diff} with V_{OC}. Small perturbation lifetime ($\tau_{\Delta n}$) is determined by fitting of TPV signal with single-exponential decays. All the TPV signals can be well fitted, except for the devices with cascade devices where two exponential components with different lifetimes are necessary to fit the data (see Fig. 3.24). The slope of n - $\tau_{\Delta n}$ gives the order of recombination λ ($dn/dt = -k_0 n^{\lambda+1}$). λ is taken into account for calculating carrier lifetime (not perturbation) τ, which is determined as $\tau = (\lambda+1)\times\tau_{\Delta n}$.

Numerical simulations of the bilayer devices

Optical simulations of the bilayer devices have been performed based on the transfer matrix model previously reported.[13] Optical constants of the materials are determined by fitting spectral ellipsometric data of the following samples: PTB7, PCBM, bisPCBM films spin-coated on SiO_2/Si wafers, glass and TiO_2 prepared for the device fabrication, MoO_3 films evaporated on SiO_2/Si wafers. The optical constants of Ag and ITO were taken from the datasheets provide from the ellipsometry company (Otsuka Electronics). No optical anisotropy was assumed for the

analysis. The electric field distributions and energy dissipations were calculated at each layers for monochromatic light. The device structure is glass (a substrate with non-coherent multiple reflection)/ITO (167 nm)/TiO_2 (40 nm)/PCBM or bisPCBM (35 nm)/PTB7 (40 nm)/MoO_3 (10 nm)/Ag (100 nm). The unit of the layer thickness and the wavelength was set to 1 nm. The simulations were performed by using a home-made code run on MATLAB.

By using the energy dissipation distributions, the exciton density at the steady state under the monochromatic irradiation was calculated by analytically solving the diffusion equation with exciton generation based on the energy dissipations, the natural decay by the lifetime, and the quenching at the interfaces. Assuming that the charge generation probability from the exciton reached to the D/A interfaces is 100%, EQE spectra could be simulated as the highest estimation. Exciton diffusion coefficients (D) and lifetimes (τ)in the pristine films of PTB7, PCBM and bisPCBM were not reported, so typical values deduced from the reports on the similar materials were used here (PTB7: τ = 1 ns, $D = 5 \times 10^{-4}$ cm^2 s^{-1}, PCBM, bisPCBM: τ = 600 ps, $D = 2.0 \times 10^{-4}$ cm^2 s^{-1}).

3.3. Results and discussion

F-PCBM and F-bisPCBM were synthesized via the acid-catalysed ester exchange reaction[14] as described in the experimental section. Firstly, the author compared the molecular electronic properties of PCBM, bisPCBM, F-PCBM and F-bisPCBM by cyclic voltammetry (CV) in solutions. The reduction potentials of the fullerene bisadducts (bisPCBM and F-bisPCBM, −1.20 V vs. Fc/Fc^+) have a lower reduction potential by 0.12 V than those of the monoadducts (PCBM and F-PCBM, −1.08 V vs. Fc/Fc^+) (Fig. 3.4). Therefore, the fullerene bisadducts have higher-lying LUMO energy levels compared to the monoadduct as previously reported.[11] There is no difference between the fluoroalkyl and methyl ester derivatives, indicating that fluoroallkyl chain attached to ester group did not affect energy level of the fullerene.[15] The identical absorption spectra of the fluoroalkyl and methyl ester derivatives in solution also support the little effect of the fluoroalkyl chains on the molecular orbitals of the fullerene group (Fig. 3.5).

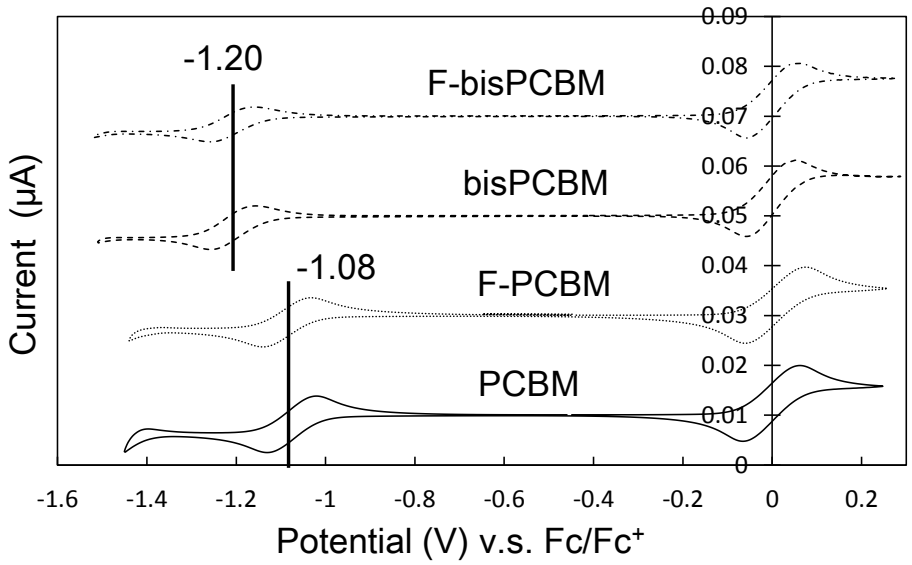

Figure 3.4. Cyclic voltammogram of PCBM (solid line), F-PCBM (dotted line), bisPCBM (dashed line), and F-bisPCBM (dash-dotted line) in CH_2Cl_2 (concentration of fullerene derivatives: 1 mM).

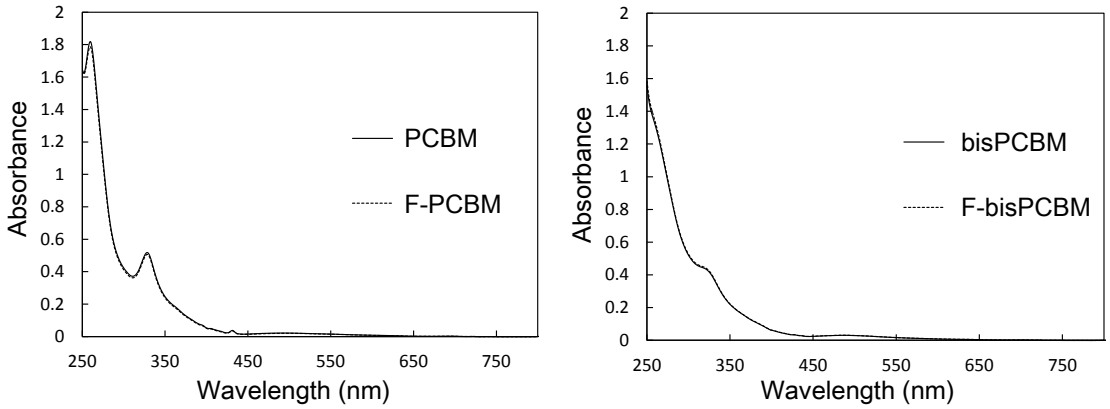

Figure 3.5. Absorption spectra of (a) PCBM (solid line), F-PCBM (dotted line), (b) bisPCBM (solid line), and F-bisPCBM (dotted line) in $CHCl_3$ (concentration: 1.10 M).

The surface segregation behaviours of F-PCBM and F-bisPCBM in the blended films was investigated by X-ray photoelectronspectroscopy (XPS). Films offer different combinations (F-PCBM/PCBM, F-bisPCBM/PCBM, F-PCBM/bisPCBM and F-bisPCBM/bisPCBM) were prepared by spin coating the solutions containing different concentration of F-PCBM and F-bisPCBM(0.2-1.2 g L^{-1}) with a fixed concentration of PCBM and bisPCBM (10 g L^{-1}). The surface F/C atomic ratio was calculated from the peak intensity of F1s and non-fluorinated C1s in XPS, and they are plotted in Fig. 3.6 as a function of the concentration of F-PCBM and F-

bisPCBM in the solutions. The results are quite similar to our previous reports on the SSM formation in F-PCBM/PCBM; the F/C ratios measured by XPS were always higher than those calculated for homogeneously mixed films for all the films, indicating the surface segregation of F-PCBM and F-bisPCBM.[14b] The clear saturation of F/C ratios was observed at the high concentrations in all the combinations, suggesting that surface of the films was fully covered by F-PCBM or F-bisPCBM. The F/C atomic ratios at the saturated conditions are 0.128, 0.111, 0.111 and 0.102 in F-PCBM/PCBM, F-bisPCBM/PCBM, F-PCBM/bisPCBMand F-bisPCBM/bisPCBM, respectively. The F/C atomic ratios reflect the density of the segregated fluoroalkyl chains at the surface. The little lower densities in the films of the bisadduct fullerene derivatives compared to that of F-PCBM/PCBM could be attributed to larger steric hindrance thus lower packing density of the fullerene bisadducts. The concentration of the surface modifiers close to the saturation point (0.56 mM (0.75 gL^{-1}) for F-PCBM and 0.56 mM (0.86 gL^{-1}) for F-bisPCBM were used for further investigation of the film properties and for the device fabrication.

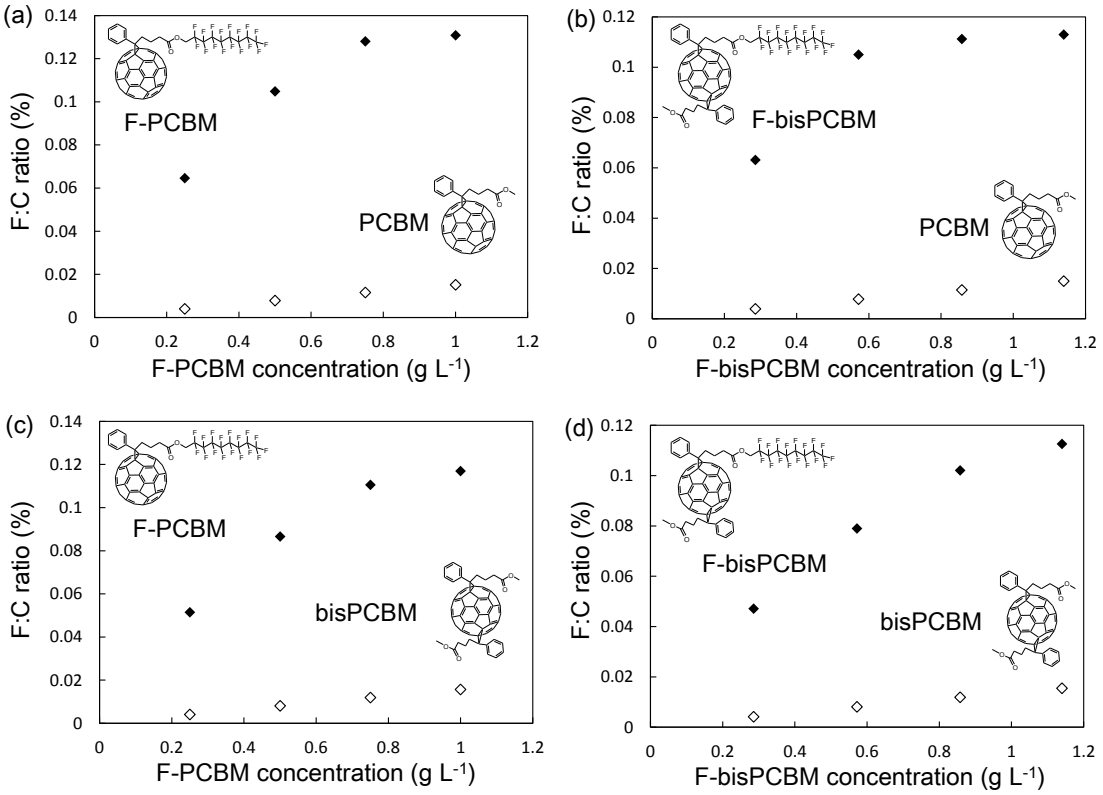

Figure 3.6. F/C atomic ratio on the surfaces of the films measured by XPS (black squares) and calculated from the composition of the solution (white squares) plotted as a function of the modifier concentrations in the solution. The solution contains a fixed concentration of PCBM and bisPCBM (10 g L^{-1}). The combinations of modifier/acceptor are (a) F-PCBM/PCBM, (b) F-bisPCBM/PCBM, (c) F-PCBM/bisPCBM, and (d) F-bisPCBM/bisPCBM.

XPS depth profiles of the films showed that the F1s peak of all the films disappeared after the surface etching of ca. 1.5 nm with Ar^+ ion beam (Fig. 3.7). This result suggests that the fluoroalkyl chains of F-PCBM and F-bisPCBM segregated to the surface and little remained in the bulk of the films.

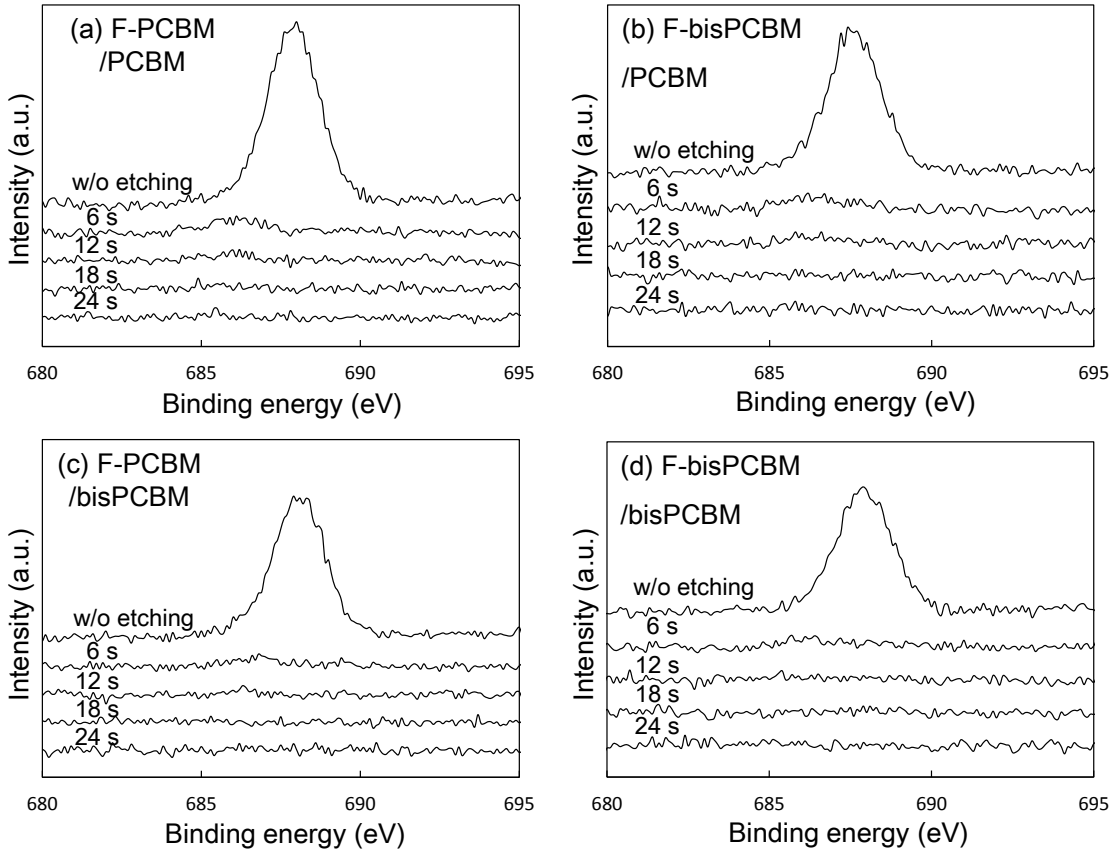

Figure 3.7. XPS depth profile of (a) F-PCBM/PCBM, (b) F-bisPCBM/PCBM, (c) F-PCBM/bisPCBM, and (d) F-bisPCBM/bisPCBM film.

To further elucidate the surface structure, the author also performed angle resolved XPS (ARXPS) analysis. The peak ratios of fluorinated and non-fluorinated carbon were used for measurements. Quantitative thickness of the fluorocarbon layer on the surface of the films were determined by angle resolved XPD (ARXPS) by using a uniform bilayer model. According to previous reports,[16]

$$\ln\left(\frac{I_F X_C}{I_C X_F \alpha} + 1\right) = \frac{d}{\lambda_C \cos\theta} \quad \text{eq. 1}$$

where I_F and I_C are the intensities of fluorinated and non-fluorinated C 1s peaks, α is the coverage of fluoroalkyl chains on the surface of films, λ_C is the attenuation length of photoelectrons (C 1s: 3.8 nm for Al K_α radiation), θ is take off angle of the measurements, and X_F and X_C are local

concentrations of the fluorinated and non-fluorinated carbons, respectively. According to previous report, X_F and X_C were calculated as 8/1.02 and 72/1.26 in F-PCBM/PCBM film.[14b] By assuming the molecular density of PCBM and bisPCBM was the same, same X_F and X_C values were also used for F-bisPCBM/PCBM, F-PCBM/bisPCBM, and F-bisPCBM/bisPCBM film. Setting the coverage α of fluoroalkyl chains in F-PCBM/PCBM film to 1 (i.e. full coverage) according to the previous report,[15] α in the other films could be calculated from F/C atomic ratio on the surfaces in Fig. 3.6 relative to F-PCBM/PCBM film as 0.87 for F-bisPCBM/PCBM, 0.87 for F-PCBM/bisPCBM, and 0.80 for F-bisPCBM/bisPCBM. Using eq. 1, a plot of $\ln(I_F X_C / I_C X_F \alpha + 1)$ as a function of $1/\cos\theta$ fitted by a straight line through the origin (Fig. 3.8). The thickness of fluoroalkyl chain layer can be calculated from the slope of these lines. The results were 0.84 nm in F-PCBM/PCBM film, 0.95 nm in F-bisPCBM/PCBM film, 0.92 nm in F-PCBM/bisPCBM film, and 0.86 nm in F-bisPCBM/bisPCBM film. The bilayer model in which the surface layers consist of fluoroalkyl chains fitted the experimental data well. This indicated that F-PCBM or F-bisPCBM formed monolayer at the surface of films with fluoroalkyl chains exposed to the surface. The thickness of fluoroalkyl chain layer (d) were in the range of 0.84-0.95 nm, whereas calculated length of the semifluoroalkyl chains is 1.02 nm.[14b] This difference might be attributed to tilting of fluoroalkyl chain. These results indicate that the formation of SSM with F-PCBM and F-bisPCBM on the surface of both PCBM and bisPCBM films.

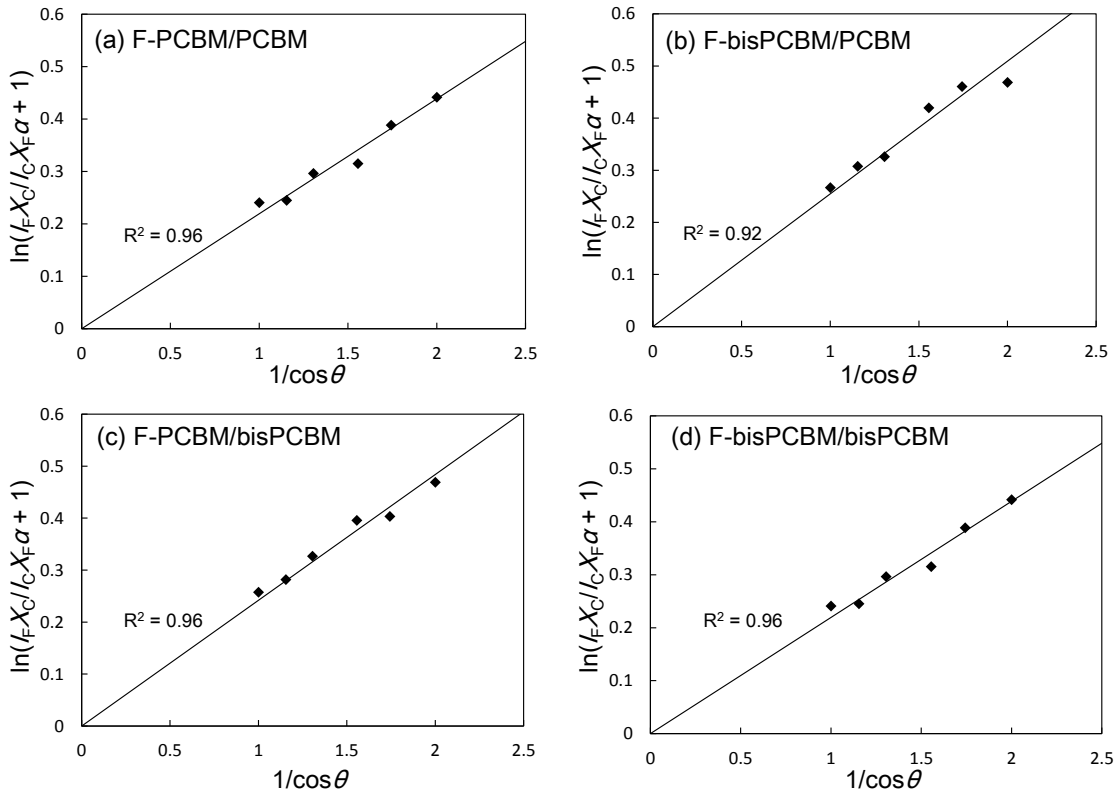

Figure 3.8. Plot of 1/cosθ *vs.* ln($I_F X_C / I_C X_F \alpha$+1) by using fluorinated carbon and non-fluorinated carbon peaks from the ARXPS spectra in (a) F-PCBM/PCBM film, (b) F-bisPCBM/PCBM, (c) F-PCBM/bisPCBM, and (d) F-bisPCBM/bisPCBM film. The lines indicate the best fitting with eq. 1.

As previously reported, the oriented fluoroalkyl chain at the surface should form surface dipole moment and therefore the ionization potentials (IPs) of the films should be shifted. The results of UPS measurement on the films are shown in Fig. 3.9 and summarized in Table 3.1. Compared to the pristine films of PCBM and bis-PCBM, the values of IP shifts were −0.40 and −0.44 eV for F-PCBM/PCBM and F-bisPCBM/PCBM, respectively, and −0.25 and −0.28 eV for F-PCBM/bisPCBM and F-bisPCBM/bisPCBM, respectively. The difference of the shift between the bulk materials (PCBM and bisPCBM) could be due to the surface density difference as suggested by XPS results.

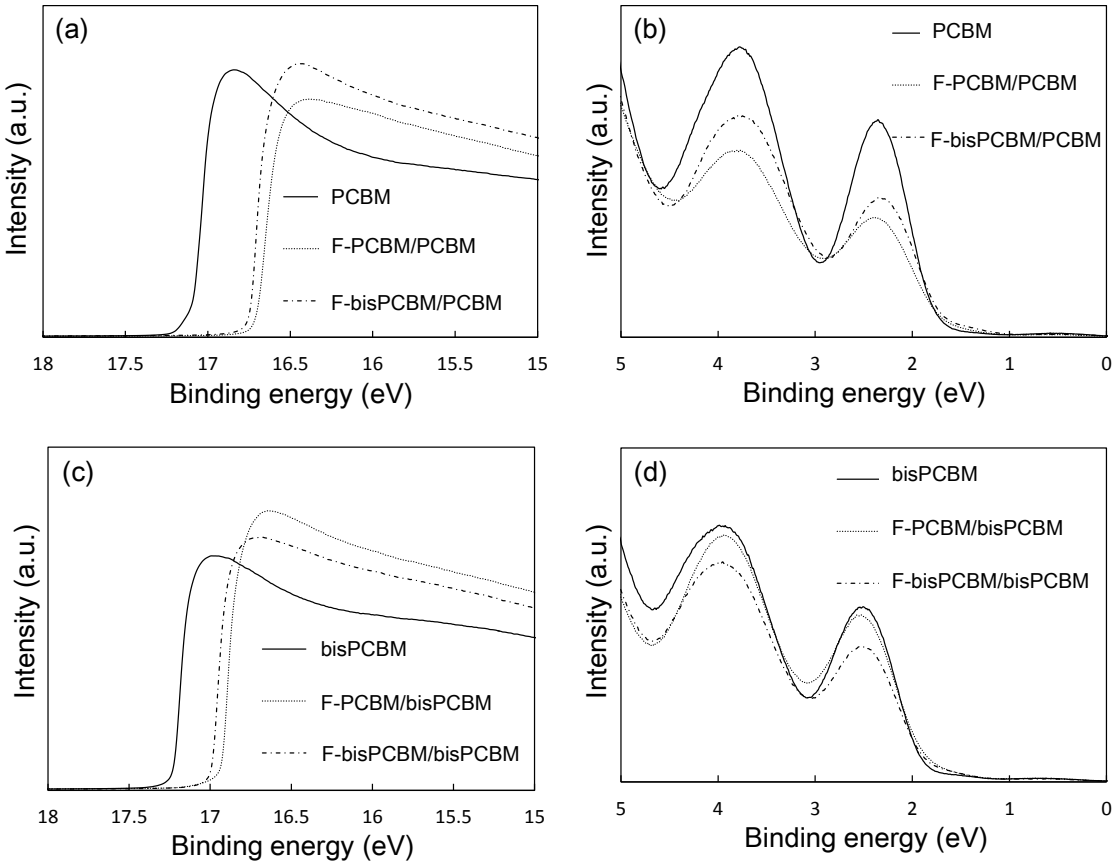

Figure 3.9. UPS spectra: (a) cut off regions of PCBM (solid line), F-PCBM/PCBM (dotted line), F-bisPCBM/PCBM (dash-dotted line), (b) HOMO regions of PCBM (solid line), F-PCBM/PCBM (dotted line), F-bisPCBM/PCBM (dash-dotted line), (c) cut off regions of bisPCBM (solid line), F-PCBM/bisPCBM (dotted line), F-bisPCBM/bisPCBM (dash-dotted line), (d) HOMO regions of bisPCBM (solid line), F-PCBM/bisPCBM (dotted line), F-bisPCBM/bisPCBM (dash-dotted line).

Table 3.1. Ionization potentials (IPs) of the films measured by UPS and reduction potentials (half potentials) *vs.* Fc/Fc^+ of PCBM and bisPCBM determined by CV in CH_2Cl_2.

	IP (eV)	E_{red} (V)
PCBM	5.81	-1.08
F-PCBM/PCBM	5.41	
F-bisPCBM/PCBM	5.45	
bisPCBM	5.79	-1.20
F-PCBM/bisPCBM	5.51	
F-bisPCBM/bisPCBM	5.54	

Combining the CV and UPS results, energy levels of the four kinds of acceptor films were deduced as schematically shown in Figure 3.1c. Energy levels between the surface monolayer and the bulk are the same in F-PCBM/PCBM and F-bisPCBM/bisPCBM films. Energy trap of LUMO with the depth of 0.12 eV formed at the surface of monolayer in F-PCBM/bisPCBM film, while energy cascade of LUMO with 0.12 eV formed at the surface of monolayer in F-bisPCBM/PCBM film. The large advantages of this model system is that besides energy levels at the surface, other properties can be set to the same conditions; the optical absorption of the films are identical (Fig. 3.10), the film thicknesses are the almost same (about 35 nm), and the surface of the films showed quite similar good planarity with R_a of 0.2-0.3 nm (Fig. 3.11). Note that the surface dipole moments always exist, but the degree of the vacuum level shift is similar to each other (the difference is 0.03-0.04 eV) with the different surface modifiers as shown by UPS. This enables us to directly compare the device performance of the bilayer OPVs.

Four bilayer devices with different energy levels at D/A interface were fabricated via CFT of the same donor polymer layer onto the four fullerene layers as illustrated in Fig. 3.1b. The structures of the devices were ITO/TiO_2/acceptor/(SSM)//donor/MoO_3/Ag. It has been shown that the D/A interfaces of the bilayer devices by CFT method are flat and sharp, thus retained the surface structure of films before the transfer.[10] As the result, the surface energy level differences of the fullerene films are preserved and the four bilayer devices with different energy landscape at D/A interface (donor/F-PCBM/PCBM: normal (PCBM), donor/F-bisPCBM/PCBM: cascade, donor/F-bisPCBM/bisPCBM: normal (bisPCBM), donor/F-PCBM/bisPCBM: trap) are fabricated as illustrated in Fig. 3.1c.

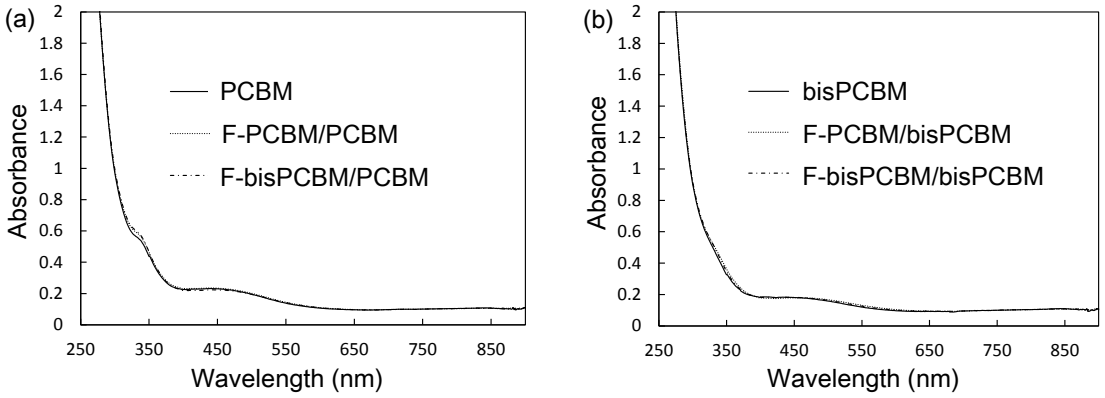

Figure 3.10. Absorption spectra of (a) PCBM (solid line), F-PCBM/PCBM (dotted line), F-bisPCBM/PCBM (dash-dotted line), and (b) bisPCBM (solid line), F-PCBM/bisPCBM (dotted line), F-bisPCBM/bisPCBM (dash-dotted line) in thin films.

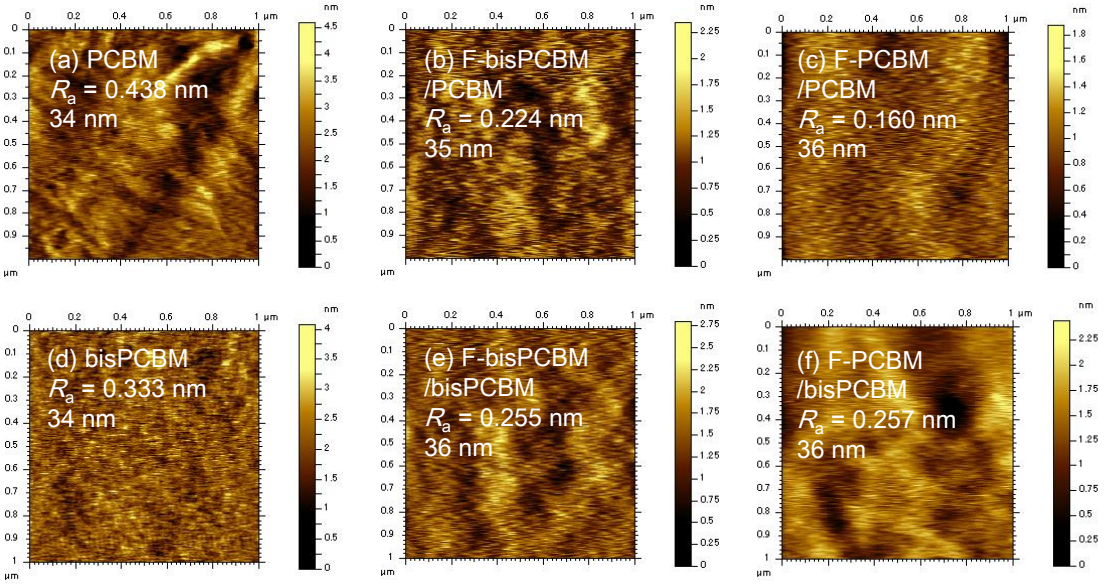

Figure 3.11. AFM height images of (a) PCBM, (b) F-PCBM/PCBM, (c) F-bisPCBM/PCBM, (d) bisPCBM, (e) F-PCBM/bisPCBM, and (f) F-bisPCBM/bisPCBM films. The arithmetic mean roughness (R_a) and film thickness are also shown.

The *J-V* characteristics of the four devices with PTB7 as the donor layer under the irradiation of simulated solar light are shown in Fig. 3.12. The cascade device exhibited significantly larger V_{OC} of 0.78 and FF of 0.67 than the normal (PCBM) device (V_{OC} of 0.66 and FF of 0.44). On the other hand, the cascade showed smaller J_{SC} compared to the normal device. In the reversed bias condition, the cascade showed less voltage dependence compared to the normal device. In contrast, the trap device exhibited much lower V_{OC} of 0.72 and FF of 0.22 than the normal (bisPCBM) device (V_{OC} of 0.88, FF of 0.49). The devices with P3HT as donor layer exhibited quite the similar behaviours as shown in Fig. 3.13; higher (lower) V_{OC} of the cascade (trap) by 0.09 V (0.12V), higher (lower) FF of the cascade (trap), except that J_{SC} of the cascade was comparable to that of the normal. These differences in device performances were attributed to the difference of the energy landscape at the D/A interface because bulk properties such as absorption or charge mobility were the same between them. Especially, the large difference in FF suggested that the charge recombination was supressed in the cascade configuration, while it is promoted in the trap configuration.

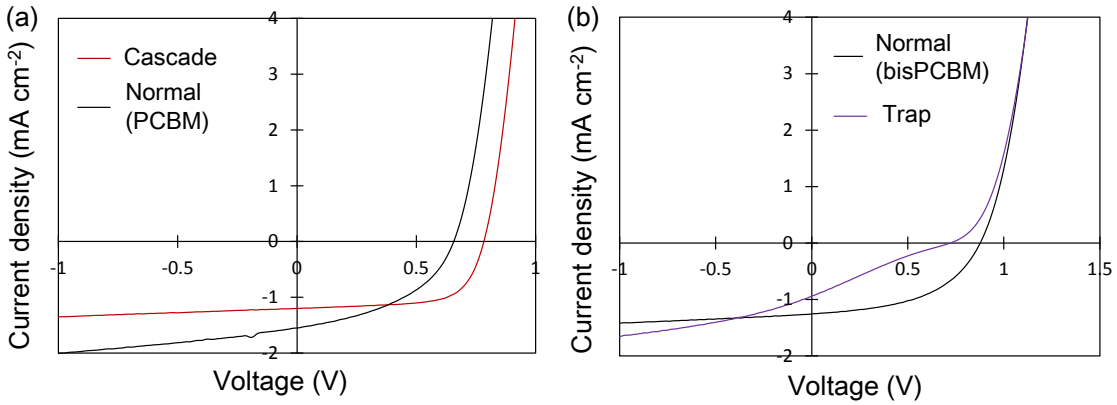

Figure 3.12. *J-V* curves under 100 mW cm^{-2}, AM 1.5 irradiation of four types of bilayer OPVs with PTB7 as the donor layer.

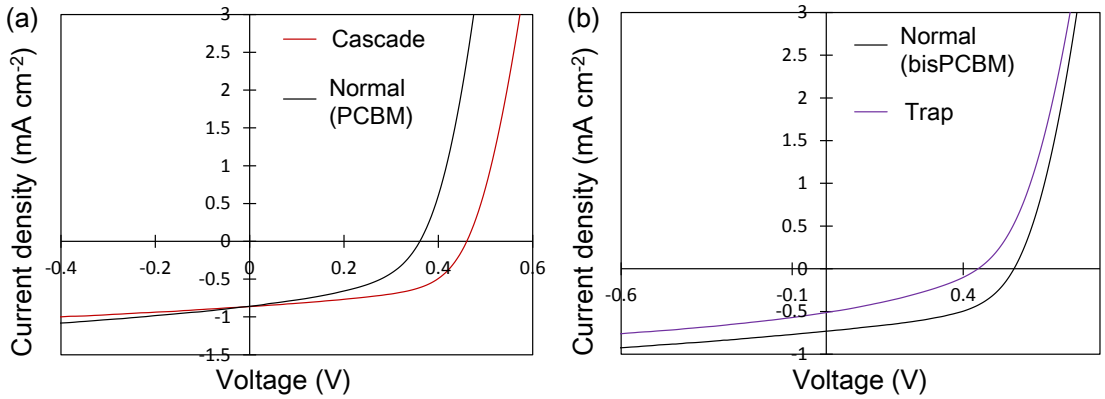

Figure 3.13. *J-V* curves under 100 mW cm^{-2}, AM 1.5 irradiation of four types of bilayer OPVs with P3HT as the donor layer.

It might be argued that small amount of the surface modifiers might exist in bulk, which could not be detected by XPS, and change the device properties. To eliminate this possibility, control bilayer devices were fabricated with PTB7 and PCBM (or bisPCBM) intentionally contaminated with bisPCBM (or PCBM). 0.62 g L^{-1} of bisPCBM and 0.51 g L^{-1} of PCBM were added to PCBM and bisPCBM solution (10 g L^{-1}), respectively, which are the concentrations of the corresponding modifiers. Since surface energy of PCBM and bisPCBM were similar (static water contact angle of PCBM: 77.5 ± 0.9 °, bisPCBM: 77.3 ± 0.9 °), they should homogeneously mix in the films. The device performances are shown in Fig. 3.14 and summarized Table 3.2. The addition of bisPCBM into PCBM layer cause increase of V_{OC} by 0.03 V compared to pure PCBM devices, and addition of PCBM into bisPCBM layer cause decrease of V_{OC} by 0.03 V compared to pure bisPCBM devices. This difference is much smaller than the observed V_{OC} change induced by the modification at the D/A interface (> 0.1 V). Note that the addition of small amount of PCBM or bisPCBM into bulk layer did not cause large FF change. These results followed the trend in

previous report, where ternary blend bulk heterojunction photovoltaics of P3HT, PCBM, and indene-C_{60} bisadduct (ICBA) showed tunable V_{OC} by the ratio of PCBM and ICBA but small change in FF.[17] From this result, the author concluded that the contamination of the surface modifiers in the bulk of the films (even if it exists) does not cause the observed changes in the device performance. This result indicated that energy level difference at the D/A interface, not in the bulk, has critical effects.

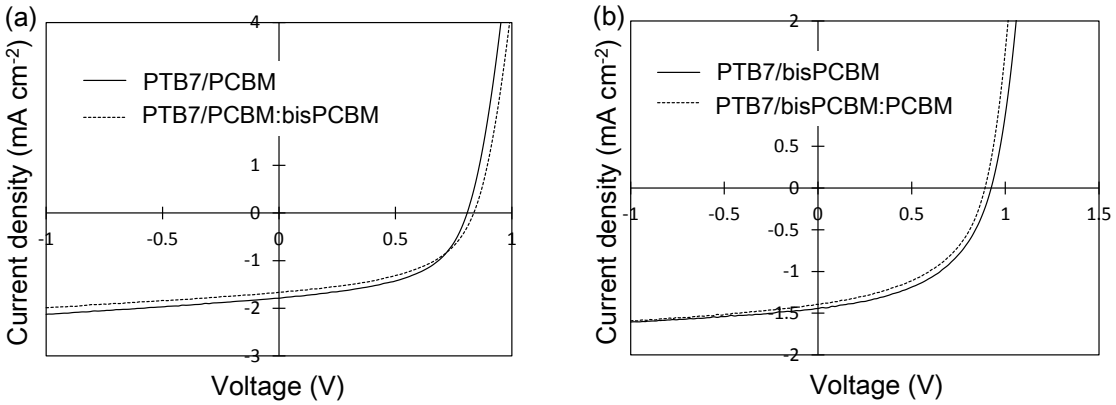

Figure 3.14. *J-V* curves of the bilayer devices (donor layer: PTB7) with different acceptor layers, (a) PCBM only (solid line), PCBM with bisPCBM (0.62 g L^{-1}) (dotted line), (b) bisPCBM (solid line), bisPCBM with PCBM (0.51 g L^{-1})

Table 3.2. Summary of the device performances. Values inside parentheses are standard deviations.

P3HT	V_{OC} (V)	J_{SC} (mA cm^{-2})	FF	PCE (%)
Cascade	0.46 (0.01)	0.76 (0.09)	0.58 (0.02)	0.20 (0.02)
Normal (PCBM)	0.37 (0.01)	0.75 (0.10)	0.45 (0.01)	0.13 (0.02)
Trap	0.42 (0.04)	0.44 (0.15)	0.32 (0.04)	0.06 (0.03)
Normal (bisPCBM)	0.54 (0.03)	0.70 (0.07)	0.50 (0.03)	0.19 (0.02)

PTB7	V_{OC} (V)	J_{SC} (mA cm^{-2})	FF	PCE (%)
Cascade	0.74 (0.04)	1.20 (0.02)	0.65 (0.02)	0.58 (0.06)
Normal (PCBM)	0.63 (0.03)	1.57 (0.06)	0.45 (0.02)	0.45 (0.02)
Trap	0.71 (0.02)	0.88 (0.05)	0.26 (0.06)	0.16 (0.03)
Normal (bisPCBM)	0.86 (0.03)	1.13 (0.17)	0.47 (0.03)	0.46 (0.11)

Mix in bulk (PTB7)	V_{OC} (V)	J_{SC} (mA cm^{-2})	FF	PCE (%)
PCBM	0.81	1.79	0.52	0.75
PCBM with bisPCBM (0.62 g L^{-1})	0.84	1.67	0.50	0.69
bisPCBM	0.92	1.44	0.49	0.65
bisPCBM with PCBM (0.51 g L^{-1})	0.89	1.39	0.48	0.60

To clarify the reason for the change in J_{SC}, external quantum efficiency (EQE) spectra of four types of devices with PTB7 as donor layer are shown in Fig. 3.15. The EQE peak at 650 nm was from the absorption of PTB7, and the peaks at 350 nm and 450 nm have large contribution from PCBM absorption. This was confirmed by optical simulation and EQE calculation of the devices based on the transfer matrix model and an exciton diffusion model (Fig. 3.17 and 3.18). As shown in Fig. 3.15a, the cascade device showed similar EQE in the donor absorption region while smaller EQE in the acceptor absorption region compared to the normal (PCBM) device. So the smaller J_{SC} in the cascade device can be attributed to the smaller contribution from the charge generation by PCBM absorption. But the photocurrent generation yield from PTB7 absorption is unchanged. In P3HT devices, EQE in the donor absorption region actually increased in the cascade device, while smaller EQE in the acceptor absorption, resulting in the similar J_{SC} under the solar light. The decrease of EQE in the fullerene absorption region can be explained by the fact that the bandgap of F-bisPCBM at the D/A interface is larger than that of PCBM in the bulk (Fig. 3.1b), so the exciton in the bulk PCBM could not reach the F-bisPCBM layer at D/A interface in the cascade devices. This might be avoided by creating the cascade situation for the HOMO levels as

well and match the optical bandgap between the interface and the bulk. In contrast, the trap device exhibited smaller EQE value in the donor absorption region compared to the normal (bisPCBM) device as shown in the Fig. 3.15b. This result indicates that the electron transferred from exciton at donor layer could be trapped in F-PCBM at D/A interface, thus photocurrent from donor absorption decreased. The photocurrent from the bisPCBM absorption could be less affected because the exciton migration from the bulk bisPCBM to F-PCBM at the interface is energetically possible (Fig. 3.1b).

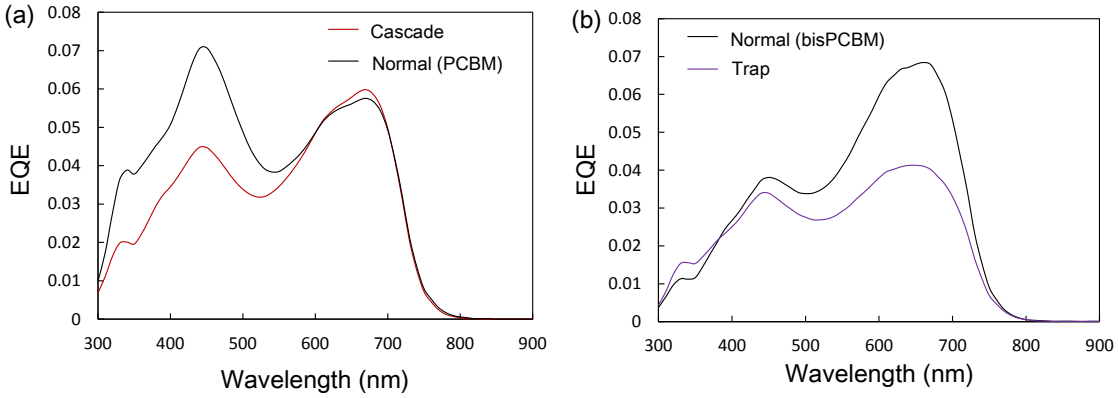

Figure 3.15. EQE plot of four types of bilayer device with P3HT as the donor layer.

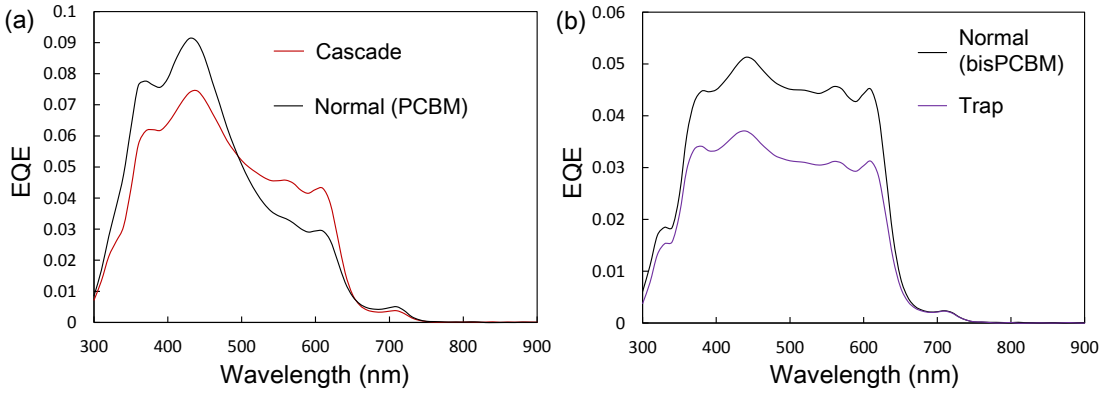

Figure 3.16. EQE plots of bilayer devices with P3HT as the donor layers.

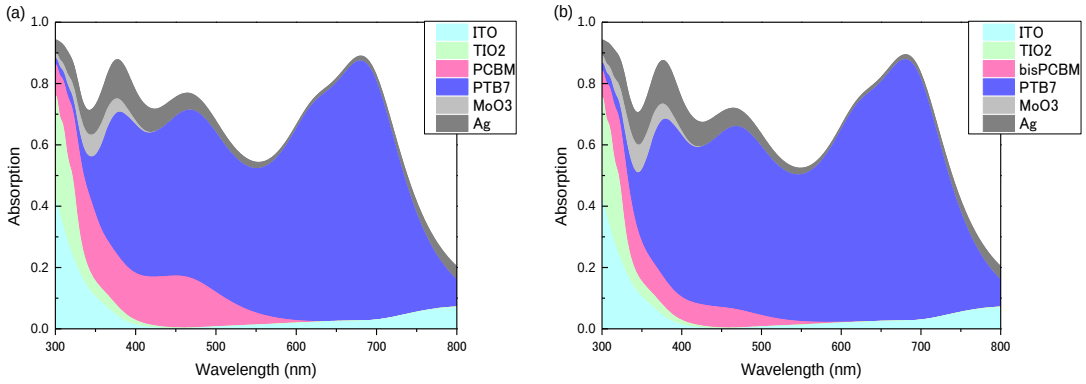

Figure 3.17. Optical absorption spectra simulated by using the transfer matrix model for (a) PTB7//PCBM and (b) PTB7//bisPCBM devices.

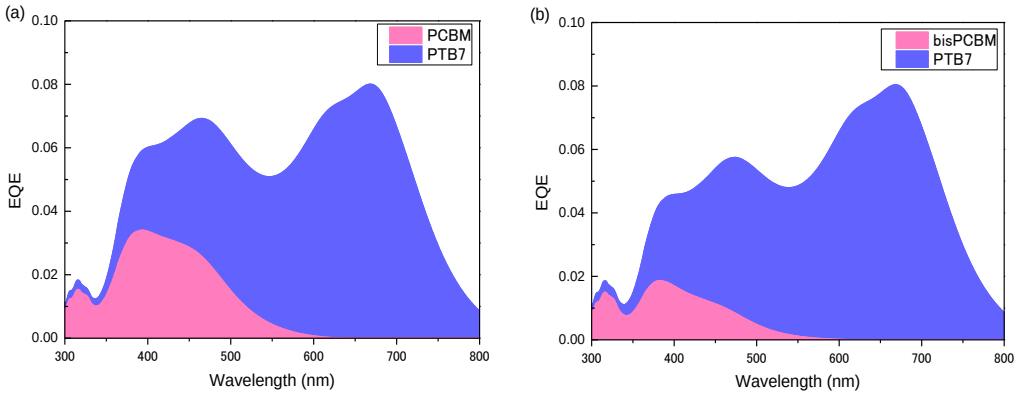

Figure 3.18. EQE spectra simulated by using the transfer matrix model and the exciton diffusion model for (a) PTB7//PCBM and (b) PTB7//bisPCBM devices.

Now we turn to the origin of the change of FF and the change of current density in the reversed bias. These changes could be related to both the geminate recombination from the initial CTS and non-geminate recombination from the once-free charges. J_{SC} under white light LED of four types of devices with P3HT as donor layer was measured at the different temperature (from 20 to −40 °C). The temperature dependence of J_{SC} was expressed by following Arrhenius equation,

$$J_{SC} = J_0(P_{light})\exp(-\frac{\Delta}{kT}) \quad \text{eq. 2}$$

Where $J_0(P_{light})$ is the pre-exponential factor, and Δ is the activation energy.[18] The results were shown in Fig. 3.19 and activation energies obtained from fitting were summarized in Table 3.3. J_{SC} decreased largely with temperature lowering in the trap device compared to that of normal (bisPCBM) device. Interestingly J_{SC} in the cascade device showed almost independence on the

temperature. Nearly linear increase of with light intensity even at low temperature (see Fig. 3.20) indicates that non-geminate recombination was a negligible loss mechanism in this temperature range. Temperature dependence of the charge mobility can be eliminated for this difference, since the bulk materials in both the donor and acceptor layers are the same.

Changes of mean drift length at lower temperature were calculated to see the effect of mobility decrease. Mean drift length is expressed by following equation,[18]

$$d_{\mathrm{m}} = \mu \cdot t \cdot E \quad \text{eq. 3}$$

where d_{m} is the mean drift length, μ is the mobility, t is the charge lifetime and E is the electric field. E is expressed by following equation,[18]

$$E = \frac{V_{\mathrm{bi}}}{L} \approx \frac{V_{\mathrm{OC}}}{L} \quad \text{eq. 4}$$

where L is the film thickness, V_{bi} is built in potential. Each parameter was substituted by following values (μ= 3×10^{-4} cm^2 V^{-1} s^{-1} (20 °C), and $9\times10^{-5}$$cm^2$ V^{-1} s^{-1} (-40°C),[19] t= 2×10^{-5} s measured by TPV in the P3HT/PCBM bilayer device, V_{OC} = 0.5 V, L = 135 nm). The results of d_{m} were 2×10^{-6} m (20 °C) and 7×10^{-7} m (-40 °C), which were much longer than the film thickness. Therefore, in this situation close to the short circuit condition, the mean drift lengths of the charges are calculated to be much larger than the film thickness.

Thus, J_{SC} was determined by generation rate of the charges with geminate recombination as the only loss mechanism. The origin of activation energy can be attributed to trapping of Coulomb attraction at D/A interface. Charge pairs were deeply trapped at D/A interface in the trap devices, thus geminate recombination was promoted. In contrast, J_{SC} showed temperature independent behaviour and free charge generation at the D/A interface without the thermal activation was achieved in the cascade devices. This result suggested CTS was destabilized enough to form free charges in the cascade device, thus geminate recombination was suppressed. These promotion and suppression of recombination were the origin of FF change.

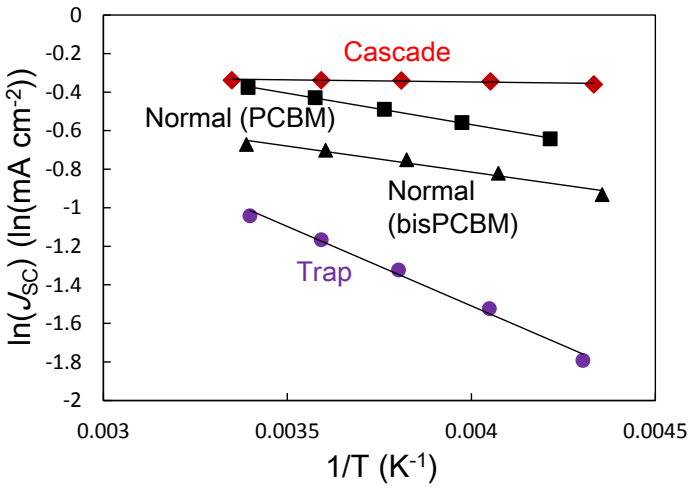

Figure 3.19. Temperature dependence of J_{SC} in the four types of the bilayer OPVs with P3HT as the donor under white light LED irradiation.

Table 3.3. Summary of the activation energies obtained from measurement for temperature dependence of J_{SC} in the bilayer OPVs with P3HT shown in Figure 3.19.

	Δ (meV)
Cascade	2
Normal (PCBM)	28
Normal (bisPCBM)	23
Trap	71

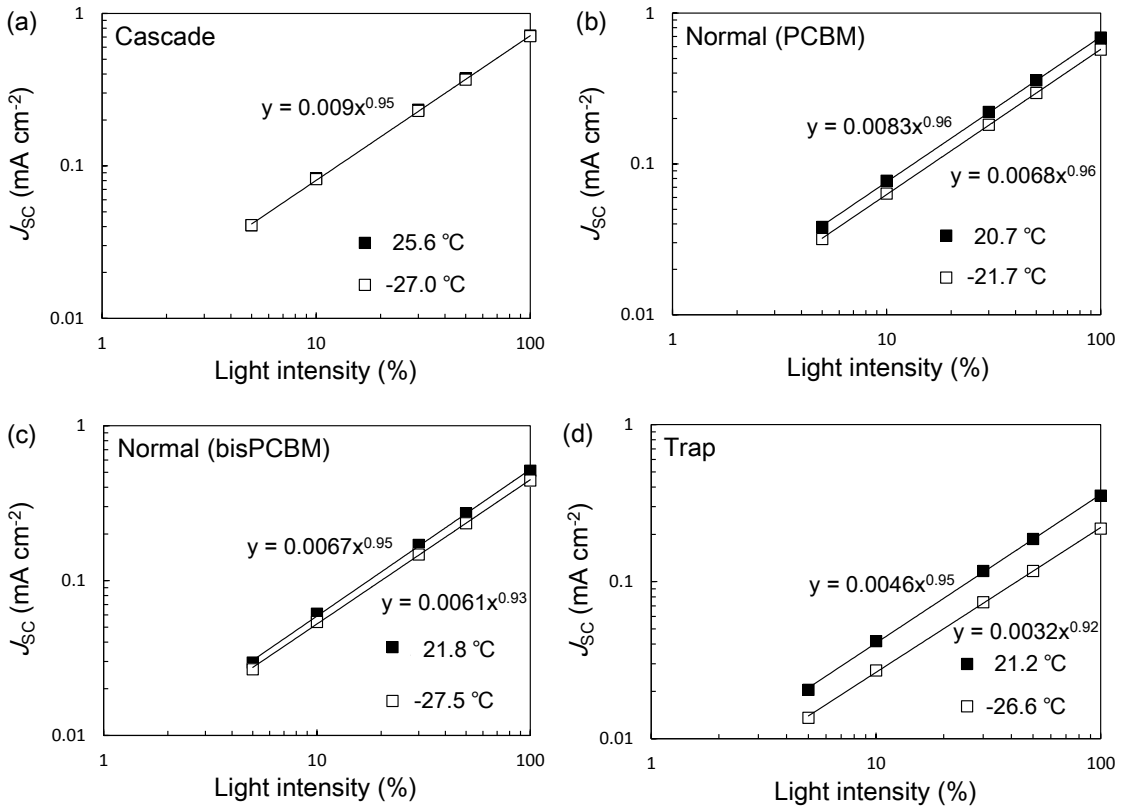

Figure 3.20. J_{SC} of the bilayer OPVs with P3HT under white light LED whose operation power was 3.4 W plotted as a function of light intensity at r.t. and low temperatures.

To clarify the reason for large V_{OC} change by different energy landscape at the D/A interface, the energy of CTS of four types of devices with P3HT as donor layer was measured by electroluminescence (EL) and temperature dependence of V_{OC}. It has been reported that V_{OC} of bulk heterojunction photovoltaic devices at the low temperature limit can be directly related to the energy of CT state (E_{CT}) measured by EL.[20] The EL spectra from the bilayer devices were shown in Fig. 3.21, and the values were summarized in Table 3.4. Due to detection limit of the detector, peak top of CTS emission from the normal device (PCBM) could not be observed. Other peaks are fitted with a Gaussian function to extract the value of peak top and the reorganization energy λ (summarized in Table 3.4). The calculated value of peak top of the cascade, normal (bisPCBM) and trap devices were 0.90, 0.94 and 0.87 eV, respectively. Shift of about 0.1 eV to higher energy in the EL spectra was observed from the normal (PCBM) device to the cascade device. On the other hand, the peak top shifted about 0.1 eV to lower energy from the normal (bisPCBM) to the trap device.

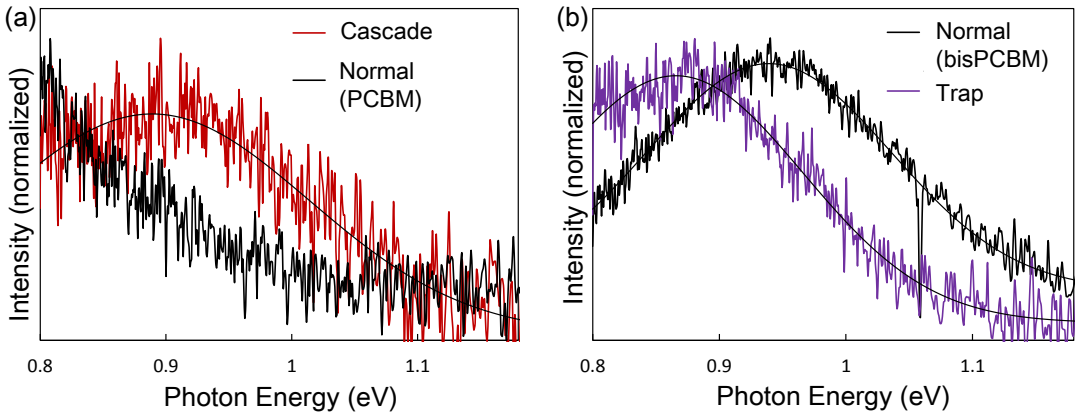

Figure 3.21. EL spectra of four types of bilayer OPVs with P3HT as the donor layer.

The shifts of CTS energy were also observed in the temperature dependence of V_{OC} under white light LED as shown in Fig. 3.22. E_{CT} extrapolated from the low temperature limits for cascade, normal (PCBM), normal (bisPCBM) and trap are 0.95, 0.86, 1.06 and 0.94 eV, respectively. The energy changes for cascade (+0.09 eV) and trap (−0.12 eV) from the corresponding normal devices reasonably match to those from EL measurements, although direct comparison would be difficult due to the temperature dependence of E_{CT}.[20]

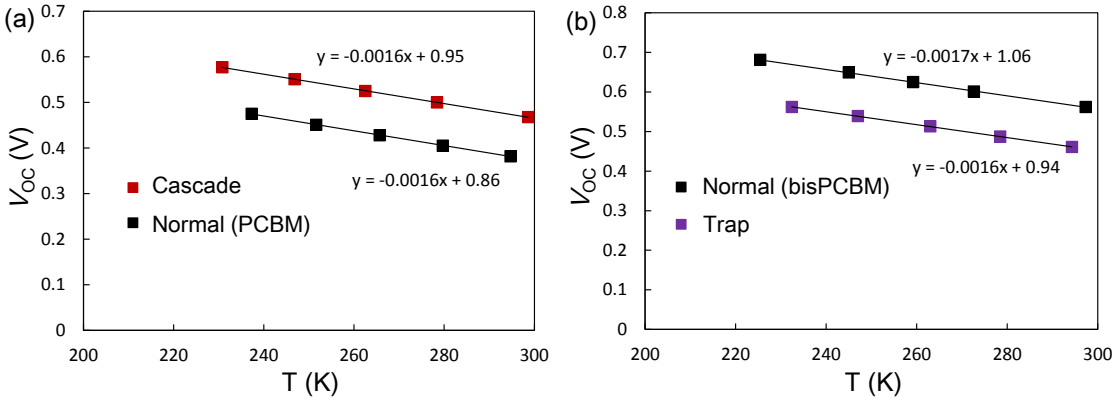

Figure 3.22. V_{OC} of the four types of the bilayer OPVs with P3HT under white light LED plotted as a function of the temperature. The lines and the formulae show the best linear fittings for the data.

Table 3.4. Summary of the energies of CTS measured by EL and temperature dependence of V_{OC}. The position of the peak top and λ (the half of the full width at half maximum) were obtained from the fitting of EL spectra. E_{CT} (EL) is the summation of the values of the peak top and λ.[20] E_{CT} (V_{OC}) is the low temperature limit of V_{OC} under white light LED.

	Peak top	λ	E_{CT} (EL)	E_{CT} (V_{OC})
Cascade	0.90	0.22	1.12	0.95
Normal (PCBM)	-	-	-	0.86
Normal (bisPCBM)	0.94	0.18	1.12	1.06
Trap	0.87	0.19	1.06	0.94

These differences of the energy of CTS were attributed to drastic change of V_{OC} in the cascade and trap devices. The energy of CTS is expressed by following equation,

$$E_{CT} = E_{DA} - \frac{e^2}{4\pi\varepsilon_0\varepsilon_r d} \quad \text{eq. 5}$$

Where E_{DA} is the energy level difference of HOMO of the donor and LUMO of the acceptor, ε_0 is the vacuum dielectric constant, ε_r is the relative dielectric constant, and d is the electron-hole distance. The energy level of LUMO at the first layer of D/A interface in the trap device was lower than the normal (bisPCBM) device, thus charge recombination occurred via the trap at D/A interface and energy of CTS in the trap device became smaller. The energy level of LUMO at the first layer of D/A interface in the cascade device was higher than the normal (PCBM) device. Electrons at the first layer of acceptor were energetically raised by higher LUMO, and spatially separated electrons from the D/A interface feel weaker Coulomb attraction. Energy of CTS was destabilized in ether cases although the author could not figure out real image of the change of charge distribution near the D/A interface by insertion of cascade layer.

The author also measured transient photovoltage measurement (TPV) on the four devices with P3HT as donor layer for tracing the recombination process from free charges after charge separation i.e. non-geminate recombination. Charge lifetimes of the four types of the devices were plotted as a function of carrier density measured by TPV and transient photocurrent (TPC) in Fig. 3.23, following the report by Durrant *et al.*[12] All the TPV signals can be fitted with single exponential decays, except for the devices with cascade devices where two exponential components with different lifetimes are necessary to fit the data ("fast" and "slow" in Fig. 3.23a). They might be assigned to the recombination processes of the electron at the first monolayer of F-bisPCBM (fast) and at the second layer of PCBM (slow). At any charge concentration, the lifetimes of free charges were longer in the cascade device than the normal device. The cascade energy level at the interface could reduce the population of the electrons at the first monolayer and the recombination could happen through spatially separated CTS, resulting in the change of

the kinetics and the suppression of the non-geminate recombination. In contrast, the trap situation showed the lifetime similar to that of the normal (bisPCBM) device. This suggests that at the open circuit condition, the trap at the interface did not further promote the bimolecular recombination.

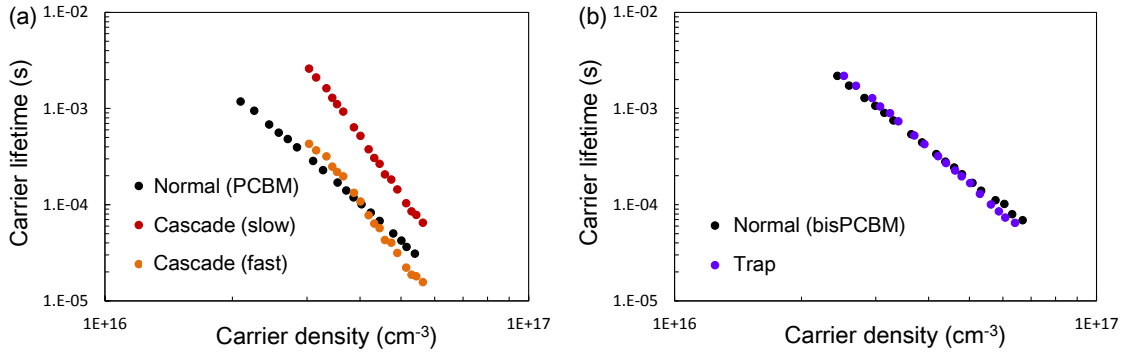

Figure 3.23. Total perturbation lifetime of the four types of the bilayer OPV devices with P3HT as the donor plotted as a function of carrier density measured by TPV and TPC.

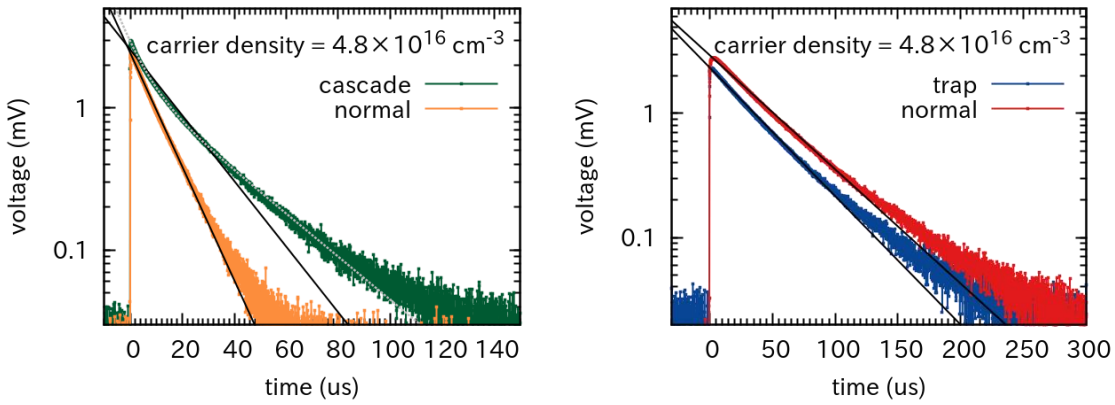

Figure 3.24. Transient photovoltage decay of the four types of the devices (cascade, normal (PCBM), trap, and normal (bisPCBM)) with P3HT as donor under same carrier density (4.8×10^{16} cm^{-3}). Black lines are single-exponential decay which well fitted to the experimental data except for cascade device. Combination of two exponential decay (gray, dotted line: A*exp(-*t*/B) + C*exp(-*t*/D)) could fit the photocurrent decay of cascade device more exactly.

3.4. Conclusions

In summary, the author conclude that the energetics of the first monolayer at the D/A interfaces control the energy of CTS, thus dominantly affect both the geminate and non-geminate recombination processes. The cascade energy landscape works in favour to supress both the processes, while trap landscape promote them. This conclusion could be extended to the D/A interfaces in the bulk heterojunction structures, in which the interfacial structures are ill-defined and have large variations. If it is possible to control the molecular interfaces more precisely in the bulk heterojunction beyond the limit of simple mixing of the materials, it could be another breakthrough for high performance OPVs.

References

1. Few, S.; Frost, J. M.; Nelson, J., Models of charge pair generation in organic solar cells. *Physical Chemistry Chemical Physics* **2015,** *17*, 2311-2325.

2. Nayak, P. K.; Narasimhan, K. L.; Cahen, D., Separating Charges at Organic Interfaces: Effects of Disorder, Hot States, and Electric Field. *Journal of Physical Chemistry Letters* **2013,** *4* (10), 1707-1717.

3. (a) Grancini, G.; Maiuri, M.; Fazzi, D.; Petrozza, A.; Egelhaaf, H. J.; Brida, D.; Cerullo, G.; Lanzani, G., Hot exciton dissociation in polymer solar cells. *Nature Materials* **2013,** *12* (1), 29-33; (b) Jailaubekov, A. E.; Willard, A. P.; Tritsch, J. R.; Chan, W.-L.; Sai, N.; Gearba, R.; Kaake, L. G.; Williams, K. J.; Leung, K.; Rossky, P. J.; Zhu, X. Y., Hot charge-transfer excitons set the time limit for charge separation at donor/acceptor interfaces in organic photovoltaics. *Nature Materials* **2013,** *12* (1), 66-73; (c) Bakulin, A. A.; Rao, A.; Pavelyev, V. G.; van Loosdrecht, P. H. M.; Pshenichnikov, M. S.; Niedzialek, D.; Cornil, J.; Beljonne, D.; Friend, R. H., The Role of Driving Energy and Delocalized States for Charge Separation in Organic Semiconductors. *Science* **2012,** *335* (6074), 1340-1344.

4. Vandewal, K.; Albrecht, S.; Hoke, E. T.; Graham, K. R.; Widmer, J.; Douglas, J. D.; Schubert, M.; Mateker, W. R.; Bloking, J. T.; Burkhard, G. F.; Sellinger, A.; Frechet, J. M. J.; Amassian, A.; Riede, M. K.; McGehee, M. D.; Neher, D.; Salleo, A., Efficient charge generation by relaxed charge-transfer states at organic interfaces. *Nature Materials* **2014,** *13* (1), 63-68.

5. (a) Sweetnam, S.; Graham, K. R.; Ndjawa, G. O. N.; Heumueller, T.; Bartelt, J. A.; Burke, T. M.; Li, W.; You, W.; Amassian, A.; McGehee, M. D., Characterization of the Polymer Energy Landscape in Polymer:Fullerene Bulk Heterojunctions with Pure and Mixed Phases. *Journal of the American Chemical Society* **2014,** *136* (40), 14078-14088; (b) Jamieson, F. C.; Domingo, E. B.; McCarthy-Ward, T.; Heeney, M.; Stingelin, N.; Durrant, J. R., Fullerene crystallisation as a key driver of charge separation in polymer/fullerene bulk heterojunction solar cells. *Chemical Science* **2012,** *3* (2), 485-492.

6. Vandewal, K.; Himmelberger, S.; Salleo, A., Structural Factors That Affect the Performance of Organic Bulk Heterojunction Solar Cells. *Macromolecules* **2013,** *46* (16), 6379-6387.

7. Groves, C., Suppression of geminate charge recombination in organic photovoltaic devices with a cascaded energy heterojunction. *Energy Environ. Sci.* **2013,** *6* (5), 1546-1551.

8. Gao, F.; Inganas, O., Charge generation in polymer-fullerene bulk-heterojunction solar cells. *Physical Chemistry Chemical Physics* **2014,** *16* (38), 20291-20304.

9. (a) Sista, S.; Yao, Y.; Yang, Y.; Tang, M. L.; Bao, Z., Enhancement in open circuit voltage through a cascade-type energy band structure. *Applied Physics Letters* **2007,** *91* (22); (b)

Kinoshita, Y.; Hasobe, T.; Murata, H., Control of open-circuit voltage in organic photovoltaic cells by inserting an ultrathin metal-phthalocyanine layer. *Applied Physics Letters* **2007,** *91* (8); (c) Tan, Z.-K.; Johnson, K.; Vaynzof, Y.; Bakulin, A. A.; Chua, L.-L.; Ho, P. K. H.; Friend, R. H., Suppressing Recombination in Polymer Photovoltaic Devices via Energy-Level Cascades. *Advanced Materials* **2013,** *25* (30), 4131-4138.

10. Tada, A.; Geng, Y.; Wei, Q.; Hashimoto, K.; Tajima, K., Tailoring organic heterojunction interfaces in bilayer polymer photovoltaic devices. *Nature Materials* **2011,** *10* (6), 450-455.

11. Lenes, M.; Wetzelaer, G.-J. A. H.; Kooistra, F. B.; Veenstra, S. C.; Hummelen, J. C.; Blom, P. W. M., Fullerene bisadducts for enhanced open-circuit voltages and efficiencies in polymer solar cells. *Advanced Materials* **2008,** *20* (11), 2116-2119.

12. (a) O'Regan, B. C.; Scully, S.; Mayer, A. C.; Palomares, E.; Durrant, J., The effect of Al2O3 barrier layers in TiO2/Dye/CuSCN photovoltaic cells explored by recombination and DOS characterization using transient photovoltage measurements. *Journal of Physical Chemistry B* **2005,** *109* (10), 4616-4623; (b) Shuttle, C. G.; O'Regan, B.; Ballantyne, A. M.; Nelson, J.; Bradley, D. D. C.; de Mello, J.; Durrant, J. R., Experimental determination of the rate law for charge carrier decay in a polythiophene: Fullerene solar cell. *Applied Physics Letters* **2008,** *92* (9).

13. Inganas, N.-K. P. a. O., *Simulations of Optical Processes in Organic Photovoltaic Devices*. CRC Press: 2010.

14. (a) Lai, Y. C.; Higashihara, T.; Hsu, J. C.; Ueda, M.; Chen, W. C., Enhancement of power conversion efficiency and long-term stability of P3HT/PCBM solar cells using C-60 derivatives with thiophene units as surfactants. *Solar Energy Materials and Solar Cells* **2012,** *97*, 164-170; (b) Izawa, S.; Hashimoto, K.; Tajima, K., Surface functionalization of organic semiconductor films by segregated monolayers. *Physical Chemistry Chemical Physics* **2014,** *16* (31), 16383-16387.

15. Wei, Q.; Tajima, K.; Tong, Y.; Ye, S.; Hashimoto, K., Surface-Segregated Monolayers: A New Type of Ordered Monolayer for Surface Modification of Organic Semiconductors. *Journal of the American Chemical Society* **2009,** *131* (48), 17597-17604.

16. Geng, Y.; Wei, Q.; Hashimoto, K.; Tajima, K., Dipole Layer Formation by Surface Segregation of Regioregular Poly(3-alkylthiophene) with Alternating Alkyl/Semifluoroalkyl Side Chains. *Chemistry of Materials* **2011,** *23* (18), 4257-4263.

17. Khlyabich, P. P.; Burkhart, B.; Thompson, B. C., Efficient Ternary Blend Bulk Heterojunction Solar Cells with Tunable Open-Circuit Voltage. *Journal of the American Chemical Society* **2011,** *133* (37), 14534-14537.

18. Riedel, I.; Dyakonov, V., Influence of electronic transport properties of polymer-fullerene blends on the performance of bulk heterojunction photovoltaic devices. *Physica Status Solidi a-Applied Research* **2004,** *201* (6), 1332-1341.

19. Goh, C.; Kline, R. J.; McGehee, M. D.; Kadnikova, E. N.; Frechet, J. M. J., Molecular-weight-dependent mobilities in regioregular poly(3-hexyl-thiophene) diodes. *Applied Physics Letters* **2005,** *86* (12).
20. Vandewal, K.; Tvingstedt, K.; Gadisa, A.; Inganas, O.; Manca, J. V., Relating the open-circuit voltage to interface molecular properties of donor:acceptor bulk heterojunction solar cells. *Physical Review B* **2010,** *81* (12).

Chapter 4.

Efficient Charge Generation and Collection in Organic Solar Cells Based on Low Band Gap Dyad Molecules

4.1. Introduction

Organic solar cells (OSCs) fabricated by solution processes using π-conjugated materials have attracted much attention as a renewable energy source, owing to their low fabrication cost, light weight, and high flexibility.[1] To date, the highest efficiency of bulk heterojunction (BHJ) structures, which are prepared by mixing electron donor and acceptor materials, has reached 7-8% when low band gap polymers and fullerene derivatives are used.[2] The large interface between the donor and the acceptor, and the formation of the nano-scale interpenetrating networks that serve as efficient charge transport pathways are considered to be important for high performance in OSCs.[3] However, such phase-separated nanostructures are not necessarily well controlled since they are made by simple mixing of two materials and subsequent thermal annealing for a short time. Hence, BHJ systems often suffer from undesirable structural changes such as too much phase segregation, which causes low reproducibility and poor stability in device performance.[4]

Consisting of covalently attached donor and acceptor moieties, dyad molecules have been widely studied with a primary aim of gaining fundamental understanding of charge separation in solution.[5] Dyads have several advantages over mixed BHJs when used in OSCs; the use of a molecular based system can avoid the many problems with polymers such as molecular weight distribution, batch-to-batch variation, end group contamination, and difficulty in purification.[6] Moreover, since the donor and acceptor molecules are connected to each other, phase segregation is suppressed, and higher charge separation, owing to the proximity of the donor and the acceptor, leads to current generation. These characteristics of dyads enable single-component OSCs to be constructed, which is advantageous in terms of nanostructure control and device reproducibility.[5b] Many research studies have been reported on the synthesis of dyads and their application in OSCs. Our group has reported dyad molecules with π-conjugated oligomers and fullerene derivatives.[5b, 5c, 7] The efficiency has been improved from about 0.1% in early studies to over 1% in recent reports.[5c] This improvement comes from changes in the design of the electron donor moiety. Introduction of a highly crystalline donor part, namely, oligo(*p*-

phenylenevinylene) (OPV), resulted in fill factor (FF) of 0.44, improved from 0.23 in less crystalline oligothiopnene-based dyad molecules.[5b, 5c] Crucial problems that must be addressed in order to improve the efficiency of dyad OSCs are low FF and the mismatch between the absorption spectrum of the donor part and the solar spectrum. So far, these shortcomings limit the short circuit current (J_{SC}) and FF of the dyad devices to 3.3 mA cm^{-2} and 0.44, respectively.[5c]

In this study, low band gap dyad molecules with diketopyrrolopyrrole (DPP) units as the donor and a fullerene group as the acceptor were synthesized to match the molecule's absorption spectrum with the solar spectrum. The number of thiophene rings in the donor part was varied in order to tune the structure of the films. OSC devices were fabricated, and in this report, the relationship between molecular structure, film morphology, and device performance is discussed.

4.2. Experimental

Materials and instruments

All chemicals were purchased from Sigma-Aldrich, Tokyo Kasei Kogyo, or Wako Chemicals and used without further purification. Cyclic voltammetry was measured on an HSV-100 automatic polarization system at Hokuto Denko Company. Anhydrous chloroform was used as the solvent under N_2, and 0.1 M tetrabutylammomium hexafluorophosphate was used as a supporting electrolyte. Glassy carbon was used as the working electrode, Pt wire was used as the counter electrode, and a Ag/AgCl wire was used as the reference electrode. UV-vis absorption spectra were measured on a V-670 system (Nippon Bunko Company). ^{1}H NMR spectra were measured in $CDCl_3$ containing 1% v/v TMS on an Oxford superconducting magnet system (500 MHz). Matrix-assisted laser desorption/ionization/time-of-flight (MALDI-TOF) MS spectra were measured with dithranol as matrix on an Applied Biosystems BioSpectrometry Workstation spectrometer (Voyager-DE STR). High-performance liquid chromatography was carried out on a system with a CBM-20A controller (Shimadzu), an LC-6AD pump (Shimadzu), an SPD-20A UV-vis detector, and a Luna Silica column (particle size: 5 μm, column length: 250 mm, and inner diameter: 21.2 mm) (Phenomenex). Atomic force microscopy (AFM) images were obtained on a Digital Instrumental Nanoscope 31 operated in tapping mode. Film thicknesses were measured by Dektak 6M, ULVAC, Japan.

Synthetic procedures

The synthetic route to the low band gap dyad molecules is shown in Scheme 4.1. The details of the synthetic procedures, and the spectral data from ^{1}H-NMR spectroscopy and MALDI-TOF-

MS, are described below. In MALDI-TOF-MS, Na^+ was sometimes attached to the detected compounds. The following compounds were synthesized according to procedures in the literature: 3,6-dithiophene-2-yl-2,5-dihydropyrrolo[3,4-*c*]pyrrole-1,4-dione (S1),[13] 17-tosyloxy-3,6,9,12,15-pentaoxaheptadecane-1-ol (S4),[9] 5-tributylstannyl-2-hexylthiophene (S9),[14] and [6,6]-phenyl-C_{61}-butyric acid (S12).[15]

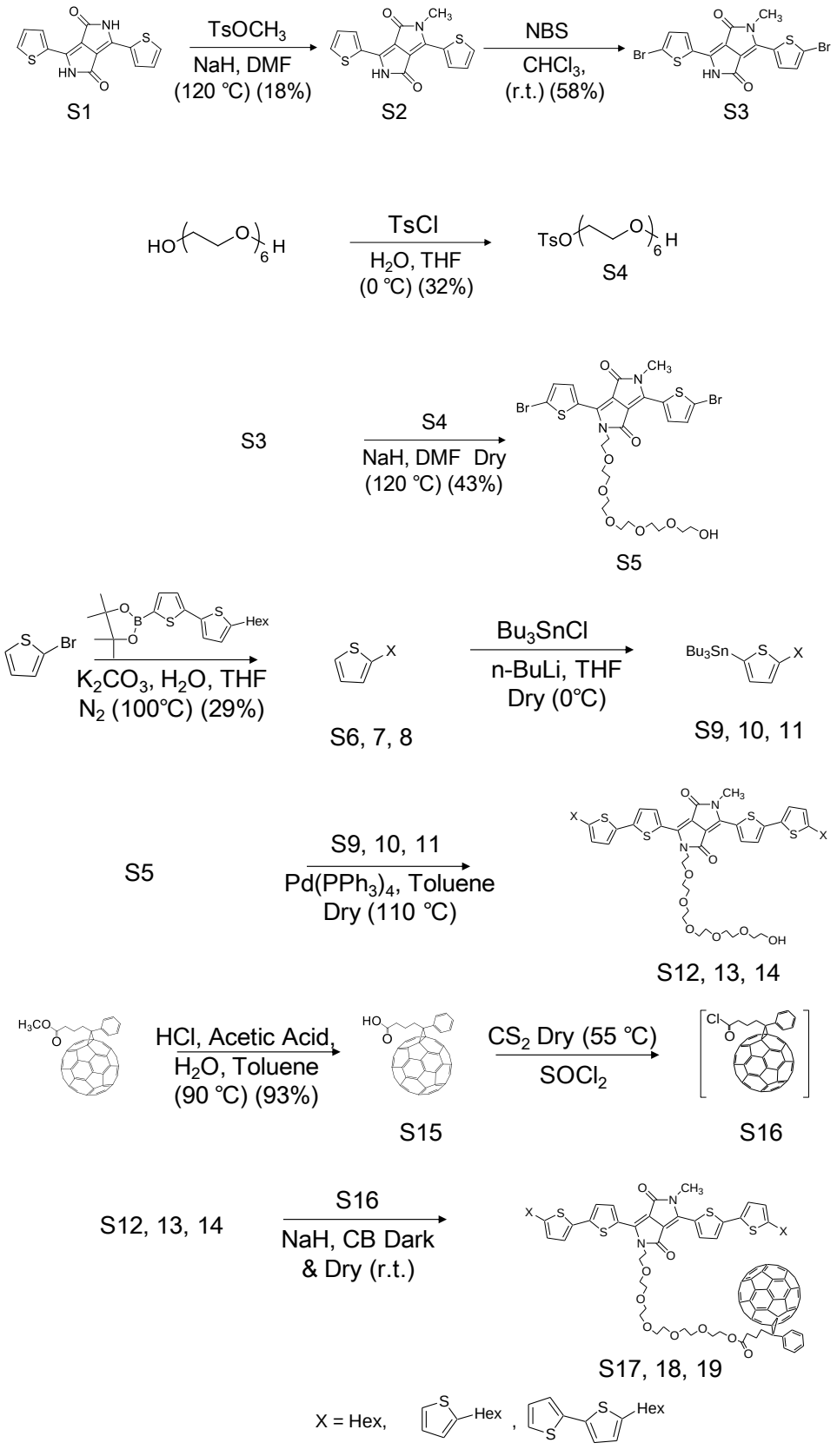

Scheme 4.1. Synthesis route to low band gap dyad molecules

3,6-Dithiophene-2-yl-2-methyl-5-hydropyrrolo[3,4-*c*]pyrrole-1,4-dione (S2)

S1 (13.5 g, 45 mmol), NaH (oil dispersion 50–72%, 3.6 g), and DMF (800 mL) were added to a 1-L three-neck round-bottom flask under N_2. Methyl-*p*-toluenesulfonate (10.2 mL, 67.5 mmol) was mixed with DMF (100 mL), and added dropwise via a dropping funnel. The reaction mixture was stirred overnight at 120 °C and then cooled to room temperature. Acetic acid (25 mL) was added to the solution, and the mixture was stirred at room temperature for 1 h, and then poured into 4.5 L of water, and stirred at room temperature for 30 min. The solid was collected by vacuum filtration, washed with several portion of distilled water, washed with methanol, and then air dried. The crude product was extracted with $CHCl_3$ by Soxhlet extraction. The product was recrystallized from $CHCl_3$ and washed with $CHCl_3$, yielding a dark green solid (2.54 g, 18%)

^{1}H NMR (DMSO-d6, 500 MHz): δ (ppm): 11.35 (s, 1H), 8.74-8.75 (m, 1H), 8.31-8.32 (m, 1H), 8.06-8.07 (m, 1H), 7.99-8.00 (m, 1H), 7.40-7.42 (m, 1H), 7.31-7.33 (m, 1H), 3.52 (s, 3H)

3,6-Bis(5-bromothiophene-2-yl)-2-methyl-5-hydropyrrolo[3,4-*c*]pyrrole-1,4-dione (S3)

In a 500-mL round-bottom flask covered with aluminum foil, compound S2 (3.30 g, 10.5 mmol) was dissolved in 330 mL of $CHCl_3$ and stirred at room temperature for 15 min. *N*-Bromosuccinimide (4.10 g, 23 mmol) was then added, and the reaction mixture was kept at room temperature with stirring for 48 h. The reaction mixture was poured into 1 L of methanol, and the resulting suspension was filtered and washed with methanol, yielding a purple solid (2.83 g, 58%).

^{1}H NMR (DMSO-d6, 500 MHz): δ (ppm): 11.42 (s, 1H), 8.44-8.45 (d, 1H), 7.97-7.98 (d, 1H), 7.53-7.54 (d, 1H), 7.46-7.47 (d, 1H), 3.45 (s, 3H), MALDI-TOF-MS (*m/z*): 472.99 (M^+)

3,6-Bis(5-bromothiophene-2-yl)-2-methyl-5-(3,6,9,12,15-pentaoxaheptadecane-18-ol)-pyrrolo[3,4-*c*]pyrrole-1,4-dione (S5)

S3 (0.74 g, 1.6 mmol) and *t*-BuOK (0.26 g, 2.3 mmol) were added to a two-neck 100-mL round-bottom flask and vacuum dried overnight. The flask was then filled with N_2. Anhydrous DMF (25 mL) was added, and the reaction mixture was stirred for 1 h at 120 ºC. Dried S4 was added with anhydrous DMF (5 mL), and the reaction mixture was stirred overnight at 120 ºC. The solution was cooled to room temperature, and water (300 mL) and acetic acid (560 μL) were added. The reaction mixture was extracted with $CHCl_3$. The solution was purified by column chromatography using silica gel and $CHCl_3$/methanol (4:1) as eluent and then by HPLC using $CHCl_3$/methanol (100:1) as eluent. Solvent was removed in vacuo, yielding a purple solid (0.50 g, 42%)

^{1}H NMR ($CDCl_3$, 500 MHz): δ (ppm): 8.61-8.62 (d, 1H), 8.50-8.51 (d, 1H), 7.24-7.25 (d, 1H), 7.20-7.21 (d, 1H), 4.16-4.20 (m, 2H), 3.57-3.77 (m, 22H) 3.55 (s, 3H), MALDI-TOF-MS (*m/z*): 759.11 ($[M + Na]^+$)

5-*n*-hexyl-[2,2';5',2'']-terthiophene (S8)

2-Bromothiophene (485 μL, 5.00 mmol), toluene (30 mL), 5'- ***n***-hexyl-2,2'-bithiophene-5-boronic acid pinacol ester (1.88 g, 5.00 mmol) dissolved in THF (30 mL), and K_2CO_3 (2.07 g, 15.0 mmol) dissolved in water (10 mL) were added to a 100-mL two-neck round-bottom flask under N_2. The solution was degassed for 30 min, and tetrakis(triphenylphosphine)palladium(0) (57.8 mg, 0.0500 mmol) was added. The reaction mixture was then refluxed at 110 ºC for 24 h. After cooling to room temperature, the mixture was extracted with ether and purified by column chromatography using silica gel and hexane as eluent. Solvent was removed in vacuo, yielding a sticky yellow-white solid (475 mg, 29%).

^{1}H NMR ($CDCl_3$, 500 MHz): δ (ppm): 7.20-7.21 (d, 1H), 7.15-7.16 (d, 1H), 7.05-7.06 (d, 1H), 6.97-7.02 (m, 3H), 6.68-6.69 (d, 1H), 2.78-2.81 (t, 2H), 1.64-1.72 (m, 2H), 1.35-1.41 (m, 2H), 1.30-1.33 (m, 4H), 0.88-0.91 (t, 3H)

General synthesis (S10, 11)

S7 (purchased) (1.29 mmol) or S8 (1.29 mmol) and anhydrous THF (6 mL) were added to a 100-mL two-neck round-bottom flask under N_2 and stirred for 10 min at 0 ºC. Then, *n*-butyllithium hexane solution (1.64 M, 865 μL, 1.42 mmol) was added and the reaction mixture was stirred for 30 min at 0 ºC. Tributyltin chloride (384 μL, 1.42 mmol) was added, and the reaction mixture was stirred for 2 h at room temperature. Water was added to quench the reaction. The mixture was extracted with ether and purified by column chromatography using alumina and hexane with triethylamine (5%) as eluent. The solvent was removed in vacuo, yielding a colorless transparent liquid.

***Compound S10*: 5-tributylstannyl-5'- *n*-hexyl-[2,2']-bithiophene** (yield: 60%)

^{1}H NMR ($CDCl_3$, 500 MHz): δ (ppm): 7.20-7.21 (d, 1H), 7.03-7.04 (d, 1H), 6.96-6.97 (d, 1H), 6.65-6.66 (d, 1H), 2.76-2.78 (t, 2H), 1.63-1.71 (m, 2H), 1.53-1.61 (m, 6H), 1.28-1.38 (m, 12H), 1.09-1.12 (m, 6H), 0.87-0.92 (m, 12H)

***Compound S11*: 5-tributylstannyl-5''- *n*-hexyl-[2,2';5',2'']-terthiophene** (yield: 73%)

^{1}H NMR ($CDCl_3$, 500 MHz): δ (ppm): 7.27-7.28 (d, 1H), 7.04-7.06 (m, 2H), 6.96-6.99 (m, 2H), 6.67-6.68 (d, 1H), 2.76-2.80 (t, 2H), 1.63-1.71 (m, 2H), 1.53-1.61 (m, 6H), 1.28-1.38 (m, 12H), 1.09-1.12 (m, 6H), 0.88-0.92 (m, 12H)

General synthesis (S12, 13, 14)

S5 (92 mg, 0.125 mmol), S9, 10, or 11 (0.375 mmol) and anhydrous toluene (10 mL) were added to a 50-mL two-neck round-bottom flask under N_2. The solution was degassed for 30 min, and tetrakis(triphenylphosphine)palladium(0) (10 mg, 0.013 mmol) was added. The reaction mixture was refluxed at 110 ºC for 24 h and then purified by column chromatography using silica

gel and $CHCl_3$/methanol (4:1) as eluent and by HPLC using $CHCl_3$/methanol (100:1) as eluent. Solvent was removed in vacuo, yielding a blue-purple solid.

***Compound S12*: 3,6-bis-(5”- *n*-hexyl-[5,2’]bithiophene-2-yl)-2-methyl-5-(3,6,9,12,15-pentaoxaheptadecane-18-ol)-pyrrolo[3,4-*c*]pyrrole-1,4-dione** (yield: 62%)

^{1}H NMR ($CDCl_3$, 500 MHz): δ (ppm): 8.87-8.88 (d, 1H), 8.78-8.79 (d, 1H), 7.26-7.27 (d, 1H), 7.22-7.23 (d, 1H), 6.73-6.75 (m, 2H), 4.31-4.32 (m, 2H), 3.80-3.81 (m, 2H), 3.57-3.66 (m, 23H), 2.79-2.82 (t, 4H), 1.66-1.72 (m, 4H), 1.36-1.42 (m, 4H), 1.30-1.34 (m, 8H), 0.89-0.91 (t, 6H, CH_2-CH_3), MALDI-TOF-MS (*m/z*): 934.52 ($[M + Na]^+$)

***Compound S13*: 3,6-bis-(5”- *n*-hexyl-[5,2’;5’,2”]terthiophene-2-yl)-2-methyl-5-(3,6,9,12,15-pentaoxaheptadecane-18-ol)-pyrrolo[3,4-*c*]pyrrole-1,4-dione** (yield: 62%)

^{1}H NMR ($CDCl_3$, 500 MHz): δ (ppm): 8.88-8.89 (d, 1H), 8.80-8.81 (d, 1H), 7.30-7.31 (m, 1H), 7.27-7.28 (m, 1H), 7.23-7.24 (m, 2H), 7.02-7.05 (m, 4H), 6.70-6.71 (m, 2H), 4.31-4.32 (m, 2H), 3.80-3.81 (m, 2H), 3.57-3.66 (m, 23H), 2.79-2.82 (t, 4H), 1.66-1.72 (m, 4H), 1.36-1.42 (m, 4H), 1.30-1.34 (m, 8H), 0.89-0.91 (t, 6H), MALDI-TOF-MS (*m/z*): 1097.48 ($[M + Na]^+$)

***Compound S14*: 3,6-bis-(5”- *n*-hexyl-[5,2’;5’,2”;5”,2”’]quaterthiophene-2-yl)-2-methyl-5-(3,6,9,12,15-pentaoxaheptadecane-18-ol)-pyrrolo[3,4-*c*]pyrrole-1,4-dione** (yield: 62%)

^{1}H NMR ($CDCl_3$, 500 MHz): δ (ppm): 8.80-8.81 (d, 1H), 8.74-8.75 (d, 1H), 7.07-7.08 (d, 1H), 7.02-7.05 (m, 3H), 6.85-7.6.91 (m, 8H), 6.62-6.63 (d, 1H), 6.59-6.60 (d, 1H), 4.31-4.32 (m, 2H), 3.78-3.79 (m, 2H), 3.53-3.70 (m, 23H), 2.73-2.76 (t, 4H), 1.64-1.67 (m, 4H), 1.30-1.42 (m, 12H), 0.89-0.91 (t, 6H), MALDI-TOF-MS (*m/z*): 1262.30 ($[M + Na]^+$)

General synthesis (S17, 18, 19)

S15 (0.0930 mmol) was added to a 50-mL two-neck round-bottom flask under N_2, and then distilled CS_2 (25 mL) and thionyl chloride (402 μL, 2.05 mmol) were added. The reaction mixture was refluxed overnight at 55 ºC. The solvent was removed, and the crude product was dried at 80 ºC for 3 h; then, anhydrous chlorobenzene (10 mL) and NaH (oil dispersion 50–72%, 10.1 mg), which had been washed with hexane, were added. The flask was covered with aluminum foil, and S12, 13, or 14 (0.0465 mmol) was added. The reaction mixture was stirred at room temperature for 48 h and then purified by column chromatography using silica gel and $CHCl_3$ as eluent and by HPLC using $CHCl_3$ as eluent. The obtained product was reprecipitated in hexane and filtered, yielding a blue solid.

***Compound S17 (*4**T dyad):**

3,6-bis-(5”- *n*-hexyl-[5,2’]bithiophene-2-yl)-2-methyl-5-(3,6,9,12,15,18-hexaoxa-19-carbonyl-23-phenyl[6.6]C_{61}-tricosane)-pyrrolo[3,4-*c*]pyrrole-1,4-dione (yield: 13%)

^{1}H NMR ($CDCl_3$, 500 MHz): δ (ppm): 8.87-8.88 (d, 1H), 8.78-8.79 (d, 1H), 7.90-7.91 (d, 2H), 7.51-7.54 (m, 2H), 7.44-7.47 (m, 1H), 7.25-7.26 (d, 1H), 7.22-7.23 (d, 1H), 7.16-7.17 (m, 2H),

6.74-6.75 (m, 2H), 4.29-4.30 (m, 2H), 4.22-4.23 (m, 2H), 3.79-3.80 (m, 2H), 3.57-3.68 (m, 21H), 2.87-2.89 (m, 2H), 2.81-2.83 (t, 4H), 2.53-2.54 (m, 2H), 2.14-2.15 (m, 2H), 1.68-1.71 (m, 4H), 1.37-1.40 (m, 4H), 1.32-1.33 (m, 8H), 0.89-0.91 (t, 6H), MALDI-TOF-MS (*m/z*): 1789.72 (M^+)

***Compound S18 (*6T dyad): 3,6-bis-(5”- *n*-hexyl-[5,2’;5’,2”]terthiophene-2-yl)-2-methyl-5-(3,6,9,12,15,18-hexaoxa-19-carbonyl-23-phenyl[6.6]C_{61}-tricosane)-pyrrolo[3,4-*c*]pyrrole-1,4-dione** (yield: 47%)

^{1}H NMR ($CDCl_3$, 500 MHz): δ (ppm): 8.87-8.88 (d, 1H), 8.80-8.81 (d, 1H), 7.89-7.90 (d, 2H), 7.50-7.53 (m, 2H), 7.45-7.50 (m, 1H), 7.24-7.25 (d, 1H), 7.21-7.22 (d, 1H), 7.18-7.19 (d, 2H), 6.99-7.01 (m, 4H), 6.68-6.69 (m, 2H), 4.28-4.29 (m, 2H), 4.21-4.22 (m, 2H), 3.79-3.80 (m, 2H), 3.58-3.67 (m, 21H), 2.87-2.89 (m, 2H), 2.78-2.80 (t, 4H), 2.52-2.53 (m, 2H), 2.13-2.15 (m, 2H), 1.67-1.70 (m, 4H), 1.36-1.40 (m, 4H), 1.32-1.33 (m, 8H), 0.89-0.92 (t, 6H), MALDI-TOF-MS (*m/z*): 1954.08 (M^+)

***Compound S19 (*8T dyad): 3,6-bis-(5”- *n*-hexyl-[5,2’;5’,2”;5”,2”’]quaterthiophene-2-yl)-2-methyl-5-(3,6,9,12,15,18-hexaoxa-19-carbonyl-23-phenyl[6.6]C_{61}-tricosane)-pyrrolo[3,4-*c*]pyrrole-1,4-dione** (yield: 13%)

^{1}H NMR ($CDCl_3$, 500 MHz): δ (ppm): 8.80-8.81 (d, 1H), 8.74-8.75 (d, 1H), 7.89-7.90 (d, 2H), 7.50-7.53 (m, 2H), 7.45-7.51 (m, 1H), 7.02-7.08 (m, 4H), 6.85-6.91 (m, 8H), 6.59-6.60 (d, 1H), 6.62-6.63 (d, 1H), 4.30-4.31 (m, 2H), 4.20-4.22 (m, 2H), 3.82-3.83 (m, 2H), 3.57-3.67 (m, 21H), 2.85-2.86 (m, 2H), 2.78-2.81 (t, 4H), 2.50-2.52 (m, 2H), 2.11-2.13 (m, 2H), 1.67-1.70 (m, 4H), 1.36-1.40 (m, 4H), 1.32-1.33 (m, 8H), 0.87-0.91 (t, 6H), MALDI-TOF-MS (*m/z*): 2118.32 (M^+)

Photovoltaic devices preparation and measurement

With the dyads, photovoltaic devices were prepared in a structure of ITO/PEDOT–PSS/Ca/Al. An indium tin oxide (ITO)-coated glass substrate (sheet resistance: 10 Ω sq^{-1}, Geomatech, Japan) was cleaned by ultrasonication in detergent, water, acetone, 2-propanol, and water. After the substrate was dried, PEDOT–PSS (H. C. Stark) was spin-coated (4000 rpm) onto ITO. The film was dried at 150 ºC under N_2 for 20 min. After cooling the substrate, $CHCl_3$ solution of dyad (4T: 20 mg/mL; 4T: 20 mg/mL; 8T: 15 mg/mL) was spin-coated (2500 rpm). Finally, Ca (20 nm) and Al (40 nm) electrodes were evaporated onto the organic layer under high vacuum (6×10^{-4} Pa). After Ca and Al evaporation, devices with 6T and 8T dyads were thermally annealed at 110 °C for 5 min under N_2 atmosphere.

I-V characteristics of the devices were measured under simulated solar light illumination (AM 1.5, 100 mW cm^{-2}) from a 150 W xenon lamp (PEC-L11, Peccell Technologies, Inc., Japan). The light intensity was calibrated with a standard silicon solar cell (BS520, Bunkoh-Keiki, Japan). The active area of the devices was defined to be 0.06 cm^2 by a photomask. The external quantum efficiency (EQE) of the devices was measured on a Hypermonolight SM-250F system

(Bunkoh-Keiki, Japan).

4.3. Results and Discussion

The chemical structures of the dyads with different lengths of the oligothiophene unit (*n* = 1-3) are shown in Figure 4.1. DPP derivatives are known as excellent dyes,[8] and have been used as an electron-withdrawing group in so-called donor–acceptor type low band gap polymers and oligomers.[9] Oligothiophene was used as an electron-donating group. Three oligothiophenes with different lengths were synthesized to investigate the influence of the connectivity of the donor part in the film and the charge collection ability. The synthesis of the low band gap dyad molecules is described in the experimental section (4.2). Briefly, a methyl group and hexaethylene glycol were attached to the DPP core. The modified DPP core was then connected to the oligothiophenes via Stille coupling.[10] Finally, the dyad molecules 4T (*n* = 1), 6T (*n* = 2) and 8T (*n* = 3) were synthesized via the esterification reaction between the DPP–oligothiopnene donor part and a fullerene derivative with a carboxylic acid chloride functional group.[5b] The π-oligomers are attached to the fullerene derivative through a long flexible spacer of hexaethylene glycol, which enables moderate segregation of the donor and acceptor groups, and leads to efficient charge separation and construction of efficient charge transport pathways at the same time.[5c] After purification by column chromatography and preparative HPLC, the product was identified by ^{1}H-NMR spectroscopy and MALDI-TOF-MS. The spectral data are available in the SI.

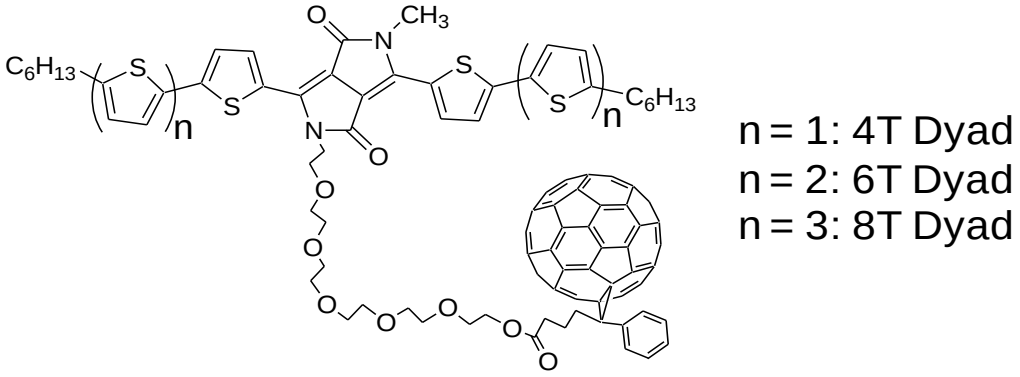

Figure 4.1. Chemical Structure of low band gap dyad molecules

The absorption spectra of 4T, 6T, and 8T in chloroform solution are shown in Figure 4.2 (a). Absorption peaks at around 330 nm correspond to fullerene, and those at around 600 nm correspond to the oligomers. As the number of thiophene units was increased from 4T to 8T, continuous shifts of absorption edges were observed due to the increased π-

conjugation length in the donor part. Absorption spectra of the dyads in thin films are shown in Figure 4.2 (b). Compared with the absorption in the solution in Figure 4.2 (a), red shifts of the absorption edges and broadening of the absorption width were observed. The absorption spectra of all dyads matched well with the solar spectrum, as shown in Figure 4.2 (b), owing to the low band gap properties.

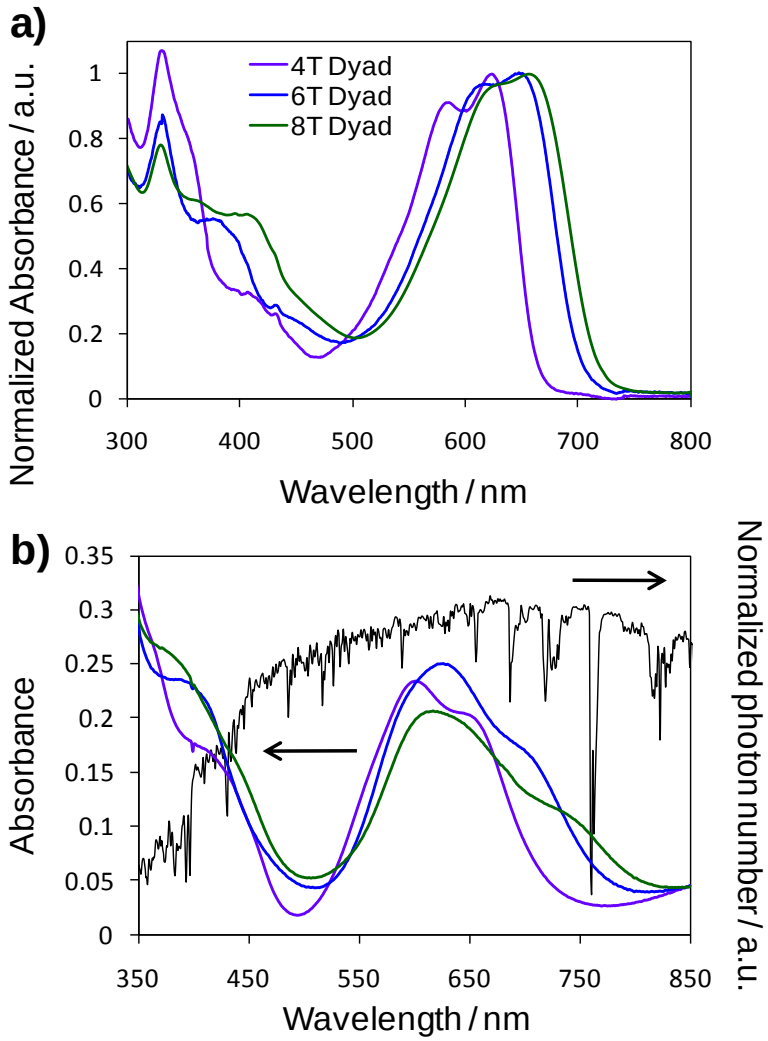

Figure 4.2 (a) Absorption spectra of dyad molecules in $CHCl_3$ solution. (b) Solar spectrum and absorption spectra of dyad molecules in thin films.

The first oxidation (E_{ox}) and reduction potentials (E_{red}) of the dyad molecules in solution were determined by cyclic voltammetry (CV). The energies of the highest occupied molecular orbital (HOMO) and lowest unoccupied molecular orbital (LUMO) were estimated by assuming the Fc/Fc^+ potential to be –4.8 eV relative to the vacuum level.[9b] The results are summarized in Table 4.1. The LUMO energy levels were almost the same

as in PCBM because the acceptor groups have analogous structures. In contrast, the energy levels of the HOMO in the donor became higher-lying as the number of thiophene increased, owing to the conjugation length in the donor part.

Table 4.1 Optical and electrochemical properties and devise performances. [a] Half potentials determined by cyclic voltammetry *vs.* Fc/Fc^+. [b]Optical band gaps

Material	E_{ox}[a]/V	E_{red}[a]/V	E_g[b]/eV	V_{OC}/V	I_{SC}/mA cm^{-2}	FF	PCE (%)
4T dyad	0.44	-1.11	1.86	0.60	0.69	0.25	0.10
6T dyad	0.33	-1.13	1.77	0.56	3.17	0.33	0.56
8T dyad	0.25	-1.11	1.73	0.51	4.79	0.46	1.11
PCBM		-1.16					

Solar cell devices were fabricated with a simple configuration of ITO/dyad/Ca (20 nm)/Al (30 nm). The solutions of 4T, 6T, and 8T had concentrations of 20, 20, and 15 g L^{-1}, respectively, and the active layers were spin-coated at a spinning rate of 2500 rpm. The active layers were respectively 90 nm, 100 nm, and 70 nm in thickness, as measured by surface profilometry. After Ca and Al evaporation, the devices with 6T and 8T dyads were thermally annealed at 110 °C for 5 min under an N_2 atmosphere, while the device with 4T dyad was not annealed because the device performance was found in preliminary studies to be degraded by annealing.[11] The OSC devices were evaluated under irradiation of simulated solar light (AM 1.5, 100 mW cm^{-2}) through a photomask with an aperture size of 0.06 cm^{-2}.

J-V characteristics of the dyad devices under AM 1.5 illumination are shown in Figure 4.3 (a), and the performance of each device is summarized in Table 4.1. As the number of thiophene units was increased in the π-conjugated oligomers, the photocurrent increased from 0.69 to 4.79 mA cm^{-2}; furthermore, FF also increased from 0.25 to 0.46. In contrast, V_{OC} decreased from 0.6 to 0.51 V when the thiophene number was increased. This is because energy level of the HOMO in the donor part became higher, as determined by CV. Due to low band gap properties and favorable hole transport properties, the device of 8T dyad showed power conversion efficiency of over 1%. In particular, J_{SC} and FF were the highest among dyad-based solar cells.

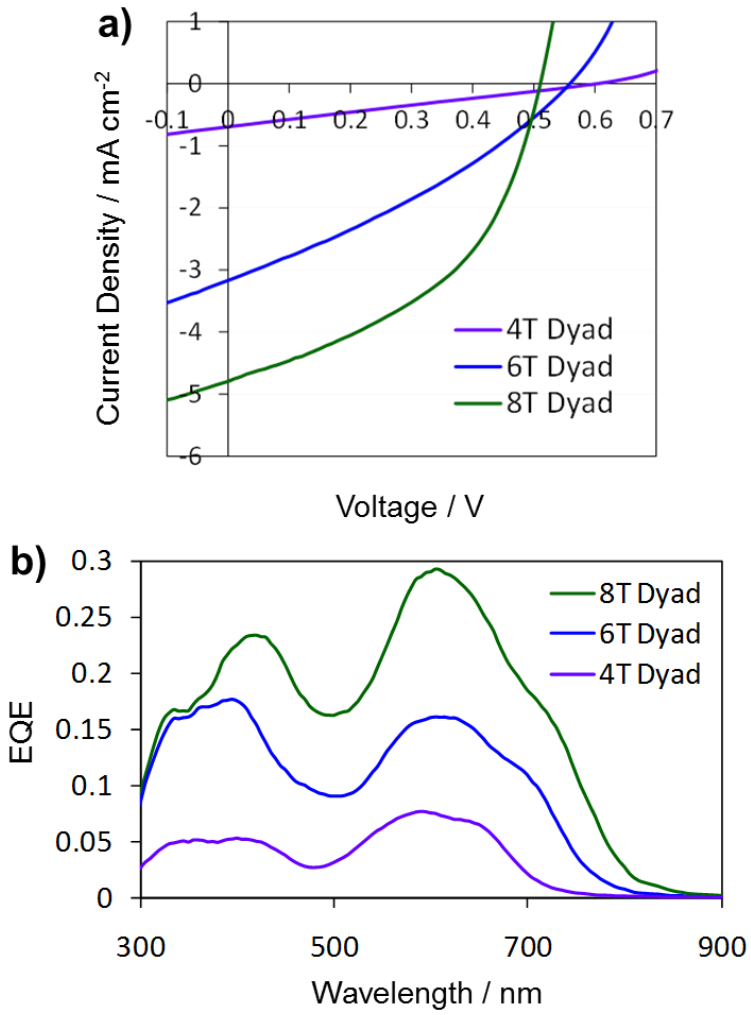

Figure 4.3. (a) EQE spectra of the dyad devices. (b) *J-V* curves of the dyad devices.

In the external quantum efficiency (EQE) spectra shown in Figure 4.3 (b), photocurrent response at longer wavelengths can be seen, owing to the low band gap properties, which led to high J_{SC}. Especially in the 8T dyad device, the photocurrent response was extended to 850 nm. Furthermore, when the number of thiophene units was increased from 4T to 8T, the EQE value increased gradually to their highest values, from 0.08 to 0.27. The increase in J_{SC} induced by the change of the absorption spectra was estimated from the normalized UV-vis spectra and the solar spectrum. The results indicate that the broader absorption of 8T compared with 4T should increase J_{SC} by only about 25%. However, the estimated increase was much smaller than the observed enhancement of J_{SC} under solar illumination for 8T (about 7-fold higher than J_{SC} for 4T). Therefore, the major factor in the improved device performance could be more effective construction of hole transport pathways with a greater number of thiophene units.

Previously, Nishizawa et al. reported two similar molecular designs of dyads based on oligothiophene (OT) and OPV.[9] In comparison with these molecules, the low band gap properties of 4T-8T led to broader absorption and better matching with the solar spectrum, resulting in the increase of J_{SC} from 0.93 in OT to 4.79 mA cm^{-2} in 8T. At the same time, by increasing the number of thiophene units in the DPP dyads, FF was improved to 0.46, which is comparable with that of highly crystalline OPV dyad molecules (0.44). These comparisons indicate the possibility of enhancing both the light absorption properties and the charge transport properties of dyads through careful molecular design.

Atomic force microscopy (AFM) images of the device surfaces revealed that all the dyad films have featureless flat surfaces (see SI). Therefore, no large-scale segregation occurs in the films, reflecting the fact that the donor and acceptor are covalently attached to each other.

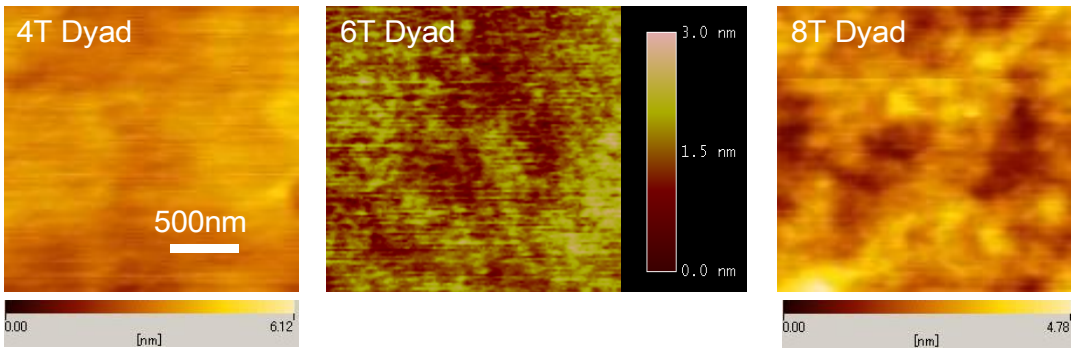

Figure 4.4. AFM images.

4.4. Conclusion

In summary, the introduction of a low band gap donor part into the dyad molecule improved the light-harvesting ability. The length of the oligothiophene greatly affected charge transport in the dyad-based solar cells. The performance should be improved by introduction of a larger hole transport part, and this study demonstrates the high potential of donor–acceptor dyads as photovoltaic materials. Further optimization of energy levels could enable realization of higher V_{OC} and J_{SC},[2, 12] and highly efficient solar cells based on a single component.

Chapter 4 is reproduced by permission of The Royal Society of Chemistry.
S. Izawa, K. Hashimoto, and K. Tajima, *Chem. Commun.*, **2011**, *47*, 6365-6367.

References

1. (a) Gunes, S.; Neugebauer, H.; Sariciftci, N. S., Conjugated polymer-based organic solar cells. *Chemical Reviews* **2007,** *107* (4), 1324-1338; (b) Brabec, C. J.; Gowrisanker, S.; Halls, J. J. M.; Laird, D.; Jia, S. J.; Williams, S. P., Polymer-Fullerene Bulk-Heterojunction Solar Cells. *Advanced Materials* **2010,** *22* (34), 3839-3856.

2. Chen, H. Y.; Hou, J. H.; Zhang, S. Q.; Liang, Y. Y.; Yang, G. W.; Yang, Y.; Yu, L. P.; Wu, Y.; Li, G., Polymer solar cells with enhanced open-circuit voltage and efficiency. *Nature Photonics* **2009,** *3* (11), 649-653.

3. Yu, G.; Gao, J.; Hummelen, J. C.; Wudl, F.; Heeger, A. J., POLYMER PHOTOVOLTAIC CELLS - ENHANCED EFFICIENCIES VIA A NETWORK OF INTERNAL DONOR-ACCEPTOR HETEROJUNCTIONS. *Science* **1995,** *270* (5243), 1789-1791.

4. (a) Nguyen, L. H.; Hoppe, H.; Erb, T.; Gunes, S.; Gobsch, G.; Sariciftci, N. S., Effects of annealing on the nanomorphology and performance of poly(alkylthiophene): fullerene bulk-heterojunction solar cells. *Advanced Functional Materials* **2007,** *17* (7), 1071-1078; (b) Yang, X. N.; van Duren, J. K. J.; Rispens, M. T.; Hummelen, J. C.; Janssen, R. A. J.; Michels, M. A. J.; Loos, J., Crystalline organization of a methanofullerene as used for plastic solar-cell applications. *Advanced Materials* **2004,** *16* (9-10), 802-806; (c) Chirvase, D.; Parisi, J.; Hummelen, J. C.; Dyakonov, V., Influence of nanomorphology on the photovoltaic action of polymer-fullerene composites. *Nanotechnology* **2004,** *15* (9), 1317-1323.

5. (a) Maggini, M.; Possamai, G.; Menna, E.; Scorrano, G.; Camaioni, N.; Ridolfi, G.; Casalbore-Miceli, G.; Franco, L.; Ruzzi, M.; Corvaja, C., Solar cells based on a fullerene-azothiophene dyad. *Chemical Communications* **2002,** (18), 2028-2029; (b) Nishizawa, T.; Tajima, K.; Hashimoto, K., Supramolecular formation of fibrous nanostructure in donor-acceptor dyad Mint. *Journal of Materials Chemistry* **2007,** *17* (23), 2440-2445; (c) Nishizawa, T.; Lim, H. K.; Tajima, K.; Hashimoto, K., Efficient dyad-based organic solar cells with a highly crystalline donor group. *Chemical Communications* **2009,** (18), 2469-2471; (d) Bu, L. J.; Guo, X. Y.; Yu, B.; Qu, Y.; Xie, Z. Y.; Yan, D. H.; Geng, Y. H.; Wang, F. S., Monodisperse Co-oligomer Approach toward Nanostructured Films with Alternating Donor-Acceptor Lamellae. *Journal of the American Chemical Society* **2009,** *131* (37), 13242-13243.

6. Walker, B.; Tomayo, A. B.; Dang, X. D.; Zalar, P.; Seo, J. H.; Garcia, A.; Tantiwiwat, M.; Nguyen, T. Q., Nanoscale Phase Separation and High Photovoltaic Efficiency in Solution-Processed, Small-Molecule Bulk Heterojunction Solar Cells. *Advanced Functional Materials* **2009,** *19* (19), 3063-3069.

7. Nishizawa, T.; Tajima, K.; Hashimoto, K., The effect of crystallinity in donor groups on the performance of photovoltaic devices based on an oligothiophene-fullerene dyad.

Nanotechnology **2008,** *19* (42), 424017-424024.

8. (a) Iqbal, A.; Jost, M.; Kirchmayr, R.; Pfenninger, J.; Rochat, A.; Wallquist, O., THE SYNTHESIS AND PROPERTIES OF 1,4-DIKETO-PYRROLO 3,4-C PYRROLES. *Bulletin Des Societes Chimiques Belges* **1988,** *97* (8-9), 615-643; (b) Hao, Z. M.; Iqbal, A., Some aspects of organic pigments. *Chemical Society Reviews* **1997,** *26* (3), 203-213.

9. (a) Bijleveld, J. C.; Gevaerts, V. S.; Di Nuzzo, D.; Turbiez, M.; Mathijssen, S. G. J.; de Leeuw, D. M.; Wienk, M. M.; Janssen, R. A. J., Efficient Solar Cells Based on an Easily Accessible Diketopyrrolopyrrole Polymer. *Advanced Materials* **2010,** *22* (35), E242-E246; (b) Zhou, E. J.; Nakamura, M.; Nishizawa, T.; Zhang, Y.; Wei, Q. S.; Tajima, K.; Yang, C. H.; Hashimoto, K., Synthesis and Photovoltaic Properties of a Novel Low Band Gap Polymer Based on N-Substituted Dithieno 3,2-b:2 ',3 '-d pyrrole. *Macromolecules* **2008,** *41* (22), 8302-8305; (c) Zhou, E. J.; Yamakawa, S. P.; Tajima, K.; Yang, C. H.; Hashimoto, K., Synthesis and Photovoltaic Properties of Diketopyrrolopyrrole-Based Donor-Acceptor Copolymers. *Chemistry of Materials* **2009,** *21* (17), 4055-4061; (d) Tamayo, A. B.; Tantiwiwat, M.; Walker, B.; Nguyen, T. Q., Design, synthesis, and self-assembly of oligothiophene derivatives with a diketopyrrolopyrrole core. *Journal of Physical Chemistry C* **2008,** *112* (39), 15543-15552.

10. Carsten, B.; He, F.; Son, H. J.; Xu, T.; Yu, L., Stille Polycondensation for Synthesis of Functional Materials. *Chemical Reviews* **2011**, null-null.

11. The devices with 4T shorted when annealed at 110 ºC.

12. Park, S. H.; Roy, A.; Beaupre, S.; Cho, S.; Coates, N.; Moon, J. S.; Moses, D.; Leclerc, M.; Lee, K.; Heeger, A. J., Bulk heterojunction solar cells with internal quantum efficiency approaching 100%. *Nature Photonics* **2009,** *3* (5), 297-303.

13. Avcibasi, N.; Smet, M.; Metten, B.; Dehaen, W.; De Schryver; F. C., Bultynck, G.; Callewaert, G.; De Smedt, H.; Missiaen, L. and Boens N., *International Journal of Photoenergy*, **2004,** *6*, 159-167.

14. Wada, H.; Taguchi, T.; Goto, M.; Kambayashi, T.; Mori, T.; Ishikawa K. and Takezoe H., *Chemistry Letters*, **2006,** *35*, 280-281.

15. Hummelen, J. C.: Knight, B. W.; Lepeq, F.; Wudl, F.; Yao, J. and Wilkins, C. L., *Journal of Organic Chemistry*, **1995,** *60*, 532-538.

Chapter 5.

Synthesis, Characterization, and Photovoltaic Properties of Diketopyrrolopyrrole-oligothiophene /Fullerene Dyads

5.1. Introduction

Organic solar cells (OSCs) have recently drawn much attention as a sustainable energy source, because their solution-based fabrication allows for potential advantages such as low cost, light weight, flexibility, and large area device.[1] In the earlier stage of OSC development, bilayer structures of electron donor and acceptor materials were used.[2] However, owing to the small exciton diffusion length of organic films, photocurrent is generated only from incident photons absorbed close to the material interface.[3] A mixed bulk heterojunction (BHJ) was developed to solve this problem by mixing the donor and acceptor in the active layer to increase the area of the material interface.[4] Currently, the most efficient OSCs relying on the mixed BHJ structure have achieved power conversion efficiencies (PCEs) of over 8%.[5] However, it is difficult to precisely control the film morphology that is suitable for charge generation and transport on the nanoscale simply by mixing, since nanostructures are sensitive to many factors such as mixing ratio, the types of organic solvent and additive used, spin coating speed, and thermal annealing conditions.[6] Moreover, mixed films often suffer from morphological changes during operation, which could result in low stability.[7] To solve these problems, the control of nanostructures in organic films by molecular design is an important research topic.[7-8]

The use of dyad molecules, in which the electron donor and acceptor are covalently attached to each other, is a promising strategy for controlling film morphology because the distance between the donor and the acceptor is fixed and strong phase segregation can, in principle, be prevented. Therefore, an increase in the area of the interface of the donor and acceptor in the active layer could lead to efficient charge separation and higher photocurrent in OSCs, in addition to stable morphology.[8b-d] Many groups have reported the synthesis of dyad molecules and their application in OSCs.[8b-d, 9] Their reports provided basic knowledge from spectroscopic analysis; however, the reported PCEs of OSCs based on dyads were lower than 0.4%. This could be attributed mainly to poor charge transport ability, since a low fill factor (FF) is often the main reason for the poor OSC

performance of dyad devices.[10] To solve this problem, Nishizawa et al. reported on the use of highly crystalline oligo(*p*-phenylenevinylene) dyad molecules, which induce moderate segregation of the donor and acceptor parts and thus create charge transport pathways. The devices based on oligo(*p*-phenylenevinylene)-fullerene dyads showed a relatively high FF of 0.44 and a PCE of 1.28%.[11] More recently, the author have also demonstrated that the size of the donor part is a critical parameter for increasing FF because it is related to the connectivity of charge transport pathways. The author has introduced the use of diketopyrrolopyrrole (DPP)-oligothiophene dyad molecules with various numbers of thiophenes in Chapter 4. By increasing the number of thiophenes from 4 to 8, FF increases from 0.25 to 0.46. Furthermore, DPP derivatives absorb a larger photon fraction because of better matching with the solar spectrum, which leads to the highest short-circuit current density (J_{SC}) of 4.7 mA cm^{-2}.[12]

As for the design of the active materials in OSCs, device performance is sensitive to the length of alkyl side chains because they largely affect the solubility and packing state of the film, resulting in differences in the intermolecular interaction and charge transport ability.[13] In addition, so-called donor-acceptor-type low-band-gap materials have absorption valleys in the middle range in the visible region.[14] To compensate for this nature, [6,6]-phenyl-C_{71}-butyric acid methyl ester ($PC_{70}BM$) is often used as the acceptor with low-band-gap donor materials because C_{70} fullerene absorbs light in the visible region.[15] Considering the above situations in OSCs, the author report here the synthesis of a series of low-band-gap dyad molecules based on DPP-hexathiophene derivatives reported previously to explore the optimum dyad structure for OSCs (Figure 5.1).[12] The author also introduced C_{70} fullerene as the acceptor group in the dyads to enhance absorption in the visible region and to investigate its effect on charge generation ability.

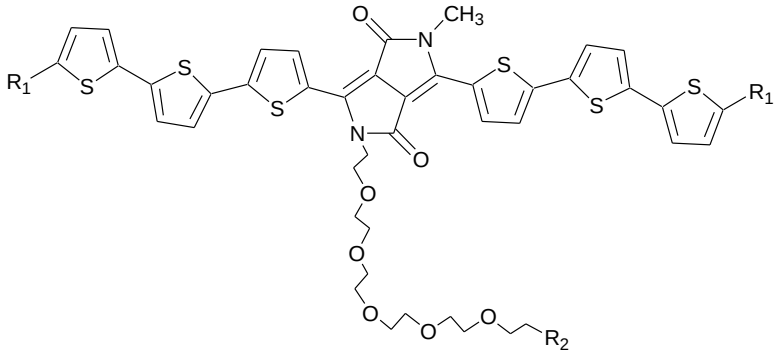

1 : R_1 = n-C_6H_{13}, R_2 = OH
2 : R_1 = CH_3, R_2 = OH
3 : R_1 = n-C_6H_{13}, R_2 =
4 : R_1 = CH_3, R_2 =
5 : R_1 = CH_3, R_2 =

Figure 5.1. Chemical structures of the donor and dyad molecules.

5.2. Experimental

Materials and instruments

All chemicals were purchased from Sigma-Aldrich, Tokyo Kasei Kogyo, or Wako Chemicals and used without further purification. ^{1}H NMR spectra were measured in $CDCl_3$ containing 1% v/v TMS on an Oxford superconducting magnet system (500 MHz). Matrix-assisted laser desorption/ionization/time-of-flight (MALDI-TOF) MS profiles were measured with dithranol as the matrix on an Applied Biosystems Bio Spectrometry Workstation spectrometer (Voyager-DE STR). High-performance liquid chromatography was carried out on a system with a CBM-20A controller (Shimadzu), an LC-6AD pump (Shimadzu), an SPD-20A UV-vis detector, and a Luna silica column (particle size: 5 μm; column length: 250 mm; and inner diameter: 21.2 mm; Phenomenex).

Syntheses

The synthetic route to dyads **4** and **5** is shown in Scheme 5.1. The details of the synthetic procedures and the spectral data from ^{1}H-NMR spectroscopy and MALDI-TOF-MS are described below. In MALDI-TOF-MS of the donor and dyads, the mass of adducts with Na^+ was sometimes observed. 3,6-Bis(5-bromothiophene-2-yl)-2-methyl-5-(3,6,9,12,15-pentaoxaheptadecane-18-ol)- pyrrolo[3,4-*c*]pyrrole-1,4-dione (**S3**),[24] [6,6]-phenyl-C_{61}-butyric acid (**S4**)[36] were synthesized according to procedures in the literature.

5-Methyl-[2,2']-bithiophene (S1)

2-Bromothiophene (683 μL, 7.04 mmol), 5-methyl-thiophene-2-boronic acid (1.00 g, 7.04 mmol), K_2CO_3 (2.91 g, 21.1 mmol), toluene (30 mL), THF (30 mL), and water (10 mL) were added into a 100 mL two-neck round-bottom flask under N_2. The solution was degassed for 30 min and tetrakis(triphenylphosphine)palladium(0) (81.3 mg, 0.0704 mmol) was added. The reaction mixture was refluxed at 110 °C for 24 h. The solution was cooled to room temperature, and the mixture was extracted with ether and purified by column chromatography using silica gel and hexane as eluent. The solvent was removed in vacuo, yielding a colorless transparent liquid (233 mg, 18%).

^{1}H NMR ($CDCl_3$, 500 MHz): δ (ppm): 7.15-7.16 (dd, 1H), 7.08-7.09 (dd, 1H), 6.96-6.99 (m, 2H), 6.65-6.66 (m, 1H), 2.46 (s, 3H)

5-Tributylstannyl-5'-methyl-[2,2']-bithiophene (S2)

5-Methyl-[2,2']-bithiophene (233 mg, 1.29 mmol) and anhydrous THF (6 mL) were added into a 100 mL two-neck round-bottom flask under N_2 and stirred for 10 min at 0 °C. Then *n*-

butyllithium hexane solution (1.64 M, 865 μL, 1.42 mmol) was added, and the reaction mixture was stirred for 30 min at 0 °C. Tributyltin chloride (384 μL, 1.42 mmol) was added and the reaction mixture was stirred for 2 h at room temperature. Water was added to quench the reaction. The mixture was extracted with ether and purified by column chromatography using alumina and hexane with triethylamine (5%) as eluent. The solvent was removed in vacuo, yielding a colorless transparent liquid (450 mg, 73%).

^{1}H NMR ($CDCl_3$, 500 MHz): δ (ppm): 7.20-7.21 (d, 1H), 7.03-7.04 (d, 1H), 6.95-6.96 (d, 1H), 6.64-6.65 (d, 1H), 2.47 (s, 3H), 1.54-1.60 (m, 6H), 1.32-1.37 (m, 6H), 1.09-1.12 (t, 6H), 0.89-0.92 (t, 9H)

3,6-Bis-(5''-methyl-[5,2';5',2'']terthiophene-2-yl)-2-methyl-5-(3,6,9,12,15-pentaoxaheptadecane-18-ol)-pyrrolo[3,4-c]pyrrole-1,4-dione (2)

S3 (92 mg, 0.125 mmol), **S2** (180 mg, 0.375 mmol), and anhydrous toluene (10 mL) were added into a 50 mL two-neck round-bottom flask under N_2. The solution was degassed for 30 min and tetrakis(triphenylphosphine)palladium(0) (10 mg, 0.013 mmol) was added. The reaction mixture was refluxed at 110 °C for 24 h and then purified by column chromatography using silica gel and $CHCl_3$/methanol (4:1) as eluent and by HPLC using $CHCl_3$/methanol (100:1) as eluent. The solvent was removed in vacuo, yielding a blue-purple solid. (55 mg, 47%)

^{1}H NMR ($CDCl_3$, 500 MHz): δ (ppm): 8.85-8.86 (d, 1H), 8.78-8.879 (d, 1H), 7.21-7.22 (m, 1H), 7.14-7.20 (m, 3H), 6.94-6.99 (m, 4H), 6.64-6.66 (m, 2H), 4.29-4.31 (m, 2H), 3.80-3.82 (m, 2H), 3.58-3.82 (m, 23H), 2.47 (s, 6H). MALDI-TOF-MS (*m/z*): 957.07 (M^+)

[6,6]-Phenyl-C_{71}-butyric acid (S6)

[6,6]-Phenyl-C_{71}-butyric acid methyl ester (500 mg, 0.485 mmol), toluene (87.5 mL), acetic acid (75 mL), and HCl (12 M, 30 mL) were added into a 300 mL round-bottom flask. The reaction mixture was stirred for 72 h at 90 °C. All the solvent was distilled out. The solid was successively washed with water, methanol, acetone, chlorobenzene, $CHCl_3$, and hexane, yielding a black-brown solid (338 mg, 69%).

^{1}H NMR (CS_2, $CDCl_3$, 500 MHz): δ (ppm): 7.83-7.85 (d, 2H), 7.45-7.48 (m, 2H), 7.37-7.40 (m, 1H), 2.37-2.47 (m, 4H), 2.01-2.18 (m, 2H)

General synthesis of 4 and 5

S4 (340 mg, 0.380 mmol) or **S5** (386 mg, 0.380 mmol) was added into a 100 mL two-neck round-bottom flask under N_2, then distilled CS_2 (100 mL) and thionyl chloride (1.64 mL, 22.8 mmol) were added. The reaction mixture was refluxed overnight at 55 °C. The solvent was removed, and the crude product was dried at 80 °C for 3 h, then anhydrous chlorobenzene (20

mL) and NaH (oil dispersion 50–72%, 41.5 mg), which had been washed with hexane, were added. The flask was covered with aluminum foil, and **2** (178 mg, 0.190 mmol) was added. The reaction mixture was stirred at room temperature for 48 h and then purified by column chromatography using silica gel and $CHCl_3$ as eluent and by HPLC using $CHCl_3$ as eluent. The obtained product was reprecipitated in hexane and filtered, yielding a blue solid.

Compound 4: 3,6-Bis-(5''-methyl-[5,2';5',2'']terthiophene-2-yl)-2-methyl-5-(3,6,9,12,15,18-hexaoxa-19-carbonyl-23-phenyl[6.6]C_{61}-tricosane)-pyrrolo[3,4-c]pyrrole-1,4-dione (yield: 26%)

^{1}H NMR ($CDCl_3$, 500 MHz): δ (ppm): 8.87-8.88 (d, 1H), 8.80-8.81 (d, 1H), 7.89-7.90 (d, 2H), 7.50-7.53 (m, 2H), 7.45-7.51 (m, 1H), 7.24-7.25 (d, 1H), 7.22-7.23 (d, 1H), 7.19-7.20 (d, 2H), 6.99-7.01 (m, 4H), 6.67-6.68 (m, 2H), 4.28-4.29 (m, 2H), 4.21-4.22 (m, 2H), 3.79-3.80 (m, 2H), 3.58-3.67 (m, 21H), 2.87-2.89 (m, 2H), 2.52-2.53 (m, 2H), 2.51 (s, 6H), 2.13-2.15 (m, 2H). MALDI-TOF-MS (*m/z*): 1813.85 (M^+)

Compound 5: 3,6-Bis-(5''-methyl-[5,2';5',2'']terthiophene-2-yl)-2-methyl-5-(3,6,9,12,15,18-hexaoxa-19-carbonyl-23-phenyl[6.6]C_{71}-tricosane)-pyrrolo[3,4-c]pyrrole-1,4-dione (yield: 13%)

^{1}H NMR ($CDCl_3$, 500 MHz): δ (ppm): 8.87-8.88 (d, 1H), 8.80-8.81 (d, 1H), 7.89-7.90 (m, 2H), 7.49-7.55 (m, 2H), 7.39-7.45 (m, 1H), 7.30-7.31 (d, 1H), 7.23-7.27(m, 3H), 7.01-7.04 (m, 4H), 6.69-6.70 (m, 2H), 4.28-4.29 (m, 2H), 4.21-4.22 (m, 2H), 3.79-3.80 (m, 2H), 3.58-3.67 (m, 21H), 2.50 (s, 6H), 2.46-2.49 (m, 2H), 2.36-2.43 (m, 2H), 2.05-2.20 (m, 2H). MALDI-TOF-MS (*m/z*): 1935.89 (M^+)

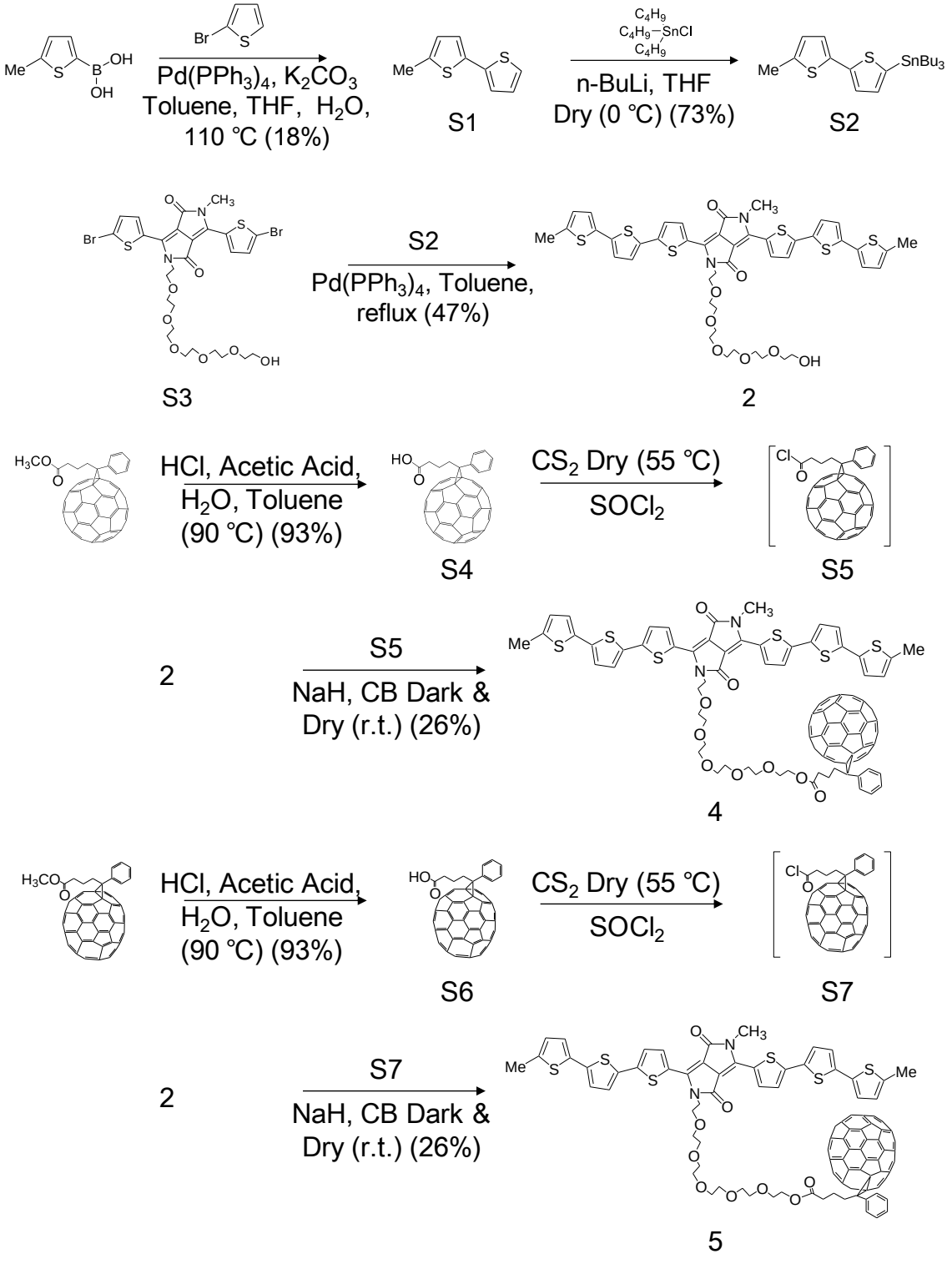

Scheme 5.1. Synthesis route to dyads **4** and **5**.

Measurements

UV-vis absorption spectra were measured on a V-670 spectrometer (Jasco). Fluorescence spectra were measured on a F-4500 fluorescence spectrophotometer (Hitachi). Cyclic voltammetry was performed on an HSV-100 automatic polarization system (Hokuto Denko). Anhydrous dichroloform was used as the solvent under N_2, and 0.1 M tetrabutyl ammonium hexafluorophosphate was used as the supporting electrolyte. A glassy carbon rod was used as the working electrode, a Pt wire was used as the counter electrode, and a Ag/AgCl wire was used as the reference electrode. DSC traces were obtained on a Rigaku Thermo plus DSC8230. XRD patterns were measured on a Smart Lab X-ray diffractometer (Rigaku) with a Cu Kα source operated at 20 kV and 10 mA. The film samples were prepared by spin coating from $CHCl_3$ solution with a concentration of 10 mg mL^{-1} on silicon wafers at 2500 rpm. Atomic force microscopy (AFM) images were obtained on a Nanoscope31 (Digital Instruments) operated in tapping mode.

Photovoltaic device preparation and measurement

An indium tin oxide (ITO)-coated glass substrate (sheet resistance: 10 Ω sq^{-1}, Geomatech, Japan) was cleaned by successive ultrasonication in detergent, water, acetone, 2-propanol, and water. After the substrate was dried, PEDOT–PSS (H. C. Stark) was spin-coated (4000 rpm) onto ITO. The film was dried at 150 ºC under N_2 for 20 min. After cooling the substrate, $CHCl_3$ solution of dyads **3**, **4**, or **5** with concentration of 20, 12.5, or 17.5 mg mL^{-1}, respectively, was spin-coated at a spinning rate of 2500 rpm. For the reference OSC device based on a mixed BHJ, the solution was prepared by dissolving 11.0 mg of **1** and 9.3 mg of PCBM (molar ratio of 1: 1) in 1 mL of $CHCl_3$, and the film was fabricated in the same manner. Finally, Al (40 nm) electrodes were deposited by evaporation onto the organic layer under high vacuum (6×10^{-4} Pa). After Al deposition, the devices with **3**, **4** and a mixture of **1** and PCBM were annealed at 110, 80, and 110 ºC, respectively, for 5 min, while that with **5** was not annealed. The *J-V* characteristics of the devices were measured under simulated solar light illumination (AM 1.5, 100 mW cm^{-2}) from a 150 W xenon lamp (PEC-L11, Peccell Technologies, Inc., Japan) with an AM 1.5 filter. Light intensity was calibrated with a standard silicon solar cell (BS520, Bunkoh-Keiki, Japan). The active area of the devices was defined to be 0.06 cm^2 by using a photomask. The external quantum efficiency (EQE) of the devices was measured on a Hypermonolight SM-250F system (Bunkoh-Keiki, Japan).

5.3. Results and discussion

Figure 5.1 shows the chemical structures of the DPP-oligothiophenes with hexaethylene glycol with different alkyl chains (**1**: hexyl and **2**: methyl) and of the dyad molecules based on them and the C_{60} (**3** and **4**) or C_{70} (**5**) group. The author previously reported DPP-oligothiophene/C_{60} dyad molecules with different numbers of thiophenes ranging from 4 to 8 in Chapter 4.[12] In this study, the author fix the number of thiophene rings in the donor part to 6 and changed the alkyl chain length of the donor and acceptor groups to C_{60} and C_{70}, and investigated their effects on OSCs.

Electronic and optical properties in solution state

Absorption spectra in chloroform solutions

Figure 5.2 shows the UV-vis absorption spectra of **1**-**5** in $CHCl_3$ solutions. The difference in the alkyl side chain attached to the DPP-hexathiophene did not cause any difference in the spectra between the donors (**1** and **2**) and the dyad molecules (**3** and **4**). This is because the energy levels of the highest occupied molecular orbitals (HOMOs) and lowest unoccupied molecular orbitals (LUMOs) of **1** and **2** are determined by the structure of the π-conjugated backbone. The optical band gaps of the donor parts were estimated from the absorption edges as 1.77 eV. This lower band gaps than those of hexathiophene have been attributed to intramolecular charge transfer between electron-withdrawing DPP and electron-donating thiophene.[16] The absorption of dyads **3**-**5** was a simple superposition of those of the corresponding donor group and $PC_{60}BM$ for **3** and **4** or $PC_{70}BM$ for **5**.[15] This result indicates that there is little electrical interaction in the ground state between the donor and acceptor parts in the dyads. Dyad **5** showed stronger absorption in the range of 350 to 550 nm than did dyads **3** and **4**, corresponding to the absorption of $PC_{70}BM$ in this region.

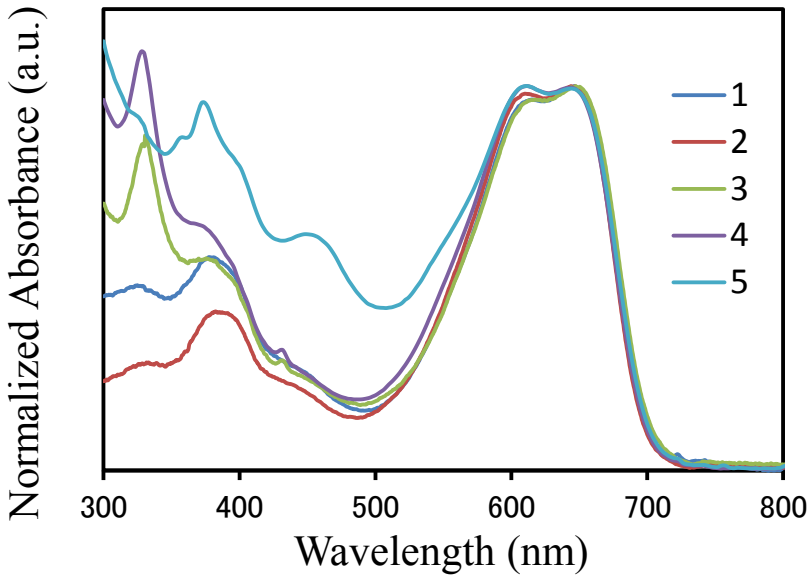

Figure 5.2. Absorption spectra of the donor and dyad molecules in CHCl3.

Fluorescence spectrum in chloroform solutions

The fluorescence spectra of **2**, **4**, and **5** in $CHCl_3$ solutions are shown in Figure 5.3. The solutions had an absorbance of approximately 600 nm at the excitation wavelength and the fluorescence intensity was normalized by the absorbance. Donor **2** showed high fluorescence with a peak maximum at 690 nm. The attachment of either C_{60} (4) or C_{70} (5) to **2** significantly decreased the fluorescence intensity in the solutions. This result indicates that the excited state of the donor parts is quenched by charge transfer from DPP-oligothiophene to the fullerene parts of the dyads. This reflects the proximity of the donor and acceptor to the hexaethylene glycol linker.[17] The fluorescence spectra of **1** and **3** showed similar quenching behavior in the solutions.

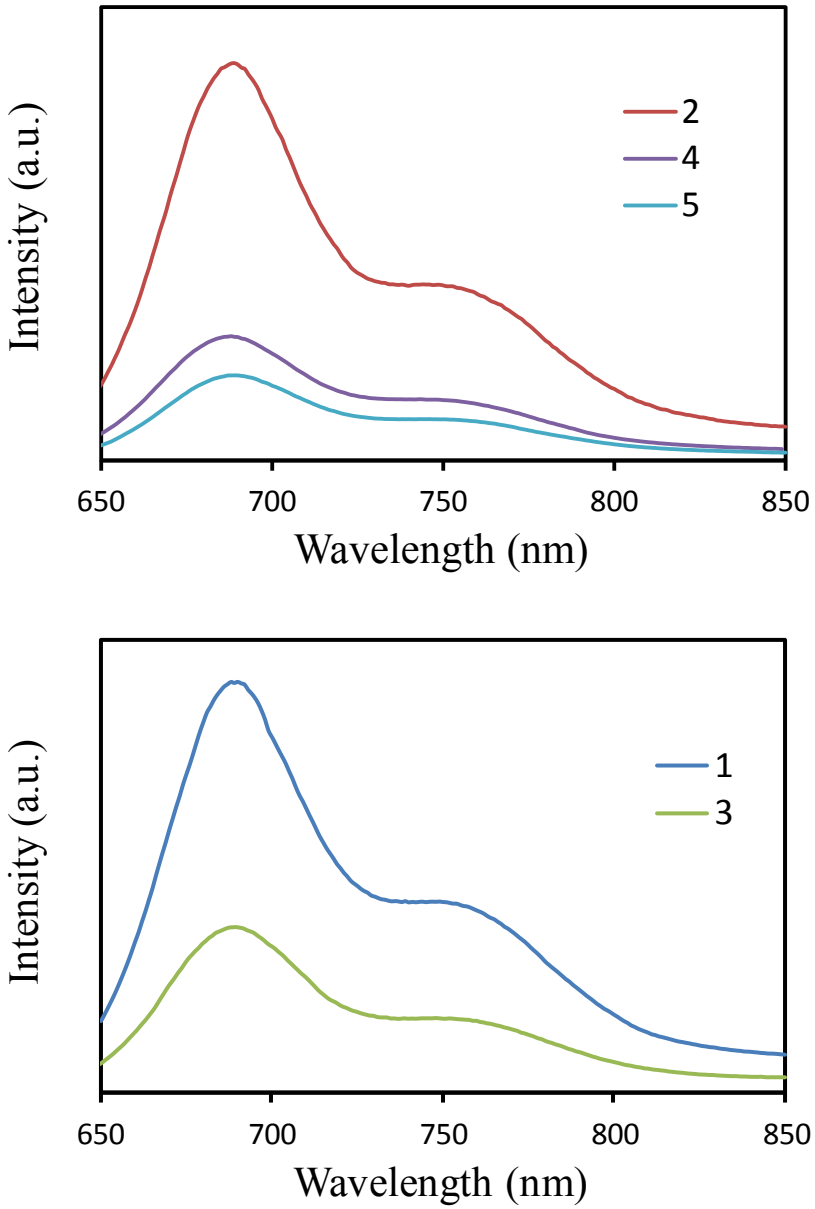

Figure 5.3. Florescence spectra of the donor and dyad molecules in $CHCl_3$.

Cyclic voltammogram

The first oxidation potential (E_{ox}) and the reduction potential (E_{red}) of **1**-**5** relative to the redox potential of Fc/Fc^+ were determined by cyclic voltammetry (CV) in $CHCl_3$. The results are summarized in Table 5.1. The HOMO and LUMO energy levels were estimated by assuming Fc/Fc^+ potential to be −4.8 eV relative to the vacuum level. Donors **1** and **2** with different alky chains showed almost no difference in E_{ox} or E_{red}, because the energy levels of HOMO and LUMO were mainly determined by the structure of the π-conjugated backbone, which coincide with the results of UV-vis absorption spectra in chloroform solution. Dyads **3**-**5** showed E_{ox} values similar

to those of the corresponding donor molecules and E_{red} values similar to those of $PC_{60}BM$ and $PC_{70}BM$. This result indicates that the oxidation of the donor groups and the reduction of the acceptor groups in **3**-**5** were not affected by covalent attachment. The LUMO energy offsets calculated for the E_{red} of the donor parts and the E_{red} of the dyads were around 0.3 eV, which is approximately the value empirically required for efficient charge separation in OSCs.[18]

Table 5.1. Optical and electrochemical properties of the donor, acceptor and dyad molecules.

Material	E_{ox}[a] (V)	E_{red}[a] (V)	E_g[b] (eV)
PCBM	-	-1.16	-
$PC_{70}BM$	-	-1.12	-
1	0.33	-1.47	1.77
2	0.38	-1.43	1.77
3	0.33	-1.14	1.77
4	0.33	-1.16	1.77
5	0.34	-1.10	1.77

[a] Half-potentials determined by cyclic voltammetry *vs.* Fc/Fc^+.

[b] Optical band gaps.

Solid-state properties

Absorption spectra of the films

The absorption spectra of **1**-**5** in the films are shown in Figure 5.4. All the molecules showed redshifts of the absorption band of the donor group in the films compared with those in the solutions (see Figure 5.2). In particular, **2** showed a larger redshift of about 100 nm in edges and higher absorption in the longer-wavelength region (730 nm) than did **1** (Figure 5.4a). This suggested that a stronger π-π interaction could be induced by shorter alkyl side chains, owing to the smaller hindrance of the methyl group in **2** than of hexyl group in **1**.[19] Figure 5.4b showed that the difference between the spectra of **3** and **4** was smaller than that between the spectra of **1** and **2**, indicating that the intermolecular interaction was disturbed by the attachment of the bulky fullerene. However, **4** still showed stronger absorption in the longer-wavelength region (710 nm) than **3**. The absorption edges of dyads **3**-**5** extended to 800 nm owing to the low band gap properties. This could lead to a better absorption match with the solar spectrum. The absorption in the range of 360-570 nm for **5** was stronger than those for the other two dyad molecules because of the stronger visible absorption of C_{70} fullerene. This could cover the weak absorption of the donor part in the valley region in OSCs.

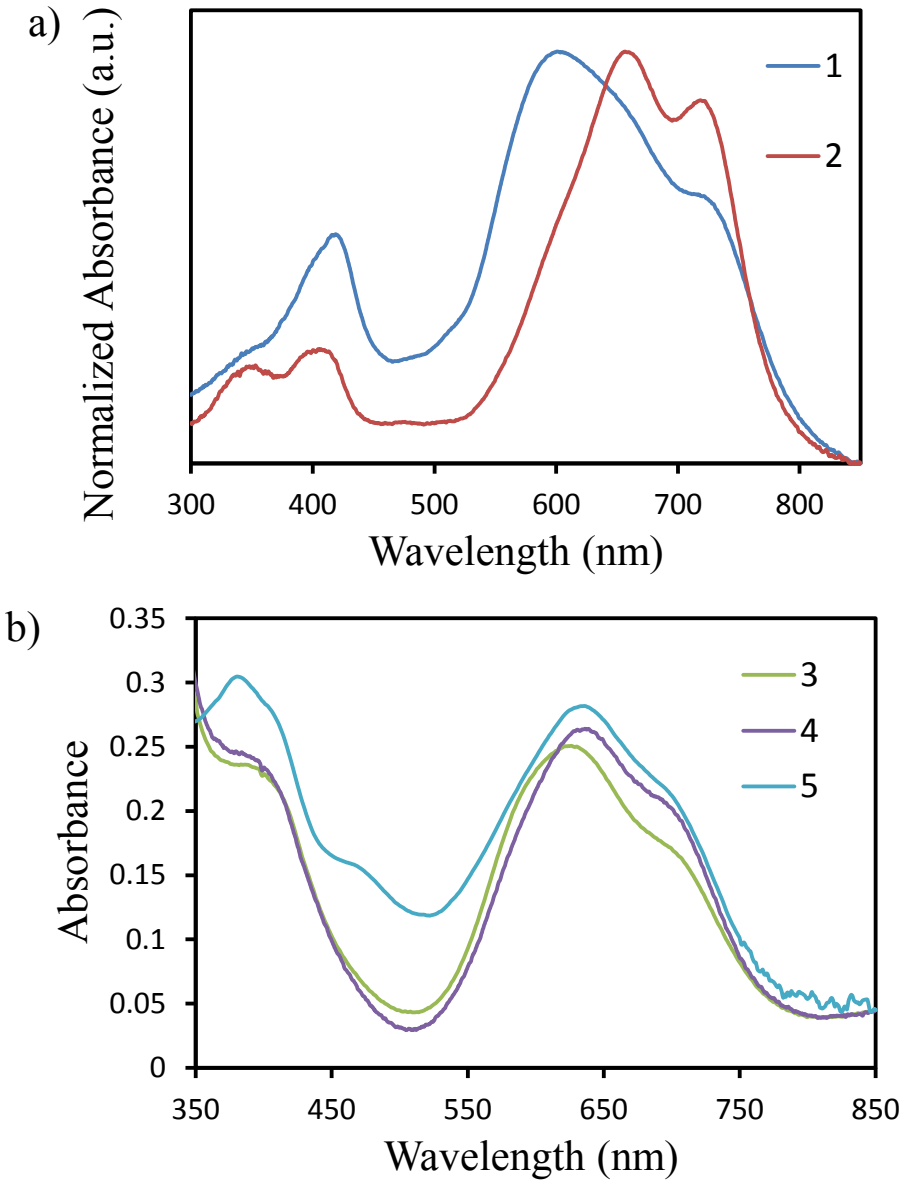

Figure 5.4. Absorption spectra of (a) 1 and 2, and (b) 3, 4, and 5 in thin films.

Thermal properties

The differential scanning calorimetry (DSC) patterns of **1** and **2** were measured at a scan rate of 10 °C min^{-1}. As shown in Figure 5.5, donor **1** showed an exothermic peak at 130 °C, endothermic peaks at 160 °C and 190 °C upon heating, and exothermic peaks at 190 °C and 130 °C upon cooling. Donor **2** showed endothermic peaks at 190 °C and 200 °C upon heating, and exothermic peaks at 190 °C and 180 ºC upon cooling (Figure 5.5b). There was a mesophase existing in both donor molecules, and the crystallization points were 130 °C and 180 °C for **1** and **2**, respectively. **2** showed a higher crystallization point than did **1**, which indicates that **2** had stronger

intermolecular interaction due to its shorter alkyl chain in comparison with **1**. No obvious peaks were observed in dyad molecules **3**-**5** in the DSC measurements (not shown). This result indicates that the strong interaction between fullerene groups suppresses the intermolecular π-π interaction of donor groups in dyad molecules and reduces the crystallinity of dyad molecules. This phenomenon was also observed in the oligothiophene dyad;[10] however, the OPV dyad showed clear crystallization and melting peaks due to the higher crystallinity of the OPV.[11]

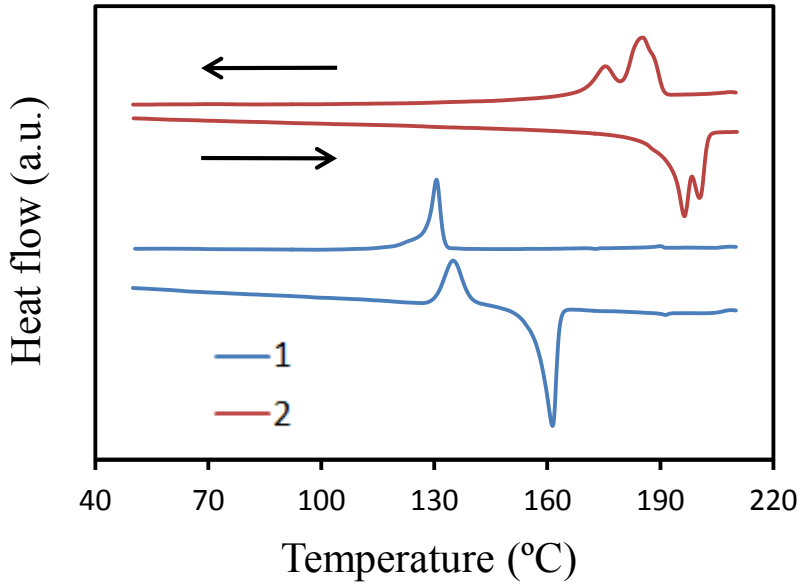

Figure 5.5. Differential scanning calorimetry patterns of 1 and 2.

XRD patterns of thin films

In-plane X-ray diffraction patterns were measured in thin films of **1**-**5** on silicon substrates. Figure 5.6 shows that the thin film of **2** showed clear peaks of π-π stacking at approximately 2θ = 25° (*d*-spacing of 0.36 nm).[20] On the other hand, donor **1** showed no clear peaks. This result indicated that **2**, because of its shorter alkyl chain, had a stronger π-π interaction than did **1**. The films of dyads **3**-**5** did not show any clear peaks. These results suggest that the fullerene groups disturbed the π-π stacking of the donor groups. Out-of-plane X-ray analysis of all the films did not give any obvious peaks.

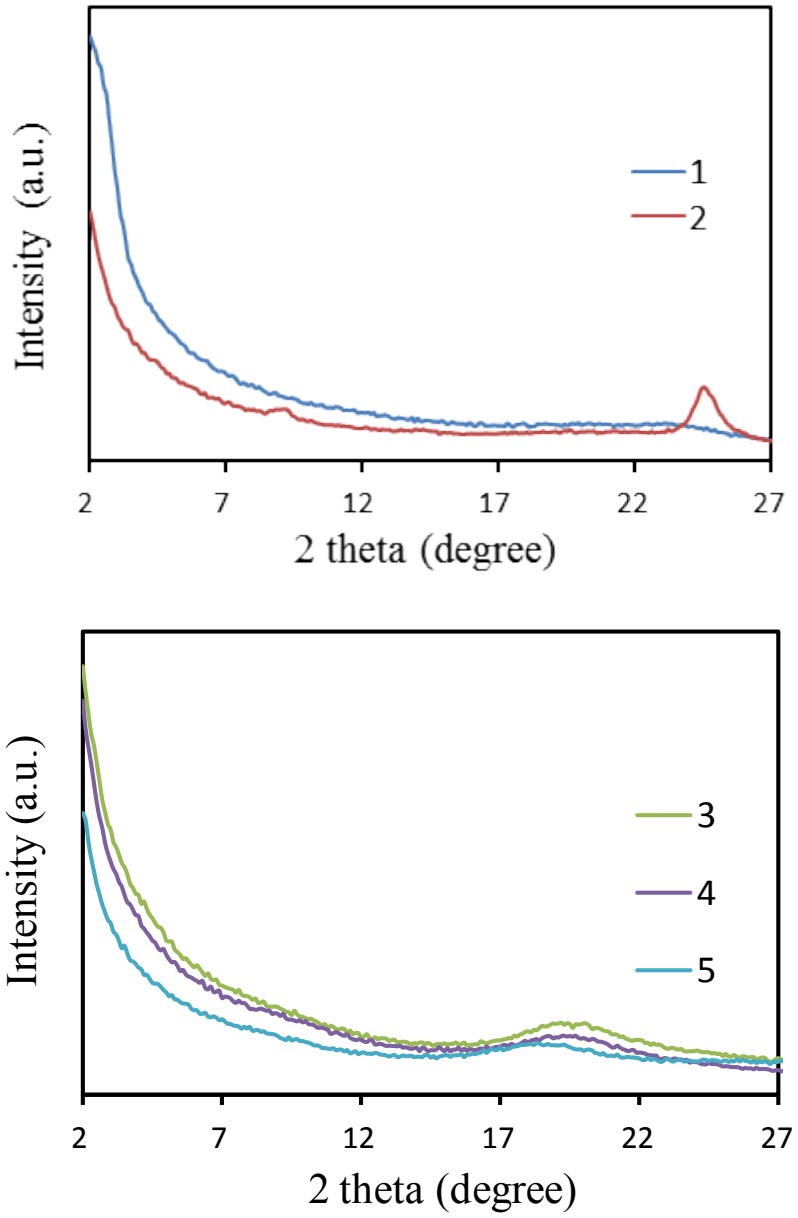

Figure 5.6. In-plane X-ray diffraction patterns of films.

Photovoltaic properties

OSCs were fabricated by using dyads **3**-**5** as the active layers. All the performance data of the devices are summarized in Table 5.2. The *J*–*V* curves of the devices and the EQE spectra are shown in Figure 5.7. The device based on dyad **3** after thermal annealing at 110 °C showed J_{SC} = 3.2 mA cm^{-2}, V_{OC} = 0.56 V, FF = 0.32, and PCE = 0.56%. As shown in Figure 5.7b, the device based on **3** had photocurrent response extended to 800 nm. This led to better matching to the maximum solar spectrum, leading to a photocurrent of 3.2 mA cm^{-2}. For reference, bulk heterojunction devices were fabricated by using a mixture of **1** and $PC_{60}BM$; their *J*–*V* curves and EQE spectra are shown in Figure 5.8. The devices showed poor performance: J_{SC} = 0.48 mA cm^{-2}, V_{OC} = 0.36 V, FF = 0.31, PCE = 0.054%, and maximum EQE value was about 0.023 at 330 nm. AFM images of the mixture films in Figure 5.9 showed large aggregations of the donor and acceptor molecules with a size of over 100 nm. This causes a decrease in the area of the interface of the donor and acceptor, and hence a decrease in photocurrent.[6c, 9b] This tendency coincides with the previous report on the oligothiophene/fullerene mixed BHJ.[9b] The difference in OSC performance between the dyad and the mixture indicates that the covalent attachment of the donor and acceptor suppresses phase separation and enhances charge separation ability.

Table 5.2. Summary of device performance.

Material	J_{SC} (mA cm^{-2})	V_{OC} (V)	FF	PCE (%)
3	3.2	0.56	0.32	0.56
1 / PCBM	0.48	0.36	0.31	0.054
4	3.8	0.59	0.32	0.72
5	4.5	0.57	0.33	0.84

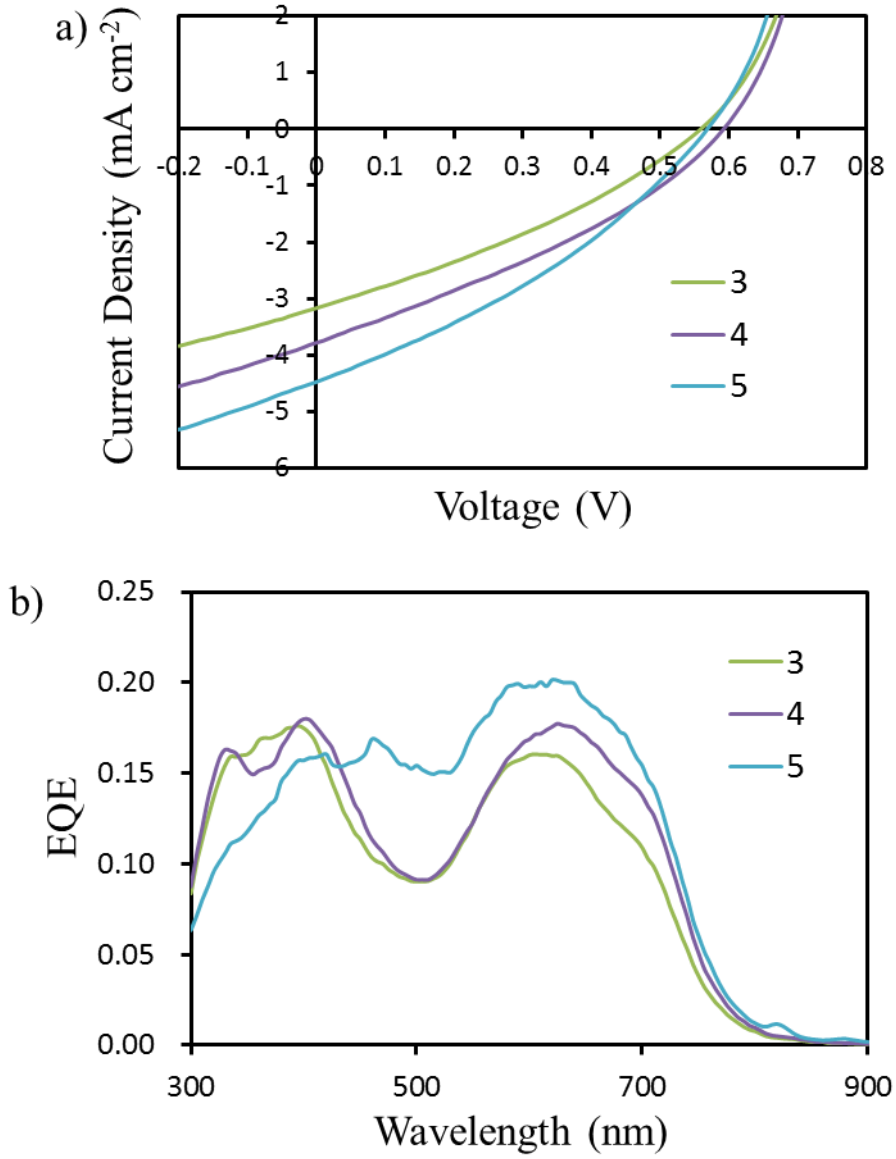

Figure 5.7. (a) Current-voltage curves under simulated solar light illumination and (b) EQE spectra of the devices based on the dyads.

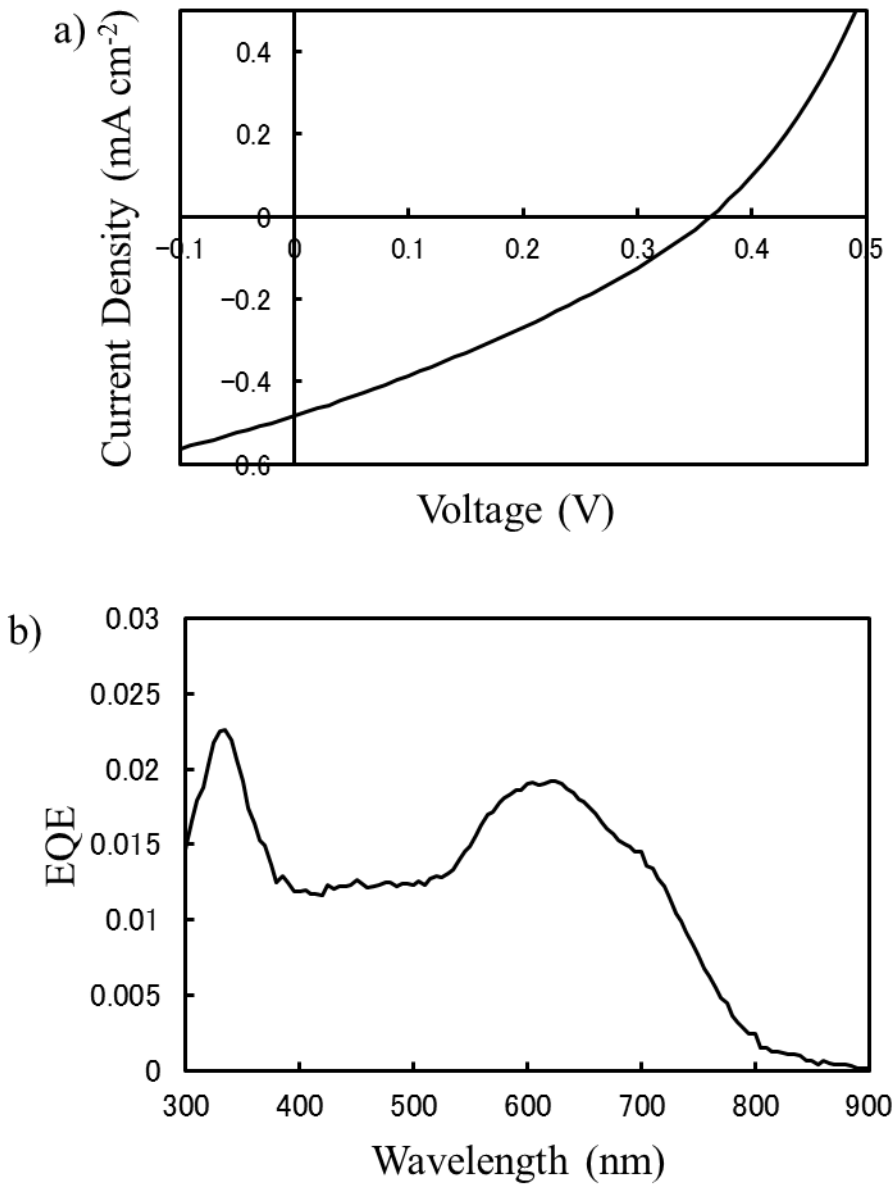

Figure 5.8. (a) *J-V* curves and (b) EQE spectra of the mixed bulk heterojunction devices.

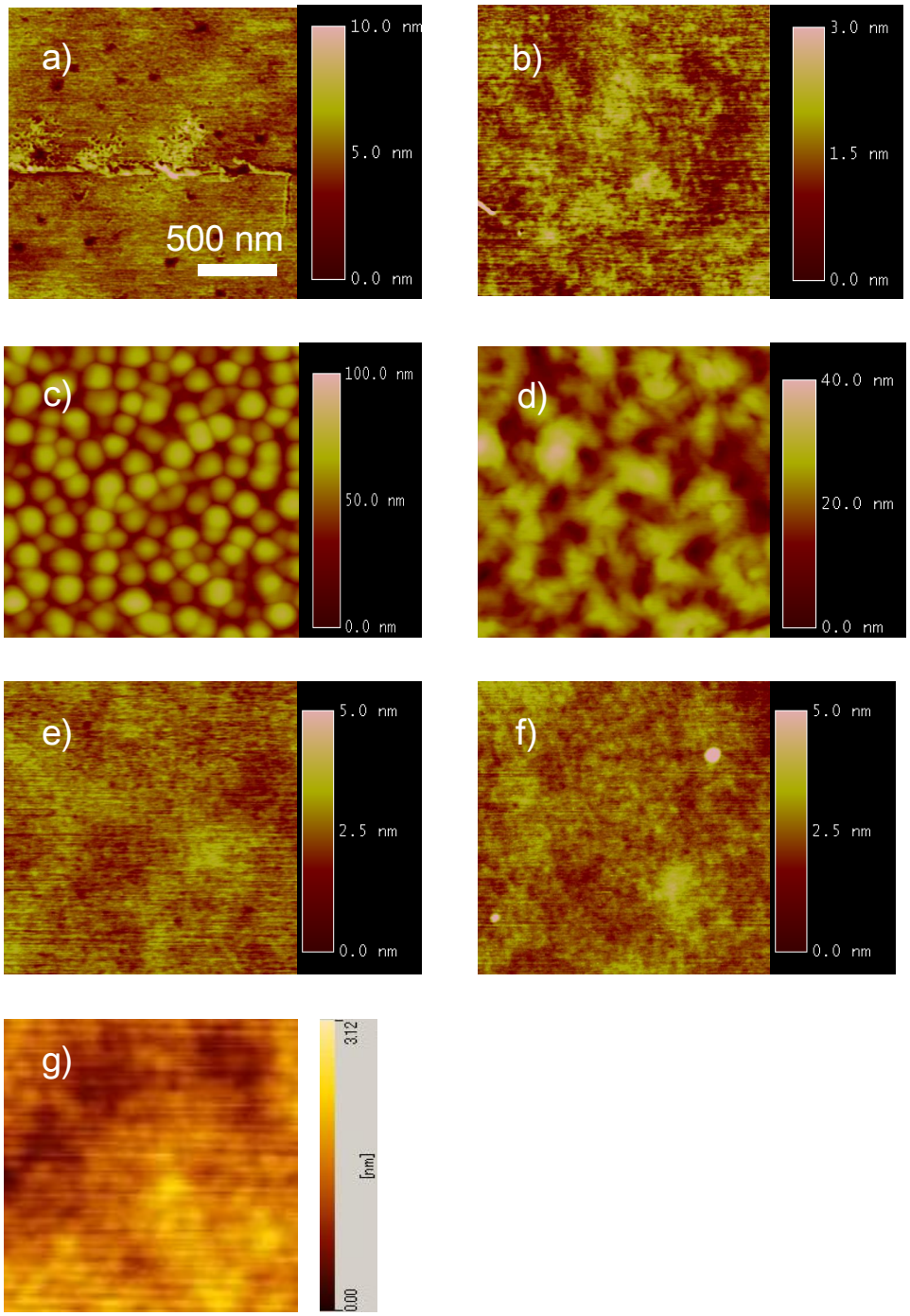

Figure 5.9. AFM height images of (a) as-cast and (b) annealed (110 °C, 5 min) films of dyad **3**, (c) as-cast and (d) annealed (110 °C, 5 min) films of the mixture of **1** and PCBM, (e) as-cast and (f) annealed (80 °C, 5 min) films of dyad **4**, and (g) as-cast film of dyad **5**.

In the devices based on dyad **4** with the methyl group, EQE spectra became redshifted and the EQE value increased; therefore, J_{SC} increased from 3.2 mA cm^{-2} to 3.8 mA cm^{-2} compared with that for the devices based on **3** with the hexyl group. Although J_{SC} increased by 19%, the increase

in current expected from the absorption spectra in Figure 5.4b and the solar spectra was only about 2%. This result suggests that the J_{SC} increase is attributed not only to the stronger absorption of the film but also to the improvement in the internal quantum efficiency of dyad **4**. Our previous study of OPV dyad molecules suggested that the highly crystalline donor part plays an important role in enhancing charge transport.[11] Owing to its shorter alkyl chains, the donor 2 showed a stronger π-π interaction than donor **1** as shown by the absorption spectra, and DSC and XRD patterns. These data indicate that a stronger π-π interaction of donor parts in dyad **4** with the methy group results in an efficient connection of the hole transport pathway, and therefore in an increase in photocurrent. However, the crystallinity of the dyad still seems low, since dyad **4** did not show clear peaks in the DSC pattern or π-π interaction in the XRD pattern, unlike the OPV-dyad in a previous report. This caused a low FF of 0.32 and an EQE value of 0.18. The introduction of more highly crystalline donor parts could improve FF and J_{SC} further.

As shown in Figure 5.7b, the EQE spectrum of the device based on dyad **5** was improved over those of the devices based on **3** and **4**. The improvement in the region of 450-550 nm was significant, corresponding to the visible absorption of C_{70} in **5**, as shown in Figure 5.4b. As a result, J_{SC} increased to a relatively high value of 4.5 mA cm^{-2} for the devices based on **5**. This result suggests that the introduction of C_{70} fullerene is a promising strategy for dyads to enhance their visible absorption, and therefore their photocurrent.

5.4. Conclusions

In summary, a series of DPP-oligothiophene fullerene dyad molecules were designed and synthesized. It was found that alkyl side chains have an important influence on π-π stacking in the solid state, as demonstrated by UV-vis spectra, and XRD and DSC patterns, consequently the side chains affect device performance, especially J_{SC}. C_{70} fullerene was introduced into dyad molecules. Their combination leads to dyad **5** with a methyl side chain and C_{70} as the acceptor, which showed a relatively high J_{SC} = 4.5 mA cm^{-2}. To improve the low FF and EQE value of the dyad devices, the introduction of more highly crystalline donor parts by increasing the size of the donor parts would be necessary.

S. Izawa, K. Hashimoto, and K. Tajima, *Synth. Met.*, **2012**, *162*, 2201-2205.

References

1. (a) Gunes, S.; Neugebauer, H.; Sariciftci, N. S., Conjugated polymer-based organic solar cells. *Chemical Reviews* **2007,** *107* (4), 1324-1338; (b) Cheng, Y.-J.; Yang, S.-H.; Hsu, C.-S., Synthesis of Conjugated Polymers for Organic Solar Cell Applications. *Chemical Reviews* **2009,** *109* (11), 5868-5923; (c) Brabec, C. J.; Gowrisanker, S.; Halls, J. J. M.; Laird, D.; Jia, S. J.; Williams, S. P., Polymer-Fullerene Bulk-Heterojunction Solar Cells. *Advanced Materials* **2010,** *22* (34), 3839-3856; (d) Walker, B.; Kim, C.; Nguyen, T.-Q., Small Molecule Solution-Processed Bulk Heterojunction Solar Cells. *Chemistry of Materials* **2011,** *23* (3), 470-482.

2. Tang, C. W., 2-LAYER ORGANIC PHOTOVOLTAIC CELL. *Applied Physics Letters* **1986,** *48* (2), 183-185.

3. Sariciftci, N. S.; Smilowitz, L.; Heeger, A. J.; Wudl, F., PHOTOINDUCED ELECTRON-TRANSFER FROM A CONDUCTING POLYMER TO BUCKMINSTERFULLERENE. *Science* **1992,** *258* (5087), 1474-1476.

4. (a) Yu, G.; Gao, J.; Hummelen, J. C.; Wudl, F.; Heeger, A. J., POLYMER PHOTOVOLTAIC CELLS - ENHANCED EFFICIENCIES VIA A NETWORK OF INTERNAL DONOR-ACCEPTOR HETEROJUNCTIONS. *Science* **1995,** *270* (5243), 1789-1791; (b) Hiramoto, M.; Fujiwara, H.; Yokoyama, M., 3-LAYERED ORGANIC SOLAR-CELL WITH A PHOTOACTIVE INTERLAYER OF CODEPOSITED PIGMENTS. *Applied Physics Letters* **1991,** *58* (10), 1062-1064.

5. Service, R. F., Outlook Brightens for Plastic Solar Cells. *Science* **2011,** *332* (6027), 293-293.

6. (a) Nguyen, L. H.; Hoppe, H.; Erb, T.; Gunes, S.; Gobsch, G.; Sariciftci, N. S., Effects of annealing on the nanomorphology and performance of poly(alkylthiophene): fullerene bulk-heterojunction solar cells. *Advanced Functional Materials* **2007,** *17* (7), 1071-1078; (b) Yang, X. N.; van Duren, J. K. J.; Rispens, M. T.; Hummelen, J. C.; Janssen, R. A. J.; Michels, M. A. J.; Loos, J., Crystalline organization of a methanofullerene as used for plastic solar-cell applications. *Advanced Materials* **2004,** *16* (9-10), 802-806; (c) Chirvase, D.; Parisi, J.; Hummelen, J. C.; Dyakonov, V., Influence of nanomorphology on the photovoltaic action of polymer-fullerene composites. *Nanotechnology* **2004,** *15* (9), 1317-1323.

7. Miyanishi, S.; Zhang, Y.; Tajima, K.; Hashimoto, K., Fullerene attached all-semiconducting diblock copolymers for stable single-component polymer solar cells. *Chemical Communications* **2010,** *46* (36), 6723-6725.

8. (a) Zhang, Y.; Tajima, K.; Hirota, K.; Hashimoto, K., Synthesis of all-conjugated diblock copolymers by quasi-living polymerization and observation of their microphase separation. *Journal of the American Chemical Society* **2008,** *130* (25), 7812-7813; (b) Segura, J.

L.; Martin, N.; Guldi, D. M., Materials for organic solar cells: the C-60/pi-conjugated oligomer approach. *Chemical Society Reviews* **2005,** *34* (1), 31-47; (c) Roncali, J., Linear pi-conjugated systems derivatized with C-60-fullerene as molecular heterojunctions for organic photovoltaics. *Chemical Society Reviews* **2005,** *34* (6), 483-495; (d) Roncali, J., Single Material Solar Cells: the Next Frontier for Organic Photovoltaics? *Advanced Energy Materials* **2011,** *1* (2), 147-160.

9. (a) Nierengarten, J. F.; Eckert, J. F.; Nicoud, J. F.; Ouali, L.; Krasnikov, V.; Hadziioannou, G., Synthesis of a C_{60}-oligophenylenevinylene hybrid and its incorporation in a photovoltaic device. *Chemical Communications* **1999,** (7), 617-618; (b) Nishizawa, T.; Tajima, K.; Hashimoto, K., Supramolecular formation of fibrous nanostructure in donor-acceptor dyad Mint. *Journal of Materials Chemistry* **2007,** *17* (23), 2440-2445; (c) Nierengarten, J. F., Chemical modification of C-60 for materials science applications. *New Journal of Chemistry* **2004,** *28* (10), 1177-1191; (d) Maggini, M.; Possamai, G.; Menna, E.; Scorrano, G.; Camaioni, N.; Ridolfi, G.; Casalbore-Miceli, G.; Franco, L.; Ruzzi, M.; Corvaja, C., Solar cells based on a fullerene-azothiophene dyad. *Chemical Communications* **2002,** (18), 2028-2029.

10. Nishizawa, T.; Tajima, K.; Hashimoto, K., The effect of crystallinity in donor groups on the performance of photovoltaic devices based on an oligothiophene-fullerene dyad. *Nanotechnology* **2008,** *19* (42) 424017-424025..

11. Nishizawa, T.; Lim, H. K.; Tajima, K.; Hashimoto, K., Efficient dyad-based organic solar cells with a highly crystalline donor group. *Chemical Communications* **2009,** (18), 2469-2471.

12. Izawa, S.; Hashimoto, K.; Tajima, K., Efficient charge generation and collection in organic solar cells based on low band gap dyad molecules. *Chemical Communications* **2011,** *47* (22), 6365-6367.

13. (a) Yue, W.; Zhao, Y.; Shao, S.; Tian, H.; Xie, Z.; Geng, Y.; Wang, F., Novel NIR-absorbing conjugated polymers for efficient polymer solar cells: effect of alkyl chain length on device performance. *Journal of Materials Chemistry* **2009,** *19* (15), 2199-2206; (b) Balakrishnan, K.; Datar, A.; Naddo, T.; Huang, J. L.; Oitker, R.; Yen, M.; Zhao, J. C.; Zang, L., Effect of side-chain substituents on self-assembly of perylene diimide molecules: Morphology control. *Journal of the American Chemical Society* **2006,** *128* (22), 7390-7398.

14. Boudreault, P.-L. T.; Najari, A.; Leclerc, M., Processable Low-Bandgap Polymers for Photovoltaic Applications. *Chemistry of Materials* **2011,** *23* (3), 456-469.

15. He, Y.; Li, Y., Fullerene derivative acceptors for high performance polymer solar cells. *Physical Chemistry Chemical Physics* **2011,** *13* (6), 1970-1983.

16. Tamayo, A. B.; Walker, B.; Nguyen, T.-Q., A low band gap, solution processable oligothiophene with a diketopyrrolopyrrole core for use in organic solar cells. *Journal of Physical Chemistry C* **2008,** *112* (30), 11545-11551.

17. (a) Imahori, H.; Tamaki, K.; Guldi, D. M.; Luo, C. P.; Fujitsuka, M.; Ito, O.; Sakata, Y.; Fukuzumi, S., Modulating charge separation and charge recombination dynamics in porphyrin fullerene linked dyads and triads: Marcus-normal versus inverted region. *Journal of the American Chemical Society* **2001,** *123* (11), 2607-2617; (b) Tkachenko, N. V.; Rantala, L.; Tauber, A. Y.; Helaja, J.; Hynninen, P. H.; Lemmetyinen, H., Photoinduced electron transfer in phytochlorin- 60 fullerene dyads. *Journal of the American Chemical Society* **1999,** *121* (40), 9378-9387.

18. Scharber, M. C.; Wuhlbacher, D.; Koppe, M.; Denk, P.; Waldauf, C.; Heeger, A. J.; Brabec, C. L., Design rules for donors in bulk-heterojunction solar cells - Towards 10 % energy-conversion efficiency. *Advanced Materials* **2006,** *18* (6), 789-794.

19. Wuerthner, F.; Kaiser, T. E.; Saha-Moeller, C. R., J-Aggregates: From Serendipitous Discovery to Supramolecular Engineering of Functional Dye Materials. *Angewandte Chemie-International Edition* **2011,** *50* (15), 3376-3410.

20. (a) Garnier, F.; Yassar, A.; Hajlaoui, R.; Horowitz, G.; Deloffre, F.; Servet, B.; Ries, S.; Alnot, P., MOLECULAR ENGINEERING OF ORGANIC SEMICONDUCTORS - DESIGN OF SELF-ASSEMBLY PROPERTIES IN CONJUGATED THIOPHENE OLIGOMERS. *Journal of the American Chemical Society* **1993,** *115* (19), 8716-8721; (b) van Hutten, P. F.; Wildeman, J.; Meetsma, A.; Hadziioannou, G., Molecular packing in unsubstituted semiconducting phenylenevinylene oligomer and polymer. *Journal of the American Chemical Society* **1999,** *121* (25), 5910-5918.

Chapter 6.

Separated Crystallization of Donor and Acceptor in Oligo(*p*-phenylenevinylene)-Naphthalenediimide Dyad Films

6.1. Introduction

Precise control of the ordering and alignment of π-conjugated molecules in solid films through molecular design is important because nanoscale film morphology strongly affects the efficiency of many organic electronic devices.[1] This is particularly important for efficient organic solar cells (OSCs) because the electron donor and acceptor molecules in the films must form separate domains on the scale of several tens of nanometers for efficient simultaneous charge generation and transport.[2] To obtain ideal nanomorphologies for the donor and acceptor in the active layer of OSCs, a solution containing a mixture of the two compounds is often used.[3] The fabrication conditions, including solvents,[4] thermal annealing,[5] and additives,[6] have been optimized. Several groups have achieved high power conversion efficiency (PCE) greater than 8% in mixed bulk heterojunction (BHJ) OSCs[7] with fullerene derivatives as the acceptor. However, the phase-separated nanostructures are not necessarily well-controlled and BHJ systems often suffer from undesirable large aggregations of either the donors or the fullerenes, which reduces the efficiency of the charge separation. This problem could also reduce the reproducibility of the device performance. In addition, the mixed structures are often not in a thermodynamically stable state and phase separation could occur after operation at high temperatures for a long time.[8] This morphological change reduced the device performance substantially.

Dyad molecules, in which the D and A moieties are covalently attached to each other, have been intensively studied for controlling the donor/acceptor (D/A) nanomorphology.[9] The efficiency has been improved from about 0.1% in early studies to more than 1% recently.[10] Nishizawa et al. reported that a dyad based on oligo(*p*-phenylenevinylene) (OPV) and C_{70} fullerene showed a record PCE of 1.92% and good morphological and device stability at high temperatures.[11] However, the PCEs of dyad-based OSCs are still much lower than those of BHJ OSCs.[7, 12] One problem is that the covalent bonds between the donor and the acceptor often disturb the molecular ordering of each moiety.[13] For example, the attachment of a fullerene to the crystalline donor significantly reduces the crystallinity,[14] resulting in the absence of X-ray

diffraction peaks.[15] Because the crystallinity of both the donor and the acceptor domains could key to achieving efficient charge transport, it would be ideal if the donor and acceptor crystallized separately in the dyad films.[16]

In this study, the author synthesized a new dyad molecule with OPV as the donor and naphthalene diimide (NDI) as the acceptor, connected by a long flexible hexaethylene glycol linker (Scheme 6.1). NDI has good electron transport properties and is often used in n-type organic field transistors.[17] Furthermore, the author expected that the planar π-plane[18] of NDI would not disturb the π-stacking of OPV. The structure of the dyad was determined by optical, thermal, and X-ray diffraction (XRD) measurements. OSC devices were fabricated with the dyad.

6.2. Experimental Section

Synthetic details

All chemicals were purchased from the chemical suppliers and used without further purification. The synthetic route to OPV (**1**) in Scheme 6.1 has been reported previously.[19] The products were characterized by ^{1}H NMR spectroscopy and MALDI-TOF-MS.

***N*-(2-Ethylhexyl)-*N'*-(hexane-6-carboxylic acid)-naphthalenebisimide (NDICOOH) (2)**

6-Aminohexanoic acid (1.968 g, 15.0 mmol), 2-ethylhexylamine (2.454 mL, 15.0 mmol), anhydrous zinc acetate (1.373 g), and anhydrous DMF (50 mL) were added to a 100 mL two-neck round-bottom flask under N_2. The reaction mixture was stirred for 1 h at 150 °C, and then 1,4,5,8-naphthalenetetracarboxylic dianhydride (2.68 g, 10.0 mmol) was added. The reaction mixture was stirred overnight at 150 °C. After cooling to room temperature, the mixture was extracted with $CHCl_3$. The crude product was purified by silica gel column chromatography ($CHCl_3$), yielding **2** as a pink solid (605 mg, 12%).

^{1}H NMR ($CDCl_3$, 300MHz): δ(ppm): 8.76 (s, 4H), 4.12-4.23 (m, 4H), 2.37-2.41 (t, 2H), 1.92-1.99 (m, 1H), 1.71-1.80 (m, 4H), 1.48-1.52 (m, 2H), 1.30-1.42 (m, 8H), 0.92-0.96 (t, 3H), 0.86-0.90 (t, 3H).

OPV-NDI dyad (3)

2 (57 mg, 0.117 mmol) was placed in a 50 mL two-neck round-bottom flask under N_2; then anhydrous chlorobenzene (5 mL) and thionyl chloride (1.012 mL, 14.0 mmol) were added. The reaction mixture was stirred overnight at 70 °C. The solvent was removed in vacuo and anhydrous chlorobenzene (5 mL) was added. NaH (oil dispersion 50–72%, 17.8 mg, washed with hexane prior to use) in anhydrous chlorobenzene (45 mL) was added to the mixture containing **1** (100 mg, 0.117 mmol). The reaction mixture was stirred at room temperature for 48 h and then purified by

column chromatography using silica gel and $CHCl_3$ as eluent, yielding **3** as a yellow solid (43 mg, 28%).

^{1}H NMR ($CDCl_3$, 300MHz): δ(ppm): 8.70 (s, 4H), 7.37-7.46 (m, 14H), 6.88-7.12 (m, 12H), 4.18-4.21 (m, 4H), 4.01-4.09 (m, 4H), 3.92-3.97 (m, 5H), 3.85 (s, 6H), 3.58-3.74 (m, 20H), 2.30-2.35 (t, 2H), 1.87-1.95 (m, 1H), 1.65-1.70 (m, 4H), 1.20-1.45 (m, 10H), 0.86-0.92 (m, 6H). MALDI-TOF-MS ($C_{81}H_{90}N_2O_{15}$) calcd. 1331.59, found 1331.39.

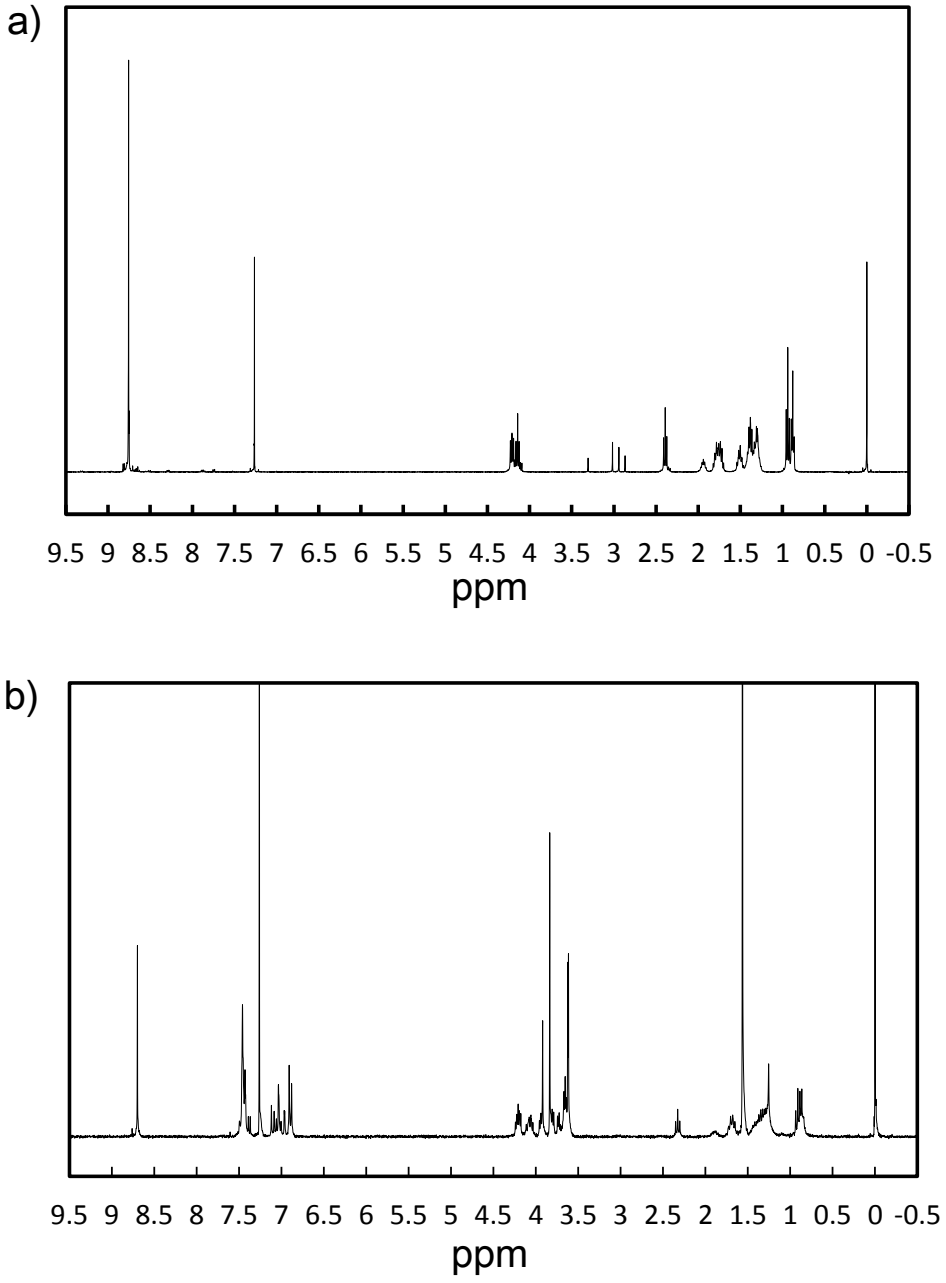

Figure 6.1. ^{1}H NMR charts of (a) NDI-COOH, and (b) OPV-NDI dyad in $CDCl_3$.

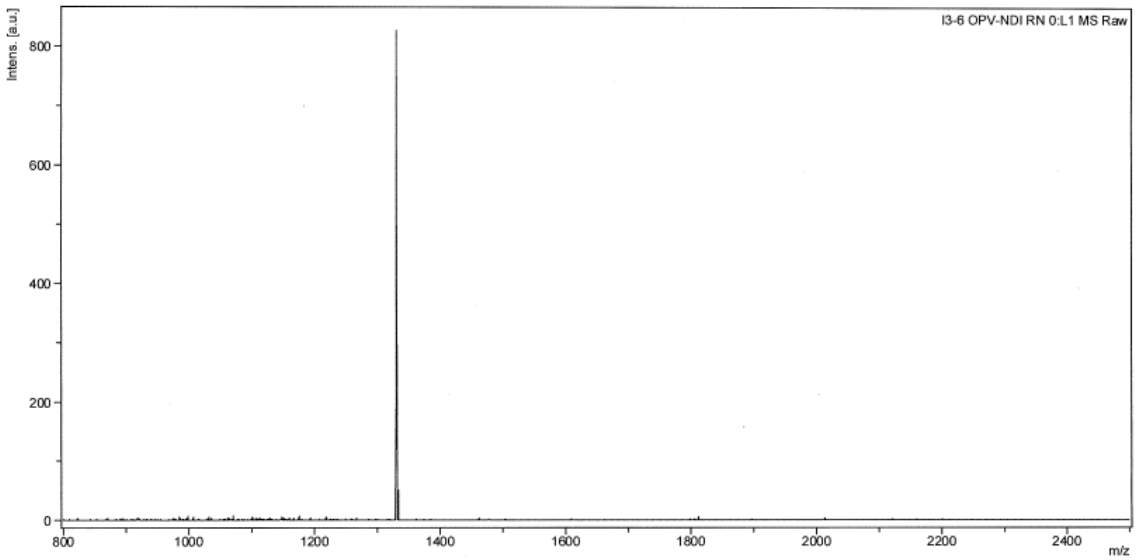

Figure 6.2. MALDI-TOF-MS chart of OPV-NDI dyad

Measurement

^{1}H NMR were measured on JNM-AL300 (JEOL). MALDI-TOF-MS spectra were measured on Ultraflex RO (Bruker Daltonics) with dithranol as the matrix. UV-vis absorption spectra were measured on a V-670 spectrometer (JASCO). Fluorescence spectra were measured on an F-4500 fluorescence spectrophotometer (Hitachi). Cyclic voltammetry (CV) was performed on an HSV-100 automatic polarization system (Hokuto Denko) in N_2. 0.1 M Tetrabutylammomium hexafluorophosphate in anhydrous $CHCl_3$ was used as the supporting electrolyte. A glassy carbon working electrode, a Pt wire counter electrode, and a Ag/AgCl reference electrode were used. Differential scanning calorimetry (DSC) traces were obtained on a Thermo plus DSC8230 calorimeter (Rigaku). 2D-GIXRD patterns were measured at an incident angle of 0.12° using synchrotron radiation at beam line BL19B2 of SPring-8 with the approval of the Japan Synchrotron Radiation Research Institute. Variable temperature θ-2θ XRD patterns were measured with a Smart Lab X-Ray diffractometer (Rigaku) with Cu K_α at 45 kV and 200 mA. The sample was covered with a plastic dome (Anton Paar, transmittance of Cu K_α: 73%) in a vacuum. The temperature of the stage was controlled by a TCU 150 temperature control unit (Anton Paar). Film thickness was measured by surface profilometry (Dektak 6M, ULVAC, Japan). Atomic force microscopy (AFM) images were obtained on a Nanonavi station/S-image (SII technology) operated in tapping mode. Films were prepared by spin coating $CHCl_3$ solutions of the OPV-NDI dyad with a total concentration of 10 mg mL^{-1} at 2500 rpm on a glass substrate for the UV-vis absorption and fluorescence measurement, and on silicon wafers for 2D-GIXRD measurements with no thermal annealing.

Photovoltaic device preparation and measurement

An indium tin oxide (ITO)-coated glass substrate (sheet resistance: 10 Ω sq^{-1}, Geomatec) was cleaned by sequential ultra-sonication in detergent solution, water, acetone, 2-propanol, and water. The substrate was dried and then spin coated with PEDOT:PSS (H. C. Stark) at 4000 rpm. The film was dried at 150 °C under N_2 for 20 min. After cooling, the substrate was spin coated with a $CHCl_3$ solution of the OPV-NDI dyad with a total concentration of 10 mg mL^{-1} at 2500 rpm. Finally, Ca (20 nm) and Al (40 nm) electrodes were evaporated onto the organic layer under high vacuum (6×10^{-4} Pa). The devices were annealed at temperatures of 100, 130, or 160 °C for 5 min, and devices without thermal annealing were also prepared. The *J-V* characteristics of the devices were measured under simulated solar illumination (AM 1.5, 100 mW cm^{-2}) from a 150 W Xe lamp (PEC-L11, Peccell Technologies) with an AM 1.5 filter. The light intensity was calibrated with a standard silicon solar cell (BS520, Bunkoh-Keiki). The active area of the devices was defined by using a 0.12 cm^2 photo mask. The external quantum efficiency (EQE) of the devices was measured on a Hypermonolight SM-250F system (Bunkoh-Keiki).

6.3. Results and discussion

Synthesis

The dyad molecule with NDI and OPV (OPV-NDI dyad) was synthesized by following Scheme 6.1. The synthesis of OPV was reported previously by us.[19] NDICOOH was synthesized by using two kinds of amines to asymmetrically convert the tetracarboxylic acid dianhydride to the diimide in one pot reaction. The symmetrically substituted diimides were removed by column chromatography. The products were characterised by ^{1}H NMR and MALDI-TOF-MS. All the peaks in ^{1}H NMR of the product were assigned to NDICOOH and the ratios of the peak area were consistent with the chemical structure, besides minor unknown peaks were observed at 3.31, 3.02, 2.94 and 2.87 ppm. Peaks correspond to alpha methylene next to diimide nitrogens were composed by triplet in 4.19-4.23 ppm from 6-carboxylic acid-hexylimide and multiplet in 4.12-4.19 ppm from 2-ethylhexylimide.[26] OPV-NDI dyad was synthesised by esterification of OPV and NDICOOH through the formation of carboxylic acid chloride. All the peaks in ^{1}H NMR of the product were assigned to OPV-NDI except residual solvent and water peaks and the ratios of the peak area were consistent with the chemical structure of the dyad. MALDI-TOF-MS showed single peak corresponding to the molecular weight of the dyad. Note that possible impurity of triad which might be formed from the symmetrical dimide in previous step was not found in MALDI-TOF-MS.

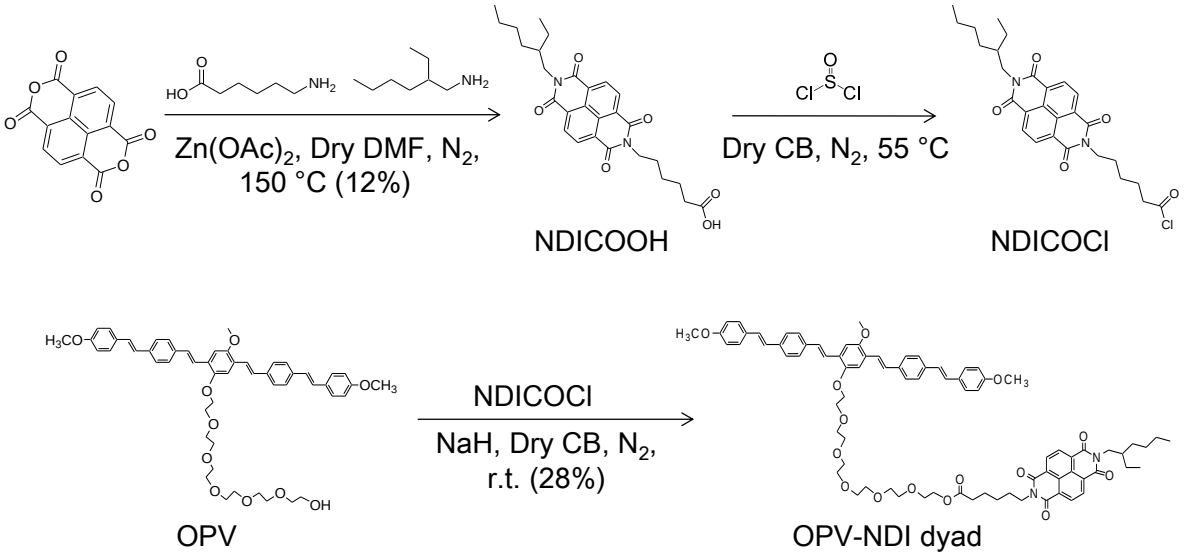

Scheme 6.1. Synthetic route to the OPV-NDI dyad.

Molecular properties

Absorption spectra

Figure 6.3a shows the UV-vis absorption spectra of the OPV-NDI dyad, OPV, and NDICOOH in $CHCl_3$. OPV has an absorption peak at 420 nm and NDICOOH has three peaks at 342, 360, and 380 nm. The absorption spectrum of the OPV-NDI dyad molecule was a simple sum of the OPV and NDICOOH spectra. This represents that there is little electrical interaction in the ground state between the OPV and NDI parts of the dyad in solution. The optical band gap of the donor part was estimated from the absorption edges as 2.56 eV, which corresponds to that of OPV. The absorption spectra of the OPV-NDI dyad, OPV, and the OPV-C_{70} dyad (as a reference) thin films are shown in Figure 6,3b. In the pristine OPV film, the peak was red shifted to 440 nm compared with the solution spectrum and an absorption shoulder appeared around 480 nm. The red shift in the OPV absorption could be caused by *J*-aggregation, which has been observed previously.[10b] This peak shift and the appearance of a shoulder in the absorption of OPV was also observed in thin films of the OPV-NDI dyad and the OPV-C_{70} dyad. This indicates that donor moiety aggregated in both the OPV-NDI dyad and the OPV-C_{70} dyad films.

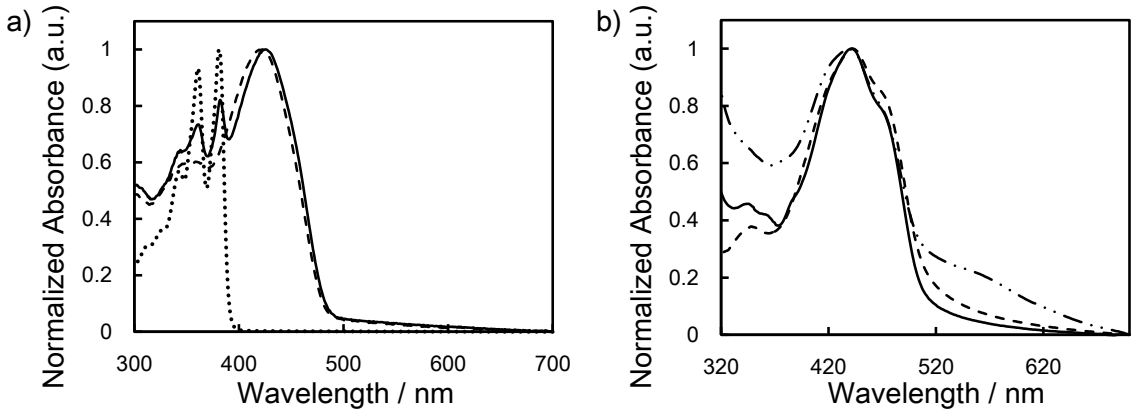

Figure 6.3. Absorption spectra of (a) the OPV-NDI dyad (solid line), OPV (dashed line), and NDICOOH (dotted line) in $CHCl_3$ and (b) OPV-NDI dyad (solid line), OPV (dashed line), and OPV-C_{70} dyad (dash-dotted line) thin films.

Fluorescence spectra

Fluorescence spectra of the OPV-NDI dyad, OPV, OPV-C_{70} dyad, and an equimolar solution of OPV and NDI in $CHCl_3$ are shown in Figure 6.4a. The solutions had a similar low absorbance of approximately 0.02 at the excitation wavelength of 420 nm to avoid aggregation and the fluorescence intensity was normalized by the absorbance. OPV showed strong fluorescence with a peak maximum at 485 nm, whereas attaching the NDI moiety significantly decreased the fluorescence intensity. This denotes that the excited state of OPV part was quenched by intramolecular charge transfer from the OPV to the NDI moiety in the dyads. In contrast, the mixture of OPV and NDICOOH showed almost the same fluorescence intensity as the OPV solution. These results reflect the proximity of the donor and the acceptor in the OPV-NDI dyad in solution because of the hexaethylene glycol linker. The fluorescence intensity of the OPV-C_{70} dyad was lower than that of the OPV-NDI dyad in solution. This result suggests that the intramolecular charge transfer from OPV to the acceptor was more efficient in the OPV-C_{70} dyad than in the OPV-NDI dyad in $CHCl_3$. The thin film fluorescence spectra of the OPV-NDI dyad, OPV, and OPV-C_{70} dyad are shown in Figure 6.4b. The films had a similar absorbance of approximately 0.5 at the excitation wavelength of 420 nm and the fluorescence intensity was normalized by the absorbance. The peak shifted from 485 nm in solution to 530 nm in the OPV pristine film. The fluorescence intensity of the OPV-NDI dyad was lower than that of OPV for the thin film spectra, demonstrating that excited state of the OPV moiety was quenched by NDI in the OPV-NDI dyad thin film. The OPV-C_{70} dyad showed a lower fluorescence intensity than the OPV-NDI dyad for the thin film spectra, similar to the solution spectra, indicating that C_{70} fullerene quenched the fluorescence of OPV more efficiently than did NDI.

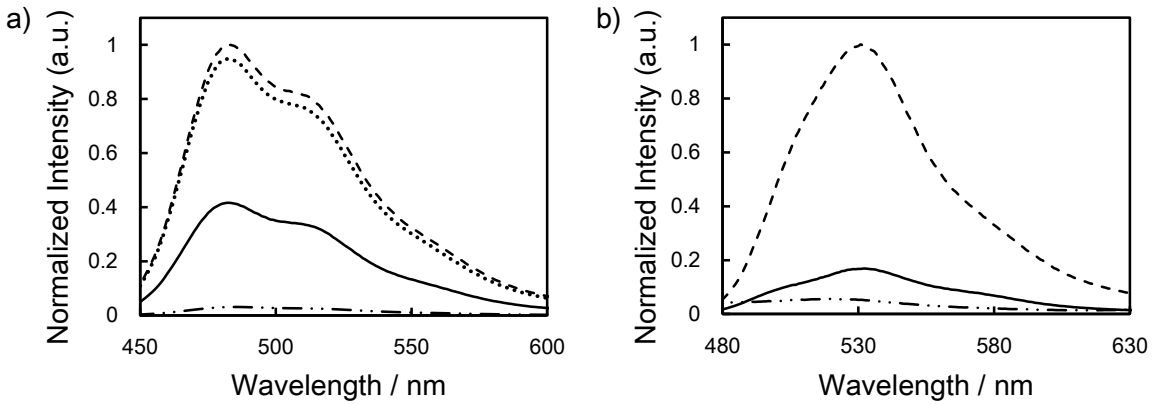

Figure 6.4. Fluorescence spectra of (a) OPV-NDI dyad (solid line), OPV (dashed line), OPV-C_{70} dyad (dash-dotted line), and mixture of OPV and NDICOOH (dotted line) in $CHCl_3$ and (b) OPV-NDI dyad (solid line), OPV (dashed line), and OPV-C_{70} dyad (dash-dotted line) thin films.

Cyclic voltammetry

The half potentials of first oxidation (E_{ox}) and the reduction (E_{red}) of $CHCl_3$ solutions of the OPV-NDI dyad, OPV, and NDICOOH relative to the redox potential of Fc/Fc^+ were determined by CV. The energy levels of the HOMO and LUMO were estimated by assuming the Fc/Fc^+ redox potential to be −4.8 eV relative to the vacuum level.[20] E_{ox} and E_{red} of the OPV-NDI dyad were 0.36 and −1.09 V, respectively, and E_{ox} of OPV and E_{red} of NDICOOH were 0.37 and −1.05 V, respectively. E_{ox} of NDICOOH and E_{red} of OPV were not observed. The OPV-NDI dyad had an E_{ox} and E_{red} similar to those of OPV and NDI, respectively. This indicates that the oxidation of the OPV moiety and the reduction of the NDI moiety in the OPV-NDI dyad were not affected by the covalent attachment. The LUMO energy offsets between the OPV and NDI moieties in the dyad, calculated from E_{ox} and the optical band gaps of the OPV moiety and E_{red} of the NDI moiety, were around 1.1 eV, which is much higher than the energy required for efficient charge separation in OSCs.[21]

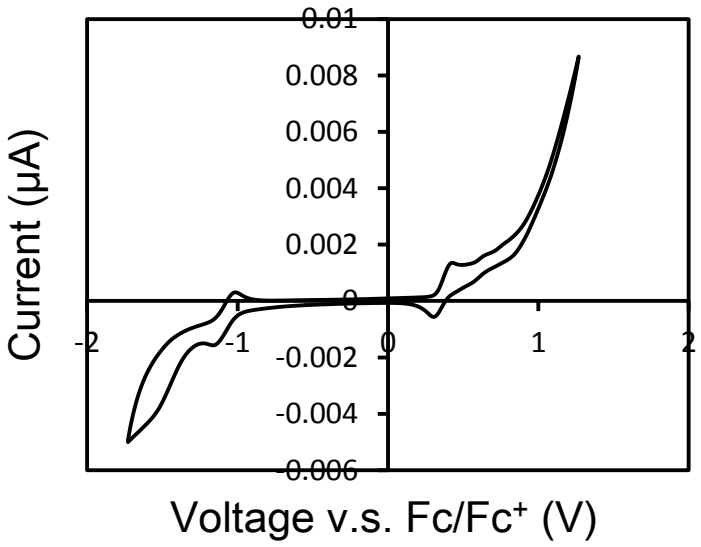

Figure 6.5. Cyclic voltammogram of OPV-NDI dyad.

Thermal properties

DSC of the OPV-NDI dyad, OPV, and NDICOOH was conducted with a scan rate of 10 °C min^{-1}, and the results of the second scans are shown in Figure 6.6. OPV exhibited an endothermic peak at 194 °C upon heating, and an exothermic peak at 176 °C upon cooling. NDICOOH showed an endothermic peak at 210 °C upon heating, and an exothermic peak at 175 °C upon cooling. In contrast, the OPV-NDI dyad showed two endothermic peaks at 148 and 172 °C upon heating, and two exothermic peaks at 146 and 122 °C upon cooling. This result suggests that there was a mesophase in the OPV-NDI dyad in the temperature range of 148-172 °C upon heating and 122-146 °C upon cooling caused by the partial melting of one of the components. The structural change at high temperatures is discussed in the following section. The OPV-C_{70} dyad showed one endothermic peak at 187 °C and one exothermic peak at 154 °C, as previously reported.[11]

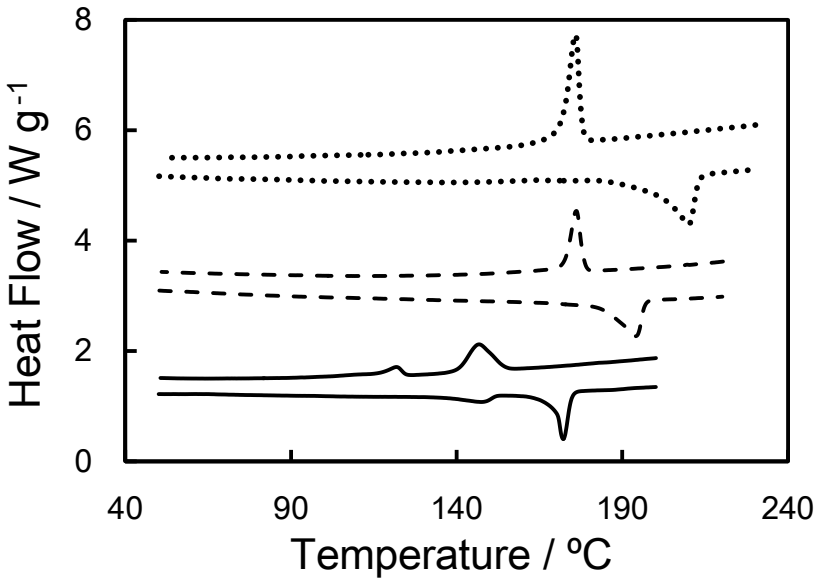

Figure 6.6. DSC charts of OPV-NDI dyad (solid line), OPV (dashed line), and NDICOOH (dotted line). The profiles are shifted in the y-axis for clarity.

Crystal structure

2D-GIXRD of thin films

2D-GIXRD patterns were measured for the spin-coated OPV, NDICOOH, OPV-NDI dyad, and OPV-C_{70} dyad films on silicon substrates. The thin films were prepared by spin coating $CHCl_3$ solutions with a total concentration of 10 mg mL^{-1} at 2500 rpm. The samples were not thermally annealed. Figure 6.7b, shows that the NDICOOH pattern contained several diffraction peaks in the out-of-plane and in-plane directions. The strongest peak at q_z = 0.34 $Å^{-1}$ in the out-of-plane direction represented a *d*-spacing of 1.9 nm. The integrated linear profiles are shown in Figure 6.8. NDI-based molecules tend to have lamellar structures in spin-coated films,[22] and the pattern suggested the preferential orientation of the lamellar structure perpendicular to the substrate. The packing lattice spacing from the diffraction peak was close to the calculated molecular length along the long axis of NDICOOH (2.2 nm). The shorter packing length implies that the molecular packing axis could be slightly tilted.[23] The OPV film showed diffraction peaks at q_z = 1.40 $Å^{-1}$ in the out-of-plane direction and q_{xy} = 1.40, 1.67 $Å^{-1}$ in the in-plane direction, with *d*-spacings of 0.45 and 0.38 nm, respectively, corresponding to the reported peaks of the herringbone structure.[24]

The OPV-NDI dyad showed diffraction peaks in the *z*-direction at q_z = 0.27 $Å^{-1}$ (Figure 6.7c), which is similar to the diffraction pattern of NDICOOH. The strongest diffraction peak at q_z = 0.27 $Å^{-1}$ represented a *d*-spacing of 2.4 nm. Assuming that NDI has a lamellar structure in OPV-NDI films similar to that of NIDCOOH, the packing lattice spacing may be longer than NDICOOH because of the hexaethylene glycol linker. The diffraction peak at q_z = 1.41 $Å^{-1}$ (*d* =

0.44 nm) of the OPV-NDI film demonstrated the existence of an OPV herringbone structure in the dyad film. No other peaks that could be assigned to the D/A alternating structures were observed. In contrast, the 2D-GIXRD pattern for the OPV-C_{70} dyad film (Figure 6.7d), contained no peaks from the OPV packing structure because the bulky C_{70} disturbed the OPV packing. These results suggest that in the OPV-NDI dyad film, OPV and NDI aggregated and crystallized separately to form the structures similar to those in the pristine films. This difference probably arose because C_{70} is globular and less crystalline whereas NDI is planar and highly crystalline. To discuss morphology further, AFM image of the dyad film were measured (see Figure 6.9). The image shows the presence of grains with the size of ca. 100 nm reflecting the highly crystalline character of OPV-NDI dyad. It is difficult to observe microphase separation of the donor and the acceptor domains probably because it is too small, so the detailed information of morphology such as crystallite size or connectivity remains unknown. Further analysis on the crystallized domain sizes and the connectivity and how to control them in the films would be challenges for the future.

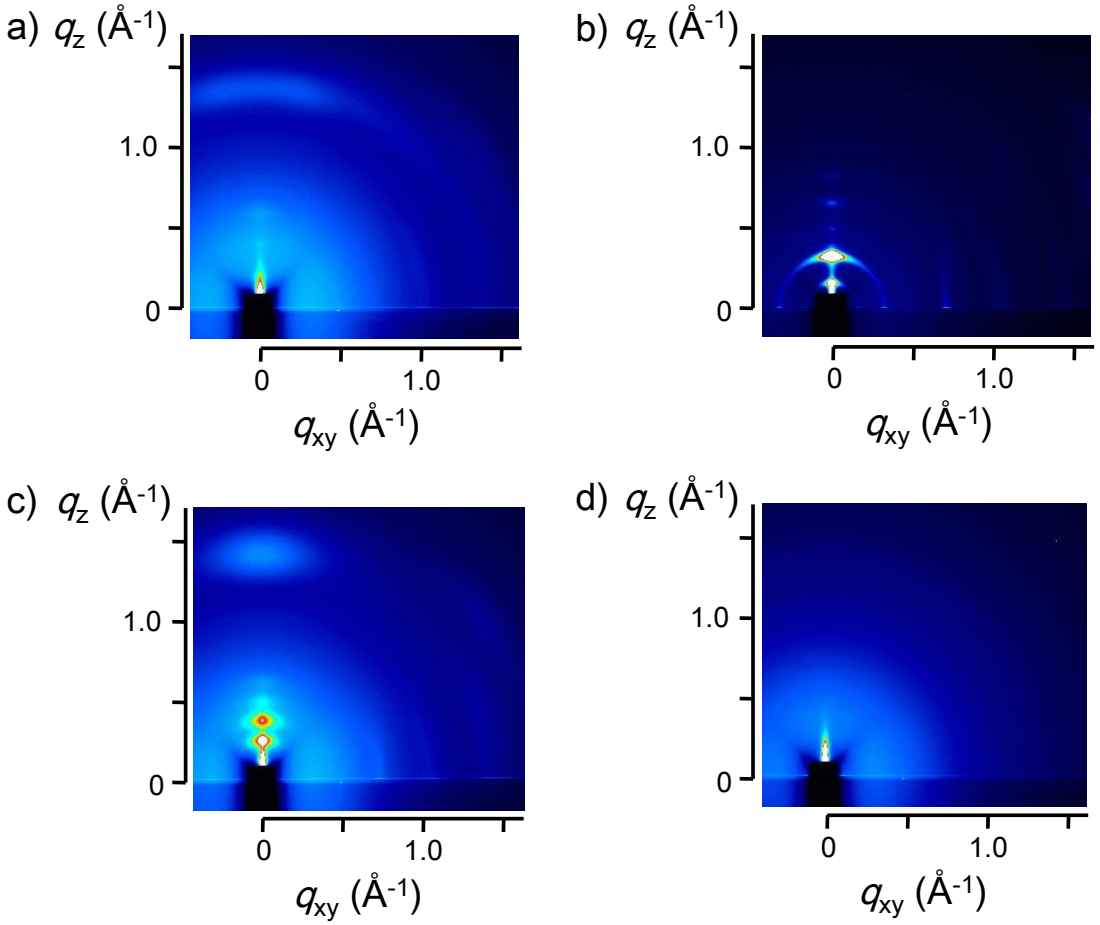

Figure 6.7. 2D-GIXRD patterns of (a) OPV, (b) NDICOOH, (c) OPV-NDI dyad, and (d) OPC-C_{70} dyad thin films.

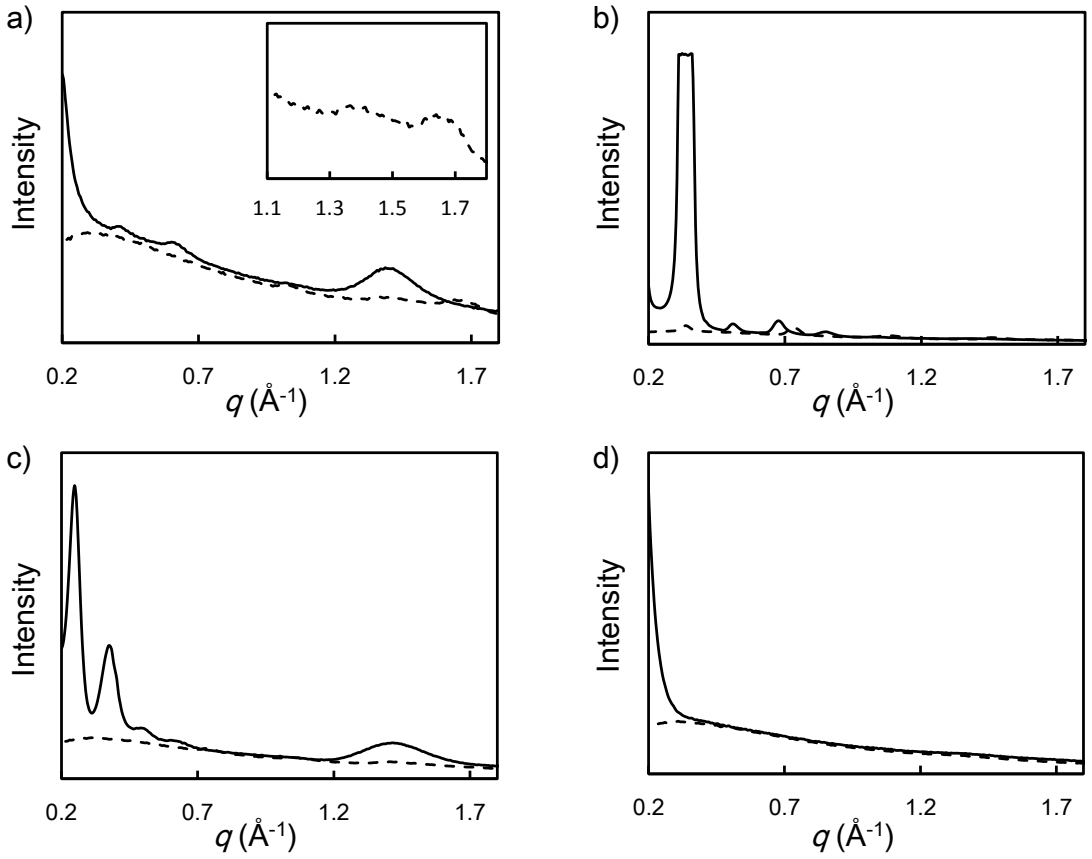

Figure 6.8. Integrated linear profiles of 2D-GIXRD patterns in Figure 6.7 of (a) OPV, (b) NDICOOH, (c) OPV-NDI dyad, and (d) OPC-C_{70} dyad (solid line: out-of-plane direction, dashed line: in-plane direction). The magnified in-plane profile of OPV was shown as inset.

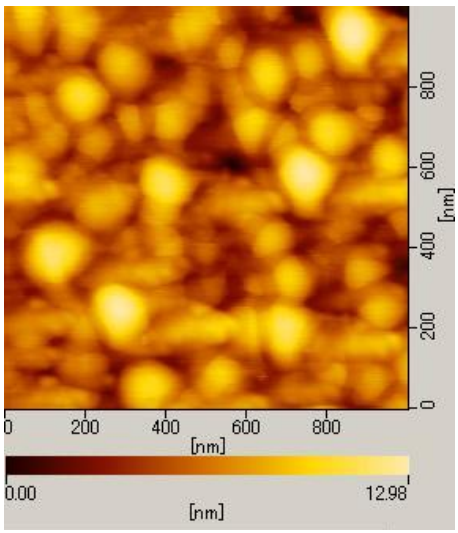

Figure 6.9. AFM height images of OPV-NDI dyad film.

Variable temperature XRD

Powder XRD patterns of OPV-NDI dyad were measured at 30, 160, and 190 °C upon heating, and 130 and 100 °C upon cooling (Figure 6.10). These temperatures corresponding to below and above the phase transitions observed in the DSC measurements (Figure 6.6). Diffraction peaks from the long axis of NDI at 5.0°, and peaks from the OPV herringbone structure at 19.5, 21.0, and 23.6° were observed at 30 °C. At 160 °C, the NDI diffraction peak at 5.0° disappeared, although the OPV peaks at 19.5, 21.0, and 23.6° remained. At 190 °C, the OPV diffraction peaks also disappeared. The film was cooled to 130 °C and only the OPV peaks at 19.5, 21.0, and 23.6° appeared. Upon further cooling to 100 °C, the diffraction peaks from the NDI lamellar structure at 5.0° were observed. This indicates that the exothermic peaks at 148 and 172 °C during heating in the DSC measurements (Figure 6.6) correspond to the melting of NDI and OPV, and the endothermic peaks at 146 and 122 °C correspond to the recrystallization of OPV and NDI, respectively. The distinct temperature responses of OPV and NDI in the OPV-NDI dyad strongly suggest that the two moieties were packed separately in the solid state. This is consistent with the 2D-GIXRD results for the thin films. Although electron donating and accepting moieties could stack alternately because of a D/A interaction,[25] the rod-like structure of OPV and the planar structure of NDI meant they formed separate ordered structures in the films.

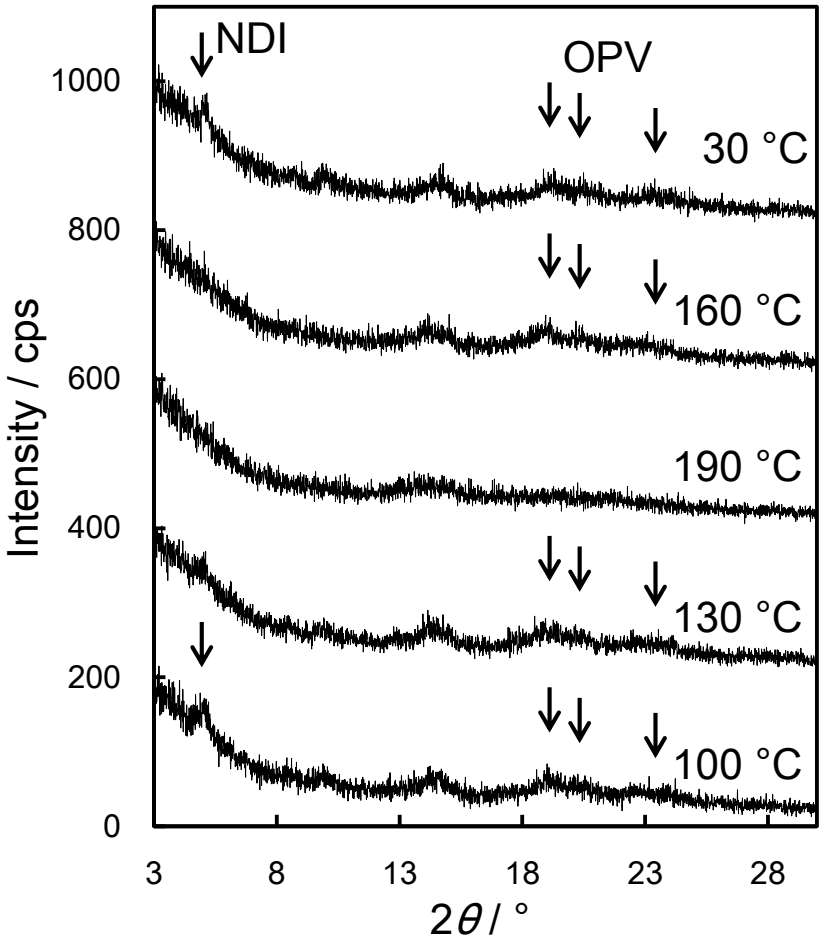

Figure 6.10. Powder XRD patterns of the OPV-NDI dyad at different temperatures. The patterns are shifted in the y-axis for clarity.

Photovoltaic properties

OSC devices containing the OPV-NDI dyad as the active layer were fabricated. Thickness of the active layers of OPV–NDI dyad was 110 nm measured by surface profilometry. The *J–V* curves and EQE spectra of the devices without thermal annealing are shown in Figure 6.11. The device properties were: J_{SC} = 0.31 mA cm^{-2}, V_{OC} = 0.91 V, FF = 0.28, and PCE = 0.08%. The EQE spectra in Figure 6.11b shows that the devices had a photocurrent response corresponding to the absorption of both the OPV moiety peaked at 440 nm and the NDI at 360 nm and 380 nm. Thermal annealing at temperatures up to 160 °C did not affect the device performance substantially.

Table 6.1. Device performance for different thermal annealing temperatures.

Annealing Temperature (°C)	J_{SC} (mA cm^{-2})	V_{OC} (V)	FF	PCE (%)
As cast	0.31	0.91	0.28	0.08
100	0.37	0.82	0.27	0.08
130	0.26	0.89	0.31	0.07
160	0.25	0.90	0.28	0.06

Compared to the photovoltaic performance reported for the OPV-C_{70} dyad (J_{SC} = 4.6 mA cm^{-2}, V_{OC} = 0.91, FF = 0.46 and PCE = 1.92%), the OPV-NDI dyad showed the same V_{OC} and a smaller photocurrent and FF, resulting in lower performance.[11] Morphology, which largely affects charge transfer, separation and transport in general, was drastically changed from OPV-C_{70} dyad to OPV-NDI dyad, therefore it is difficult to consider the limiting factor of J_{SC} and FF in OPV-NDI dyad. One possible reason for the lower photocurrent in OPV-NDI is the lower efficiency of the photoexcited charge transfer from OPV to NDI, as suggested by the fluorescence measurements in Figure 6.4. There are few reports of highly efficient OSCs using non-functionalized NDI as an electron acceptor,[13] even though NDI has a high electron mobility.[17] Recent report clarified that local molecular orientation at the D/A interface played a key role for charge generation in asymmetric acceptors alternative to fullerene acceptors.[26] Smaller electronic coupling between OPV and NDI in thin films might be the other possible reason for lower charge generation ability in OPV-NDI than in OPV-C_{70} dyad. Although the author observed the separated crystallization of the donor and acceptor in the film, the FF of the cell was quite low. This could be because of the molecular orientation; 2D-GIXRD denotes that the π-π stacking is oriented parallel to the substrate in the NDI phases, which is not suitable for charge conduction in the vertical direction. Control of the molecular orientation in the films could improve the transport.[19] Recently, non-fullerene small molecule acceptors have been explored,[27] such as perylenediimides (PDI) derivatives,[28] vinazene derivatives,[29] and oligothiophene-functionalized NDI.[29] Sharenko et al. reported an OSC performance of 3.0% by using a PDI derivative.[30] Substitution of NDI with another efficient planar acceptor, such as PDI, might produce a well-defined nanostructure and efficient OSC device performance.

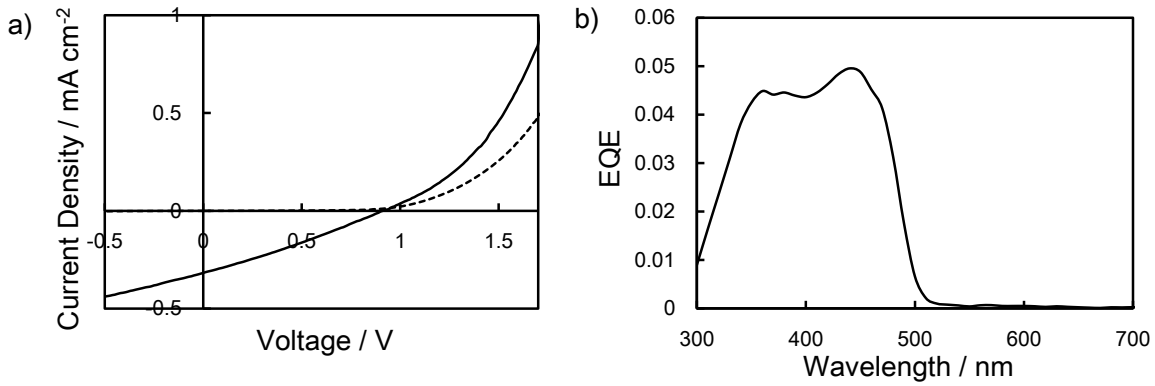

Figure 6.11. (a) *J-V* curves (dashed line: in the dark, solid line: under simulated solar light irradiation (AM 1.5)) and (b) EQE spectrum of the OSC devices containing the OPV-NDI dyad.

6.4. Conclusions

In OPV-NDI dyad films, the OPV and NDI moieties aggregate and crystallize separately because of the different crystalline properties of the components. This suggests that separate donor and acceptor phases can be spontaneously constructed in the spin-coated films by using the dyad system with flat, crystalline molecules. This design for the dyad molecules could be used to achieve nanoscale ordering in organic electronics devices.

S. Izawa, T. Nishizawa, K. Hashimoto, T. Koganezawa, and K. Tajima, *Synth. Met*., **2014**, *197*, 175-181.

References

1. (a) Dimitrakopoulos, C. D.; Malenfant, P. R. L., Organic thin film transistors for large area electronics. *Advanced Materials* **2002,** *14* (2), 99-117; (b) Fichou, D., Structural order in conjugated oligothiophenes and its implications on opto-electronic devices. *Journal of Materials Chemistry* **2000,** *10* (3), 571-588; (c) Bujak, P.; Kulszewicz-Bajer, I.; Zagorska, M.; Maurel, V.; Wielgus, I.; Pron, A., Polymers for electronics and spintronics. *Chemical Society Reviews* **2013,** *42* (23), 8895-8999.

2. Dang, M. T.; Hirsch, L.; Wantz, G.; Wuest, J. D., Controlling the Morphology and Performance of Bulk Heterojunctions in Solar Cells. Lessons Learned from the Benchmark Poly(3-hexylthiophene): 6,6 -Phenyl-C-61-butyric Acid Methyl Ester System. *Chemical Reviews* **2013,** *113* (5), 3734-3765.

3. (a) Yu, G.; Gao, J.; Hummelen, J. C.; Wudl, F.; Heeger, A. J., POLYMER PHOTOVOLTAIC CELLS - ENHANCED EFFICIENCIES VIA A NETWORK OF INTERNAL DONOR-ACCEPTOR HETEROJUNCTIONS. *Science* **1995,** *270* (5243), 1789-1791; (b) Hiramoto, M.; Fujiwara, H.; Yokoyama, M., 3-LAYERED ORGANIC SOLAR-CELL WITH A PHOTOACTIVE INTERLAYER OF CODEPOSITED PIGMENTS. *Applied Physics Letters* **1991,** *58* (10), 1062-1064.

4. Wienk, M. M.; Turbiez, M.; Gilot, J.; Janssen, R. A. J., Narrow-bandgap diketo-pyrrolo-pyrrole polymer solar cells: The effect of processing on the performance. *Advanced Materials* **2008,** *20* (13), 2556-2560.

5. Padinger, F.; Rittberger, R. S.; Sariciftci, N. S., Effects of postproduction treatment on plastic solar cells. *Advanced Functional Materials* **2003,** *13* (1), 85-88.

6. Lee, J. K.; Ma, W. L.; Brabec, C. J.; Yuen, J.; Moon, J. S.; Kim, J. Y.; Lee, K.; Bazan, G. C.; Heeger, A. J., Processing additives for improved efficiency from bulk heterojunction solar cells. *Journal of the American Chemical Society* **2008,** *130* (11), 3619-3623.

7. (a) Zhou, J. Y.; Zuo, Y.; Wan, X. J.; Long, G. K.; Zhang, Q.; Ni, W.; Liu, Y. S.; Li, Z.; He, G. R.; Li, C. X.; Kan, B.; Li, M. M.; Chen, Y. S., Solution-Processed and High-Performance Organic Solar Cells Using Small Molecules with a Benzodithiophene Unit. *Journal of the American Chemical Society* **2013,** *135* (23), 8484-8487; (b) Liu, Y. S.; Chen, C. C.; Hong, Z. R.; Gao, J.; Yang, Y.; Zhou, H. P.; Dou, L. T.; Li, G., Solution-processed small-molecule solar cells: breaking the 10% power conversion efficiency. *Scientific Reports* **2013,** *3*, 3356-3363.

8. (a) Chirvase, D.; Parisi, J.; Hummelen, J. C.; Dyakonov, V., Influence of nanomorphology on the photovoltaic action of polymer-fullerene composites. *Nanotechnology* **2004,** *15* (9), 1317-1323; (b) Miyanishi, S.; Tajima, K.; Hashimoto, K., Morphological Stabilization of Polymer Photovoltaic Cells by Using Cross-Linkable Poly(3-(5-

hexenyl)thiophene). *Macromolecules* **2009,** *42* (5), 1610-1618.

9. Roncali, J., Single Material Solar Cells: the Next Frontier for Organic Photovoltaics? *Advanced Energy Materials* **2011,** *1* (2), 147-160.

10. (a) Izawa, S.; Hashimoto, K.; Tajima, K., Efficient charge generation and collection in organic solar cells based on low band gap dyad molecules. *Chemical Communications* **2011,** *47* (22), 6365-6367; (b) Nishizawa, T.; Lim, H. K.; Tajima, K.; Hashimoto, K., Efficient dyad-based organic solar cells with a highly crystalline donor group. *Chemical Communications* **2009,** (18), 2469-2471; (c) Bu, L.; Guo, X.; Yu, B.; Qu, Y.; Xie, Z.; Yan, D.; Geng, Y.; Wang, F., Monodisperse Co-oligomer Approach toward Nanostructured Films with Alternating Donor-Acceptor Lamellae. *Journal of the American Chemical Society* **2009,** *131* (37), 13242-13243.

11. Izawa, S.; Hashimoto, K.; Tajima, K., Morphological stability of organic solar cells based upon an oligo(p-phenylenevinylene)-C_{70} dyad. *Physical Chemistry Chemical Physics* **2012,** *14* (46), 16138-16142.

12. Sun, Y.; Welch, G. C.; Leong, W. L.; Takacs, C. J.; Bazan, G. C.; Heeger, A. J., Solution-processed small-molecule solar cells with 6.7% efficiency. *Nature Materials* **2012,** *11* (1), 44-48.

13. Lin, Y.; Li, Y.; Zhan, X., Small molecule semiconductors for high-efficiency organic photovoltaics. *Chemical Society Reviews* **2012,** *41* (11), 4245-4272.

14. Kamkar, D. A.; Wang, M.; Wudl, F.; Thuc-Quyen, N., Single Nanowire OPV Properties of a Fullerene-Capped P3HT Dyad Investigated Using Conductive and Photoconductive AFM. *Acs Nano* **2012,** *6* (2), 1149-1157.

15. Izawa, S.; Hashimoto, K.; Tajima, K., Synthesis, characterization, and photovoltaic properties of diketopyrrolopyrrole-oligothiophene/fullerene dyads. *Synthetic Metals* **2012,** *162* (24), 2201-2205.

16. Nishizawa, T.; Tajima, K.; Hashimoto, K., The effect of crystallinity in donor groups on the performance of photovoltaic devices based on an oligothiophene-fullerene dyad. *Nanotechnology* **2008,** *19* (42), 424017-424025.

17. (a) Katz, H. E.; Lovinger, A. J.; Johnson, J.; Kloc, C.; Siegrist, T.; Li, W.; Lin, Y. Y.; Dodabalapur, A., A soluble and air-stable organic semiconductor with high electron mobility. *Nature* **2000,** *404* (6777), 478-481; (b) See, K. C.; Landis, C.; Sarjeant, A.; Katz, H. E., Easily synthesized naphthalene tetracarboxylic diimide semiconductors with high electron mobility in air. *Chemistry of Materials* **2008,** *20* (11), 3609-3616.

18. Bhosale, S. V.; Jani, C. H.; Langford, S. J., Chemistry of naphthalene diimides. *Chemical Society Reviews* **2008,** *37* (2), 331-342.

19. Nishizawa, T.; Lim, H. K.; Tajima, K.; Hashimoto, K., Highly Uniaxial Orientation in Oligo(p-phenylenevinylene) Films Induced During Wet-Coating Process. *Journal of the American Chemical Society* **2009,** *131* (7), 2464-2465.

20. Zhou, E. J.; Nakamura, M.; Nishizawa, T.; Zhang, Y.; Wei, Q. S.; Tajima, K.; Yang, C. H.; Hashimoto, K., Synthesis and Photovoltaic Properties of a Novel Low Band Gap Polymer Based on N-Substituted Dithieno 3,2-b:2 ',3 '-d pyrrole. *Macromolecules* **2008,** *41* (22), 8302-8305.

21. Scharber, M. C.; Wuhlbacher, D.; Koppe, M.; Denk, P.; Waldauf, C.; Heeger, A. J.; Brabec, C. L., Design rules for donors in bulk-heterojunction solar cells - Towards 10 % energy-conversion efficiency. *Advanced Materials* **2006,** *18* (6), 789-794.

22. Ahmed, E.; Ren, G.; Kim, F. S.; Hollenbeck, E. C.; Jenekhe, S. A., Design of New Electron Acceptor Materials for Organic Photovoltaics: Synthesis, Electron Transport, Photophysics, and Photovoltaic Properties of Oligothiophene-Functionalized Naphthalene Diimides. *Chemistry of Materials* **2011,** *23* (20), 4563-4577.

23. Lee, Y. L.; Hsu, H. L.; Chen, S. Y.; Yew, T. R., Solution-processed naphthalene diimide derivatives as n-type semiconductor materials. *Journal of Physical Chemistry C* **2008,** *112* (5), 1694-1699.

24. Nierengarten, J. F.; Eckert, J. F.; Nicoud, J. F.; Ouali, L.; Krasnikov, V.; Hadziioannou, G., Synthesis of a C-60-oligophenylenevinylene hybrid and its incorporation in a photovoltaic device. *Chemical Communications* **1999,** (7), 617-618.

25. (a) Pisula, W.; Kastler, M.; Wasserfallen, D.; Robertson, J. W. F.; Nolde, F.; Kohl, C.; Mullen, K., Pronounced supramolecular order in discotic donor-acceptor mixtures. *Angewandte Chemie-International Edition* **2006,** *45* (5), 819-823; (b) Jonkheijm, P.; Stutzmann, N.; Chen, Z. J.; de Leeuw, D. M.; Meijer, E. W.; Schenning, A.; Wurthner, F., Control of ambipolar thin film architectures by co-self-assembling oligo(p-phenylenevinylene)s and perylene bisimides. *Journal of the American Chemical Society* **2006,** *128* (29), 9535-9540; (c) Li, W.-S.; Saeki, A.; Yamamoto, Y.; Fukushima, T.; Seki, S.; Ishii, N.; Kato, K.; Takata, M.; Aida, T., Use of Side-Chain Incompatibility for Tailoring Long-Range p/n Heterojunctions: Photoconductive Nanofibers Formed by Self-Assembly of an Amphiphilic Donor-Acceptor Dyad Consisting of Oligothiophene and Perylenediimide. *Chemistry-an Asian Journal* **2010,** *5* (7), 1566-1572.

26. Schubert, M.; Collins, B. A.; Mangold, H.; Howard, I. A.; Schindler, W.; Vandewal, K.; Roland, S.; Behrends, J.; Kraffert, F.; Steyrleuthner, R.; Chen, Z.; Fostiropoulos, K.; Bittl, R.; Salleo, A.; Facchetti, A.; Laquai, F.; Ade, H. W.; Neher, D., Correlated Donor/Acceptor Crystal Orientation Controls Photocurrent Generation in All-Polymer Solar Cells. *Advanced Functional Materials* **2014**, *24* (26), 4068-4081.

27. (a) Eftaiha, A. a. F.; Sun, J.-P.; Hill, I. G.; Welch, G. C., Recent advances of non-fullerene, small molecular acceptors for solution processed bulk heterojunction solar cells. *Journal of Materials Chemistry A* **2014,** *2* (5), 1201-1213; (b) Walker, B.; Kim, C.; Nguyen, T.-Q., Small Molecule Solution-Processed Bulk Heterojunction Solar Cells. *Chemistry of Materials*

2011, *23* (3), 470-482.

28. Kozma, E.; Catellani, M., Perylene diimides based materials for organic solar cells. *Dyes and Pigments* **2013,** *98* (1), 160-179.

29. Woo, C. H.; Holcombe, T. W.; Unruh, D. A.; Sellinger, A.; Frechet, J. M. J., Phenyl vs Alkyl Polythiophene: A Solar Cell Comparison Using a Vinazene Derivative as Acceptor. *Chemistry of Materials* **2010,** *22* (5), 1673-1679.

30. Sharenko, A.; Proctor, C. M.; van der Poll, T. S.; Henson, Z. B.; Nguyen, T. Q.; Bazan, G. C., A High-Performing Solution-Processed Small Molecule: Perylene Diimide Bulk Heterojunction Solar Cell. *Advanced Materials* **2013,** *25* (32), 4403-4406.

Chapter 7.

Morphological Stability of Organic Solar Cells Based upon Oligo(*p*-phenylenevinylene)-C_{70} Dyad

7.1. Introduction

Organic solar cells (OSCs) have drawn much attention as a sustainable energy source due to potential advantages such as low fabrication cost, light weight and flexibility.[1] One of the most promising OSC device structure is based upon mixed bulk heterojunction (BHJ) thin film.[2] This structure provides a large interface between electron donor and acceptor groups by forming nanometre scale domains and interpenetrating carrier transport networks of components.[2] As a result, efficient charge separation and transport are achieved in the films, leading to high power conversion efficiency (PCE) above 8% with a conjugated polymer as the electron donor and a fullerene derivative as the acceptor.[3]

In this mixed BHJ structure, however, the nanostructure is difficult to control. The morphology of the domains in the films are strongly dependent upon the fabrication conditions, such as the mixing ratio, organic solvent, additives, spin-coating speed and thermal annealing conditions.[4] Even if the resulting film morphology is ideal immediately after fabrication, this could be easily changed by long-term operation or high temperature conditions, because this mixed structure is not the thermodynamically stable state.[5] The fullerene derivative tends to aggregate as a result of diffusion, and thus unfavourable large phase separation is formed.[6] This morphological change drastically lowers device performance.

Extensive research has been done on nanostructure control of domains to overcome the obstacles to high efficiency.[7] In particular, stability has been investigated through the use of compatibilisers,[8] cross-linkable polymers,[9] and block copolymers.[10] Our recent report revealed that fully conjugated diblock copolymer with a fullerene derivative covalently attached to one of the blocks formed an ideal nanoscale pattern in the films and achieved high device performance with high thermal stability.[10a] The system did not rely on the mixing of the donor/acceptor materials, showing that the proper molecular design could lead to the stable nanostructure for OSCs.

Dyad molecules (i.e. covalently attached donor and acceptor groups) have an advantage in terms of nanostructure control, and thus also hold promise for stabilising the phase

separation of domains.[11] In contrast to fullerene-bearing block copolymers, small molecules do not have the problems of the polymers, such as molecular weight distribution, end-group contamination and difficulty in purification, leading to the advantages of less batch-to-batch variation, and better reproducibility.[1c, 12] Nishizawa et al. previously disclosed dyad molecules that showed PCE exceeding 1%.[13] Nevertheless, no reports have covered the construction of morphologically stable OSCs using dyad molecules.

In this paper, the author examine the morphological stability on dyad molecules. The author used previously reported highly crystalline oligo(*p*-pheneylenevinylene) (OPV) as the donor part, and newly introduced C_{70} fullerene, which has high absorption in the visible region, as the acceptor part[14] in the dyad molecule. OSC devices were fabricated and the relations between the thermal stability of film morphology and the device performance parameters were examined. For comparison, mixed BHJ devices with OPV and a C_{70} derivative were also prepared.

7.2. Experimental

Materials and instruments

All chemicals were purchased from Sigma-Aldrich, Tokyo Kasei Kogyo, or Wako Chemicals and used without further purification. Cyclic voltammetry was measured on an HSV-100 automatic polarisation system (Hokuto Denko Company). Anhydrous chloroform was used as the solvent under N_2, and 0.1 M tetrabutylammomium hexafluorophosphate was used as a supporting electrolyte. Glassy carbon was used as the working electrode, a Pt wire was used as the counter electrode and a Ag/AgCl wire was used as the reference electrode. UV-vis absorption spectra were measured on a V-670 system (Nippon Bunko Company). ^{1}H NMR spectra were measured in $CDCl_3$ containing 1% v/v TMS on an Oxford superconducting magnet system (500 MHz). Matrix-assisted laser desorption/ionisation/time-of-flight (MALDI-TOF) MS spectra were measured with dithranol as the matrix on an Applied Biosystems BioSpectrometry Workstation spectrometer (Voyager-DE STR). High-performance liquid chromatography was carried out on a system with a CBM-20A controller (Shimadzu), an LC-6AD pump (Shimadzu), an SPD-20A UV-vis detector and a Luna Silica column (particle size: 5 μm; column length: 250 mm; inner diameter: 21.2 mm) (Phenomenex). Differential scanning calorimetry (DSC) traces were obtained on a Rigaku Thermo plus DSC8230.

Syntheses

The details of the synthetic procedures, and the spectral data from ^{1}H NMR spectroscopy and MALDI-TOF-MS, are described below. OPV was synthesised according to procedures in the literature.[15]

[6,6]-Phenyl-C_{71}-butyric acid

[6,6]-Phenyl-C_{71}-butyric acid methyl ester (500 mg, 0.485mmol), toluene (87.5 mL), acetic acid (75 mL) and HCl (12 M, 30 mL) were added to a 300 mL round-bottom flask. The reaction mixture was stirred for 72 h at 90 ºC. All solvent was removed by evaporation. The solid was washed sequentially with water, methanol, acetone, chlorobenzene, $CHCl_3$ and hexane, yielding black-brown solid (338 mg, 69%).

^{1}H NMR (CS_2, $CDCl_3$, 500MHz): δ (ppm): 7.83-7.85 (d, 2H), 7.45-7.48 (m, 2H), 7.37-7.40 (m, 1H), 2.37-2.47 (m, 4H), 2.01-2.18 (m, 2H)

OPV-C_{70} dyad

[6,6]-Phenyl-C_{71}-butyric acid (107 mg, 0.105 mmol) was placed in a 100 mL two-neck round-bottom flask under N_2, then distilled CS_2 (35 mL) and thionyl chloride (706 μL, 9.79 mmol) were added. The reaction mixture was refluxed overnight at 55 ºC. The solvent was removed, the crude product was dried at 80 ºC for 3 h, and then anhydrous chlorobenzene (10 mL) was added. The flask was covered with aluminium foil, and OPV (70 mg, 0.109 mmol) and NaH (oil dispersion 50–72%, 17.8 mg) that had been washed with hexane were added. The reaction mixture was stirred at room temperature for 48 h and then purified by column chromatography using silica gel and $CHCl_3$ as eluent and by HPLC using $CHCl_3$ as eluent. The obtained product was precipitated in hexane and filtered, yielding the dyad as a brown solid (50 mg, yield: 33%).

^{1}H NMR ($CDCl_3$, 500MHz): δ (ppm): 7.87-7.89 (m, 2H), 7.40-7.54 (m, 17H), 6.96-7.22 (m, 8H), 6.90-6.92 (d, 4H), 4.23-4.25 (t, 2H), 4.20-4.22 (t, 2H), 3.92-9.94 (m, 5H), 3.84 (s, 6H), 3.61-3.79 (m,18H), 2.46-2.49 (m, 2H), 2.39-2.43 (m, 2H), 2.03-2.20 (m, 2H).
MALDI-TOF-MS (*m/z*): 1855.51 (M^+)

Photovoltaic device preparation and measurement

Using OPV-C_{70} dyad and BHJ of OPV:$PC_{70}BM$, photovoltaic devices were prepared in a structure of indium tin oxide (ITO)/PEDOT:PSS/Active layer/$PC_{70}BM$/Ca/Al. ITO-coated glass substrate (sheet resistance: 10 Ω sq^{-1}, Geomatech, Japan) was cleaned by ultrasonication in detergent, water, acetone, 2-propanol and water. After the substrate was dried, PEDOT:PSS (H. C. Stark) was spin-coated (4000 rpm) onto ITO. The film was dried

at 150 ºC under N_2 for 20 min. After cooling the substrate, $CHCl_3$ solution of OPV-C_{70} dyad (10 mg/mL) or mixture of OPV and $PC_{70}BM$ (4.62/5.55 mg/mL) was spin-coated (2500 rpm). Films with OPV-C_{70} dyad were thermally annealed at 80, 110, 150 °C for 5 min under N_2 atmosphere before deposition of buffer layer and electrode. In thermal stability measurement, films with OPV-C_{70} dyad and OPV/$PC_{70}BM$ were thermally annealed at 110 °C for 5 min, 1 day, 2 days and 3 days, respectively, under N_2 atmosphere. $PC_{60}BM$ (20 nm) buffer layer and, Ca (20 nm) and Al (40 nm) electrodes were evaporated onto the organic layer under high vacuum (6×10^{-4} Pa).

I-V characteristics of the devices were measured under simulated solar light illumination (AM 1.5, 100 mW cm^{-2}) from a 150 W xenon lamp (PEC-L11, Peccell Technologies, Inc., Japan). The light intensity was calibrated with a standard silicon solar cell (BS520, Bunko-Keiki, Japan). The active area of the devices was defined to be 0.12 cm^2 by a photomask. The external quantum efficiency (EQE) of the devices was measured on a Hypermonolight SM-250F system (Bunko-Keiki, Japan). Atomic force microscopy (AFM) images were obtained on a Digital Instrumental Nanoscope 31 operated in tapping mode. Film thickness was measured by surface profilometry (Dektak 6M, ULVAC, Japan).

7.3. Results and discussion

Syntheses

C_{70} fullerene-bearing OPV dyad molecule (OPV-C_{70} dyad) was synthesised by esterification of OPV and C_{70} fullerene derivative with an acyl chloride group (Scheme 7.1). The synthetic route to the OPV donor part has been reported previously.[15] The products were characterised by ^{1}H NMR and MALDI-TOF-MS, and synthetic details and spectral data are described in above. ^{1}H NMR chart of OPVC_{70}Dyad used for the OSC fabrications is available in ESI. All the peaks of OPV-C_{70} dyad were assigned and the ratios of the peak area were consistent with the chemical structure of OPV-C_{70} dyad as described in the experimental sections. Besides the peak of water at 1.56 ppm, only a few minor unknown peaks were observed in the aliphatic region at 1.25, 0.87, 0.49 ppm.

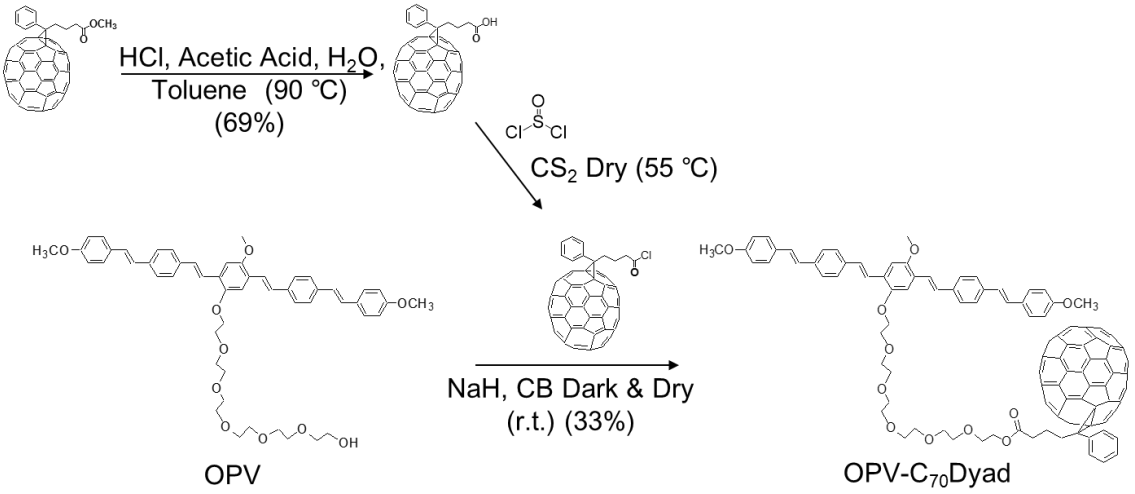

Scheme 7.1 Synthetic route to OPV-C_{70} dyad.

Molecular properties

Absorption spectra

Absorption spectra of OPV-C_{70} dyad and OPV in $CHCl_3$ solution are shown in Figure 7.1a. An absorption shoulder from 480 nm to 700 nm appeared in the spectrum of OPV-C_{70} dyad, which corresponds to the absorption of C_{70} fullerene. Compared with previously reported C_{60}-bearing OPV (OPV-C_{60} dyad),[13a] OPV-C_{70} showed higher absorption in the visible region due to the absorption of C_{70} fullerene. Absorption spectrum of OPV-C_{70} dyad in thin film is shown in Figure 7.1b. The peak of OPV-C_{70} dyad is shifted from 420 nm in solution to 440 nm in thin film. The redshift in OPV absorption could be attributed to the formation of *J*-aggregation in the donor part.[16] This result indicates that strong π-π interaction was present in the OPV part of OPV-C_{70} dyad, and agrees with our previous report.[13a]

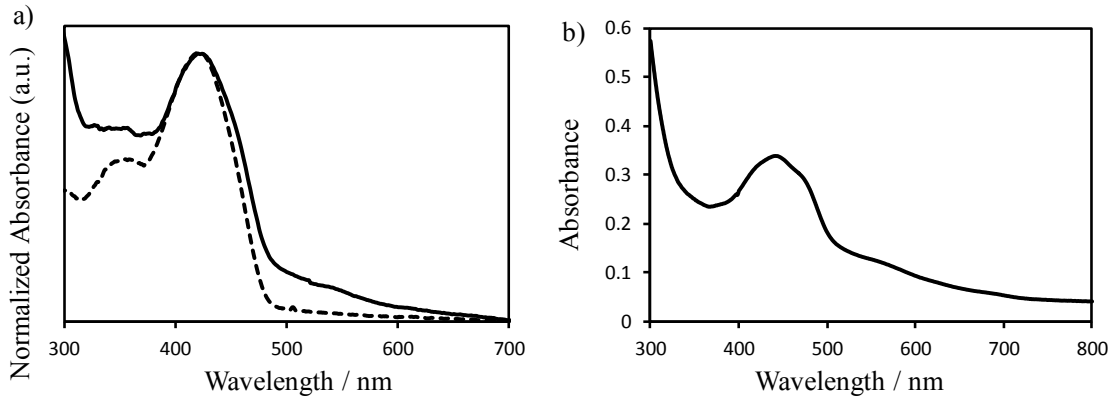

Figure 7.1 Absorption spectra of (a) OPV (doted line) and OPV-C_{70} dyad (solid line) in $CHCl_3$ solution and (b) OPV-C_{70} dyad in thin film.

Cyclic voltammetry (CV)

The first oxidation (E_{ox}) and the reduction potentials (E_{red}) of OPV-C_{70} dyad relative to the redox potential of Fc/Fc^+ were determined by cyclic voltammetry (CV) in $CHCl_3$ solution. The energy levels of OPV-C_{70} dyad were estimated by assuming the Fc/Fc^+ potential to be −4.8 eV relative to the vacuum level. Cyclic voltammogram of OPV-C_{70} dyad was shown in Figure 7.2a. Half potentials of E_{ox} and E_{red}, were +0.44 and −1.17 V, respectively. E_{ox} and E_{red} correspond to HOMO of OPV (electron donor part) and LUMO of the fullerene derivative (electron acceptor part). E_{ox} of OPV-C_{70} dyad was larger than low band gap dyad that the author reported in Chapter 4,[13b] which lead to higher V_{OC} of OPV-C_{70} dyad.

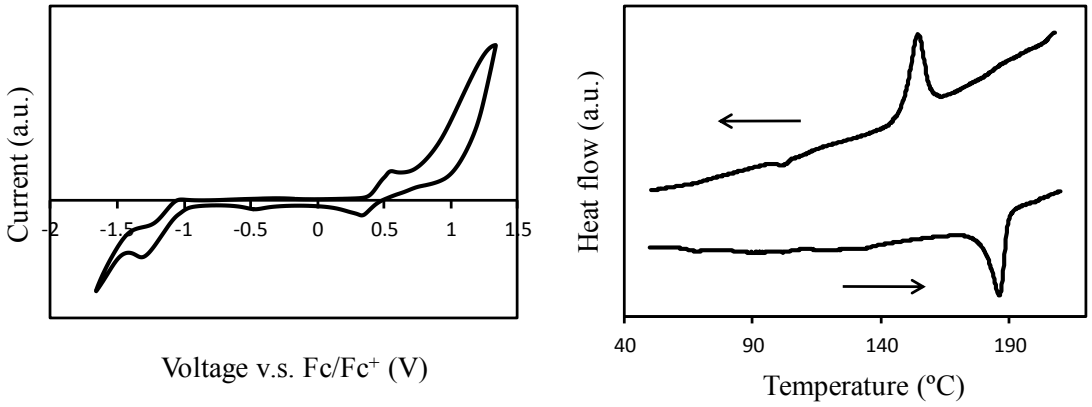

Figure 7.2. (a) Cyclic voltammogram of OPV-C_{70} dyad , (b) DSC chart of OPV-C_{70} dyad.

Differential scanning calorimetry (DSC)

The DSC chart of OPV-C_{70} dyad is shown in Figure 7.2b. One endothermic peak (187 ºC) and one enxothermic peak (154 ºC) were observed. The phase transition temperatures of OPV-C_{70} dyad were similar to those of OPV-C_{60} dyad which had high crystallinity (192 ºC and 152 ºC, respectively).[13a]

Photovoltaic properties

The OSC devices were fabricated with a configuration of ITO/ PEDOT:PSS/OPV-C_{70} dyad/[6,6]-phenyl-C61-butyric acid methyl ester ($PC_{60}BM$) (20 nm)/Ca (20 nm)/Al (40 nm). $PC_{60}BM$ buffer layer was evaporated to suppress the leakage current due to Al penetration. The solution of OPV-C_{70} dyad had a concentration of 10 g L^{-1}, and the active layers were spin-coated at 2500 rpm. Before forming the $PC_{60}BM$, Ca and Al layers, the devices were thermally annealed at 110 °C for 5 min under N_2 atmosphere in optimized condition. The devices annealed at 80 °C and 150 °C were also fabricated. Thermal

annealing was performed before deposition of those layers to avoid the diffusion of $PC_{60}BM$ into the active layer.[17] The OSC devices were evaluated under simulated solar light illumination (AM 1.5, 100 mW cm^{-2}) through a photomask with an aperture size of 0.12 cm^2. Device fabrication conditions and performance parameters were summarized in ESI.

The external quantum efficiency (EQE) spectrum of the device with OPV-C_{70} dyad annealed at 110 °C is shown in Figure 7.3a. The device based upon OPV-C_{70} dyad showed an EQE value of 0.45 at 450 nm, which is higher than that of other dyads because the highly crystalline nature of OPV realised efficient hole transport.[13a] A broad photocurrent response up to 700 nm was observed due to the absorption of C_{70} fullerene in the visible region.

The *J-V* plot of the best device annealed at 110 °C under AM 1.5 illumination is shown in Figure 7.3b. The device showed a relatively high fill factor (FF) of 0.46 due to the strong π-π interactions in OPV, as well as high open-circuit voltage (V_{OC}) because of the low-lying HOMO energy level of OPV. As expected from the broad absorption and photocurrent response of C_{70} fullerene in the visible region, the short circuit current density (J_{SC}) increased from 3.3 mA cm^{-2} for OPV-C_{60} dyad to 4.6 mA cm^{-2} for OPV-C_{70} dyad. This photocurrent increase led to PCE of 1.92%. This is the highest PCE reported to date for dyad-based OSCs, exceeding the value of 1.50% reported for oligo(fluorene-*alt*-bithiophene)-perylene diimide dyad[18] as well as the value of 1.28% for OPV-C_{60} dyad.[13a, 16]

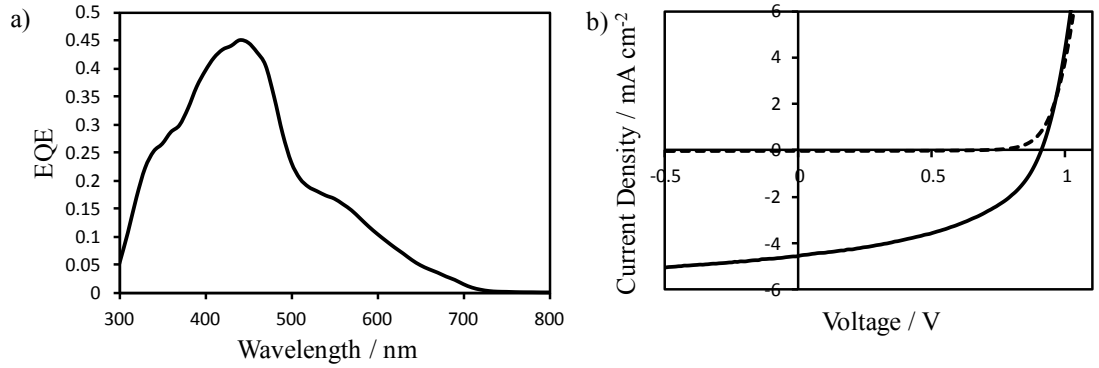

Figure 7.3. (a) EQE spectrum of OSC devices of OPV-C_{70} dyad and (b) *J-V* curves of the OSC devices based upon OPV-C_{70} dyad (dotted line: in the dark; solid line: under simulated solar light illumination (AM 1.5).

Thermal stability

The thermal stability of morphology in the films with OPV-C_{70} dyad was studied compared with physically mixed BHJ films with OPV and [6,6]-phenyl-C71-butyric acid methyl ester ($PC_{70}BM$). The devices based upon OPV-C_{70} dyad were fabricated under the same conditions except for the thermal annealing time. The mixed solution of OPV and $PC_{70}BM$ for the BHJ was prepared with the concentrations of 4.62 and 5.55 g L^{-1}, respectively, which had the same molar ratio as OPV-C_{70} dyad (1:1). The BHJ device configuration was ITO/PEDOT:PSS/active layer (OPV:$PC_{70}BM$)/ $PC_{60}BM$ (20 nm)/Ca (20 nm)/Al (40 nm). The active layers were spin-coated at 2500 rpm. Before the deposition of $PC_{60}BM$, Ca and Al, all the devices were thermally annealed at 110 °C for 5 min, 1 day, 2 days and 3 days under N_2 atmosphere. For comparison, devices not subject to thermal annealing were also fabricated for both OPV-C_{70} dyad and OPV:$PC_{70}BM$ BHJ. Thickness of the active layers of both OPV-C_{70} dyad and OPV:$PC_{70}BM$ BHJ were 80 nm in as-casted film measured by surface profilometry. This value remained unchanged after the prolonged annealing.

Atomic force microscopy (AFM) images of mixed films and dyad films subject to different annealing times are shown in Figure 7.4 (images after annealing for 1, 2 and 3 days are in ESI). For BHJ films, the aggregation sizes were over 100 nm even in the as-cast film, and larger aggregation was observed as annealing time was prolonged. Roughness factors (R_a) of these films were 2.0, 3.3, 3.4, 3.9 and 3.9 nm for as-cast film and films annealed for 5 min, 1, 2 and 3 days, respectively. The gradual increase of the roughness with longer annealing time indicates that the morphology changed in the mixed films by aggregation of the domains. On the other hand, such large phase separation was not observed in OPV-C_{70} dyad films, although there were small patterns. Compared with the mixed films, the dyad films had smaller surface roughness, R_a: 0.29, 0.98, 0.85, 0.93 and 0.86 nm for as-cast film and films annealed for 5 min, 1 day, 2 days and 3 days, respectively. This difference in the AFM images demonstrated the suppression of the large phase separation and the improvement of morphological thermal stability of domains in the dyad films.

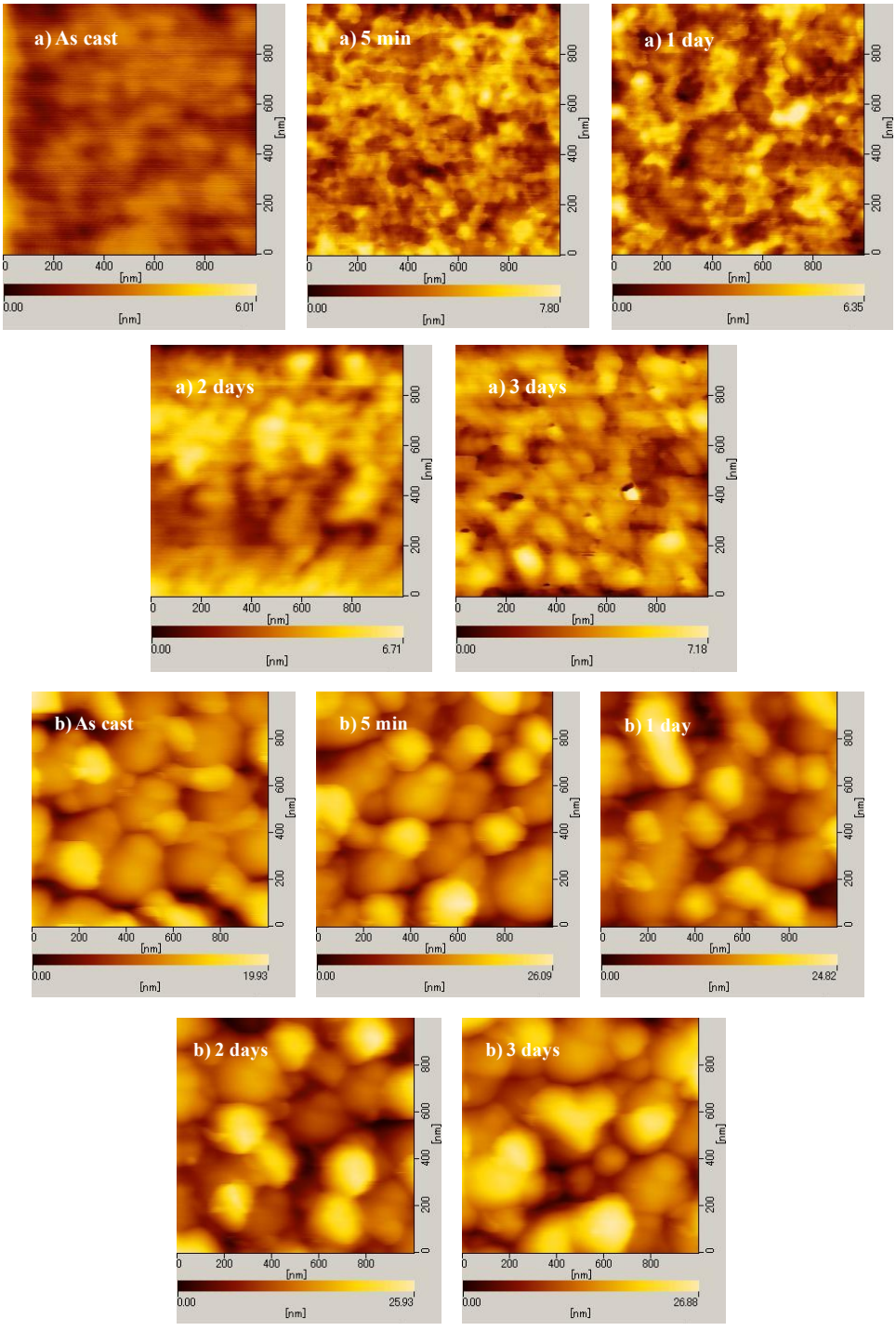

Figure 7.4. AFM images of (a) OPV-C_{70} dyad (b) OPV:$PC_{70}BM$ films after thermal annealing at 110 °C for 5 min, 1 day, 2 days and 3 days. Annealing times are presented in the images.

Selected device performance parameters for different annealing times are plotted in Figure 7.5, and all the parameters are available in ESI. The mixed devices showed a low PCE of 0.65% for the as-cast film. Moreover, PCE decreased rapidly to 0.32% upon annealing for 5 min, and then gradually decreased upon annealing for longer times due to the deterioration of J_{SC} and FF. The mixed device annealed for 3 days showed J_{SC} of 1.13 mA cm^{-2}, FF of 0.31 and PCE of 0.23%. In the mixed films, the phase separation was of a scale larger than the typical exciton diffusion length, as observed by AFM (Figure 7.4a, b); such phase separation could decrease the size of the interface between the electron donor and acceptor. This could lead to inefficient charge separation and thus smaller photocurrent. Furthermore, this decrease of the interface area proceeded with longer thermal annealing, as suggested by the R_a increase. According to a previous report, deterioration of device performance was also observed in P3HT: $PC_{60}BM$ mixed BHJ devices, which is one of the most widely studied combinations in OSCs, and thermal annealing for 80 h at 130 °C decreased the PCE from 3.0% to 0.6% due to the aggregation of $PC_{60}BM$.[10a] Diffusion of $PC_{60}BM$ within the active layer was also observed at 110 °C in another paper.[17b] In contrast, all the parameters of the dyad devices were constant within this period of thermal annealing. Annealing for 5 min improved J_{SC} from 3.45 to 3.93 mA cm^{-2}, FF from 0.45 to 0.48 and PCE from 1.37 to 1.66%. Even after 3 days of thermal annealing, the devices showed high PCE of 1.52%. J_{SC} was much higher in the dyad devices than the mixed devices because of the larger donor/acceptor interface due to the suppression of large phase separation. The dyad devices also showed higher FF due to the construction of an interpenetration network by the highly crystalline OPV group. Furthermore, this ideal nanostructure and high device performance were preserved after long thermal annealing. These comparisons indicated that the dyad film had a thermally stable morphology.

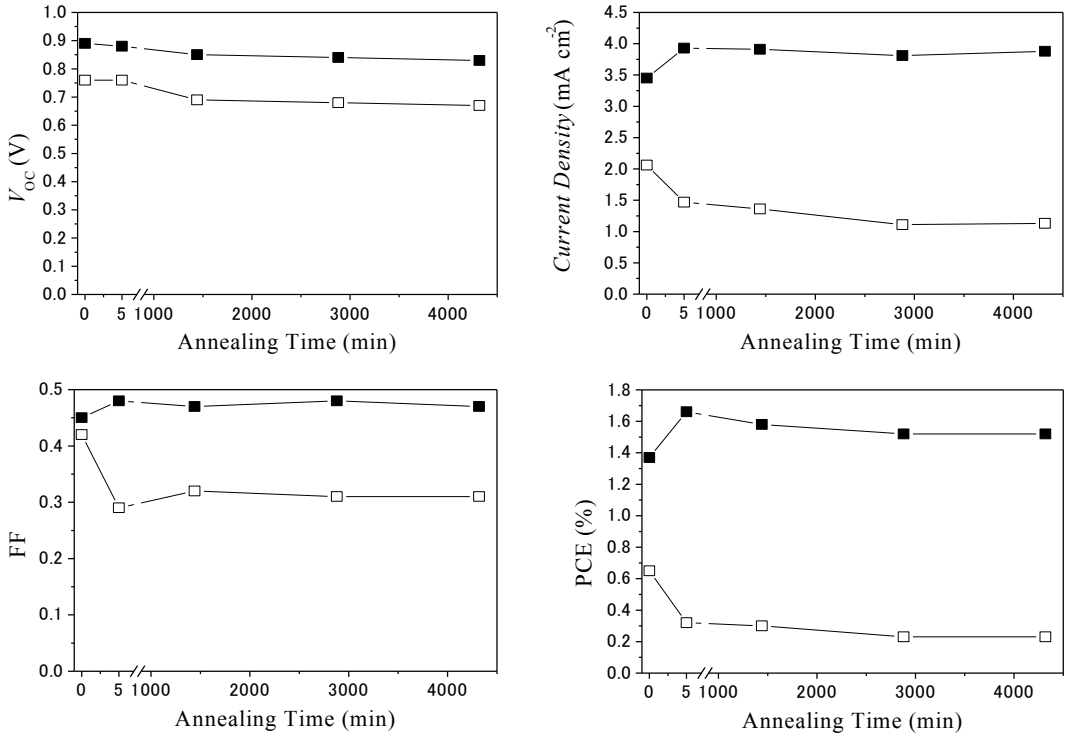

Figure. 7.5 Device performances with different annealing time (as cast, 5 minutes, 1 day, 2 days, 3 days).

Table 7.1. Summary of the best device performance based upon OPV-C_{70} dyad with different annealing temperature.

Materials	Annealing temperature (°C)	Annealing time	J_{SC} (mA cm^{-2})	V_{OC} (V)	FF	PCE (%)
OPV-C_{70} dyad	80	5 min	4.20	0.83	0.46	1.59
	110	5 min	4.55	0.91	0.46	1.92
	150	5 min	4.36	0.81	0.44	1.54

Table 7.2. Summary of device performance parameters for (a) OPV-C_{70} dyad and (b) OPV:$PC_{70}BM$ under different annealing time at 110 °C.

Materials	Annealing time	J_{SC} (mA cm^{-2})	V_{OC} (V)	FF	PCE (%)
(a) OPV-C_{70} dyad	As cast	3.45	0.89	0.45	1.37
	5 min	3.93	0.88	0.48	1.66
	1 day	3.91	0.85	0.47	1.58
	2 days	3.81	0.84	0.48	1.52
	3 days	3.88	0.83	0.47	1.52
(b) OPV:$PC_{70}BM$	As cast	2.06	0.76	0.42	0.65
	5 min	1.47	0.76	0.29	0.32
	1 day	1.36	0.69	0.32	0.30
	2 days	1.11	0.68	0.31	0.23
	3 days	1.13	0.67	0.31	0.23

7.4. Conclusions

In summary, the introduction of C_{70} fullerene improved light-harvesting ability, and realised high PCE of 1.92%. Furthermore, the dyad films exhibited much higher morphological stability even under prolonged annealing, in contrast to the mixed BHJ films. This study demonstrates the considerable promise of the donor-acceptor dyad approach for realising efficient and stable organic solar cells.

Chapter 7 is reproduced by permission of the PCCP Owner Societies.
S. Izawa, K. Hashimoto, and K. Tajima, *Phys. Chem. Chem. Phys.*, **2012**, *14*, 16138-16142.

References

1. (a) Gunes, S.; Neugebauer, H.; Sariciftci, N. S., Conjugated polymer-based organic solar cells. *Chemical Reviews* **2007,** *107* (4), 1324-1338; (b) Brabec, C. J.; Gowrisanker, S.; Halls, J. J. M.; Laird, D.; Jia, S. J.; Williams, S. P., Polymer-Fullerene Bulk-Heterojunction Solar Cells. *Advanced Materials* **2010,** *22* (34), 3839-3856; (c) Walker, B.; Kim, C.; Nguyen, T.-Q., Small Molecule Solution-Processed Bulk Heterojunction Solar Cells. *Chemistry of Materials* **2011,** *23* (3), 470-482; (d) Cheng, Y.-J.; Yang, S.-H.; Hsu, C.-S., Synthesis of Conjugated Polymers for Organic Solar Cell Applications. *Chemical Reviews* **2009,** *109* (11), 5868-5923.

2. (a) Yu, G.; Gao, J.; Hummelen, J. C.; Wudl, F.; Heeger, A. J., POLYMER PHOTOVOLTAIC CELLS - ENHANCED EFFICIENCIES VIA A NETWORK OF INTERNAL DONOR-ACCEPTOR HETEROJUNCTIONS. *Science* **1995,** *270* (5243), 1789-1791; (b) Hiramoto, M.; Fujiwara, H.; Yokoyama, M., 3-LAYERED ORGANIC SOLAR-CELL WITH A PHOTOACTIVE INTERLAYER OF CODEPOSITED PIGMENTS. *Applied Physics Letters* **1991,** *58* (10), 1062-1064.

3. (a) He, Z.; Zhong, C.; Huang, X.; Wong, W.-Y.; Wu, H.; Chen, L.; Su, S.; Cao, Y., Simultaneous Enhancement of Open-Circuit Voltage, Short-Circuit Current Density, and Fill Factor in Polymer Solar Cells. *Advanced Materials* **2011,** *23* (40), 4636-4643; (b) Service, R. F., Outlook Brightens for Plastic Solar Cells. *Science* **2011,** *332* (6027), 293-293.

4. (a) Yang, X. N.; van Duren, J. K. J.; Rispens, M. T.; Hummelen, J. C.; Janssen, R. A. J.; Michels, M. A. J.; Loos, J., Crystalline organization of a methanofullerene as used for plastic solar-cell applications. *Advanced Materials* **2004,** *16* (9-10), 802-806; (b) Chirvase, D.; Parisi, J.; Hummelen, J. C.; Dyakonov, V., Influence of nanomorphology on the photovoltaic action of polymer-fullerene composites. *Nanotechnology* **2004,** *15* (9), 1317-1323; (c) Nguyen, L. H.; Hoppe, H.; Erb, T.; Gunes, S.; Gobsch, G.; Sariciftci, N. S., Effects of annealing on the nanomorphology and performance of poly(alkylthiophene): fullerene bulk-heterojunction solar cells. *Advanced Functional Materials* **2007,** *17* (7), 1071-1078.

5. Gholamkhass, B.; Holdcroft, S., Toward Stabilization of Domains in Polymer Bulk Heterojunction Films. *Chemistry of Materials* **2010,** *22* (18), 5371-5376.

6. Bertho, S.; Janssen, G.; Cleij, T. J.; Conings, B.; Moons, W.; Gadisa, A.; D'Haen, J.; Goovaerts, E.; Lutsen, L.; Manca, J.; Vanderzande, D., Effect of temperature on the morphological and photovoltaic stability of bulk heterojunction polymer: fullerene solar cells. *Solar Energy Materials and Solar Cells* **2008,** *92* (7), 753-760.

7. Jorgensen, M.; Norrman, K.; Gevorgyan, S. A.; Tromholt, T.; Andreasen, B.; Krebs, F. C., Stability of Polymer Solar Cells. *Advanced Materials* **2012,** *24* (5), 580-612.

8. Sivula, K.; Ball, Z. T.; Watanabe, N.; Frechet, J. M. J., Amphiphilic diblock copolymer

compatibilizers and their effect on the morphology and performance of polythiophene: Fullerene solar cells. *Advanced Materials* **2006,** *18* (2), 206-210.

9. Miyanishi, S.; Tajima, K.; Hashimoto, K., Morphological Stabilization of Polymer Photovoltaic Cells by Using Cross-Linkable Poly(3-(5-hexenyl)thiophene). *Macromolecules* **2009,** *42* (5), 1610-1618.

10. (a) Miyanishi, S.; Zhang, Y.; Tajima, K.; Hashimoto, K., Fullerene attached all-semiconducting diblock copolymers for stable single-component polymer solar cells. *Chemical Communications* **2010,** *46* (36), 6723-6725; (b) Lin, Y.; Lim, J. A.; Wei, Q.; Mannsfeld, S. C. B.; Briseno, A. L.; Watkins, J. J., Cooperative Assembly of Hydrogen-Bonded Diblock Copolythiophene/Fullerene Blends for Photovoltaic Devices with Well-Defined Morphologies and Enhanced Stability. *Chemistry of Materials* **2012,** *24* (3), 622-632.

11. (a) Segura, J. L.; Martin, N.; Guldi, D. M., Materials for organic solar cells: the C-60/pi-conjugated oligomer approach. *Chemical Society Reviews* **2005,** *34* (1), 31-47; (b) Roncali, J., Single Material Solar Cells: the Next Frontier for Organic Photovoltaics? *Advanced Energy Materials* **2011,** *1* (2), 147-160; (c) Roncali, J., Linear pi-conjugated systems derivatized with C-60-fullerene as molecular heterojunctions for organic photovoltaics. *Chemical Society Reviews* **2005,** *34* (6), 483-495.

12. Walker, B.; Tomayo, A. B.; Dang, X. D.; Zalar, P.; Seo, J. H.; Garcia, A.; Tantiwiwat, M.; Nguyen, T. Q., Nanoscale Phase Separation and High Photovoltaic Efficiency in Solution-Processed, Small-Molecule Bulk Heterojunction Solar Cells. *Advanced Functional Materials* **2009,** *19* (19), 3063-3069.

13. (a) Nishizawa, T.; Lim, H. K.; Tajima, K.; Hashimoto, K., Efficient dyad-based organic solar cells with a highly crystalline donor group. *Chemical Communications* **2009,** (18), 2469-2471; (b) Izawa, S.; Hashimoto, K.; Tajima, K., Efficient charge generation and collection in organic solar cells based on low band gap dyad molecules. *Chemical Communications* **2011,** *47* (22), 6365-6367.

14. He, Y.; Li, Y., Fullerene derivative acceptors for high performance polymer solar cells. *Physical Chemistry Chemical Physics* **2011,** *13* (6), 1970-1983.

15. Nishizawa, T.; Lim, H. K.; Tajima, K.; Hashimoto, K., Highly Uniaxial Orientation in Oligo(p-phenylenevinylene) Films Induced During Wet-Coating Process. *Journal of the American Chemical Society* **2009,** *131* (7), 2464-2465.

16. Wuerthner, F.; Kaiser, T. E.; Saha-Moeller, C. R., J-Aggregates: From Serendipitous Discovery to Supramolecular Engineering of Functional Dye Materials. *Angewandte Chemie-International Edition* **2011,** *50* (15), 3376-3410.

17. (a) Chen, D.; Liu, F.; Wang, C.; Nakahara, A.; Russell, T. P., Bulk Heterojunction Photovoltaic Active Layers via Bilayer Interdiffusion. *Nano Letters* **2011,** *11* (5), 2071-2078; (b)

Treat, N. D.; Brady, M. A.; Smith, G.; Toney, M. F.; Kramer, E. J.; Hawker, C. J.; Chabinyc, M. L., Interdiffusion of PCBM and P3HT Reveals Miscibility in a Photovoltaically Active Blend (vol 1, pg 82, 2010). *Advanced Energy Materials* **2011,** *1* (2), 145-145.

18. Bu, L.; Guo, X.; Yu, B.; Qu, Y.; Xie, Z.; Yan, D.; Geng, Y.; Wang, F., Monodisperse Co-oligomer Approach toward Nanostructured Films with Alternating Donor-Acceptor Lamellae. *Journal of the American Chemical Society* **2009,** *131* (37), 13242-13243.

Chapter 8.

Summary and Perspective

In this thesis study, the nanostructure of the D/A interface and the domain structure were controlled by the rational ways, and the effects of the difference in the nanostructures to the photovoltaic performances were studied.

At first, fullerene-based surfactants with semifluoroalkyl chains bearing one of five different functional groups at the end were synthesized and used for the facile surface modification of organic semiconductor films in Chapter 2. Surface analysis showed that the modifiers formed surface segregated monolayer (SSM) and the functional groups were exposed at the surface.

In Chapter 3, I reported the manipulation of the energy levels of the first monolayer at D/A interfaces in planar heterojunction OPVs by using SSM. "Cascade" energy landscape in which the first monolayer of the acceptor interface has a higher energy level showed thermal activation-free charge generation by photo-irradiation (i.e. little geminate recombination). At the same time, the energy of the interfacial charge transfer state was increased and the bimolecular charge recombination was suppressed. These effects resulted in higher open circuit voltage and fill factor without losing much of the photocurrent generation from the donor absorption. The results demonstrate that the energetics of the first monolayer at the donor/acceptor interfaces have dominant effects on the photophysics in organic photovoltaic devices and "cascade" energy landscape is the key structure to achieve the suppression of both geminate and bimolecular recombinations. These findings also give us the insights about the mechanism of efficient free charge generation in OPVs, which is an important fundamental question. The results suggested that interfacial energy landscape which destabilize the energy of interfacial charge transfer state is highly important for the free charge formation and also implies that charge separation occurs via interfacial charge transfer state.

In Chapter 4, low band gap dyad molecules were prepared that have absorption spectra matched well with the solar spectrum. The longer π-conjugation in the donor parts of the dyad helped the construction of efficient charge transport pathways in the active layer. Under A.M. 1.5 illumination, the devices have achieved the highest J_{SC} (4.79 mA cm^{-2}) and FF (0.46) in dyad-based organic solar cells to date.

In Chapter 5, low-band-gap dyad molecules containing diketopyrrolopyrole (DPP) chromophore and hexathiophene were designed and synthesized in combination with C_{60} and C_{70} derivatives as the electron acceptors. The donor part with a shorter alkyl side chain showed stronger π-π interaction and an enhancement of absorption in the longer-wavelength region, which led to higher J_{SC} of the devices.

A dyad molecule with oligo(*p*-phenylenevinylene) as the electron donor and naphthalene diimide (NDI) as the acceptor was synthesized in Chapter 6. The X-ray diffraction measurements of the film structure showed that the oligo(*p*-phenylenevinylene) and NDI moieties of the dyad crystallized separately in the spin-coated films. This is in striking contrast to the fullerene dyads, in which the introduction of bulky fullerenes severely disrupted the packing of oligo(*p*-phenylenevinylene). The separated crystallization in the dyad was attributed to the planar shape of the acceptor and the differences in the crystalline structures of planar NDI and rod-like OPV.

Finally, an oligo(*p*-phenylenevinylene)–C_{70} dyad achieved the highest power conversion efficiency (1.92%) in dyad-based organic solar cells to date as shown in Chapter 7. Covalent attachment in the dyad prevented large phase separation, resulting in good morphological and device stability at high temperatures as compared with mixed bulk heterojunction devices. These results suggested the control of the domain structures by the donor-acceptor dyad approach had high potentials for realizing highly efficient and stable OPVs.

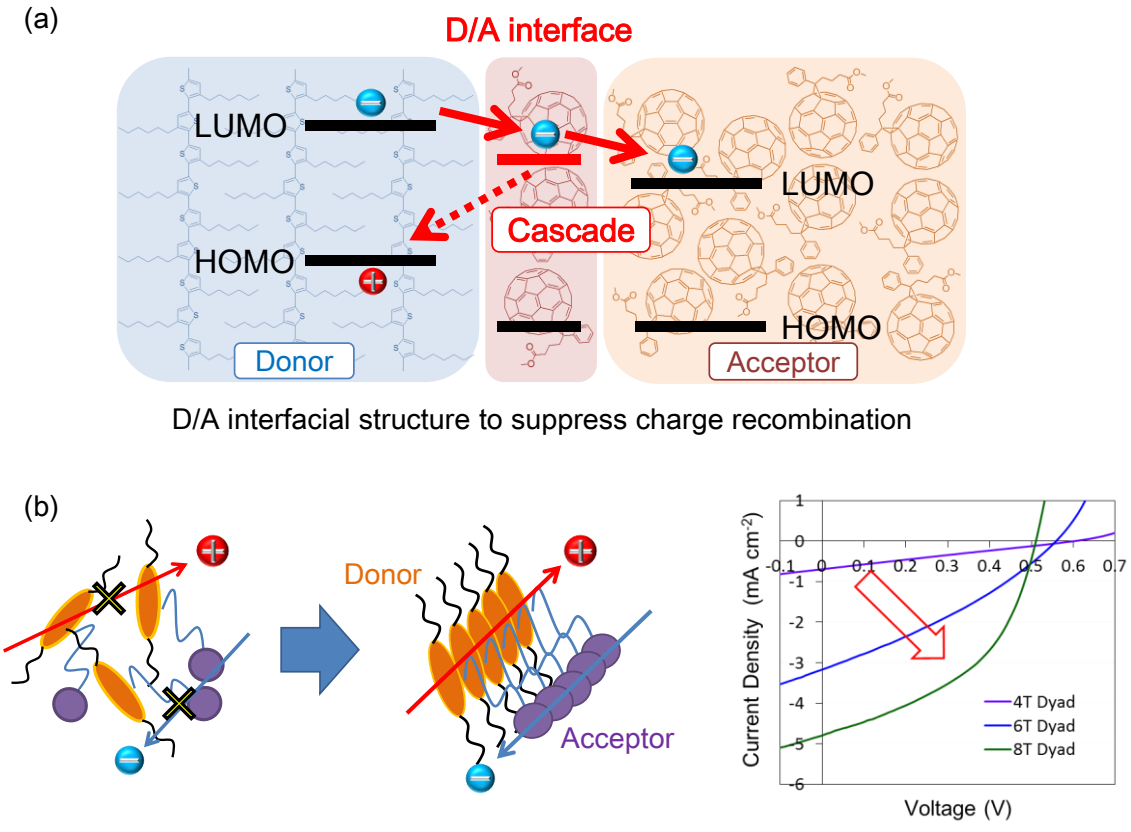

Figure 7.1. Schematic images of nanostructure control in this study, (a) the energy structure at the D/A interface, (b) the D/A domain structure in dyad films.

These findings in the thesis gave us the insights of the nanostructure for further improvement of OPVs. Specifically, "cascade" energy landscape could be extended to the D/A interfaces in the BHJ to suppress both geminate and bimolecular recombination. Mixed BHJ structure is difficult to control the interfacial energetics precisely because the donor and the acceptor are simply mixed. I also found that the domain structures could be controlled by the donor-acceptor dyad approach. The position of donor and acceptor in dyad films are easy to regulate, therefore appropriate molecular design of dyad molecules enables us to locate the "cascade" energy landscape at the middle of D/A domains as shown in Fig. 7.2. The nanostructure control of both D/A interface and D/A domains could be a breakthrough for high performance OPVs.

"Cascade" energy landscape can suppress of both geminate and bimolecular recombinations, but there still exist LUMO offsets between the donor and the acceptor to dissociate the excitons, and between the first monolayer at the D/A interface and the bulk to dissociate interfacial charge transfer state. The energy offsets causes the energy loss in output voltage of OPVs. Therefore, the next big challenge is to search for the minimum energy offsets which can form the free charges. The other way to decrease the energy offsets is to decrease the exciton binding energy and the Coulomb binding energy of the charges. Thus, tailoring local dielectric constant which affects both the binding energies might also be important approach to realize high performance OPVs.

Nanostructure control at the D/A interface and the D/A domains can be applicable not only to OPVs but also to other fields in organic electronics. I found the charge recombination occurred via the trap in which the first monolayer of the acceptor interface has a lower energy level than the bulk. Alignment of the "trap" energy landscape at the middle of D/A domains will lead to the regulation of the charge recombination sites in light emitting devices. The approach of the nanostructure control in the organic semiconductor films will realize precise control of the charge transport, charge separation and recombination processes and will bring the bright futures of organic electronics devices.

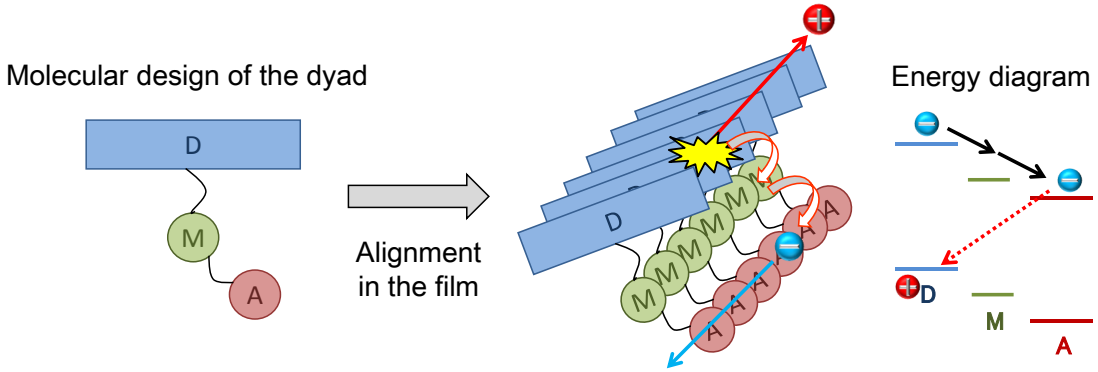

Figure 7.2. Schematic image of the introduction of "cascade" energy landscape into D/A interface in BHJ by the donor-acceptor dyad approach

Acknowledgements

This study has been conducted under the supervision of Prof. Kazuhito Hashimoto. First of all, I am greatly thankful to Prof. Hashimoto for providing me an opportunity to study in his group. His sharp and fruitful comments for scientific research have always encouraged me. I have learned a lot from him, and his scientific insight, research vision, logical thinking and attractive presentation have been very important guidance for me.

I am also really thankful to Dr. Keisuke Tajima for giving me valuable comments and constructive advice to promote this research. I have been always encouraged a lot while discussion with him.

I am really thankful to the members in Dr. Tajima's team; Dr. Kyohei Nakano and Dr. Kouki Akaike helped me for the construction of the systems for the device measurements, and gave me valuable advice; Ms. Kaori Suzuki helped me for the device fabrication; Dr. Takeshi Nishizawa, Dr. Qingshuo Wei, Dr. Shoji Miyanishi for their helpful advice on research directions as well as experiments; Dr. Erjun Zhou, Mr. Shigeyoshi Sato for their helpful advice on organic synthesis; Dr. Yufei Zhong, Mr. Akira Tada for their helpful advice on device fabrication; Mr. Jusha Ma for his helpful advice on characterization; Mr. Sosuke Higuchi, Ms. Junko Sakai, Mr. Masahiro Furuhashi, Ms. Inori Onishi, Mr. Peihong Chen, Mr. Fanji Wang, Mr. Tomohiro Mayumi, for their kind help.

2D-GIXRD experiments were performed at BL19B2 at SPring-8 with the approval of the Japan Synchrotron Radiation Research Institute (JASRI) (Proposal2013A1634). I would like to thank Dr. Itaru Osaka at RIKEN and Dr. Tomoyuki Koganezawa at the Japan Synchrotron Radiation Research Institute for help with 2D-GIXRD measurements. I would like to thank Prof. Ohkita at Kyoto Univ. for his advice on EL measurements. I thank JSPS for financial support.

I would like to thank Prof. Kayano Sunada, Prof. Syuji Nakanishi and Dr. Ryuhei Nakamura for giving me important comments and suggestions during seminar.

I am also thankful to Ms. Kaoru Nakajima, Ms. Yoko Shinoda, Ms. Miyako Iyonaga, Ms. Naoko Mitsuzawa for their great support to do the research.

I am really grateful to all the staff and members in Prof. Hashimoto's laboratory and Dr. Tajima's team in RIKEN for their help and discussion.

Finally, I would like to thank my family and fiends, who always support me.

Seiichiro Izawa

List of Publications

For PhD thesis

[1] **S. Izawa**, K. Hashimoto, and K. Tajima, *Chem. Commun.*, **2011**, *47*, 6365-6367.
"Efficient Charge Generation and Collection in Organic Solar Cells Based on Low Band Gap Dyad Molecules"

[2] **S. Izawa**, K. Hashimoto, and K. Tajima, *Synth. Met.*, **2012**, *162*, 2201-2205.
" Synthesis, Characterization, and Photovoltaic Properties of Diketopyrrolopyrrole-oligothiophene/Fullerene Dyads"

[3] **S. Izawa**, K. Hashimoto, and K. Tajima, *Phys. Chem. Chem. Phys.*, **2012**, *14*, 16138-16142.
"Morphological Stability of Organic Solar Cells Based upon Oligo(*p*-phenylenevinylene)-C_{70} Dyad"

[4] **S. Izawa**, K. Hashimoto, and K. Tajima, *Phys. Chem. Chem. Phys.*, **2014**, *16*, 16383-16387.
"Surface Functionalization of Organic Semiconductor Films by Segregated Monolayers"

[5] **S. Izawa**, T. Nishizawa, K. Hashimoto, T. Koganezawa, and K. Tajima, *Synth. Met*., **2014**, *197*, 175-181.
" Separated Crystallization of Donor and Acceptor in Oligo(*p*-phenylenevinylene)-Naphthalenediimide Dyad Films"

[6] **S. Izawa**, K. Nakano, K. Suzuki, K. Hashimoto, and K. Tajima, *submitted*.
"Dominant Effects of First Monolayer Energetics at Donor/Acceptor Interfaces on Organic Photovoltaics"

Others

[7] Y. Zhong, A. Tada, **S. Izawa**, K. Hashimoto, and K. Tajima, *Adv. Energy Mater.* **2014**, *4*, 1301332-1301340.
" Enhancement of V_{OC} without Loss of J_{SC} in Organic Solar Cells by Modification of Donor/Acceptor Interfaces"

[8] E. Zhou, M. Nakano, **S. Izawa**, J. Cong, I. Osaka, K. Takimiya, and K. Tajima, *Macro. Lett.*, **2014**, *3*, 872-875.
"All-Polymer Solar Cell with High Near-infrared Response Based on a Naphthodithiophene Diimide (NDTI) Copolymer"

[9] Y. Zhong, **S. Izawa**, K. Hashimoto, K. Tajima, T. Koganezawa, and H. Yoshida, *J. Phys. Chem. C*, **2015**, *119*, 23-28.
"Crystallization-Induced Energy Level Change of [6,6]-Phenyl-C_{61}-Butyric Acid Methyl Ester (PCBM) Film: Impact of Polarization Energy"

[10] K. Nishio, S. Kato, **S. Izawa**, T. Pornpitra, T. Nishiwaki-ohkawa, K. Hashimoto, and S. Nakanishi, *submitted*.
" Electrochemical Detection of Circadian Redox Rhythm in Cyanobacterial Cells via Extracellular Electron Transfer "